[03]

Eur. J. Inorg. Chem. 2009, 321–452

D 3715

3/2009
3rd January Issue

EurJIC
European Journal of Inorganic Chemistry

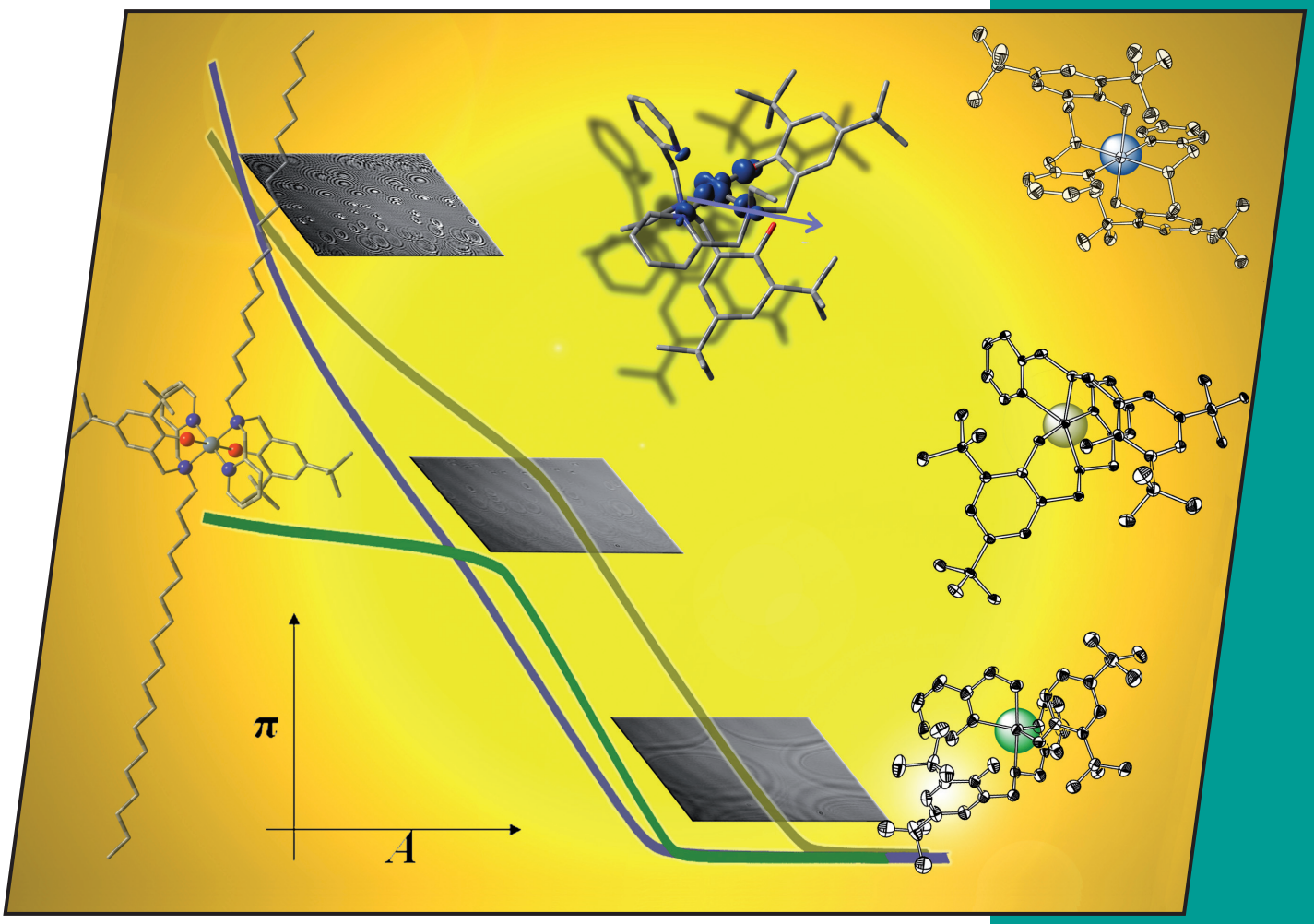

Cover Picture

Cláudio N. Verani et al.

Metallosurfactants with Asymmetric Headgroups

Microreview

Pedro Tartaj

Supramagnetic Composites: Magnetism with No Memory

A Journal of

ChemPubSoc Europe

WILEY-VCH

www.eurjic.org

EJICFK (3) 321–452 (2009) · ISSN 1434-1948 · No. 3/2009

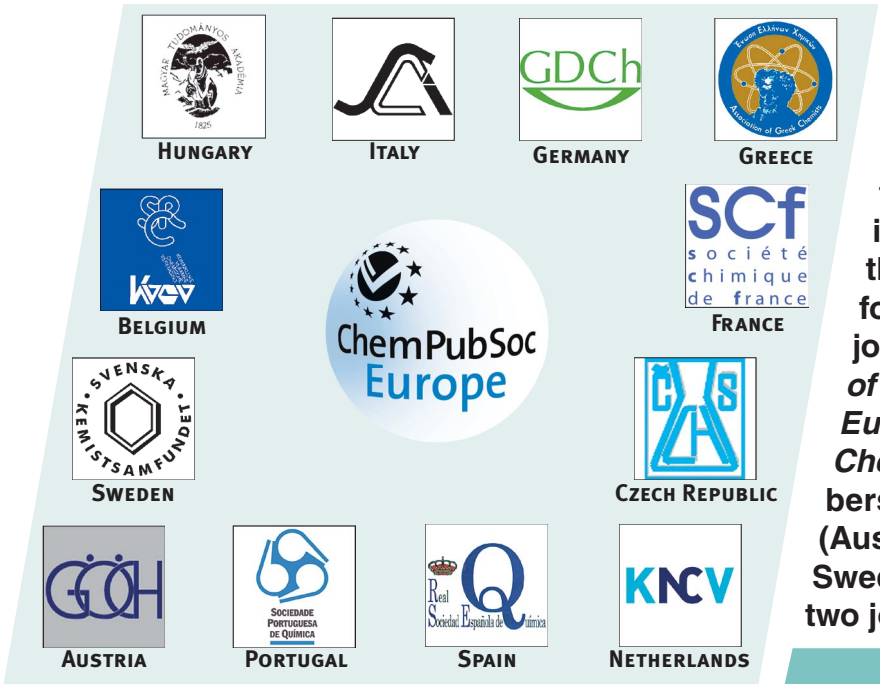

A union formed by chemical societies in Europe (ChemPubSoc Europe) has taken the significant step into the future by merging their traditional journals, to form two leading chemistry journals, the *European Journal of Inorganic Chemistry* and the *European Journal of Organic Chemistry*. Three further members of ChemPubSoc Europe (Austria, Czech Republic and Sweden) are Associates of the two journals.

COVER PICTURE

The cover picture shows an artistic rendition of the main chemical motifs in the paper, namely, a metalloamphiphile, compression isotherms, and Brewster angle micrographs, along with model complexes with distinctive protonation states. Details are discussed in the article by C. N. Verani et al. on p. 345ff.

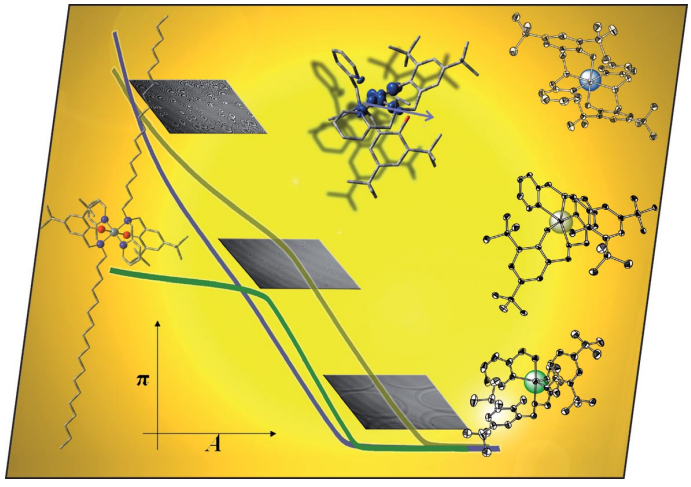

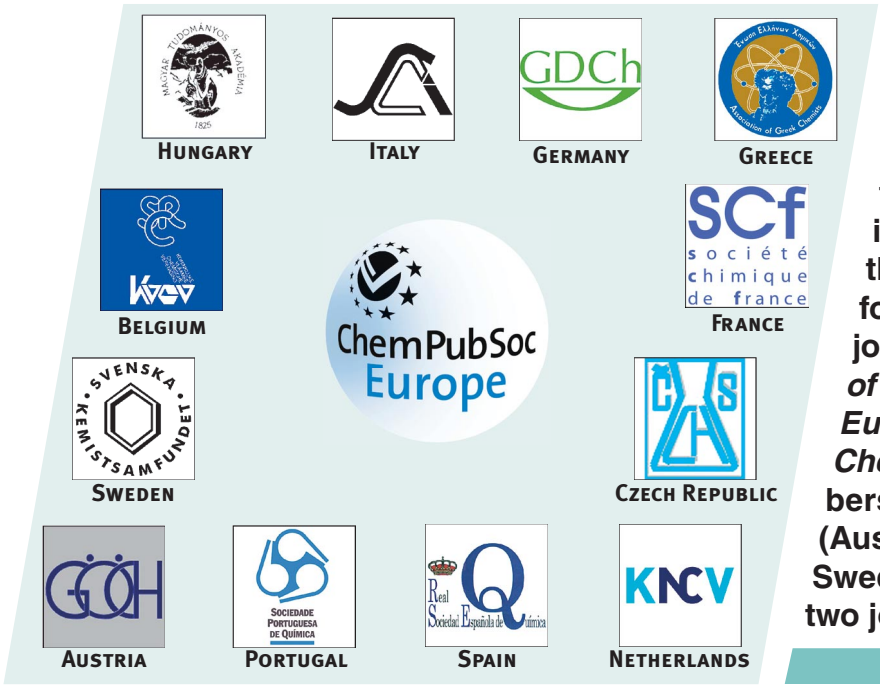

A union formed by chemical societies in Europe (ChemPubSoc Europe) has taken the significant step into the future by merging their traditional journals, to form two leading chemistry journals, the *European Journal of Inorganic Chemistry* and the *European Journal of Organic Chemistry*. Three further members of ChemPubSoc Europe (Austria, Czech Republic and Sweden) are Associates of the two journals.

COVER PICTURE

The cover picture shows an artistic rendition of the main chemical motifs in the paper, namely, a metalloamphiphile, compression isotherms, and Brewster angle micrographs, along with model complexes with distinctive protonation states. Details are discussed in the article by C. N. Verani et al. on p. 345ff.

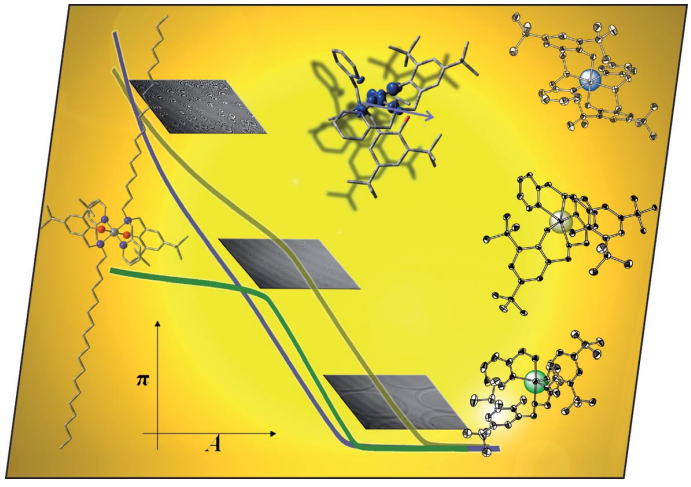

CONTENTS

MICROREVIEW

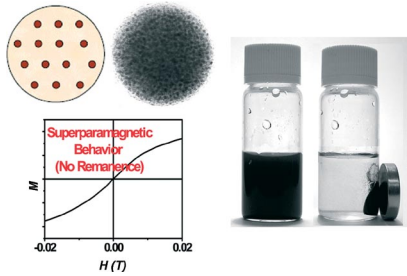

Superparamagnetic composites represent a good example of how mixing at the nanoscale solves fundamental and technological challenges.

FULL PAPERS

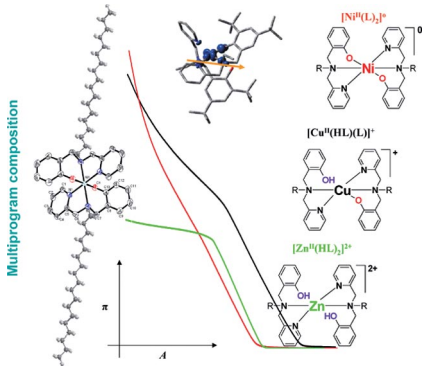

Metallosurfactants containing Ni^{II}, Cu^{II}, and Zn^{II} ions were synthesized and studied by compression isotherms and Brewster angle microscopy. Structure/function relationships between amphiphilic properties, coordination modes, and protonation status were drawn based on archetypical modeling and DFT calculations.

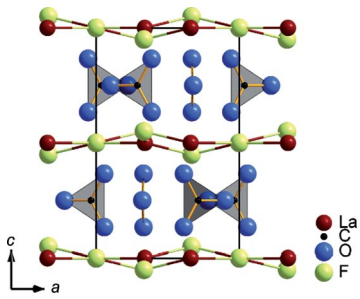

Solution-born, precipitated $LaF[CO_3]$ with a *bastnaesite*-type structure was used as a precursor for the synthesis of three forms of LaOF by thermal decomposition. The three LaOF forms were tested as host materials for Eu^{3+}-doped red phosphors on the basis of both the fluoride oxocarbonates and the different oxide fluoride phases.

Zinc Complexes

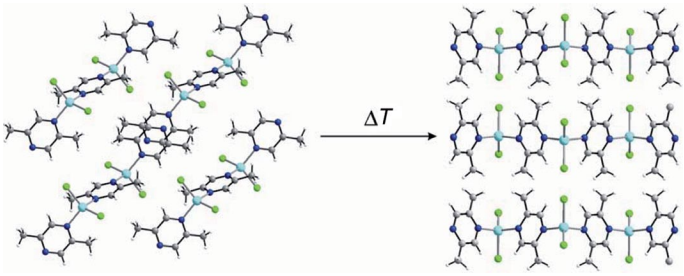

Keywords: Coordination compounds / N ligands / Synthesis design / Structure elucidation / Thermal reactivity

Eight new halidozinc(II) coordination compounds with 2,5-dimethylpyrazine as a ligand were prepared and characterized. Their structures and thermal properties were determined. Upon heating, the ligand-rich compounds transform quantitatively into new ligand-deficient compounds.

Copper(II) Compounds

The dimensionality of [2-amino-5-(pyridin-2-yl)-1,3,4-oxadiazole]copper(II) entities and their 4-*N*-methyl derivatives largely depends on the coligands employed and the experimental parameters. Their magnetic properties and nuclease activity are explored.

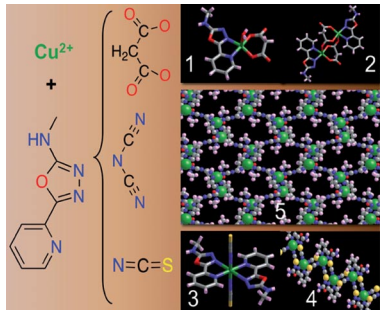

Keywords: Copper / DNA cleavage / Magnetic properties / Oxadiazole / Structure elucidation

Bioorganometallic Chemistry

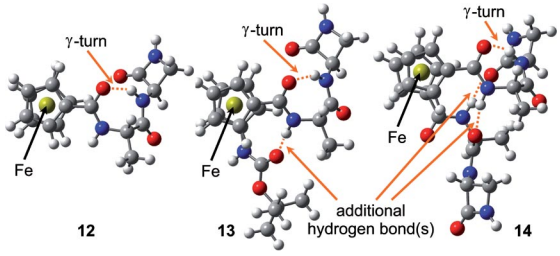

Keywords: Conformation analysis / Density functional calculations / Hydrogen bonds / Metallocenes / Molecular modeling

The synthesis and characterization of ferrocene bioconjugates with alanine and the β-lactam [3-amino-1-(4-methoxyphenyl)-4-phenyl-β-lactam (≡ Alm)] Fc-CO-Ala-Alm (**12**), Boc-Fca-Ala-Alm (**13**), and Fn(CO-Ala-Alm)$_2$ (**14**) is reported. The conformational preferences of these organometallic peptidomimetics in solution were determined experimentally and corroborated theoretically by DFT calculations.

Anion Coordination Effects

A pendant-armed crown ether containing benzimidazole pendants (L^4) forms mononuclear complexes with Co^{II}, Ni^{II}, Cu^{II}, and Zn^{II} perchlorates, which upon treatment with chloride anions readily convert into dimeric species of the general formula $[M_2(L^4)(Cl)_2(H_2O)_n](ClO_4)_2$ (M = Co, Cu, n = 0; M = Ni, n = 2).

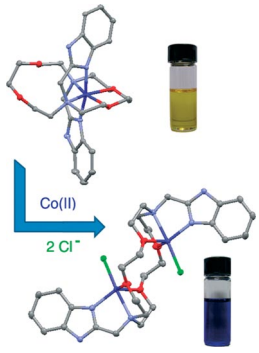

Keywords: Macrocyclic ligands / Crown compounds / X-ray diffraction / N,O ligands / Transition metals

CONTENTS

Amidometal Chemistry

Keywords: Aluminium / N ligands / Ligand transfer / Rare earths / Silylamide route

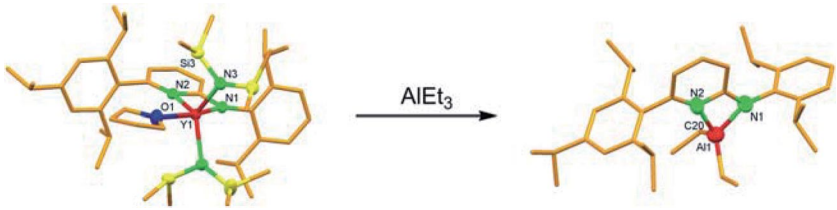

Aminopyridinato-stabilized (silylamido)-lanthanoid complexes were synthesized and investigated with regard to coordinative chain transfer polymerization. Such complexes are not stable in the presence of alkylaluminium compounds and decompose by aminopyridinato ligand transfer from the rare earth metal to the aluminium atom.

Cluster-Bridged Metallacycles

Keywords: Transition metals / N ligands / Self-assembly / Structure elucidation / Electrochemistry

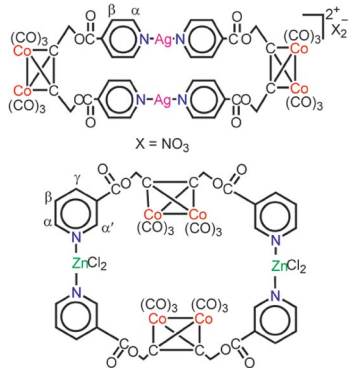

The self-assembly of isomeric bipyridine ligands [(4-$C_5H_4NCO_2CH_2)_2C_2Co_2(CO)_6$] and [(3-$C_5H_4NCO_2CH_2)_2C_2Co_2(CO)_6$] with transition-metal compounds results in the formation of novel metallamacrocycles and 2D polymers in high yields.

Hydroamination Catalysts

Keywords: Titanium / N ligands / Bis(phenolato) ligand / Hydroamination / Homogeneous catalysis

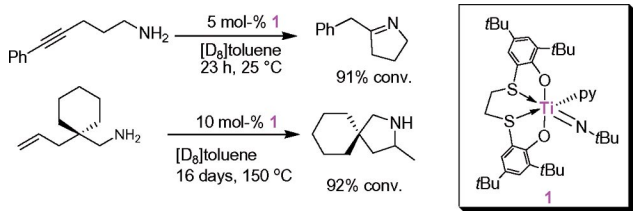

Imido and amido titanium catalysts containing a [OSSO]-type tetradentate bis(phenolato) ligand were readily synthesized and characterized. The imido titanium catalysts showed good activity in both intramolecular aminoalkyne and aminoalkene hydroamination.

Magnetic Effects

Keywords: Reaction conditions / Nickel / Nanostructures / Microwave absorption / Magnetic properties

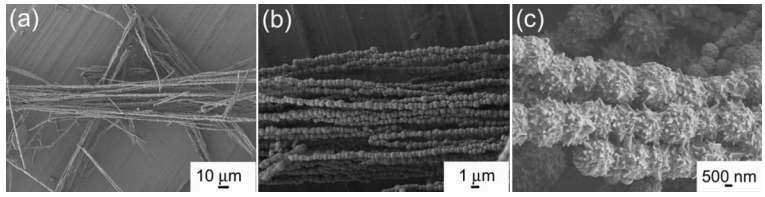

The formation and properties of 1D nickel wires can be influenced by magnetic fields. The magnetic properties of a sample formed in a magnetic field are improved relative to those of a sample formed in the absence of an applied field. Moreover, microwave absorption is enhanced, indicating that the anisotropic wires are not simply an assembly of particles, but that the magnetic domain structure in the wires has been changed by the applied field.

By the reaction of fluorides with liquid ammonia the new compounds $[MF_4(NH_3)_4F_4]\cdot NH_3$ (M = Zr, Hf), N_2H_7F, and $[Ag(NH_3)_2]F\cdot 2NH_3$ were obtained. The latter is the first diaminesilver(I) halide characterized by single-crystal X-ray analysis, and N_2H_7F presents the first ammoniate of ammonium fluoride.

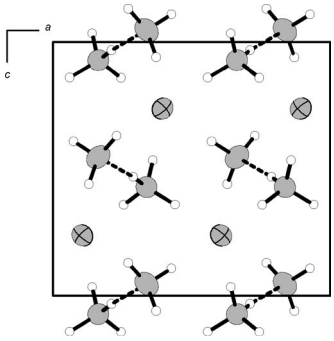

Keywords: Fluorides / Ammonia / Hafnium / Zirconium / Silver

* Author to whom correspondence should be addressed.

Supporting information on the WWW (see article for access details).

If not otherwise indicated in the article, papers in issue 2 were published online on December 30, 2008

Photosensitizers

A. Ikeda,* M. Nagano, M. Akiyama, M. Matsumoto, S. Ito, M. Mukai, M. Hashizume, J.-i. Kikuchi, K. Katagiri, T. Ogawa, T. Takeya

Photodynamic Activity of C_{70} Caged within Surface-Cross-Linked Liposomes

A fierce fullerene in a cage: C_{70} encapsulated into a surface-cross-linked liposome (a morphologically stable cerasome) was prepared by an exchange reaction. The photodynamic activity of the cerasome with incorporated C_{70} in HeLa cells was similar to that of a lipid membrane with incorporated C_{70}, indicating that the cerasome can be used in photodynamic therapy without the need for prior drug release from the cerasome.

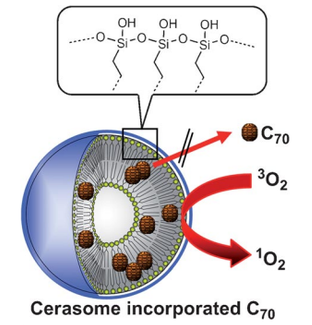

Chem. Asian J.
DOI: **10.1002/asia.200800271**

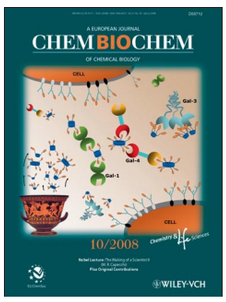

Kinase Inhibitors

G. E. Atilla-Gokcumen, N. Pagano, C. Streu, J. Maksimoska, P. Filippakopoulos, S. Knapp, E. Meggers*

Extremely Tight Binding of a Ruthenium Complex to Glycogen Synthase Kinase 3

Perfect match: An organoruthenium complex with at most a low picomolar binding constant for glycogen synthase kinases 3 is reported, whose binding to the ATP-binding site has been analyzed by X-ray crystallography. The complex, (R_{Ru})-**NP549**, is one of the most potent protein kinase inhibitors reported to date, almost four orders of magnitude more potent than the related natural product staurosporine.

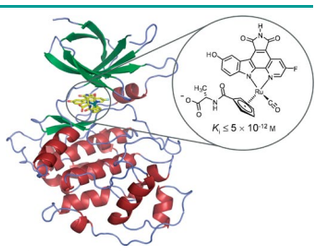

ChemBioChem
DOI: **10.1002/cbic.200800489**

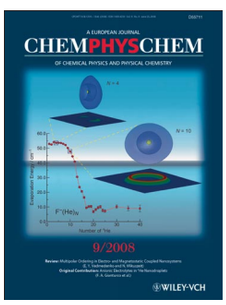

Quantum Dots

P. Ball*

Water as a Biomolecule

Busy busy busy: Water is not a passive solvent in biology, but plays an active role in many biomolecular and cell processes. It can be regarded as a kind of biomolecule in its own right, adapting its structure and dynamics to the biological macromolecules and other cell solutes that it accommodates. In particular, water may hold the key to the way some proteins interact, fold and bind their substrates.

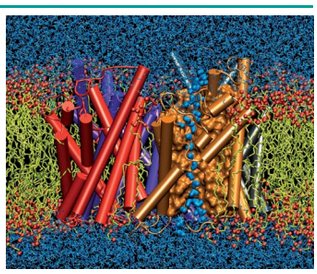

ChemPhysChem
DOI: **10.1002/cphc.200800515**

Virtual Screening

E. Proschak, H. Zettl, Y. Tanrikulu, M. Weisel, J. M. Kriegl, O. Rau, M. Schubert-Zsilavecz, G. Schneider*

From Molecular Shape to Potent Bioactive Agents I: Bioisosteric Replacement of Molecular Fragments

Ligand-based virtual screening: By means of shape- and pharmacophore-based virtual screening, a potent PPARα-selective activator was identified from a large compound collection with minimal experimental effort. This compound represents a scaffold-hop from known PPAR agonists and provides proof-of-concept for a novel ligand-based virtual screening approach.

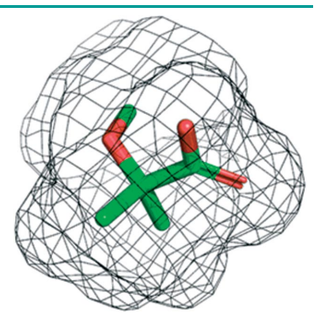

ChemMedChem
DOI: **10.1002/cmdc.200800313**

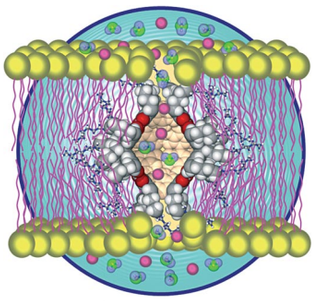

Angew. Chem. Int. Ed.
DOI: **10.1002/anie.200804099**

Ion Transport

O. V. Kulikov, R. Li, G. W. Gokel*

A Synthetic Ion Channel Derived from a Metallogallarene Capsule That Functions in Phospholipid Bilayers

Changing the channel: Dodecanal and pyrogallol were condensed to give a tetramer, which was crystallized as the bilayer and the hexameric molecular capsule. A copper-seamed metallogallarene capsule functioned as an ion transporter and showed selectivity for potassium over chloride ion transport in a phospholipid bilayer (see picture). The capsule also showed voltage-dependent gating of its open–close behavior when examined in asolectin membranes.

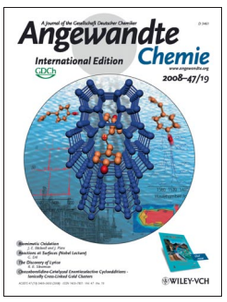

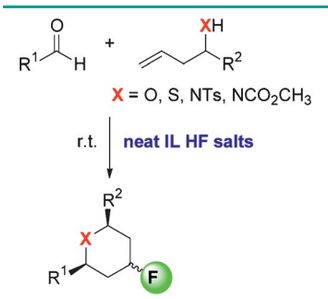

Eur. J. Org. Chem.
DOI: **10.1002/ejoc.200800872**

Fluorocyclization

Y. Kishi, S. Inagi, T. Fuchigami*

Prins Cyclization in Ionic Liquid Hydrogen Fluoride Salts: Facile and Highly Efficient Synthesis of 4-Fluorinated Tetrahydropyrans, Thiacyclohexanes, and Piperidines

Prins cyclization of homoallylic alcohols with various aldehydes was investigated in ionic liquid hydrogen fluoride (HF) salts, which played roles as a reaction medium, a catalyst, and a fluorine source. The reaction afforded the corresponding 4-fluorinated tetrahydropyrans in excellent yields with a high stereoselectivity (*cis* form exclusively). Thia- and aza-Prins cyclization were also studied.

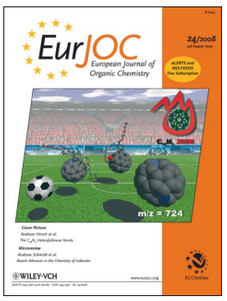

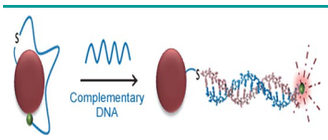

Chem. Eur. J.
DOI: **10.1002/chem.200801812**

Gold Nanoparticles

J. Griffin, A. K. Singh, D. Senapati, P. Rhodes, K. Mitchell, B. Robinson, E. Yu, P. C. Ray*

Size- and Distance-Dependent Nanoparticle Surface-Energy Transfer (NSET) Method for Selective Sensing of Hepatitis C Virus RNA

Size matters! This article demonstrates for the first time that size- and distance-dependent nanoparticle surface-energy transfer (NSET) properties of gold nanoparticles can be used for recognizing hepatitis C virus RNA sequences (see scheme) sensitively (300 fM concentration) and selectively (single-base mutations) in a homogeneous format.

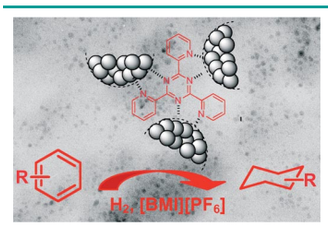

ChemSusChem
DOI: **10.1002/cssc.200800194**

Biphasic Catalysis

B. Léger, A. Denicourt-Nowicki, H. Olivier-Bourbigou, A. Roucoux*

Rhodium Colloidal Suspensions Stabilised by Poly-N-donor Ligands in Non-Aqueous Ionic Liquids: Preliminary Investigation into the Catalytic Hydrogenation of Arenes

In a state of suspension: Colloidal suspensions of Rh^0 nanoparticles stabilised by polynitrogen ligands such as 2,4,6-tris(2-pyridyl)-s-triazine were prepared in the ionic liquid l-*n*-butyl-3-methylimidazolium hexafluorophosphate ([BMI][PF_6]) by chemical reduction of Rh^{III}. The resulting suspensions of ligand-stabilised metallic nanoparticles were then applied as catalysts in the hydrogenation of arenes with excellent results.

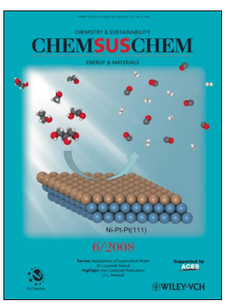

DOI: 10.1002/ejic.200800875

Superparamagnetic Composites: Magnetism with No Memory

Pedro Tartaj*[a]

Keywords: Magnetic properties / Organic–inorganic hybrid composites / Nanotechnology / Mesoporous materials / Polymers

The past five years have witnessed a renewed interest in the field of superparamagnetic composites driven by both the excitement of understanding individual and cooperative properties at the nanoscale and the potential for the use of such composites in catalysis, magneto-optics, and specially bioscience, where new applications are emerging. The basis for the interest in superparamagnetic composites lies in the combination of superparamagnetic nanoparticles with matrixes of different nature. Superparamagnetic nanoparticles endow the composites with adequate magnetic functionality (guiding, monitoring, heating), while the matrixes improve stability (sedimentation, shielding), chemical functionality, and compatibility (hydrophobicity or hydrophilicity, toxicity, stealth).

1. Introduction

Superparamagnetic composites (SPCs) represent a good example of how the adequate combination of at least two components could solve or help to solve fundamental and technological challenges. These composites are model systems to understand individual and cooperative properties at the nanoscale and have the potential to be used in catalysis, magneto-optics, and specially bioscience, where new applications are emerging.[1–8]

Particularly interesting physics occurs when superparamagnetic nanoparticles (SPNPs) are dispersed in matrixes of different nature, as in the case of SPCs.[1,9–11] For example, interparticle interactions arising from dipole–dipole interactions can become significant. The result is that the behavior of SPCs will not longer be governed by the intrinsic anisotropy energy of the nanoobject but also by the coupling with its neighbors.[12] The potential of SPCs to be used in catalysis, magneto-optics, and specially bioscience lies in the advantages of combining SPNPs with matrixes of different nature. SPNPs are characterized by the absence of remanence (no magnetic memory) when the external magnetic field is switched off and can quickly respond to magnetic fields. Thus, SPNPs endow the SPCs with magnetic functionality (guiding, which is obvious, and monitoring and heating both due to magnetic relaxation phenomena) while reducing the probability for the formation of irreversible aggregates associated with magnetic memory effects (dipolar interactions are also present in SPNPs, so total exclusion of magnetically driven aggregation is not possible). The matrixes improve stability (sedimentation, shielding), chemical functionality, and compatibility (hydrophobicity or hydrophilicity, toxicity, stealth). Polymer matrixes that enhance stability and biocompatibility are frequently used to disperse SPNPs. In fact, many polymeric SPCs have been developed as magnetic carriers in separation processes including proteins, DNA, cells, and bacteria.[13] Liposomes, polyelectrolyte multilayer microcapsules, or micelles are also typical examples of organic matrixes that can be used for encapsulation of SPNPs. However, organic matrixes still face unsolved problems, such as their limited chemical and mechanic stability, swelling, and susceptibility to microbiological contamination.[14] As an alternative, inorganic coatings do not experience swelling or porosity changes with a change in pH, and they are not vulnerable to microbial attacks.[15] They also effectively protect doped molecules

[a] Instituto de Ciencia de Materiales de Madrid (CSIC), Campus Universitario de Cantoblanco,
28049 Madrid, Spain
E-mail: ptartaj@icmm.csic.es

Pedro Tartaj graduated in Physical Chemistry from the Universidad Autónoma de Madrid and obtained his Ph.D. in Materials Chemistry. He developed his scientific career in three different countries (Spain, US, and UK), mainly working in all aspects related to colloids. He holds a permanent position at the Instituto de Ciencia de Materiales de Madrid (CSIC). His current research interests lie in nanoparticulate materials displaying properties that are the result of finite and surface size effects (for details visit www.icmm.csic.es/ptartaj).

(enzymes, drugs, etc.) against denaturation induced by extreme pH and temperature.[16,17] Whatever applications SPCs are used for, the renewed interest in the field of SPCs arises from biomedical applications such as magnetic resonance imaging, hyperthermic treatment of malignancy, and drug delivery/targeting. In catalysis, guiding the reaction while avoiding substantial aggregation is the main application of SPCs. Of course, some SPCs can catalyze chemical reactions in a highly efficient way. However, this is a parallel consequence associated with the conditions that must be satisfied for the formation of those SPCs. As we will describe below, the superparamagnetic effect is a finite-size effect that is observed within the nanoscale (we can actually indistinctly talk about superparamagnetic composites or superparamagnetic nanocomposites). It happens that some of the nanomaterials used to implement the superparamagnetic effect can also catalyze chemical reactions. A similar explanation (scattering must be diminished) can be given for the use of SPCs for magneto-optical applications such as sensors based on the Faraday effect.[18]

Even though this microreview is presented in an inorganic chemistry forum, the nature of the review (the title includes the word superparamagnetic) points to the importance of this physical property. Thus, we firstly describe the concept of superparamagnetism and identify the factors that could make some composites present such an effect. In this part of the review, we are especially motivated to clarify some concepts about the possible presence of interparticle interactions. This is important, because their presence could affect the reliability of some experimental parameters used to obtain information on the intrinsic properties of SPNPs. From the chemistry standpoint, the limited size of this microreview and the existence of a wide variety of reviews dealing with magnetic nanoparticles have prompted us to explain and describe some recent examples that to our understanding can open some new avenues in the field of SPCs. For example, we describe some examples in which smart or biodegradable polymers are used as matrixes to implement new functionalities. We also describe some examples in which the use of inorganic matrixes provides the SPCs with multifunctionality. Readers interested in particular aspects of this review can obtain additional information from the reviews that have appeared in the last five years.[1–11,13,19–29]

2. Theoretical Aspects of Superparamagnetism

2.1. Definition and Parameters Affecting Superparamagnetism

The first aspect to remark is that superparamagnetism is a finite-size effect. Magnetic particles below a critical diameter cannot support more than one domain and are thus described as single-domain. This critical diameter is approximately, $2A_{1/2}/M_S$ (A: exchange constant, M_S: moment per unit volume),[30] and for typical materials its value is 10–100 nm. Much of the behavior of single-domain particles can be described by assuming that all the atomic moments are rigidly aligned as a single giant spin. For a single-domain magnetic particle of volume V to hold its magnetic polarization in the face of thermal agitation requires that its magnetic anisotropy energy KV far exceed the characteristic thermal energy k_BT, that is $KV >> k_BT$. For example, a typical criterion for data storage lifetime is $KV/k_BT > 50$–80.[31] The superparamagnetic effect occurs when the magnetic anisotropy energy is too small to prevent thermal fluctuations from spontaneously reversing the grain magnetization direction (Figure 1).

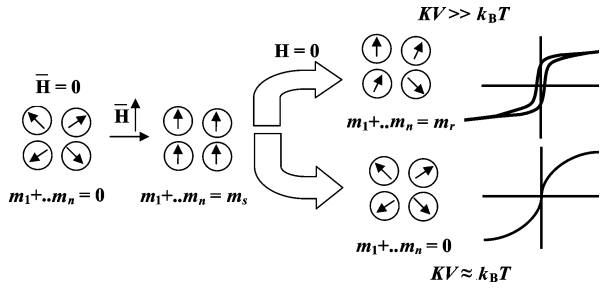

Figure 1. A simple schematic representation of the superparamagnetic effect in absence of interparticle interactions. In absence of a magnetic field, all the moments point to the easy directions (single domains are randomly oriented and the sum of magnetic moments is zero). When a high magnetic field is applied, all moments are oriented parallel to the field, and the magnetic moment reaches its highest value. After the field is switched off, two scenarios can be expected. In the scenario shown in the upper right, the thermal energy (k_BT) is not sufficient to overcome the anisotropy energy barrier (KV), and magnetic memory is developed. The sum of magnetic moments equals to the so-called "remanence magnetization" (experimentally we observe the typical hysteresis loop associated with data recording). In the scenario shown in the lower right, the thermal energy (k_BT) overcomes the anisotropy energy barrier (KV), and as a result no magnetic memory is developed (superparamagnetic effect). The sum of magnetic moments equals to zero as in the initial state (experimentally we observe reversibility, that is, no hysteresis). Importantly, these two scenarios are time-dependent, so using different techniques such as a vibrating sample magnetometer or Mössbauer spectroscopy (different measurement times) can lead to different results. In fact, thermal energy will be able to relax any system to its initial conditions if the system is left without perturbation for sufficient time interval.

Superparamagnetism is a purely finite-size effect that is observed when the particle length is within the nanoscale. However, the superparamagnetic limit also depends on the magnetic anisotropy constant, which, in bulk materials, has contributions from magnetocrystalline, magnetoelastic, and shape anisotropy. For example, in bulk, the magnetocrystalline anisotropy of metallic α-Fe (4.8×10^4 J m^{-3}) is about 10 times higher than that of iron oxide ferrites (magnetite, Fe_3O_4 or maghemite γ-Fe_2O_3, 4.7×10^3 J m^{-3}). Thus, it is rather normal that SPCs containing α-Fe as nanodispersed phase can only be prepared when the α-Fe sizes are about 5 nm.[32,33] Shape anisotropy (elongated nanoparticles) is another important term that must be taken into account. In fact, needlelike FeCo metallic nanomagnets coated with an oxide protecting layer and deposited longitudinally on a film are routinely used for the storage of digital and analog signals in the area of advanced flexible media.[34]

As the particle size decreases, a large percentage of all the atoms in a nanoparticle become surface atoms, which implies that surface and interface effects become more important. For example, near surfaces, the magnitude of the magnetic moment per atom in ferromagnetic metals can change drastically as a result of reduced coordination at the surface.[35] In contrast, in ionic compounds the moment of each ion is less sensitive to the proximity of a surface, because the distribution of valence electrons is highly localized. However, the orientation of each moment can be altered as a result of competing exchange interactions in an incomplete coordination shell for surface ions. This can lead to a disordered spin configuration near the surface and a reduced average net moment relative to the bulk material.[36] All of these effects have an influence on the size in which the superparamagnetic limit is observed. A clear example is recent experiments in which exchange-coupled ferromagnetic (FM) and antiferromagnetic (AFM) nanostructures experience an improved thermal stability, that is, an extra interfacial anisotropy term is developed.[37] Dobrynin et al., in a study of the magnetic properties of oxidized 3-nm Co nanoparticles embedded in an amorphous Al_2O_3 matrix, have shown that there is a critical grain size for the interfacial exchange energy to dominate over other energies in the system.[38] Surface effects are also very important in SPCs, because the matrix may affect the magnitude of the magnetization due to quenching of surface moments or interactions with d electrons.[39]

2.2. Is Superparamagnetism Affected by Collective Phenomena?

For sufficiently dilute dispersions, interparticle interactions are negligible, and the crossover to the blocked state with decreasing temperature depends only on the physical properties of the individual particles. When the interparticle interactions become significant, the behavior of a magnetic moment is not only governed by its own intrinsic anisotropy energy but also by the coupling with its neighbors. Interparticle interactions may arise from dipole–dipole interactions between nanoparticles or the exchange interactions occurring between the magnetic ions at the surface of neighboring particles. When the interactions are strong enough, the particles may behave as a spin glass.

A useful tool to characterize SPCs is to carry out zero-field cooling (ZFC) experiments. ZFC curves are routinely used to estimate blocking temperatures from the temperature in which those curves reach a maximum (T_{max}). In the framework of a Néel model, which assumes an assembly of independent single-domain particles, the ZFC might be expected to exhibit T_{max} at the blocking temperature, T_B, at which point the relaxation time equals the time scale of the magnetization measurements. A distribution in particle size will result in a shift of the maximum to a temperature defined by $T_{max} = \beta<T_B>$, where $<T_B>$ is the mean blocking temperature and β is in the order of 1.0–2.0. Dipolar interactions between SPNPs incorporated into the matrixes also affect the temperature at which T_{max} appears and make difficult to estimate the real values of $<T_B>$ from the ZFC curves.[40] In fact, ZFC experiments show an increase in the temperature at which the ZFC peak reaches its cusp with the increase in volume packing fraction in γ-Fe_2O_3/SiO_2 SPCs, Fe/SiO_2 SPCs, and FePt/ferritin assemblies.[33,41,42] This is important because very frequently the value of $<T_B>$ is associated with T_{max} and used to estimate the volume size, V, or the magnetic anisotropy constant, K, of the nanodispersed phase through the well-known expression $KV = k_B T_B \ln(\tau_m/\tau_0)$, where k_B is the Boltzmann constant, τ_0 is the characteristic time and τ_m is the measuring time. This can only be done when the interparticle interactions are negligible. A few words also deserves the use of the expression $KV = k_B T_B \ln(\tau_m/\tau_0)$. Considering the typical values for τ_0 and assuming $\tau_m \approx 100$ s for a measurement carried out in a vibrating sample magnetometer (VSM), $\ln(\tau_m/\tau_0)$ takes on the typical value of 25. However, τ_m is different if data are taken, for example, from Mössbauer spectroscopy.

In systems containing $Fe^{III}_2Fe^{II}_{1-x}O_{4-x}$ nanosized spinels, values of the blocking temperature can be derived from the decay of remanence as a function of temperature in the region where the SPCs composites are magnetically blocked by assuming a lognormal size distribution. However, in general the magnitude of interparticle effects must be estimated by using more sophisticated approaches. For example, the presence and magnitude of dipolar interactions can be analyzed within the framework of a mean-field model.[12,33,43–46] In this model, the dipolar interaction can be characterized by a parameter T^*, proportional to the dipolar energy, appearing in the denominator of a modified Langevin function analogous to the Curie–Weiss law. The parameter T^* can be obtained from Equation (1).

$$T^* = \frac{\alpha}{k_B}\frac{M_s^2}{N} \quad (1)$$

where α is a proportionality constant derived from the sum of all dipolar energy contributions,[47] M_s is the saturation magnetization, N is the number of moments per unit volume, and k_B is the Boltzman constant. α and N can obtained from the low-field susceptibility data, χ, by using Equation (2).

$$\frac{\rho}{\chi} = 3kN\left(\frac{T}{M_s^2}\right) + 3\alpha \quad (2)$$

If the SPCs can be modeled using this theory, we can expect a linear dependence of the quantity ρ/χ on the ratio T/M_s^2 (where T is the temperature and M_s is the value of saturation magnetization at which the magnetization curves are registered). This model has been shown to be adequate to describe the magnetic behavior of a series of SPCs with very different composition.[12,33,43–46] Very recently, it has been shown very useful to describe the collective properties of SPCs (including clustering effects) that have practical

interest as magnetic carriers in the fields of bioscience and catalysis.[48] SPCs with practical interest are those with particle sizes within the colloidal size regime and whose magnetism is provided by SPNPs that are stable, nontoxic, and have adequate magnetic moment.

3. Superparamagnetic Composites (SPCs)

The search for materials able to fulfil some of the requirements needed in catalysis or biotechnological applications such as enzyme immobilization, drug delivery, separation, requires the SPNPs to be dispersed/coated/encapsulated in organic or inorganic matrixes (in other words, it requires the formation of SPCs).

3.1. Polymeric Matrixes

Smart polymers are well known for their quick response to the changing environment. The surface of nanoparticles can be modified by smart polymers with particular functional groups that can change physical-chemical properties and colloidal properties when stimulated by external factors such as temperature, pH, ionic strength, and magnetic field. The fabrication of SPCs with a combination of thermosensitive and magnetic properties has received great interest for instant dispensability, thermoreversible formation of magnetic fluids, and novel magnetoresponsive properties.[28,29] Special interest is gained by the magnetic heatability of magnetic particles that allows the activation of thermal effects by the application of a high-frequency electromagnetic field. This field could induce rotational motion of the SPNPs that are coated with the polymer chains or embedded in a polymeric matrix.[49] The energy dissipated when the system cannot follow the oscillating magnetic field causes an increase in temperature in the medium surrounding the thermosensitive polymer. Poly(*N*-isopropylacrylamide) (PNIPAM) is a smart polymer that can respond to the change in external temperature.[50] It presents a coil-to-globule transition in aqueous solution when the temperature is raised above the lower critical solution temperature at around 32 °C, a temperature that can be achieved by copolymerization with hydrophilic comonomers.[51] SPCs consisting of microspheres with a core (magnetic nanoparticle)–shell (thermosensitive polymer) structure have been prepared by first coating the magnetic nanoparticles with a silica layer followed by functionalization with 3-(trimethoxysilyl)propyl methacrylate for further polymerization of PNIPAM.[52] A variant of this process based on using reverse microemulsion and free radical polymerization allows a better control of coating.[53] Furthermore, if the SPCs are marked with a fluorescent substance, the temperature of the medium surrounding a collection of nanoparticles may be determined by monitoring fluorescence changes.[54]

The porosity and reversibility behavior of polymer-gel SPCs can be exploited for a wide variety of applications. For example, functionalized SPNPs can be incorporated into a polyacrylamide gel structure to obtain a chemical sponge. This sponge can be loaded with microemulsions or micelle solutions for the cleaning of historical stones or painted surfaces without undesired residues.[55] The SPC gel can be shaped as desired and applied to a specific area with fine spatial control of the area. In addition, the adhesion of the SPC to the artifact can be modulated by controlling the polymer cross linking during the chemical synthesis of the sponge.

Some applications based on magnetic separation have few requirements of the type of polymer used; however, others such as those that require intravenous administration must meet strict criteria of being nontoxic, nonimmunogenic, nonantigenic, and biodegradable (with nontoxic byproducts). Polysaccharides fulfil these criteria.[56] The most common natural additive of this family is dextran that can be added either unsubstituted, monosubstituted as carboxydextran or polysubstituted as poly(carboxymethyldextran). Recent investigations, however, aim to prepare SPCs having matrixes composed of biodegradable polymers.

Engineering delivery systems of therapeutic agents has grown into an independent field, transcending the scope of traditional disciplines and capturing the interest of both academic and industrial research. At the same time, the acceleration in the discovery of new therapeutic moieties (chemical, biological, genetic, and radiological) has led to an increasing demand for delivery systems capable of protecting, transporting, and selectively depositing those therapeutic agents to desired sites.[57,58] The obvious advantage of using SPCs with biodegradable polymers for the delivery of biocompounds is that the system can be easily localized by using an external magnetic field and controlled release must be achieved. The biodegradable polymers that are most often used for formulation of therapeutic agents are poly(D, L-lactide) (PLA) and poly(D, L-lactide-co-glycolide) (PLGA), which are FDA approved polymers for clinical application.[59] Formulation of SPCs by biodegradable polymeric particles has been developed in the literature, but their use is limited by size (micrometer range composites) and slow degradation.[60] Very recently, a modified water-in-oil-in-water (w/o/w) double-emulsion technique has been developed for the production of biodegradable poly(lactide-coglycolide)-methoxy poly(ethylene glycol) (PLGA-mPEG) superparamagnetic composites. These SPCs have better magnetic properties and ex vivo imaging effects in comparison with the commercial product Resovist.[59]

3.2. Inorganic Matrixes

As mentioned in the Introduction, organic matrixes still face unsolved problems, such as their limited chemical and mechanic stability, swelling, and susceptibility to microbiological contamination.[14] As an alternative, inorganic coatings do not experience swelling or porosity changes with a change in pH, and they are not vulnerable to microbial attack.[15] They also effectively protect doped molecules (enzymes, drugs, etc.) against denaturation induced by extreme pH and temperature.[16,17]

The development of inorganic SPCs of a large surface area and an accessible porosity is highly attractive for the generalization of the magnetic separation technique to different fields.[61] Magnetically driven separation makes the recovery of catalysts in a liquid-phase reaction much easier than that by cross-flow filtration and centrifugation, especially when the catalysts are in the submicrometer size range. Such small and magnetically separable catalysts could combine the advantages of high dispersion and reactivity with easy separation. In terms of recycling expensive catalyst or ligands, immobilization of these active species on magnetic nanoparticles leads to the easy separation of catalysts in a quasi-homogeneous system.[5] For example, carbon-supported palladium catalysts with a fully accessible pore system show high activity and stability in the hydrogenation of octane, and, more importantly, are easily separated by applying a magnetic field.[62] As an alternative to cooperative surfactant templating in solution, the nanocasting pathways developed over the last ten years, which use hard templates to create ordered replicas, provide promising routes for the preparation of mesostructured materials with novel framework compositions.[63] Nanocasting is the process in which a mold with relevant structures on the length scale of nanometers is filled with another material, and the initial mold is afterwards removed. Nanocasting was introduced by the group of Ryoo, who described the synthesis of mesoporous carbon with an ordered structure, where the replication of the MCM-48 structure led to the formation of a new type of mesoporous carbon material (CMK-1).[64] This technique has been routinely used in recent years for the synthesis of porous SPCs. For example, commercial activated carbon has been used as matrix for the incorporation of SPNPs.[65] The method consists of the formation of SPNPs of iron oxide spinels of uniform and tunable particle size (i.e. 4–8 nm range), which are highly dispersed along the porous structure of the activated carbon. The preparation procedure consists firstly in filling the porosity of the activated carbon with an appropriate amount of $Fe(NO_3)_3 \cdot 9H_2O$ dissolved in ethanol. The filling is followed by the impregnation of the dried sample with an organic reducing agent (ethylene glycol). Finally, the impregnated sample is heat-treated under nitrogen at a moderate temperature to implement the superparamagnetic functionality. A variation of this method allows the preparation of SPCs consisting of superparamagnetic α-Fe homogenously dispersed in the porous structure of the activated carbon.[66] Stabilization of the α-Fe nanoparticles against corrosion is achieved by coating these nanoparticles with a carbon layer (this layer is produced by chemical vapor deposition with benzene as precursor).

Magnetic and plasmonic particles are of increasing interest for biomedical applications.[25] Noble-metal nanostructures are beneficial not only because of their relative ease of biofunctionalization but also for plasmonic biosensing.[67] Unlike quantum dots, these particles do not show optical bistability or blinking, which makes them competitive with fluorophores for quantifying the number of cell surface markers.[68] The main advantages of plasmonic particles are their extremely large molar extinction coefficients and resonant Rayleigh scattering efficiencies, and the exceptional sensitivity of the surface plasmon resonance peak wavelength to changes in the local dielectric environment.[69] The local temperature around nanorods, nanocages, or nanocomposites composed of a dielectric core and an outer thin metal shell can be sharply increased by near-IR (NIR) laser illumination because of the surface plasmon resonance effect.[70] The hyperthermia induced by this effect, in turn, leads to a possible noninvasive thermocidal treatment for cancer.[71] Grafting represents a viable and facile route for the preparation of SPNCs with core/shell structure. Essentially a reactive moiety attached to the surface of the SPNPs directs the formation of the coating. Polymer grafting on the surface of SPNMs is routinely used for the formation of core/shell SPNCs.[72,73] Grafting has been used to prepare monodisperse SPNPs coated with Au nanoparticles with a size of about 20 nm.[68] Owing to the difference in surface energies, gold does not wet an iron oxide surface. The strategy developed by the group of Majetich for preparing bifunctional plasmonic magnetic nanoparticles of around 20 nm was to synthesize monodisperse SPNPs and then attach discrete Au clusters to the surface with bidentate ligands to finally complete the shell through electrodeless deposition of more gold onto the Au clusters. 11-Mercaptoundecanoic acid (MUA) was used as the bidentate ligand. MUA serves as a bridge between the iron oxide and the gold seed clusters. The thiol group of MUA promotes binding of small gold nanoparticles, while the carboxylic acid group attaches to the iron oxide surface (Figure 2).

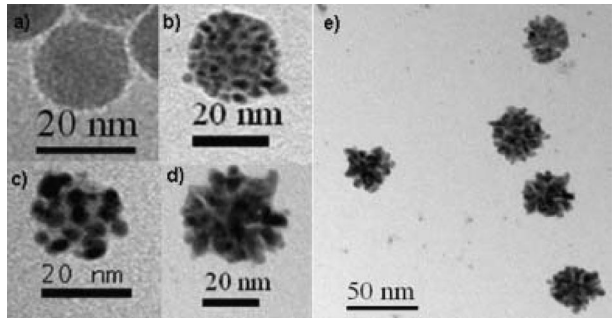

Figure 2. Transmission electron microscopy images of Fe_3O_4 nanoparticles at different stages of the Au coating process: (a) uncoated Fe_3O_4 particle, (b) after binding small Au clusters to the iron oxide particle surface, (c) after reducing more Au to grow the clusters, (d) when the clusters have nearly merged into a complete shell, and (e) final bifunctional nanoparticles with 18 nm iron oxide cores and a gold shell with an average thickness of ca. 5 nm. Reprinted with permission from ref.[68] Copyright 2008 Wiley-VCH.

SPCs are routinely used as contrast agents in nuclear magnetic resonance imaging.[4,8] First introduced as contrast agents in the mid-1980s, these composites have been used in nuclear magnetic imaging for location and diagnosis of brain and cardiac infarcts, liver lesions or tumors, where the composites tend to accumulate at higher levels due to the differences in tissue composition and/or endocytotic uptake processes. Lumirem® (silica-coated iron oxide SPNPs with a diameter of 300 nm) and Endorem® (dextran-coated

iron oxide SPNPs with a diameter of 150 nm) are commercial names of superparamagnetic iron oxides (so called SPIO) available on the market. Sinerem® (dextran-coated iron oxide SPNPs with a diameter of 30 nm) is an example of USPIO (ultrasmall superparamagnetic iron oxide) on the market. Due to their long-circulating properties, USPIOs can be used for blood pool and tumor imaging (experimental imaging) based upon the detection and characterization of lesions by their vascular appearance.

In some technological applications, aggregation of SPNPs in the SPCs is preferred over dispersed nanoobjects. In magnetic separation, the magnetic force, $\vec{F}_m = (\mu_p \cdot \nabla)B$, that can be applied to a particle depends on the magnetic moment of the particle, μ_p. Since $\mu_p = M_s V_p$, where M_s is the saturation magnetization of the material and V_p is the particle volume, a larger size or an aggregate is generally preferable for a strong magnetic response.[68] A particle of 10 nm, for example, cannot be separated with a typical commercial magnet. Another clear but less intuitive example in which aggregation of SPNPs within the SPCs is preferred over good dispersion is the use of SPNPs as contrast agents in nuclear magnetic resonance imaging. It has been reported that the relaxivity (r_2) values can be greatly increased by clustering the so-called T_2 contrast agents in reservoirs such as liposomes or cells.[74] This effect results from the intrinsic mechanism of spin–spin relaxation (T_2 relaxation as opposed to spin-lattice, T_1, relaxation), which relies on the local concentration of the contrast agents. SPCs consisting of magnetic kernels (aggregates of ultrasensitive $MnFe_2O_4$ magnetic nanocrystals wrapped in polymer) and silica–gold nanoparticles have been recently shown to be effective materials for magnetic resonance and hyperthermal applications.[70] $MnFe_2O_4$ nanoparticles were synthesized by the thermal decomposition method and further wrapped and aggregated with polyvinyl alcohol by ultrasonic emulsification. Then, the Stöber method was used to develop a silica coating, which was further functionalized with (3-aminopropyl) trimethoxysilane to allow the attachment of gold nanoparticles.

3.3. Encapsulation in Liposomes and Artificial Capsules

Hollow particles also referred to as capsules have recently attracted considerable attention, because their suitability for emergent applications such as drug delivery vehicles, high efficient catalysts, core/shell composites, dye encapsulation, or immobilization of biomolecules.[75] These materials have the unique feature of providing a protected core that turns out to be suitable to encapsulate a large variety of substances. Liposomes, nanoengineered polyelectrolyte multilayer microcapsules, or micelles are typical examples of capsules. Lipids usually form lamellar bilayer structures over the majority of their phase diagram, and in dilute solutions they form vesicles (from the Latin vesicle, small bubble).[76] Liposomes can be considered as a special class of vesicles, in which the building blocks are lipids. Magnetoliposomes consist of nanometer-sized iron oxide particles encapsulated in liposomes.[77] Several methods have been described for the preparation of magnetoliposomes: dialysis of single unilamellar vesicles in the presence of magnetite nanoparticles;[78] magnetite cores stabilized by lauric acid;[79] or extrusion of a mixture of SPNPs with large phospholipid–cholesterol unilamellar vesicles.[80]

Polyelectrolyte multilayer micro- and nanocapsules were introduced[81,82] as an extension of polyelectrolyte multilayers on flat substrate surfaces.[83] When decomposable colloids are used as templates, they can be removed after completion of the polyelectrolyte multilayer coating, and hollow capsules or shells are obtained. One of the advantages of these capsules is the variability of their physical and chemical properties by variation of composition and fabrication as well as application conditions. Several dozen of natural and synthetic polyelectrolytes or other charged substances are suitable as layer components, e.g. chitosan, poly(diallyldimethylammonium chloride), chitosan sulfate, poly(L-lysine), poly(acrylic acid), dextran sulfate, and proteins. Many of them can be functionalized to provide special surface structures of biological or technical relevance. Of special relevance is the work carried out recently by Sukhoroukov, Mohwald, and co-workers.[84] These authors were able to produce shell-in-shell microcapsules with SPNPs of magnetite located in the inner compartment. The technique involves the fabrication of spherical ball-in-ball particles consisting of two concentric calcium carbonate compartments that can be independently loaded with biopolymers. Through deposition of polyelectrolyte multilayers, these ball-in-ball particles can be employed for the fabrication of completely novel capsule-in-capsule systems containing biomolecules separated by a semipermeable membrane (Figure 3).

Capsules composed by a macroporous core and a mesoporous inorganic shell are also attracting considerable interest.[85–90] Important advantages of the porous inorganic capsules are that they combine a high surface area and a large mesopore volume with good chemical inertness and mechanical stability. They present the possibility to fabricate functional materials made up of nanoparticles confined within macroporous cores or deposited in the porous layer of the capsule. Examples of these nanocomposites have been reported recently.[91–93] The techniques usually employed to fabricate core/shell nanocomposites normally entail first the synthesis of the nanoparticles to be encapsulated and then the growing of a coating layer (normally of silica or carbon). These procedures are somewhat complex and involve a multistep process. Moreover, they give rise to core/shell nanocomposites that in most cases contain only a few nanoparticles confined inside the macroporous core (nanorattles). Alternatively, other methods based on aerosol techniques that are continuous and easily scaleable lead to materials with a nonpermeable shell.[94] Recently, carbon capsules have been filled with a significant amount of SPNPs.[95] The methodology involves first the impregnation of carbon capsules with a solution of $Fe(NO_3)_3$ dissolved in ethanol, which is further dried and exposed to propanoic acid vapors. Finally, the composite is heated to develop the

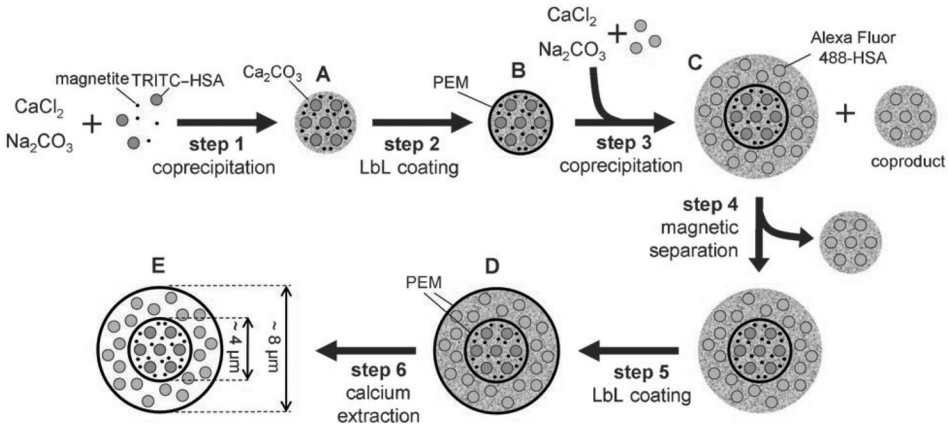

Figure 3. General route for the synthesis of shell-in-shell microcapsules. A: initial core; B: core–shell particle; C: ball-in-ball particle (type I); D: ball-in-ball particle (type II); E: shell-in-shell microcapsule. Reprinted with permission from ref.[84] Copyright 2007 Wiley-VCH.

superparamagnetic functionality. A similar methodology has been used to prepare magnetic mesoporous hollow nanocomposites (diameter ≈ 400 nm) made up of ferrite nanoparticles incorporated to mesoporous shell (shell thickness ≈ 50 nm) of carbon capsules.[96]

4. Conclusions and Outlook

The magnetic behavior of SPCs remains to be better understood. While mean-field theories explain the qualitative behavior of some interacting systems, a more rigorous approach to the problem is needed. For example, recently the behavior of a random arrangement of SPNP- dispersed polymeric matrix has been simulated by using numerical methods.[97] A Monte Carlo method was used to treat the influence of dipolar interaction on the blocking temperature of a random distribution of SPNPs. For the simulation procedure, the energy of each particle is considered to have three main contributions: anisotropy, Zeeman, and dipolar interactions. At low sample concentrations, the blocking temperature remains almost constant, suggesting that particles behave independently of each other as a noninteracting system; at higher sample concentrations, the blocking temperature increases clearly with the volume fraction. Hence, simulation results obtained for a random distribution of SPNPs in a polymer matrix are in good agreement with experimental results.

From the chemistry side, the work carried out during the last years has put SPCs into a mature state. The strict requirements imposed by biomedical applications, the main driving force behind the development of SPCs, make superparamagnetic colloidal composites the SPCs in which more effort should be seen in the upcoming years. The development of processing routes to improve the colloidal stability of the SPCs is thus of extreme importance. Immobilization of organic molecules on SPNPs through silanization reactions is a route to enhance colloidal stability and compatibility.[98] Polymers with enhanced functionalities will be regularly used as matrixes for the formation of SPCs. The control of morphology and size in these SPCs could be achieved by using nanocasting techniques. Filling of porous silica spherical particles with monomers, followed by polymerization and removing of the silica matrix at basic pH is a route to reach that control.[99] In fact, polymeric SPCs with colloidal size and bimodal mesoporous structure have been recently prepared.[100] The number of reports on the encapsulation of SPNPs in silica matrixes is extensive.[33,41,61,94,101–105] However, the search for silica SPCs with pore sizes larger than 3–4 nm and appropriate magnetic and colloidal properties is essential for the adequate immobilization of enzymes, which in general have larger sizes. As pointed out by Schüth and co-workers for applications (mainly catalysis) in which a basic pH is needed, silica cannot be used because it suffers from dissolution.[5] Carbon matrixes represent a good alternative to silica matrixes, because they present a higher chemical stability. Arc, sonochemical, and laser pyrolysis techniques have been already shown to be adequate for the large-scale production of SPCs with good magnetic properties and high chemical stability.[106] Separation of Fe SPNPs coated with carbon, which are byproducts produced in the gram-scale synthesis of single-walled carbon nanotubes by the high-pressure CO process has also been reported to be an adequate method for the large-scale production of this type of SPCs.[107] In any case, though progress has been made in the last years to impart functionality to carbon matrixes, it seems clear that replacement of silica by these matrixes requires significant advances in this direction. The addition of functionalizable polymers to the carbon matrixes, that is, the formation of hybrid matrixes, is a reasonable route to impart new functionalities to the carbon matrixes.[108] For example, quaternized polycholoromethylstyrene (with anion exchange sites) has been recently inserted in the pores of the monodisperse carbon SPCs with spherical shape.[109] The presence of active surface sites (positively charged) can be suitable for the adsorption of negatively charged biocompounds. We have recently proposed the use of zirconia matrixes because of their high stability at different pHs and high reactivity with phosphate compounds.[110] Zirconia easily reacts with phosphate compounds,[111] and in fact is

used as a highly selective adsorbent for compounds containing phosphonic acid.[112] Titania matrixes could also be considered a good replacement to silica, especially because they can impart photocatalytic properties to the SPCs.[113] Alumina matrixes have also been used for dispersion of SPNPs.[114] The problem with alumina is that it also suffers from dissolution at basic pH. Zeolite matrixes have also been used for the stabilization of ultrasmall Co nanoparticles; however, while this is interesting from a fundamental side, the magnetic moment is too low for practical applications.[115]

It is clear that multifunctionality is one of the routes to follow in order to place SPCs into the real world. The combination of magnetic separation with sensing provided by multifunctional SPCs seems one of the most promising approaches on which future developments should be based. In this direction, the so-called bio-barcode method developed by Mirkin and co-workers is worth noting. This group has used SPCs in combination with Au nanoparticles for the ultrasensitive detection of biocompounds.[116] However, other routes that depart from the routine must be followed. For example, while substantial research exists in the field of SPCs having equiaxial structure, no effort has been put in the preparation of SPCs with anisometric shape. The most plausible reason is the difficulty in overcoming the magnetic shape anisotropy. Anisometric and isometric SPCs are likely to behave quite differently both magnetically and when interacting with biological entities. In magnetic resonance imaging, anisometric nanoparticles are expected to influence the relaxation times of neighboring protons in quite a different way from isometric nanoparticles. In hyperthermic treatment of malignancy, substantial changes in relaxation times are also expected. In drug/gene delivery/targeting, apart from the fact that genes are also anisometric, magnetic vectorization is likely to be favored (magnetophoresis is favored in anisometric particles). Regarding the interaction with biological entities, the influence of shape has been well-established in other materials in the recent years. For example, cellular uptake has been found to be dependent on the axial ratio in gold nanoparticles.[117] Nanocylinders have been found to deliver drugs better that nanospheres, because they align with the blood flow and persist in circulation considerably longer than spherical particles.[118] On the other hand, experiments with human blood plasma show that blood clotting above rectangular patches only occurs when the ratio of the lengths of the sides of the rectangle meet a particular criterion.[119] Two approaches are now being considered to produce elongated SPCs. Carbon nanotubes (CNTs) are used as a guest matrix to be coated with iron oxide SPNPs by using the polymer wrapping and layer-by-layer assembly techniques.[120] It was demonstrated that the magnetized CNTs can form aligned chains in relatively small external magnetic fields. Very recently, we have reported the preparation of SPCs consisting of iron oxide SPNPs dispersed in a hematite (α-Fe_2O_3) nanorod matrix and having tunable surface functionality provided by inorganic coatings such as zirconia and alumina.[110] The method we have used combines the superior advantages of the synthesis of nanorods by a carbonate route (say uniformity specially at long axial lengths below 200 nm, adequate particle size and production rate) with the unique characteristics of the electrostatically induced self-assembly methods that under particular conditions (mainly pH and salt and solid concentrations) can produce homogeneous coatings.

The possibility of controlling the interparticle spacing and thus the photonic properties of colloidal assemblies is a very promising approach for enhancing the capabilities of photonic crystals.[121] The choice of magnetic fields as the external stimulus may offer improved spectral tunability, response rate, and facility of integration into existing photonic systems. SPCs consisting of polymer colloids embedded with SPNPs of iron oxide may fulfil these objectives.[122] In addition, macroporosity associated with colloidal structures could also be exploited for different applications.[105]

Acknowledgments

This work has been supported by the Spanish Ministerio de Ciencia e Innovación under contract MAT2008-03224/NAN.

[1] X. Batlle, A. Labarta, *J. Phys. D: Appl. Phys.* **2002**, *35*, R15.
[2] Q. A. Pankhurst, A. J. Connolly, S. K. Jones, J. Dobson, *J. Phys. D: Appl. Phys.* **2003**, *36*, R167.
[3] P. Tartaj, M. P. Morales, S. Veintemillas-Verdaguer, T. Gonzalez-Carreño, C. J. Serna, *J. Phys. D: Appl. Phys.* **2003**, *36*, R182.
[4] S. Mornet, S. Vasseur, F. Grasset, E. Duguet, *J. Mater. Chem.* **2004**, *14*, 2161.
[5] A.-H. Lu, E. L. Salabas, F. Schüth, *Angew. Chem. Int. Ed.* **2007**, *46*, 1222.
[6] U. Jeong, X. Teng, Y. Wang, Y. N. Xia, *Adv. Mater.* **2007**, *19*, 33.
[7] G. F. Goya, V. Grazu, M. R. Ibarra, *Curr. Nanoscience* **2008**, *4*, 1.
[8] S. Laurent, D. Forge, M. Port, A. Roch, C. Robic, L. V. Elst, R. N. Muller, *Chem. Rev.* **2008**, *108*, 2064.
[9] R. H. Kodama, *J. Magn. Magn. Mater.* **1999**, *200*, 359.
[10] J. Nogues, J. Sort, V. Langlais, V. Skumryev, S. Suriñach, J. S. Muñoz, M. D. Baro, *Phys. Rep.* **2005**, *422*, 65.
[11] O. Iglesias, A. Labarta, X. Batlle, *J. Nanosc. Nanotech.* **2008**, *8*, 2761.
[12] P. Allia, M. Coisson, P. Tiberto, F. Viani, M. Knobel, M. A. Novak, W. C. Nunes, *Phys. Rev. B* **2001**, *64*, 144420.
[13] a) I. Safarik, M. Safarikova, *Biomagn. Res. Technol.* **2004**, *2*, 45; b) C. J. Chen, Y. Haik, V. M. Pai, *US Patent 6036857*, **2000**; c) S. Sieben, C. Bergemann, A. Lübbe, B. Brockmann, D. Rescheleit, *J. Magn. Magn. Mater.* **2001**, *225*, 175; d) M. Shinkai, *J. Biosci. Biotechnol.* **2002**, *94*, 606; e) H. Gu, P.-L. Ho, K. W. T. Tsang, L. Wang, B. Xu, *J. Am. Chem. Soc.* **2003**, *125*, 15702; f) J. P. Lellouche, N. Perlman, A. Joseph, S. Govindaraji, L. Buzhansky, A. Yakir, I. Bruce, *Chem. Commun.* **2004**, 560; g) J. P. Lellouche, G. Shentil, A. Joseph, L. Buzhansky, I. Bruce, E. R. Bauminger, J. Schlesinger, *J. Am. Chem. Soc.* **2005**, *127*, 11998.
[14] M. Arruebo, M. Galan, N. Navascues, C. Tellez, C. Marquina, M. R. Ibarra, J. Santamaria, *Chem. Mater.* **2006**, *18*, 1911.
[15] H. H. Weetal, *Biochim. Biophys. Acta* **1970**, *212*, 1.
[16] T. K. Jain, I. Roy, T. K. De, A. N. Maitra, *J. Am. Chem. Soc.* **1998**, *120*, 11092.
[17] I. Roy, T. Y. Ohulchanskyy, H. E. Pudavar, E. J. Bergey, A. R. Oseroff, J. Morgan, T. J. Dougherty, P. N. Prasad, *J. Am. Chem. Soc.* **2003**, *125*, 7860.

[18] a) R. Ziolo, E. P. Giannelis, B. A. Weinstein, M. P. O'Horo, B. N. Ganguly, V. Mehrotra, M. W. Russel, D. R. Huffman, *Science* **1992**, *257*, 219; b) H. Guerrero, G. Rosa, M. P. Morales, F. del Monte, E. M. Moreno, D. Levy, R. P. del Real, T. Berenguer, C. J. Serna, *Appl. Phys. Lett.* **1997**, *71*, 2698; c) M. Zayat, F. del Monte, M. P. Morales, G. Rosa, H. Guerrero, C. J. Serna, D. Levy, *Adv. Mater.* **2003**, *15*, 1809; d) R. M. Anderson, C. R. Vestal, A. C. S. Samia, Z. J. Zhang, *Appl. Phys. Lett.* **2004**, *84*, 3115.

[19] P. Tartaj, M. P. Morales, S. Veintemillas-Verdaguer, T. Gonzalez-Carreño, C. J. Serna, *J. Magn. Magn. Mater.* **2005**, *290–291*, 28.

[20] T. Neuberger, B. Schöpf, H. Hofmann, M. Hofmann, B. von Rechenberg, *J. Magn. Magn. Mater.* **2005**, *293*, 483.

[21] C. C. Berry, *J. Mater. Chem.* **2005**, *15*, 543.

[22] P. Tartaj, *Curr. Nanoscience* **2006**, *2*, 43.

[23] A. K. Gupta, R. R. Naregalkar, V. D. Vaidya, M. Gupta, *Nanomedicine* **2007**, *2*, 23.

[24] M. Arruebo, R. Fernandez-Pacheco, M. R. Ibarra, J. Santamaria, *Nano Today* **2007**, *2*, 22.

[25] V. Salgueriño-Maceira, M. A. Correa-Duarte, *Adv. Mater.* **2007**, *19*, 4131.

[26] Y.-W. Jun, J.-W. Seo, J. Cheon, *Acc. Chem. Res.* **2008**, *41*, 179.

[27] L. Wang, H.-Y. Park, S. I. Lim, M. J. Schadt, D. Mott, J. Luo, X. Wang, C.-J. Zhong, *J. Mater. Chem.* **2008**, *18*, 2629.

[28] A. Kaiser, T. Gelbrich, A. M. Schmidt, *J. Phys.: Condens. Matter* **2006**, *18*, S2563.

[29] A. M. Schmidt, *Colloid Polym. Sci.* **2007**, *285*, 953.

[30] E. H. Frei, S. Shtrikman, D. Treves, *Phys. Rev.* **1957**, *106*, 446.

[31] T. W. McDaniell, *J. Phys.: Condens. Matter.* **2005**, *17*, R315.

[32] P. Tartaj, C. J. Serna, *J. Am. Chem. Soc.* **2003**, *125*, 15754.

[33] P. Tartaj, T. Gonzalez-Carreño, O. Bomatí-Miguel, C. J. Serna, P. Bonville, *Phys. Rev. B* **2004**, *69*, 094401.

[34] a) S. Hisano, K. Saito, S. Aizawa, K. Sano, K. Matsumoto, K. Murata, US Patent 5591535, **1997**; b) K. O'Grady, H. Laidler, *J. Magn. Magn. Mater.* **1999**, *200*, 616; c) N. O. Núñez, P. Tartaj, M. P. Morales, R. Pozas, M. Ocaña, C. J. Serna, *Chem. Mater.* **2003**, *15*, 3558.

[35] I. M. L. Billas, A. Chatelain, W. A. de Heer, *Science* **1994**, *265*, 1682.

[36] a) R. H. Kodama, A. E. Berkowitz, E. J. McNiff Jr, S. Foner, *Phys. Rev. Lett.* **1996**, *77*, 394; b) N. Moumen, M. P. Pileni, *J. Phys. Chem.* **1996**, *100*, 1867; c) N. Moumen, M. P. Pileni, *Chem. Mater.* **1996**, *8*, 128; d) B. Martinez, X. Obradors, L. I. Balcells, A. Rovanet, C. Monty, *Phys. Rev. Lett.* **1998**, *80*, 181; e) M. P. Morales, S. Veintemillas-Verdaguer, M. I. Montero, C. J. Serna, A. Roig, L. Casas, B. Martinez, F. Sandiumenge, *Chem. Mater.* **1999**, *11*, 3058; f) E. Tronc, D. Fiorani, M. Nogues, A. M. Testa, F. Lucari, F. D'Orazio, J. M. Greneche, W. Wernsdorfer, N. Galvez, C. Chaneac, D. Mailly, J. P. Jolivet, *J. Magn. Magn. Mater.* **2003**, *262*, 6; g) A. G. Roca, J. F. Marco, M. P. Morales, C. J. Serna, *J. Phys. Chem. C* **2007**, *111*, 18577.

[37] a) V. Skumryev, S. Stoyanov, Y. Zhang, G. C. Hadjipanayis, D. Givord, J. Nogues, *Nature* **2003**, *423*, 850; b) K. Liu, J. Nogues, C. Leighton, H. Masuda, K. Nishio, I. V. Roshchin, I. K. Schuller, *Appl. Phys. Lett.* **2002**, *81*, 4434; c) J. Eisenmenger, I. K. Schuller, *Nat. Mater.* **2003**, *2*, 437; d) C. Frandsen, C. W. Ostenfeld, M. Xu, C. S. Jacobsen, L. Keller, K. Lefmann, S. Morup, *Phys. Rev. B* **2004**, *70*, 134416; e) D. Givord, V. Skumryev, J. Nogues, *J. Magn. Magn. Mater.* **2005**, *294*, 111.

[38] A. N. Dobrynin, D. N. Levlev, K. Temst, P. Lievens, J. Margueritat, J. Gonzalo, C. N. Afonso, S. Q. Zhou, A. Vantomme, E. Piscopiello, G. van Tendeloo, *Appl. Phys. Lett.* **2005**, *87*, 012501.

[39] a) D. K. Kim, M. Mikhaylova, Y. Zhang, M. Muhammed, *Chem. Mater.* **2003**, *15*, 1617; b) C. R. Vestal, Z. J. Zhang, *J. Am. Chem. Soc.* **2003**, *125*, 9828; c) A. G. Roca, M. P. Morales, K. O'Grady, C. J. Serna, *Nanotechnology* **2006**, *17*, 2783; d) T. J. Daou, J. M. Greneche, G. Pourroy, S. Buathong, A. Derory, C. Ulhaq-Bouillet, B. Donnio, D. Guillon, S. Begin-Colin, *Chem. Mater.* **2008**, *20*, 5869.

[40] a) J. L. Gittleman, B. Abeles, S. Bozowsky, *Phys. Rev. B* **1974**, *9*, 3891; b) M. El-Hilo, K. O'Grady, R. W. Chantrell, *J. Magn. Magn. Mater.* **1992**, *114*, 295; c) S. Mørup, F. Bødker, P. V. Hendriksen, S. Linderoth, *Phys. Rev. B* **1995**, *52*, 287; d) C. Cannas, M. F. Casula, G. Concas, A. Corrias, D. Gatteschi, A. Falqui, A. Musinu, C. Sangregorio, G. Spano, *J. Mater. Chem.* **2001**, *11*, 3180.

[41] P. Tartaj, C. J. Serna, *Chem. Mater.* **2002**, *14*, 4396.

[42] S. Srivastava, B. Samanta, B. J. Jordan, R. Hong, Q. Xiao, M. T. Tuominen, V. M. Rotello, *J. Am. Chem. Soc.* **2007**, *129*, 11776.

[43] C. Binns, M. J. Maher, Q. A. Pankhurst, D. Kechrakos, K. N. Trohidou, *Phys. Rev. B* **2002**, *66*, 184413.

[44] P. Tartaj, *ChemPhysChem* **2003**, *4*, 1371.

[45] M. Knobel, W. C. Nunes, A. L. Brandl, J. M. Vargas, L. M. Socolovsky, D. Zanchet, *Phys. B* **2004**, *354*, 80.

[46] P. Tartaj, T. Gonzalez-Carreño, C. J. Serna, *Adv. Mater.* **2004**, *16*, 529.

[47] C. Kittel, *Introduction to Solid State Physics*, Wiley, New York, **1968**.

[48] A. F. Rebolledo, A. B. Fuertes, T. González-Carreño, M. Sevilla, T. Valdes-Solís, P. Tartaj, *Small* **2008**, *4*, 254.

[49] a) Y. Deng, C. Wang, X. Shen, W. Yang, L. Jin, H. Gao, S. Fu, *Chem. Eur. J.* **2005**, *11*, 6006; b) S. Starodubtsev, E. Saenko, M. Dokukin, V. Aksenov, V. Klechkovskaya, I. Zanaveskina, A. Khokhlov, *J. Phys.: Condens. Matter* **2005**, *17*, 1471; c) P. Dallas, V. Georgakilas, D. Niarchos, P. Komninou, T. Kehagias, D. Petridis, *Nanotechnology* **2006**, *17*, 2046.

[50] X. Z. Zhang, R. X. Zhuo, J. Z. Cui, J. T. Zhang, *Int. J. Pharm.* **2002**, *235*, 43.

[51] F. Eeckman, A. J. Moës, K. Amighi, *Eur. Polym. J.* **2004**, *40*, 873.

[52] Y. Deng, W. Yang, C. Wang, S. Fu, *Adv. Mater.* **2003**, *15*, 1729.

[53] Y.-H. Lien, T.-M. Wu, *J. Colloid Interf. Sci.* **2008**, *326*, 517.

[54] A. P. Herrera, M. C. Rodriguez, M. Torres-Lugo, C. Rinaldi, *J. Mater. Chem.* **2008**, *18*, 855.

[55] M. Bonini, S. Lenz, R. Giorgi, P. Baglioni, *Langmuir* **2007**, *23*, 8681.

[56] R. Arshady, D. Pouliquen, A. Halbreich, J. Roger, J-N. Pons, J-C Bacri, M-F Da Silva, U. Häfeli, *Magnetic Nanospheres and Nanocomposites in MML Series, Volume 5*, **2002**.

[57] K. Kostarelos, *Adv. Colloid Interface Sci.* **2003**, *106*, 147.

[58] D. A. Lavan, T. McGuire, R. Langer, *Nat. Biotechnol.* **2003**, *21*, 1184.

[59] Y. Wang, Y. W. Ng, Y. Chen, B. Shuter, J. Yi, J. Ding, S.-C. Wang, S.-S. Feng, *Adv. Funct. Mater.* **2008**, *18*, 308.

[60] a) R. H. Muller, S. Maassen, H. Weyhers, F. Specht, J. S. Lucks, *Int. J. Pharm.* **1996**, *138*, 85; b) S. A. Gomez-Lopera, R. C. Plaza, A. V. Delgado, *J. Colloid Interface Sci.* **2001**, *240*, 40; c) P. A. Dresco, V. S. Zaitsev, R. J. Gambino, B. Chu, *Langmuir* **1999**, *15*, 1945.

[61] a) A. Bourlinos, A. Simopoulos, N. Boukos, D. Petridis, *J. Phys. Chem. B* **2001**, *105*, 7432; b) J. El Haskouri, S. Cabrera, C. Guillem, J. Latorre, A. Beltran, M. D. Marcos, J. C. Gomez-Garcia, D. Beltran, P. Amoros, *Eur. J. Inorg. Chem.* **2004**, 1799; c) B. Julian-Lopez, C. C. Boissiere, C. Chaneac, D. Grosso, S. Vasseur, S. Miraux, E. Duguet, C. Sanchez, *J. Mater. Chem.* **2007**, *17*, 1563; d) E. Ruiz-Hernandez, A. Lopez-Noriega, D. Arcos, I. Izquierdo-Barba, O. Terasaki, M. Vallet-Regi, *Chem. Mater.* **2007**, *19*, 3455.

[62] A.-H. Lu, W. Schmidt, N. Matoussevitch, H. Bönnermann, B. Spliethoff, B. Tesche, E. Bill, W. Kiefer, F. Schüth, *Angew. Chem. Int. Ed.* **2004**, *43*, 4303.

[63] A.-H. Lu, F. Schuth, *Adv. Mater.* **2006**, *18*, 1793.

[64] R. Ryoo, S. H. Joo, S. Jun, *J. Phys. Chem. B* **1999**, *103*, 7743.

[65] A. B. Fuertes, P. Tartaj, *Chem. Mater.* **2006**, *18*, 1675.

[66] M. Schwickardi, S. Olejnik, E. L. Salabas, W. Schmidt, F. Schüth, *Chem. Commun.* **2006**, 3987.

[67] C. J. Murphy, A. M. Gole, S. E. Hunyadi, J. W. Stone, P. N. Sisco, A. Alkilany, B. E. Kinard, P. Hankins, *Chem. Commun.* **2008**, 544.
[68] J. Lim, A. Eggeman, F. Lanni, R. D. Tilton, S. A. Majetich, *Adv. Mater.* **2008**, *20*, 1721.
[69] L. M. Liz-Marzan, *Langmuir* **2006**, *22*, 32.
[70] J. Lee, J. Yang, H. Ko, S. J. Oh, J. Kang, J.-H. Son, K. Lee, S.-W. Lee, H.-G. Yoon, J.-S. Suh, Y.-M. Huh, S. Haam, *Adv. Funct. Mater.* **2008**, *18*, 258.
[71] L. R. Hirsch, R. J. Stafford, J. A. Bankson, S. R. Sershen, B. Rivera, R. E. Price, J. D. Hazle, N. J. Halas, J. L. West, *Proc. Natl. Acad. Sci. USA* **2003**, *100*, 3549.
[72] C. R. Vestal, Z. J. Zhang, *J. Am. Chem. Soc.* **2002**, *124*, 14312.
[73] R. Matsuno, K. Yamamoto, H. Otsuka, A. Takahara, *Chem. Mater.* **2003**, *15*, 3.
[74] a) J. M. Perez, L. Josephson, T. Loughlin, D. Hogemann, R. Weissleder, *Nat. Biotechnol.* **2002**, *20*, 816; b) H. Ai, C. Flask, B. Weinberg, X. Shuai, M. D. Pagel, D. Farrell, J. Duerk, J. Gao, *Adv. Mater.* **2005**, *17*, 1949; c) J.-F. Berret, N. Schonbeck, F. Gazeau, D. El Kharrat, O. Sandre, A. Vacher, M. Airiau, *J. Am. Chem. Soc.* **2006**, *128*, 1755; d) J.-H. Lee, Y.-W. Jun, S.-I. Yeon, J.-S. Shin, J. Cheon, *Angew. Chem. Int. Ed.* **2006**, *45*, 8160; e) J. Lee, Y.-M. Huh, Y. Jun, J. Seo, J. Jang, H. Song, S. Kim, E. Cho, H. Yoon, J. Suh, J. Cheon, *Nat. Med.* **2007**, *13*, 95.
[75] a) F. Caruso, *Adv. Mater.* **2001**, *13*, 11; b) S.-W. Kim, M. Kim, W. Y. Lee, T. Hyeon, *J. Am. Chem. Soc.* **2002**, *124*, 7642; c) D. A. Lavan, T. Mcguire, *Nat. Biotechnol.* **2003**, *21*, 1184; d) N. Ren, A.-G. Dong, W.-B. Cai, Y.-H. Zhang, W.-L. Yang, S.-J. Huo, Y. Chen, S.-H. Xie, Z. Gao, Y. Tang, *J. Mater. Chem.* **2004**, *14*, 3548; e) A. G. Skirtach, A. Muñoz-Javier, O. Kreft, K. Köhler, A. Piera-Alberola, H. Möhwald, W. J. Parak, G. B. Sukhorukov, *Angew. Chem. Int. Ed.* **2006**, *45*, 4612.
[76] M. Antonietti, S. Forster, *Adv. Mater.* **2003**, *15*, 1323.
[77] S. Lesieur, C. Grabielle-Madelmont, C. Menager, V. Cabuil, D. Dadhi, P. Pierrot, K. Edwards, *J. Am. Chem. Soc.* **2003**, *125*, 5266.
[78] M. De Cuyper, S. Valtonen, *J. Magn. Magn. Mater.* **2001**, *225*, 89.
[79] J. W. M. Bulte, M. de Cuyper, D. Despres, J. A. Frank, *J. Magn. Magn. Mater.* **1999**, *194*, 204.
[80] J. W. M. Bulte, L. D. Ma, R. L. Magin, R. L. Kamman, C. E. Hulstaert, K. G. Go, T. H. The, L. de Leij, *Magn. Reson. Med.* **1993**, *29*, 32.
[81] S. W. Keller, S. A. Johnson, E. S. Brigham, E. H. Yonemoto, T. E. Mallouk, *J. Am. Chem. Soc.* **1995**, *117*, 12879.
[82] E. Donath, G. B. Sukhorukov, F. Caruso, S. Davis, H. Möhwald, *Angew. Chem. Int. Ed.* **1998**, *37*, 2202.
[83] G. Decher, J. D. Hong, *Macromol. Chem. Macromol. Symp.* **1991**, *46*, 321.
[84] O. Kraft, M. Prevot, H. Mohwald, G. B. Sukhorukov, *Angew. Chem. Int. Ed.* **2007**, *46*, 5605.
[85] S. B. Yoon, K. Sohn, J. Y. Kim, C. H. Shin, J. S. Yu, T. Hyeon, *Adv. Mater.* **2002**, *14*, 19.
[86] J. W. Wang, Y. D. Xia, W. X. Wang, R. Mokaya, M. Poliakoff, *Chem. Commun.* **2005**, 210.
[87] J. S. Yu, S. B. Yoon, Y. J. Lee, K. B. Yoon, *J. Phys. Chem. B* **2005**, *109*, 7040.
[88] S. H. Im, U. Jeong, Y. Xia, *Nat. Mater.* **2005**, *4*, 671.
[89] S. B. Yoon, J. Y. Kim, J. H. Kim, S. G. Park, C. W. Lee, J. S. Yu, *Curr. Appl. Phys.* **2006**, *6*, 1059.
[90] J. Lee, J. Kim, T. Hyeon, *Adv. Mater.* **2006**, *18*, 2073.
[91] M. Kim, K. Sohn, H. Na, T. Hyeon, *Nano Lett.* **2002**, *2*, 1383.
[92] J. Y. Kim, S. B. Yoon, J. S. Yu, *Chem. Commun.* **2003**, 790.
[93] G. S. Chai, S. B. Yoon, J. H. Kim, J. S. Yu, *Chem. Commun.* **2004**, 2766.
[94] P. Tartaj, T. Gonzalez-Carreño, C. J. Serna, *Adv. Mater.* **2001**, *13*, 1620.
[95] A. B. Fuertes, M. Sevilla, T. Valdés-Solís, P. Tartaj, *Chem. Mater.* **2007**, *19*, 5418.
[96] A. B. Fuertes, T. Valdés-Solís, M. Sevilla, P. Tartaj, *J. Phys. Chem. C* **2008**, *112*, 3648.
[97] C. E. Hoppe, F. Ribadulla, M. A. Lopez-Quintela, M. C. Bujan, J. Rivas, D. Serantes, D. Baldomir, *J. Phys. Chem. C* **2008**, *112*, 13099.
[98] B. Srinivasan, X. Huang, *Chirality* **2008**, *20*, 265.
[99] a) S. A. Johnson, P. J. Ollivier, T. E. Mallouk, *Science* **1999**, *283*, 963; b) J. Y. Kim, S. B. Yoon, F. Kooli, J.-S. Yu, *J. Mater. Chem.* **2001**, *11*, 2912; J. Lee, J. Kim, S.-W. Kim, C.-H. Shin, T. Hyeon, *Chem. Commun.* **2004**, 562.
[100] A. B. Fuertes, M. Sevilla, S. Alvarez, T. Valdes-Solis, P. Tartaj, *Adv. Funct. Mater.* **2007**, *17*, 2321.
[101] a) A. P. Philipse, M. P. B. Vanbruggen, C. Pathmamanoharan, *Langmuir* **1994**, *10*, 92; b) C. Cannas, D. Gatteschi, A. Musinu, G. Piccaluga, C. Sangregorio, *J. Phys. Chem. B* **1998**, *102*, 7721; c) M. Fröba, R. Köhn, G. Bouffaud, *Chem. Mater.* **1999**, *11*, 2858; d) P. Tartaj, T. Gonzalez-Carreño, C. J. Serna, *Langmuir* **2002**, *18*, 4556; e) R. Köhn, M. Fröba, *Z. Anorg. Allg. Chem.* **2003**, *629*, 1673; f) R. Köhn, D. Paneva, M. Dimitrov, T. Tsoncheva, I. Mitov, C. Minchev, M. Fröba, *Microporous Mesoporous Mater.* **2003**, *63*, 125; g) P. Tartaj, T. Gonzalez-Carreño, C. J. Serna, *J. Phys. Chem. B* **2003**, *107*, 20.
[102] a) C. Cannas, E. Musu, A. Musinu, G. Piccaluga, G. Spano, *J. Non-Cryst. Solids* **2004**, *345–346*, 653; b) U. Jeong, T. Herricks, E. Shahar, Y. N. Xia, *J. Am. Chem. Soc.* **2005**, *127*, 1098; c) W. Zhao, J. Gu, L. Zhang, H. Chen, J. J. Shi, *J. Am. Chem. Soc.* **2005**, *127*, 8916; d) S. Giri, B. G. Trewyn, M. P. Stellmaker, V. S. Y. Lin, *Angew. Chem. Int. Ed.* **2005**, *44*, 5038; e) J. Kim, J. E. Lee, J. Lee, Y. Jang, S.-W. Kim, K. An, J. H. Yu, T. Hyeon, *Angew. Chem. Int. Ed.* **2006**, *45*, 4789; f) J. Kim, J. E. Lee, J. Lee, J. H. Ju, B. C. Kim, K. Ang, Y. Hwang, C. H. Sin, J. G. Park, T. Hyeon, *J. Am. Chem. Soc.* **2006**, *128*, 688; g) R. Fernandez-Pacheco, M. Arruebo, C. Marquina, R. Ibarra, J. Arbiol, J. Santamaría, *Nanotechnology* **2006**, *17*, 1188; h) V. Salgueriño-Maceira, M. A. Correa-Duarte, *J. Mater. Chem.* **2006**, *16*, 3593.
[103] a) M. Shokouhimehr, Y. Z. Piao, J. Kim, Y. J. Jang, T. Hyeon, *Angew. Chem. Int. Ed.* **2007**, *46*, 7039; b) S. T. Selvan, P. K. Patra, C. Y. Ang, J. Y. Ying, *Angew. Chem. Int. Ed.* **2007**, *46*, 2448; c) D. Ma, T. Veres, L. Clime, F. Normandin, J. Guan, D. Kingston, B. Simard, *J. Phys. Chem. C* **2007**, *111*, 1999; d) M. Arruebo, R. Fernandez-Pacheco, B. Velasco, C. Marquina, J. Arbiol, S. Irusta, M. R. Ibarra, J. Santamaría, *Adv. Funct. Mater.* **2007**, *17*, 1473; e) L. Burgos-Asperilla, M. Darder, P. Aranda, L. Vazquez, M. Vazquez, E. Ruiz-Hitzky, *J. Mater. Chem.* **2007**, *17*, 4233.
[104] a) J. Lee, Y. Lee, J. K. Youn, H. B. Na, T. Yu, H. Kim, S.-M. Lee, Y.-M. Koo, J. H. Kwak, H. G. Park, H. N. Chang, M. Hwang, J.-G. Park, J. Kim, T. Hyeon, *Small* **2008**, *4*, 143; b) C.-W. Lai, Y.-H. Wang, C.-H. Lai, M.-Y. Yang, C.-Y. Chen, P.-T. Chou, C.-S. Chan, Y. Chi, Y.-C. Chen, J.-K. Hsiao, *Small* **2008**, *4*, 218; c) Y. Deng, D. Qi, C. Deng, X. Zhang, D. Zhao, *J. Am. Chem. Soc.* **2008**, *130*, 28; d) S.-H. Hu, T.-Y. Liu, H.-Y. Huang, D.-M. Liu, S.-Y. Chen, *Langmuir* **2008**, *24*, 239; e) M. Stjerndahl, M. Andersson, H. E. Hall, D. M. Pajerowski, M. W. Meisel, R. S. Duran, *Langmuir* **2008**, *24*, 3532; f) M. I. Shukoor, F. Natalio, H. A. Therese, M. N. Tahir, V. Ksenofontov, M. Panthofer, M. Eberhardt, P. Theato, H. C. Schroder, W. E. G. Muller, W. Tremel, *Chem. Mater.* **2008**, *20*, 3567; g) M. Arruebo, W. Y. Ho, K. F. Lam, X. G. Chen, J. Arbiol, J. Santamaria, K. L. Yeung, *Chem. Mater.* **2008**, *20*, 3567; h) L. Li, E. S. G. Choo, J. Yi, J. Ding, X. Tang, J. Xue, *Chem. Mater.* **2008**, *20*, 6292.
[105] T. Nakamura, Y. Yamada, K. Yano, *J. Mater. Chem.* **2006**, *16*, 2417.
[106] a) M. E. Machenry, S. A. Majetich, J. O. Artman, M. Degraef, S. W. Staley, *Phys. Rev. B* **1994**, *49*, 11358; b) S. I. Nikitenko, Y. Koltypin, O. Palchik, I. Felner, X. N. Xu, A. Gedanken, *Angew. Chem. Int. Ed.* **2001**, *40*, 4447; c) O. Bomatí-Miguel, M. P. Morales, P. Tartaj, J. Ruiz-Cabello, P. Bonville,

M. Santos, X. Zhao, S. Veintemillas-Verdaguer, *Biomaterials* **2005**, *26*, 5695; d) O. Bomati-Miguel, P. Tartaj, M. P. Morales, U. Golla-Schindler, P. Bonville, X. Zhao, S. Veintemillas-Verdaguer, *Small* **2006**, *2*, 1476.

[107] Y. Wang, W. Wei, D. Maspoch, J. Wu, V. P. Dravid, C. A. Mirkin, *Nano Lett.* **2008**, *8*, 3761.

[108] M. Choi, F. Kleitz, D. Liu, H.-Y. Lee, W.-S. Ahn, R. Ryoo, *J. Am. Chem. Soc.* **2005**, *127*, 1924.

[109] A. B. Fuertes, P. Tartaj, *Small* **2007**, *3*, 275.

[110] A. F. Rebolledo, O. Bomatí-Miguel, J. F. Marco, P. Tartaj, *Adv. Mater.* **2008**, *20*, 1760.

[111] D. Carriere, M. Moreau, P. Barboux, J. P. Boicot, *Langmuir* **2004**, *20*, 3449.

[112] L. Xu, H. Kee-Lee, *Anal. Chem.* **2007**, *79*, 5241.

[113] Y. Li, J. Wu, D. Qi, X. Xu, C. Deng, P. Yang, X. Zhang, *Chem. Commun.* **2008**, 564.

[114] a) A. Corrias, M. F. Casula, A. Falqui, G. Paschina, *Chem. Mater.* **2004**, *16*, 3567; b) P. Tartaj, T. Gonzalez-Carreño, M. L. Ferrer, C. J. Serna, *Angew. Chem. Int. Ed.* **2004**, *43*, 6304.

[115] a) E. M. Barea, V. Fornes, A. Corma, P. Bourges, E. Guillon, V. F. Puntes, *Chem. Commun.* **2004**, 1974; b) E. M. Barea, X. Batlle, P. Bourges, A. Corma, V. Fornes, A. Labarta, V. F. Puntes, *J. Am. Chem. Soc.* **2005**, *127*, 18026.

[116] J.-M. Nam, C. S. Thaxton, C. A. Mirkin, *Science* **2003**, *301*,1884.

[117] B. D. Chithrani, A. A. Ghazani, W. C. W. Chan, *Nano Lett.* **2006**, *6*, 662.

[118] Y. Geng, P. Dalhaimer, S. S. Cai, R. Tsai, M. Tewari, T. Minko, D. E. Discher, *Nature Nanotech.* **2007**, *2*, 249.

[119] C. J. Kastrup, F. Shen, R. F. Ismagilov, *Angew. Chem. Int. Ed.* **2007**, *46*, 3660.

[120] M. A. Correa-Duarte, M. Grzelczak, V. Salgueirino-Maceira, M. Giersig, L. M. Liz-Marzan, M. Farle, K. Sierazdki, R. Diaz, *J. Phys. Chem. B* **2005**, *109*, 19060.

[121] a) J. P. Ge, Y. X. Hu, M. Biasini, W. P. Beyermann, Y. D. Yin, *Angew. Chem. Int. Ed.* **2007**, *46*, 4342; b) J. P. Ge, Y. X. Hu, T. R. Zhang, T. Huynh, Y. D. Yin, *Langmuir* **2008**, *24*, 3671.

[122] a) X. Xu, G. Friedman, K. D. Humfeld, S. A. Majetich, S. A. Asher, *Adv. Mater.* **2001**, *13*, 1681; b) X. Xu, G. Friedman, K. D. Humfeld, S. A. Majetich, S. A. Asher, *Chem. Mater.* **2002**, *14*, 1429; c) S. Saccana, A. P. Philipse, *Langmuir* **2006**, *22*, 10209.

Received: September 1, 2008
Published Online: December 18, 2008

DOI: 10.1002/ejic.200800761

On the Effect of Coordination and Protonation Preferences in the Amphiphilic Behavior of Metallosurfactants with Asymmetric Headgroups

Frank D. Lesh,[a] Sarmad Sahiel Hindo,[a] Mary Jane Heeg,[a] Marco M. Allard,[a] Prateek Jain,[a] Bo Peng,[a] Lew Hryhorczuk,[a] and Cláudio N. Verani*[a]

Keywords: Metallosurfactants / Nickel / Copper / Zinc / Thin films / Brewster angle microscopy

The metallosurfactants $[Ni^{II}(L^{tBuODA})(OAc)]$ (**1**), $[Ni^{II}(L^{tBuODA})_2]$ (**2**), $[Cu^{II}(HL^{tBuODA})(L^{tBuODA})]ClO_4{\cdot}CH_3OH$ (**3**), and $[Zn^{II}(HL^{tBuODA})_2](ClO_4)_2$ (**4**) {where HL^{tBuODA} = 2,4-di-*tert*-butyl-6-[(octadecyl(pyridin-2-ylmethyl)amino)methyl]phenol} were synthesized and characterized in an attempt to establish how coordination modes and protonation preferences relate to amphiphilic behavior. The archetypical compounds $[Ni^{II}(L^{tBuI})(OAc)]{\cdot}CH_3OH$ (**5**), $[Ni^{II}(L^{A})_2]{\cdot}CH_3OH{\cdot}H_2O$ (**6**), $[Ni^{II}(L^{tBuA})_2]{\cdot}2CH_3OH$ (**7**), $[Cu^{II}(HL^{tBuA})(L^{tBuA})]ClO_4$ (**8**), and $[Zn^{II}(HL^{tBuA})(L^{tBuA})]ClO_4$ (**9**) were synthesized to model the stoichiometric, coordination, and protonation chemistry in the waxy metallosurfactants **1**–**4**. Detailed data analysis and comparison between **1**–**4** and **5**–**9** involved mass spectrometric and spectroscopic methods along with crystallographic determination of **5** ($P2_1/c$), **6** ($P\bar{1}$), **7** ($P2_1/c$), **8**′ (the analogue of **8** with tetraphenylborate counterions, $P2_1/c$), and **9** ($P\bar{1}$). DFT calculations were used to identify the frontier orbitals, polarizability, and dipole moments. Species **1**–**4** had their compression isotherms measured and monitored by means of Brewster angle miscroscopy. The nickel-containing **1** is square planar, while **2** has a neutral octahedral core with two deprotonated ligands. The five-coordinate copper-containing **3** has a monocationic core associated with one protonated ligand, whereas the dicationic zinc-containing **4** has a four-coordinate core with protonated ligands. It was observed that Langmuir films of **1** display approximately half of the average molecular area observed for **2**–**4** and that the flexibility and coordination number of the cores foster distinctive collapse mechanisms. Therefore, careful choice of the metal ion leads to control of surfactant-to-metal ratio, selection of coordination modes and structural properties, and the understanding of the protonation preferences of the ligands. This information will play an important role in the development of metal-containing responsive films.

Introduction

Molecular architectures displaying cooperativity among transition metals and amphiphilic organic scaffolds combine unique geometric, electronic, redox, and magnetic behavior[1–4] with distinctive ordering morphologies. The approach has been used with impressive results in the design of soft materials with tixothropic,[5] mesogenic,[6] ionophoric,[7] luminescent,[8] and micellar[9] properties. This fact points out to the potential role of discrete metallosurfactant materials in the emerging field of responsive thin films.[10,11,12] However, metallosurfactants (i.e. surfactants containing transition-metal ions) are usually assembled at the air/water interface without isolation of the precursors. As a consequence, lack of precise control in (i) the surfactant-to-metal ratio, (ii) the coordination modes and the final structure of the material, and (iii) protonation preferences limit reproducibility leading to adventitious defects. Therefore having well defined, isolated, and characterized precursors is of paramount importance. Nevertheless, the small body of work available on the isolation and air/water interface behavior of metallosurfactant precursors still poses a major drawback to the approach.[13,14]

At the forefront of this area, our group has focused on synthetic, modeling, and surface protocols involving the incorporation of magnetic μ-oxo-Cu_4 clusters in Langmuir–Blodgett films,[15,16] the observation of distinctive collapse mechanisms on cobalt(II) films,[17] and the design of redox-active copper-containing amphiphiles.[18,19] In a series of studies with iron(III),[20] cobalt(II/III),[21] and gallium(III)[22] we have demonstrated that structural and electronic effects can determine the preferential geometry of redox-active asymmetric NN′O ligands in $[ML_2]$ metallosurfactants. Structural rigidity of the ligand takes precedence to the electronic configuration of the metal ion and favors *meridional* coordination when asymmetric amines and imines are compared. On the other hand, electronic configuration is a determining factor when flexible amines are involved; a *facial* coordination mode is preferred, and the metal dictates the preferential *cis* or *trans* orientation of equivalent phenolates and other donor sets in vicinal ligands. Consequently, $3d^5$ high-spin configuration leads to *cis*-arrangement while $3d^6$ low-spin and $3d^7$ high-spin ions support

[a] Department of Chemistry, Wayne State University,
5101 Cass Ave., Detroit, MI 48202, USA
Fax: +1-313-577-8822
E-mail: cnverani@chem.wayne.edu
Supporting information for this article is available on the WWW under http://www.eurjic.org or from the author.

trans-orientation. Gallium(III), with $3d^{10}$ configuration, does not seem to exhibit a clear preference. These observations are serving as guidelines to the design of metal-containing amphiphiles for redox-responsive Langmuir–Blodgett films.

In this article we describe the synthesis and amphiphilic behavior of nickel(II), copper(II), and zinc(II) complexes with an asymmetric NN′O ligand. Due to the $3d^{8-10}$ electronic configurations found in these bivalent metal ions, stoichiometric preferences, coordination modes, and ligand protonation status can lead to distinct $[M^{II}(HL)X]^{2+}$, $[M^{II}(L)X]^{+}$, $[M^{II}(L)_2]^{o}$, $[M^{II}(HL)(L)]^{+}$, and $[M^{II}(HL)_2]^{2+}$ products (Scheme 1). Because of the waxy texture of most of the resulting metallosurfactants, archetypical modeling (i.e. the investigation of a series of discrete complexes that retain key structural and electronic attributes) was used to assess the nature of these products. A careful comparison between the stoichiometric and protonation status and the amphiphilic behavior is offered.

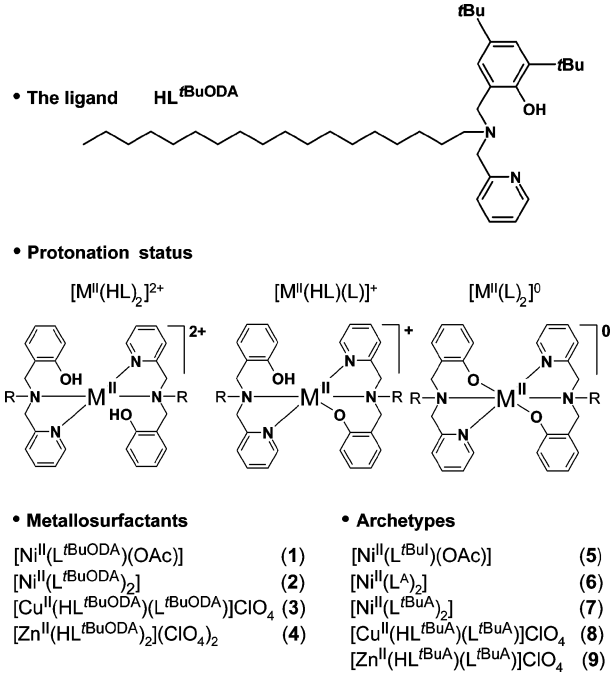

Scheme 1. The ligand HL^{tBuODA}, possible protonation status for metallosurfactants and archetypes studied.

Results and Discussion

The Ligands

Condensation of 1-octadecylamine with 2-pyridinecarboxaldehyde in methanol with subsequent reduction in the presence of sodium borohydride gave the amine precursor that was treated with 2,4-di-*tert*-butyl-6-(chloromethyl)phenol to generate the ligand HL^{tBuODA}. Similarly, the archetypical ligands were synthesized with 80–85% yields following literature procedures[17,20,21] and characterized by means of ESI mass spectrometry, ^{1}H NMR, and infrared spectroscopy.

The Metallosurfactants

Treatment of the ligand HL^{tBuODA} with several metal salts yielded products with textures varying from waxy to solid. Compound [Ni^{II}(L^{tBuODA})(OAc)] (**1**) was isolated upon complexation in methanol of HL^{tBuODA} with nickel(II) acetate tetrahydrate in a 1:1 ligand-to-metal ratio. Similarly, treatment of the ligand with hexahydrated perchlorate salts of nickel(II), copper(II), or zinc(II) in a 2:1 ratio yielded [Ni^{II}(L^{tBuODA})$_2$] (**2**), [Cu^{II}(HL^{tBuODA})(L^{tBuODA})]-ClO$_4$·CH$_3$OH (**3**), and [Zn^{II}(HL^{tBuODA})$_2$](ClO$_4$)$_2$ (**4**), respectively. Triethylamine was used as a base to assist phenol deprotonation in all cases. The waxy constitution of compounds **1** and **2** precluded elemental analysis as a tool for characterization. The ESI mass analysis of **1** indicates the presence of peak clusters at m/z = 635.4 and m/z = 695.4 corresponding respectively to [Ni(L^{tBuODA})]$^+$ and [Ni-(L^{tBuODA})(OAc) + H]$^+$. The former peak is favored at higher cone voltages, whereas the latter is more abundant at lower cone voltages. Similarly, **2** shows a peak cluster at m/z = 1214.0 providing evidence for species such as [Ni(L^{tBuODA})$_2$ + H]$^+$ or [Ni(HL^{tBuODA})(L^{tBuODA})]$^+$. The use of triethylamine in the synthetic procedure, as well as the absence of infrared peaks at 1090 cm^{-1} for perchlorate counterions, supports that the ligands are fully deprotonated and that the singly charged peak observed is formed in situ. The ESI mass analysis of **3** suggests the formation of the cationic species [Cu^{II}(HL^{tBuODA})(L^{tBuODA})]$^+$ with a peak cluster at m/z = 1219.0. Likewise, **4** shows a peak cluster at m/z = 1220.0 implying the formation of the species [Zn^{II}(HL^{tBuODA})(L^{tBuODA})]$^+$. Additional interpretation of the fragmentation patterns suggests the existence of the species [Zn^{II}(HL^{tBuODA})$_2$]$^{2+}$, as confirmed by a prominent peak cluster at m/z = 641.5 for the species [Zn^{II}-(HL^{tBuODA})$_2$ + CH$_3$OH]$^{2+}$. This dicationic species is par-

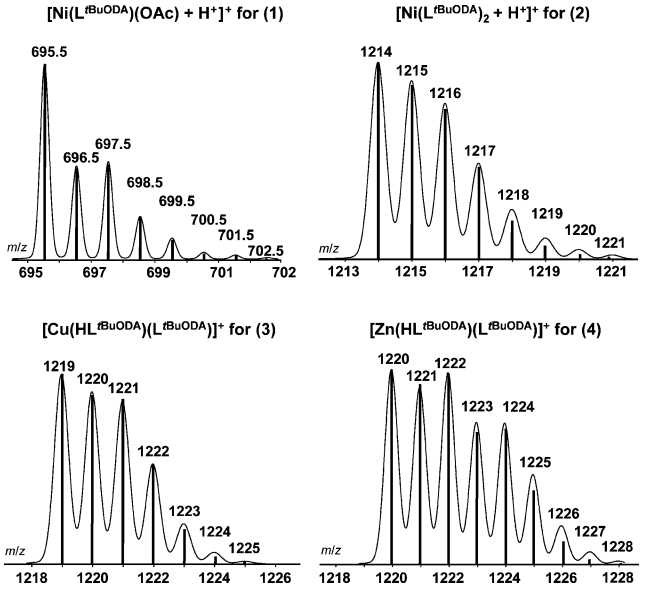

Figure 1. ESI(pos) peak clusters with experimental (bars) and simulated (continuum) isotopic distributions for **1**–**4**. The relative abundance axis of each complex is omitted for clarity.

ticularly visible at low cone voltages. The peak clusters of interest were simulated and agree well in their patterns, positions, and isotopic distributions, and substantiate the behavior of the metal ions. These spectrometric profiles are shown in Figure 1. Infrared analysis further suggests metal coordination by the sharp doublet of the C=N bonds in pyridine rings between 1590–1570 cm^{-1}. These peaks are shown broadened and shifted in the spectra of the compounds, along with the presence of characteristic C–H stretching contribution of the alkyl chain and tertiary butyl groups from the ligand. Additionally, **1** shows an antisymmetric stretch at 1574 cm^{-1} for its coordinated acetate. While the neutral compound **2** lacks a perchlorate peak, **3** and **4** display strong Cl–O stretchings at ca. 1105 cm^{-1}, indicative of the presence of perchlorate counterions. Because precipitates were isolated for **3** and **4**, elemental analyses were carried out and are in good agreement with these formulations.

The Archetypes

Archetypical modeling was used in order to correlate the amphiphilic behavior observed for **1**–**4** with detailed structural information. A series of discrete complexes was studied in which the long alkyl chain is replaced by a hydrogen atom, whereas other key features like the chelating headgroup are left unchanged. These species were synthesized using perchlorate salts analogously to the metallosurfactants above, and are described as $[Ni^{II}(L^{tBuI})(OAc)]\cdot CH_3OH$ (**5**), $[Ni^{II}(L^{A})_2]\cdot CH_3OH\cdot H_2O$ (**6**), $[Ni^{II}(L^{tBuA})_2]\cdot 2CH_3OH$ (**7**), $[Cu^{II}(HL^{tBuA})(L^{tBuA})]ClO_4$ (**8**), and $[Zn^{II}(HL^{tBuA})(L^{tBuA})]ClO_4$ (**9**). The archetypical ligands HL^{tBuI}, HL^{A}, and HL^{tBuA} are depicted in Scheme 2. Species **7** has been recently studied by Thomas et al.,[23] along with a series of related $[Ni^{II}(NN'O)_2]$ complexes, but no X-ray structure was available. Elemental analyses of the compounds **5**–**9** are in excellent agreement with theoretical percentages, and the ESI(pos) mass spectra exhibit distinct *m*/*z* = $[M^{II}(L)_2]^+$ and $[M^{II}(HL)(L)]^+$ peaks in methanol. Peak cluster simulation of these archetypes parallel those obtained for the metallosurfactants **1**–**4**, reinforcing the notion

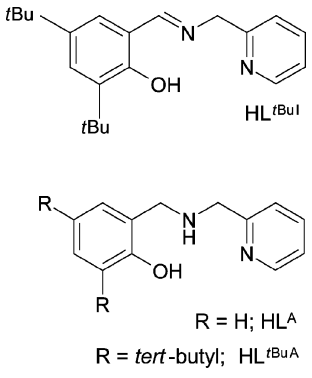

Scheme 2. The ligands HL^{tBuI}, HL^{A}, and HL^{tBuA} used in the archetypes.

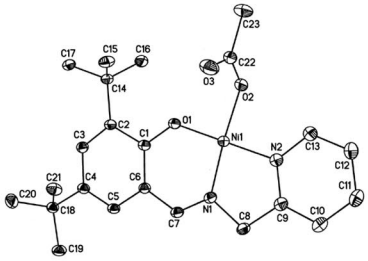

$[Ni^{II}(L^{tBuI})(OAc)]\cdot CH_3OH$ (**5**)

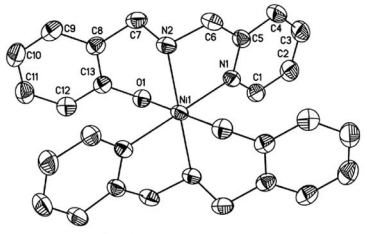

$[Ni^{II}(L^{A})_2]\cdot CH_3OH\cdot H_2O$ (**6**)

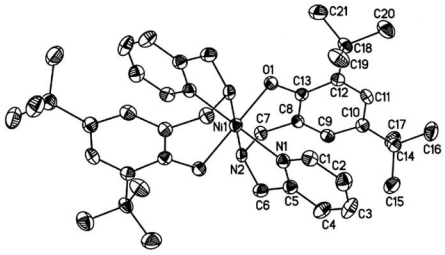

$[Ni^{II}(L^{tBuA})_2]\cdot 2CH_3OH$ (**7**)

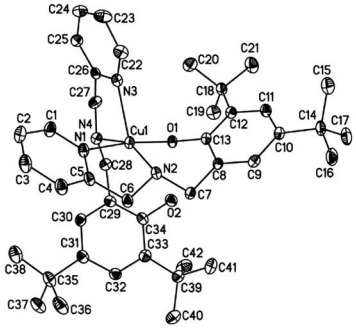

$[Cu^{II}(HL^{tBuA})(L^{tBuA})]ClO_4$ (**8**)

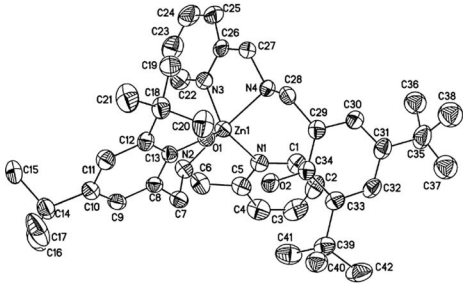

$[Zn^{II}(HL^{tBuA})(L^{tBuA})]ClO_4$ (**9**)

Figure 2. ORTEP diagrams at 50% probability for **5**, **6**, **7**, **8**′, and **9**. Solvents, counterions, and hydrogen atoms are excluded for clarity.

that the expected ligand-to-metal ratios were achieved. The neutrality of the nickel(II) complexes, as well as the presence of protonated ligands, is once again confirmed by the

respective absence or presence of a peak associated with the perchlorate counterion at around 1100–1090 cm^{-1} in their IR spectra.

Molecular Structures and Coordination Modes

Discrete mononuclear crystals of archetypes **5**–**9** were structurally resolved by X-ray diffraction. The ORTEP diagrams are displayed in Figure 2, and selected bond lengths and angles summarized in Table 1.

The Nickel Archetypes 5, 6, and 7: The coordination environment for the nickel(II) metal center in complex **5** approximates a square-planar geometry with the deprotonated ligand $(L^{tBuI})^-$ meridionally coordinated through an NN′O donor set of N_{imine} and $N_{pyridine}$, and $O_{phenolate}$ atoms, along with a deprotonated terminally coordinated acetate group occupying the fourth position. Both *trans* angles are smaller than 180°, thus confirming a distorted square-planar geometry. The bond angles and lengths at the metal center agree with literature values of mono-substituted imine complexes with similarly organized donor frameworks. For example, the Ni–$O_{phenolate}$, Ni–$O_{acetate}$, and Ni–N_{imine} bonds herein are 1.82, 1.88 and 1.84 Å, respectively, closely resembling the values found for the complex [Ni(L)(OAc)], where L is the deprotonated form of the 6-[(*E*)-({[(2*S*)-1-benzylpyrrolidin-2-yl]methyl}imino)-methyl]-2-*tert*-butyl-4-methylphenol.[24] Finally, it is noteworthy that the ligand $(L^{tBuI})^-$ in **5** is definitely an imine, as evidenced by the short bond length between C7–N1 (1.30 Å). Even though the ligand $(L^{tBuODA})^-$ in **1** is more flexible than that in **5** and could possibly adopt a facial conformation in a tetrahedral coordination sphere, the preferential coordination modes of a low-spin $3d^8$ ion like nickel(II) should favor a square-planar geometry. Therefore, **5** provides an acceptable model for the coordination environment for the surfactant **1**.

Complexes **6** and **7** are intended to act as archetypical models for species **2**, which displays two fully deprotonated ligands $(L^{tBuODA})^-$ and neutral character. In fact the results observed for both archetypes with ligands $(L^{A})^-$ for **6** and $(L^{tBuA})^-$ for **7** give consistent information about the coordination modes of NN′O ligands around nickel(II). The coordination geometries resemble those observed for cobalt(III/II) complexes recently reported by this group.[17,21] These structures are arranged pseudo-octahedrally in an approximate D_{2h} local symmetry about the nickel(II) center, coordinated by two deprotonated, facially coordinated ligands. Hence, **6** and **7** are described in BMT[25] notation as [Ni <$N_{am1}N_{am2}$> <$N_{py1}N_{py2}$> <$O_{phen1}O_{phen2}$>]. The Ni–N_{amine} bond lengths consistently measure 2.11 Å, while the Ni–$O_{phenolate}$ bond lengths are 2.09 Å and the Ni–$N_{pyridine}$ bond lengths are 2.08 and 2.10 Å. The six-coordinate geometry and absorption spectra (vide infra) indicate the presence of a high spin $3d^8$ ion.[23,26] On the basis of the structures of these two archetypes, an accurate picture of the coordination modes present in **2** can be drawn.

The Copper Archetype 8′: By means of counterion exchange, single crystals of the complex $[Cu^{II}(HL^{tBuA})(L^{tBuA})]B(Ph)_4$ (**8′**) were obtained from the perchlorate parent species **8** to gather comparative information about the coordination modes and geometrical parameters of the copper-containing surfactant **3**. It contains a discrete $[Cu^{II}(HL^{tBuODA})(L^{tBuODA})]^+$ cation in which a single ligand is deprotonated, whereas another one remains protonated. Therefore, the coordination sphere around the copper(II) center in **8′**, and consequently in **8** and **3** as well, approximates a distorted $N_2N_2'O$ square-pyramidal geometry (τ = 0.34)[27] in which the protonated O_{phenol} assumes a remote position (viz. Cu1···O2 > 3.80A). The angles between adjacent corner atoms of the basal plane (O1–Cu1–N2 93.0°, O1–Cu1–N4 91.2°, N1–Cu1–N4 92.4°, and N2–Cu1–N1 81.0°) are consistent with pseudo-square pyramidal interplane angles approximating 90°, where the atoms O1, N4, N1, and N2 are situated on the vertices of the plane, while the pyridine nitrogen, N3, is apically coordinated to the copper center (2.27 Å). The *trans* amine nitrogen to opposing amine nitrogen bond angle is 152.4° and the *trans* phenolate oxygen to pyridine nitrogen bond angle is 173.0°, leaving the bond angles comprising the apical pyridine ni-

Table 1. Selected bond lengths [Å] and angles [°] for **5**, **6**, **7**, **8′**, and **9**.

5	**6**	**7**	**8′**	**9**
Ni1–O1 1.8215(9)	Ni1–O1 2.0916(17)	Ni1–O1 2.0869(13)	Cu1–O1 1.9501(15)	Zn1–O1 1.960(3)
Ni1–N1 1.8416(10)	Ni1–N1 2.0829(18)	Ni1–N1 2.1039(16)	Cu1–N2 1.9938(18)	Zn1–N3 2.074(4)
Ni1–N2 1.8863(10)	Ni1–N2 2.1119(19)	Ni1–N2 2.1117(17)	Cu1–N4 2.0419(19)	Zn1–N2 2.141(4)
Ni1–O2 1.8840(8)			Cu1–N1 2.0609(19)	Zn1–N1 2.147(4)
			Cu1–N3 2.2708 (19)	Zn1–N4 2.175(4)
Bite angles	Bite angles	Bite angles	Bite angles	Bite angles
O1–Ni1–N1 94.87(4)	O1–Ni1–N2 89.60(7)	O1–Ni1–N2 89.66(6)	O1–Cu1–N2 93.01(7)	O1–Zn1–N2 94.10(13)
N1–Ni1–N2 85.72(4)	N1–Ni1–N2 79.86(7)	N1–Ni1–N2 80.12(6)	N2–Cu1–N1 81.02(7)	N2–Zn1–N1 78.96(15)
			N4–Cu1–N3 79.21(7)	N3–Zn1–N4 80.44(14)
Average distances	Average distances	Average distances	Average distance	Average distances
Py C–C 1.3856(18)	Py C–C 1.3835(3)	Py C–C 1.371(3)	Py C–C 1.381(3)	Py C–C 1.374(8)
Py C–N 1.3534(15)	Py C–N 1.3395(3)	Py C–N 1.347(2)	Py C–N 1.345(3)	Py C–N 1.346(6)
Ph C–C 1.4081(16)	Py C–C 1.3933(4)	Ph C–C 1.3975(3)	Ph C–C 1.398(3)	Ph C–C 1.396(7)

trogen (O1–Cu1–N3 98.3°, N2–Cu1–N3 126.9°, N4–Cu1–N3 79.2°, and N1–Cu1–N3 88.2°) to reveal the degree of structural distortion. The increased copper to apical pyridine nitrogen bond length (2.27 Å) grants further evidence concerning the structure: the phenol group is neither bonded nor contributing structurally to the rigidity of the system. The other pyridine is situated *cis* to this apical pyridine with a Cu–N distance of 2.06 Å. Also occupying *cis* positions are the $O_{phenolate}$ atom (Cu1–O1 1.95 Å) and the N_{amine} atom (Cu1–N2 2.0 Å) of the deprotonated ligand. In addition, the N_{amine} of the protonated ligand is positioned *trans* (Cu1–N4 2.04 Å) to its opposing N_{amine} of the deprotonated ligand. These bond lengths are in good agreement with reported values.[28,29]

The Zinc Archetype 9: Analogous to the copper(II) center in the archetypical systems **8** and **8′**, the zinc(II) metal center in complex **9** bears ligand coordination through an $N_2N_2'O$ donor set consisting of two tertiary amine and pyridine nitrogen atoms, and a single deprotonated phenolate oxygen atom. Similarly, the second phenol oxygen atom is protonated and lies 3.42 Å from the metal center. Calculation of the relative amount of trigonality reveals that the structural coordination geometry is more characteristic of trigonal bipyramidal geometry with a τ value of 0.79. The pseudo-trigonal bipyramidal geometry of the complex demonstrates facial ligand coordination organized in an approximate C_{2v} local symmetry, where the phenolate oxygen atom (Zn1–O1 1.96 Å) and pyridine nitrogen atoms (Zn1–N1 2.15, Zn1–N3 2.07 Å) are positioned on the vertices of the equatorial plane, and the *trans* tertiary amine nitrogen atoms are apically coordinated to the zinc center (Zn1–N2 2.14, Zn1–N4 2.17 Å). The angles at the zinc ion center around the equatorial plane are consistent with pseudo-trigonal bipyramidal inter-plane angles approximating the ideal 120° (O1–Zn1–N1 128.41°, N1–Zn1–N3 114.29°, N3–Zn1–O1 117.24°), while the N2–Zn1–N4 axial bond angle is 175.98°, deviating slightly from 180° linearity. The range for the pyridine nitrogen to amine nitrogen axial-to-equatorial bond angles containing the zinc ion center, N_{ax}–Zn–N_{eq}, is 80–100°, and the amine nitrogen to phenolate oxygen axial-to-equatorial bond angle range at the zinc ion center, N_{ax}–Zn–O_{eq}, is 89–94°. For purpose of contrast, it is interesting to consider the distinguishing features that exist between zinc complexes with local pseudo-trigonal bipyramidal geometries. For instance the cation $[Zn(TMPA)(OBz)]^+$,[30] where TMPA is tris[(2-pyridyl)-methyl]amine and OBz is a benzoate ligand, is functionally comparable to **9**. The TMPA-based complex exhibits a slightly elongated Zn^{II} to axial N_{amine} bond length (2.26 Å) along with shorter Zn–$N_{pyridine}$ distances, when compared to **9**. The axial Zn–$O_{benzoate}$ bond (1.95 Å), on the other hand, is nearly equivalent to the equatorial Zn–$O_{phenolate}$ bond (1.96 Å) in **9**. Equally relevant is the precise crystallographic work described by Neves et al.[31–33] on zinc-phenolate ligands. It has been postulated that both the nature of the phenol ring substituent and the geometry adopted around the metal play a crucial role in the length of the Zn–$O_{phenolate}$ bond. Unsubstituted ligands yield the longest bonds (2.15 Å), whereas bromo- and *tert*-butyl-substituted phenolates yield comparable bonds reaching 1.90 to 1.96 Å, respectively. This is in good agreement with the value observed for **9**. It is noteworthy that while most ligands yield $[ZnL_2]$ species, *tert*-butyl-substituted ligands are prone to form partially protonated $[Zn(HL)(L)]^+$ species. This has been observed even when zinc acetate, which fosters phenol deprotonation, is used. Unfortunately, **9** does not seem to be a valid archetypical model for **4**. The archetype possesses a single protonated ligand, whereas elemental analysis and mass spectrometry support the presence of two protonated ligands in the surfactant. This is also consistent with an unusual collapse mechanism pattern observed in the Langmuir films of **4**.

Table 2. UV/vis parameters for ligands and complexes.

Compounds [a] Ligands	λ [nm] (ε) [L mol^{-1} cm^{-1}][b]
HL^{tBuODA}	263 (7290), 268 (7200), 280 (5600)
HL^{tBuA}	262 (3750), 268 (3550), 282 (2990)
Nickel species	
$[Ni^{II}(L^{tBuODA})(OAc)]$ (**1**)	288 (6180), 422 (860), 604 {11} [c]; 965 {8}
$[Ni^{II}(L^{tBuI})(OAc)]\cdot CH_3OH$ (**5**)	261(6250), 348 sh (4030), 425, (915), 510 {10}
$[Ni^{II}(L^{tBuODA})_2]$ (**2**)	264 (9350), 620 {31}, 965 {12}
$[Ni^{II}(L^{A})_2]\cdot 2CH_3OH$ (**6**)	304 (8250), 605 {14}, 952 {5}
$[Ni^{II}(L^{tBuA})_2]\cdot 2CH_3OH$ (**7**)	306 (9220), 610 {18}, 960 {8}
Copper species[d]	
$[Cu^{II}(HL^{tBuODA})(L^{tBuODA})]ClO_4\cdot CH_3OH$ (**3**)	247 (18200), 287 (9340), 328 sh (4900), 498 (1060), 651 (660)
$[Cu^{II}(HL^{tBuA})(L^{tBuA})]ClO_4$ (**8**)	241 (20900), 289 (9800), 474 (1140), 640 (490)
Zinc species	
$[Zn^{II}(HL^{tBuODA})_2](ClO_4)_2$ (**4**)	263 (9540), 269 (8300), 290 (6340)
$[Zn^{II}(HL^{tBuA})(L^{tBuA})]ClO_4$ (**9**)	240 (12530), 289 (4600)

[a] Spectra measured in dichloromethane/methanol (1:1), unless otherwise noted. [b] Values for equivalent peaks within a similar group are sorted in columns. [c] All solutions are 1.0×10^{-4} M, except for values indicated in curly brackets where 1.0×10^{-2} M solutions were used. [d] Spectra measured in dichloromethane.

Electronic Spectroscopy

The electronic spectra of the ligands $\mathbf{HL}^{t\mathrm{BuODA}}$ and $\mathbf{HL}^{t\mathrm{BuA}}$, surfactant complexes **1**–**4**, and archetypes **5**–**9** were measured either in dichloromethane or in 1:1 solutions of dichloromethane/methanol. The results are summarized in Table 2 and selected spectra for the copper species **3** and **8** are shown in Figure 3. The ligands $\mathbf{HL}^{t\mathrm{BuODA}}$ and $\mathbf{HL}^{t\mathrm{BuA}}$ show expected similarities in the ultraviolet region, assigned to intense intraligand $\sigma \rightarrow \pi^*$ and $\pi \rightarrow \pi^*$ bands.

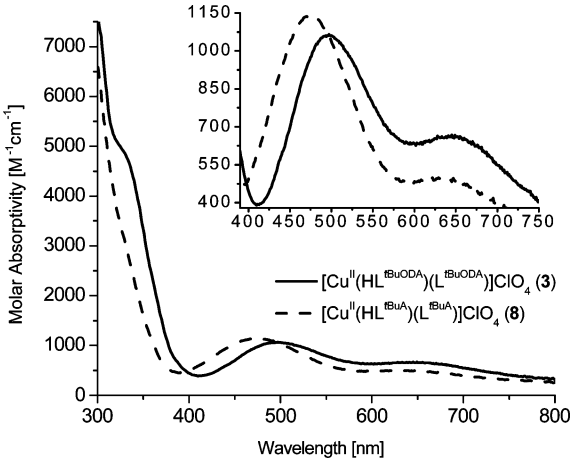

Figure 3. UV/vis spectra of complexes **3** and **8** in dichloromethane, 1.0×10^{-4} M. Inset: **3** and **8** at 1.0×10^{-2} M.

Electronic information is also limited for **4** and **9** as a consequence of the intrinsic nature of the $3d^{10}$ zinc(II) ion. The interpretation of the spectra is restricted to the observation of comparable profile contours for the intraligand $\pi \rightarrow \pi^*$ bands in both species. Assessment of the differences in coordination geometry revealed by mass spectrometry and elemental analysis was not possible. The square-planar $3d^8$ low-spin ($S = 0$) nickel(II) complex **1** reveals its nature with a medium-intensity band at 422 nm, attributed to a $^1A_{1g} \rightarrow {}^1A_{2g}$ spin-allowed d–d transition. [34] The archetype **5** displays a similar, albeit slightly more intense, band at 425 nm, along with a ill-defined shoulder at 348 nm. These features are less intense but comparable with those of low-spin [Ni^{II}(salen)],[26] and attributed respectively to charge transfer and π–π^* transitions. The nickel-centered d–d transitions are also comparable at 510 nm. The pseudo-octahedral nickel(II) species **2**, **6**, and **7** do not display this band and are characterized by less intense signals around 605–620 nm, ($\varepsilon \approx 20$–30) and 950–965 nm ($\varepsilon \approx 5$–15), respectively attributed to $^3A_{2g} \rightarrow {}^3T_{1g}(P)$ and $^3A_{2g} \rightarrow {}^3T_{2g}$ spin-allowed d–d transitions.[35] This is in good agreement with the observation that lower wavelength absorption bands are associated with low-spin square planar electronic configurations, while higher wavelength bands are found for high-spin octahedral configurations.[36] The positions of the observed absorptions in **1**, **2**, **5**–**7** indicate that in solution, **1** and **5** remain low-spin and **2**, **6**, and **7** remain high-spin. The high-spin ($S = 1$) nature of these species can be inferred by the presence of broad and ill-defined H^1 NMR peaks, but EPR detection is precluded due to the presence of an integer spin associated to the approximate $[e_g^2\ t_{2g}^4]$ configuration (in an idealized O_h symmetry) for the Ni^{II} ion. Very recently Thomas et al.[23] have isolated a series of nickel compounds related to the archetypes **6**, and **7** confirming the high-spin nature of pseudo-octahedral [$Ni^{II}(NN'O)_2$] systems. The most noticeable parallel between the nickel(II) surfactant **2** and the archetypes **6** and **7** is the similarity in shape and wavelength ranges for the two overlaid spectral curves. This validates further the use of archetypical complexes in providing direct insight to the coordination mode and local geometry of the metal center in architectures of higher complexity.

The agreement between the copper-containing surfactant **3** and archetype **8** is excellent. A broad band transition present at 498 and 474 nm, respectively in **3** and **8**, is attributed to a well characterized[37–39] phenolate $\rightarrow$ copper(II) charge-transfer transition. A lower intensity band centered at 640–650 nm is likely to have overlapping charge transfer and d–d band nature. The only evident deviation is the presence of a shoulder at 328 nm in the spectrum of **3** and absent in **8**. This shoulder is ascribed to a $N(\pi) \rightarrow Cu^{II}$ charge transfer observed for square-pyramidal copper(II) species.[40] It is possible to hypothesize that the alkyl group attached to the N_{amine} atom in **3** impinges a certain degree of distortion to the coordination environment around copper, thus causing bathochromic shifts. Indeed, all the charge-transfer bands in **3** seem to be red-shifted by about 10–20 nm. Therefore, the shoulder at 328 nm in **3** would be overlapped by more intense intraligand bands in **8**. Similar shifts have been observed by our group in phenolate-containing copper amphiphiles with distinct apolar chains.[18]

Electronic Structure Calculations

A series of electronic structure calculations were carried out on archetypical nickel-containing **6**, copper-containing **8**, and zinc-containing **9**, as well as on model **3′** (a model for the copper metallosurfactant **3** comprising of shortened alkyl chains). Attempts to model **4** were made considering multiple different geometrical arrangements, but lack of convergence towards a satisfactory minimum preclude discussion at this time. Single point energy calculations on **6** were carried out with nuclear coordinates obtained directly from the crystallographic structure (see Figure 2 above). The optimized geometries for structures of **8** and **9** are in good agreement with the crystallographic data presented above. Structural and electronic properties were evaluated to gain insight on the binding modes of the amphiphilic complexes. A recent study on **7**[23] supports the favorable *trans* facial coordination of the ligands over the meridional mode by ca. 5.0 kcal mol^{-1} using a comparable level of theory. Similar values were obtained for **6** suggesting that the $3d^8$ ion favors *trans*,*fac* coordination.

This is similar to the results observed for $3d^7$ ions, and in clear opposition to the preferred *cis*,*fac* observed for $3d^5$ ions. As shown in Figure 4, the spin density plot for the nickel archetype **6** is consistent with two unpaired electrons being arranged in the $d_{x^2-y^2}$ and d_{z^2} orbitals and resulting

in an $S = 1$ ground state. This triplet state is expected for six-coordinate high-spin bivalent nickel ($3d^8$) complexes. The molecular orbital plots of the singly occupied orbitals, namely the SOMO ($d_{x^2-y^2}$) and SOMO-1(d_{z^2}) orbitals are also available. The dipole moment for **6** is small in magnitude, reaching 0.10 Debye. This is not unexpected if the high symmetry of the all-*trans* binding mode of the ligands is taken into account, as it becomes clear by inspection of the spin density plot.

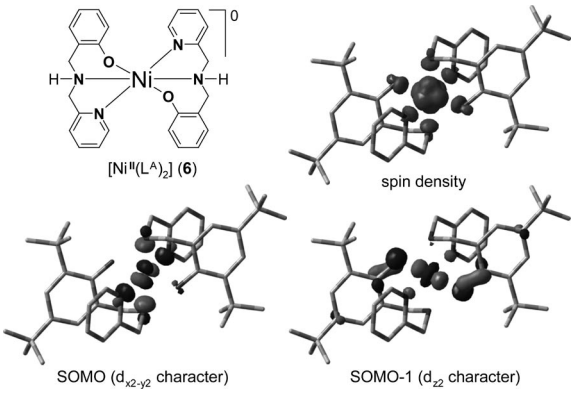

Figure 4. Selected MOs and spin density plot for the archetype **6**.

The copper archetype **8** displays the SOMO consistent with a $d_{x^2-y^2}$ orbital in good agreement with the expected behavior of a bivalent copper ($3d^9$) ion in a five coordinate complex (Figure 5). Comparison between **8** and the model **3′** shows similar geometrical arrangement and comparable bond lengths and angles. An almost identical hydrogen-bonding mode between the phenolate-phenol oxygen atoms is also present. One noticeable difference is the presence of a longer Cu–N_{amine} bond length for **3′** (ca. 0.03 Å) as compared to that of **8**. This lengthening must be associated with the change from a secondary amine in **8** to a tertiary amine in **3′**, and corroborates with the observations from the UV/vis spectra. The model **3′** also displays a SOMO consistent with a $d_{x^2-y^2}$ orbital. The spin density plots reinforce this notion. Both **3′** and **8** have comparable dipole moments of 13.9 and 13.7 Debye, respectively. Overall, the archetypical **8** can be considered in excellent agreement with model **3′**, and therefore, with metallosurfactant **3**.

Owing to their $3d^{10}$ configuration, the zinc complexes exhibit an $S = 0$ spin state. Consequently, **9** has no spin density plot and its frontier bonding orbitals are predominantly ligand-based (see Figure S1, Supporting Information). This increase in ionic character can be reinforced by comparing the Mulliken charges in archetypes **8** and **9**. An increase is observed in the Mulliken charge from 0.84 for the copper center in **8** to 0.94 for the zinc center in **9**. Similarly, the copper-bound phenolate-oxygen shows a charge of –0.77, compared to –0.80 in the zinc-bound phenolate-oxygen. The increasing charge separation in **9** corroborates with a decreased covalent character. The dipole moment of **9** is on the same order of magnitude as for **3′** and **8**, though slightly larger at 14.5 Debye.

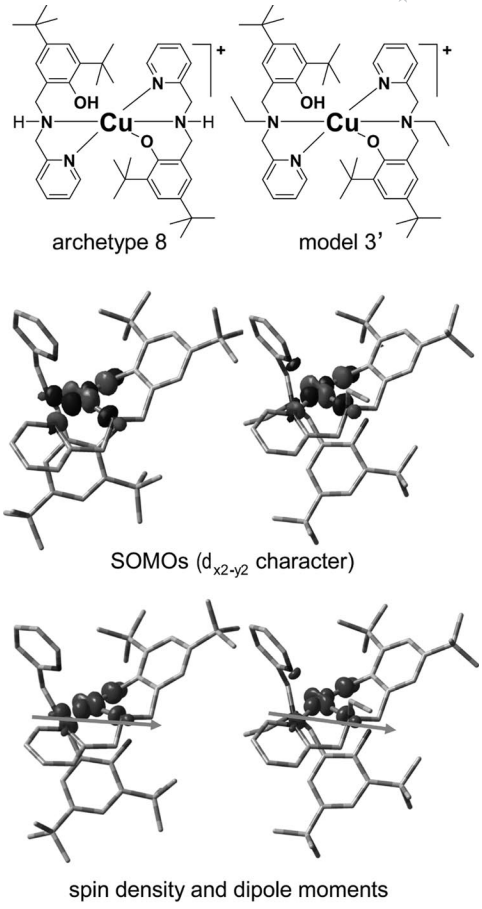

Figure 5. Selected molecular orbitals and spin-density plot for the optimized structures of the archetype **8** and model **3′**.

Amphiphilic Properties

The amphiphilic properties of species **1**–**4** were studied by way of compression isotherms[41] plotting surface pressure (Π, mN m^{-1}) vs. average area per molecule [A (Å)^2] and Brewster angle microscopy. Compression isotherms are performed in a minitrough with movable barriers and allow for two-dimensional activities that transpire at the air/water interface, which result in the formation of Langmuir films. The assessment of mono- or multilayers, collapse pressures (π_c), limiting areas per molecule (A_{lim}), and the area at the collapse of the monolayer (A_c) become evident. When the barriers of a minitrough are compressed, the tension (γ) of the amphiphile-containing air/water interface decreases as compared to that of the air/water interface only (γ_0 = 72 mN m^{-1} at 23 °C), following in an increase in Π (= γ_0 – γ). When conducting compression isotherms in concert with Brewster angle microscopy, polarized light passes throughout media with different refractive indexes at the air/water interface revealing agglomerates and domains, as well homogeneity in films.

Species **1**–**4** resemble structurally a series of *tert*-butyl-substituted phenolate-containing amphiphiles published recently by our group.[18] The main difference is the presence

of a methylpyridine arm attached to the N_{amine} atom. Similarly, the ligand HL^{tBuODA} used in this article is related to the ligand HL^{IODA} with iodo groups occupying the 2nd and 4th position of the phenolate ring. This ligand stabilizes bivalent cobalt ions in the $[Co^{II}(L^{IODA})_2]$ species.[17] A detailed comparison among these species will be provided. The isotherms for **1**–**4** are shown in Figure 6 and present moderate collapse pressures. For **1**, with a single alkyl chain and a higher dipole moment, the individual molecules start interacting at the air/water interface at around 85 $Å^2$ molecule^{-1}, whereas the molecules of **2**, **3**, and **4** interact at much higher areas of 185, 230, and 195 $Å^2$ molecule^{-1}, respectively. Hence, species **2**–**4** are characterized by large average areas per molecule reflecting the *trans* arrangement of the alkyl chains. At least partially, the high areas observed for **3** and **4** are also related to the presence of a cationic core. However, no clear pattern can be observed correlating an increase in average areas with increasing core charge, since the monocationic **3** displays higher areas than the dicationic **4**. In spite of the distinctive average areas, **1**, **3**, and **4** present similar profiles with an inflection point around 10–14 mN m^{-1} followed by a less steep compression pattern. Interestingly, species **4** shows a much more accentuated decline, resembling the profile of a system with constant-pressure collapse,[42] while **2** shows the opposite behavior, displaying a more steep isotherm after the inflection point at 18 mN m^{-1}. This led to the suspicion that in spite of a continuous compression profile and lack of traditional collapse, the inflection point in these systems may coincide with folding, bending, and breaking into multilayers proposed by the Ries mechanism.[43,44] Brewster angle microscopy was used to evaluate the homogeneity of the films and corroborates with the idea that agglomerates similar to those expected in multilayers exist after the inflection points. The results are shown in Figure 7, where it can be seen that for **1**–**4** flat domains coexist before compression at low surface pressures. Upon compression, seemingly homogeneous films are observed up to pressures that precede the inflection points, when the appearance of multiple ring-shaped events predominates. These rings are multilayer granules formed from the ejection of matter from the compressed monolayer when localized oscillations are present and account for the thermodynamic instability of the film.[45]

In an attempt to correlate structural and amphiphilic properties of **1**–**4**, as well as to compare with other similar metalloamphiphiles the following conclusions can be drawn: It is evident that **2**–**4** have roughly twice the area per molecule than **1**, this is due to the fact that **2**–**4** have two HL^{tBuODA} ligands coordinated to the metal center, while **1** contains a single ligand. The areas observed for **2**–**4** are the comparable to other *tert*-butyl-substituted phenolate-containing amphiphiles.[18] Replacement of these substituents by more polar groups, as well as the design of surfactants with a single alkyl chain as in **1**, seems to be necessary to achieve ordered films with higher collapse pressures. The nickel(II) complex **2** has a neutral octahedral core with two deprotonated $(L^{tBuODA})^-$ ligands, while copper-containing **3** has a five-coordinate monocationic core associated with one protonated HL^{tBuODA} ligand, and zinc-containing **4** has a dicationic four-coordinate core with both HL^{tBuODA} ligands protonated. It seems that in moving from rigid octahedral cores as in **2** to more flexible cores in **3** and **4**, a tendency toward constant-pressure collapse can be observed. This is in excellent agreement with the behavior observed for cobalt amphiphiles,[18] in which increased core-flexibility also led to a constant-pressure collapse mechanism. Finally, it is not clear why **2** and **4** display similar average areas per molecule, while **3** shows higher areas.

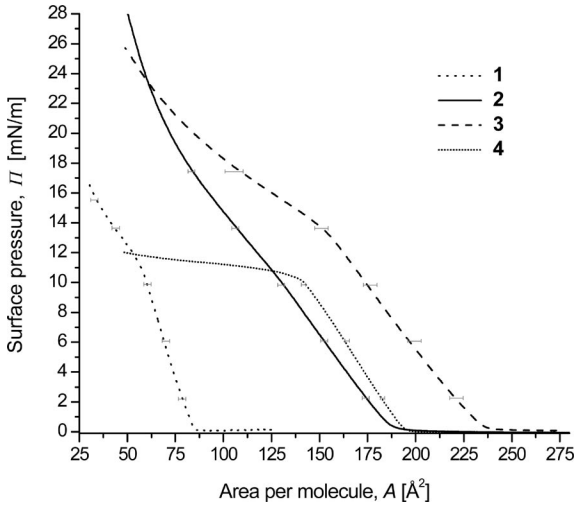

Figure 6. Langmuir–Blodgett isotherms of the metallosurfactants.

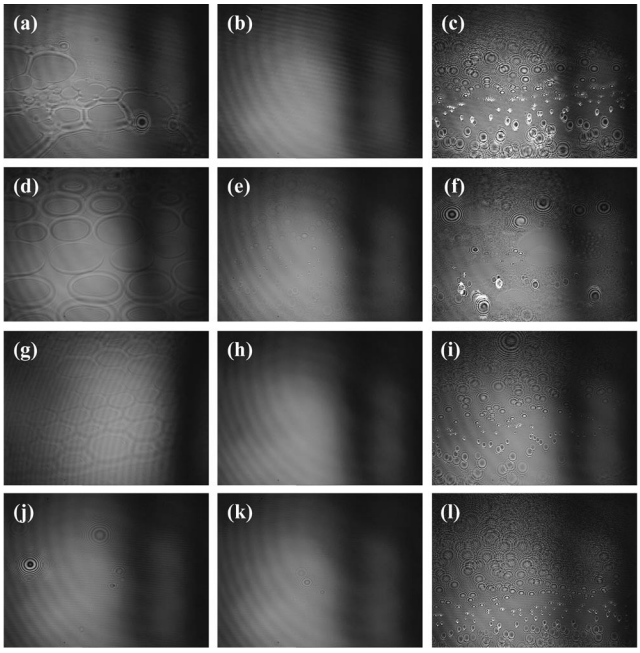

Figure 7. Selected Brewster angle micrographs. For **1**: (a) before compression, (b) between 1–10 mN m^{-1}, (c) after 11 mN m^{-1}. For **2**: (d) before compression, (e) between 3–10 mN m^{-1}, (f) after 11 mN m^{-1}. For **3**: (g) before compression, (h) between 2–12 mN m^{-1}, (i) after 13 mN m^{-1}. For **4**: (j) before compression, (k) between 1–10 mN m^{-1}, and (l) after 11 mN m^{-1}.

Summary and Conclusions

In this article we have synthesized and characterized the metallosurfactants $[Ni^{II}(L^{tBuODA})(OAc)]$ (**1**) $[Ni^{II}(L^{tBuODA})_2]$ (**2**), $[Cu^{II}(HL^{tBuODA})(L^{tBuODA})]ClO_4{\cdot}CH_3OH$ (**3**), and $[Zn^{II}(HL^{tBuODA})_2](ClO_4)_2$ (**4**). Due to the waxy texture of some of the metallosurfactants and due to the inability of getting crystal structures for **1**–**4**, archetypical modeling was used to assess the nature of these products. For this reason, species $[Ni^{II}(L^{tBuI})(OAc)]{\cdot}CH_3OH$ (**5**), $[Ni^{II}(L^{A})_2]{\cdot}CH_3OH{\cdot}H_2O$ (**6**), $[Ni^{II}(L^{tBuA})_2]{\cdot}2CH_3OH$ (**7**), $[Cu^{II}(HL^{tBuA})(L^{tBuA})]ClO_4$ (**8**), and $[Zn^{II}(HL^{tBuA})(L^{tBuA})]ClO_4$ (**9**) were synthesized. Careful analysis of **5**–**9** allowed us to evaluate the relationship between stoichiometric, coordination, and protonation preferences in metallosurfactants **1**–**4**, and therefore, draw structure/amphiphilic function relationships.

The nickel(II) complex **1** is square planar, whereas **2** has a neutral octahedral core with two deprotonated $(L^{tBuODA})^-$ ligands. Copper-containing **3** has a five-coordinate monocationic core associated with one protonated HL^{tBuODA} ligand, whereas the zinc-containing **4** has a dicationic four-coordinate core with both HL^{tBuODA} ligands protonated. DFT calculations were used to identify the frontier orbitals, polarizability, and dipole moments. In an attempt to correlate structural and amphiphilic properties of **1**–**4**, as well as to compare with other similar metalloamphiphiles the following conclusions can be drawn: in Langmuir films of **1**, the average molecular area is approximately half of that needed for **2**–**4**. Nonetheless the areas observed for **2**–**4** are comparable to other *tert*-butyl-substituted phenolate-containing amphiphiles. The nature of the core, reflected by its flexibility and coordination number seems to foster distinctive collapse mechanisms. Flexible penta- and tetracoordinate cores show a tendency to support constant-pressure collapse mechanisms. This behavior was also observed for structurally related cobalt amphiphiles, but in that case, the coordination modes were kept constant while the ligand flexibility was variable. The results reported here suggest that (i) control of the surfactant-to-metal ratio, (ii) selection of the coordination modes and structural properties of the material, and (iii) understanding of the protonation preferences of the ligands can be achieved by careful choice of the metal ion. Awareness of this information will allow to push current limits in reproducibility of thin films of metallosurfactants and is expected to pave the way toward the development of metal-containing responsive films.

Experimental Section

Materials and Methods: Reagents and solvents were used as received from commercial sources. Methanol was distilled from CaH_2, and dichloromethane was doubly purified on alumina columns using an Innovative Technologies solvent purification system. Infrared spectra were measured from 4000 to 400 cm^{-1} with a Tensor 27 FTIR-Spectrophotometer as KBr pellets. ^1H NMR spectra were measured with Varian 300 and 400 MHz instruments. ESI(+) spectra were measured in a triple quadrupole Micromass QuattroLC mass spectrometer with ESCi source. Elemental analyses were performed by Midwest Microlab, Indianapolis, IN. UV/Vis spectroscopy from 1.0×10^{-2} to 1.0×10^{-4} M dimethylformamide, dichloromethane, or dichloromethane/methanol (1:1) solutions were performed using a Cary 50 spectrometer within the 250 to 1100 nm range.

Compression Isotherms: The compression isotherms were measured in an automated KSV 2000 minitrough at 23 ± 0.5 °C. Ultrapure water (Barnstead NANO pure) was used with a resistivity of 17.5–18 $M\Omega cm^{-1}$ for all experiments. Surface impurities of the freshly poured aqueous subphases were removed by vacuum after barrier compression. Solutions of the complexes were prepared by dissolving 1.0 $mg\,mL^{-1}$ in chloroform. A known quantity (≈ 30 μL) of chloroform solutions was dispersed on the aqueous subphase, followed by ca. 20 min. equilibrium time before monolayer compression. The compression-isotherms were obtained at a compression rate of 5 $mm\,min^{-1}$. The surface pressure was measured using the Wilhelmy plate method (paper plates, 40 mm perimeter). A minimum of three independent measurements were carried out per sample with excellent reproducibility.

Brewster Angle Microscopy: A KSV-Optrel BAM 300 with a HeNe laser (10 mW, 632.8 nm) and a CCD detector were used in all micrographs. The compression rate was 5 $mm\,min^{-1}$, the field of view was 800×600 microns, and the lateral resolution was about 2 μm.

X-ray Structural Determinations: Diffraction data were measured using a Bruker P4/CCD or a Bruker X8 APEX-II kappa geometry diffractometer with Mo radiation and a graphite monochromator at 100 or 213 K. Frames were collected for 10 s and 0.2 or 0.3 ° between each frame. The frame data was indexed and integrated with the manufacturer's software.[46] SHELX-97 was used for refinement.[47] The collected crystal data for the five structures is shown in Table 3.

CCDC-703004 (for **5**), -703005 (for **6**), -703006 (for **7**), -703007 (for **8**), -703008 (for **9**) contain the supplementary crystallographic data for this paper. These data can be obtained free of charge from The Cambridge Crystallographic Data Centre via www.ccdc.cam.ac.uk/data_request/cif.

$[Ni(C_{23}H_{30}N_2O_3)]{\cdot}CH_3OH$ (5): Crystallized as red-amber rods, and a sample approximately $0.26\times0.20\times0.16$ mm^3 was used for data collection. 6513 frames were collected, yielding 101662 reflections, of which 8947 were independent. Hydrogen positions were placed in calculated or observed positions. The asymmetric unit consists of one neutral complex, with one equivalent of methanol solvate. $[Ni(C_{26}H_{26}N_4O_2)]{\cdot}(H_2O){\cdot}(CH_3OH)$ (**6**) crystallized as pale violet rods. A sample $0.28\times0.12\times0.15$ mm^3 was used for data collection. 1850 frames were collected, yielding 6605 reflections, of which 5292 were independent. Hydrogen positions were observed or calculated. The asymmetric unit contains two half coordination molecules, each with Ni occupying a crystallographic inversion center, and one equivalent each of solvents water and methanol.

$[Ni(C_{42}H_{58}N_4O_2)]{\cdot}2CH_3OH$ (**7**) crystallized as pale yellow-green rods and plates.

A sample $0.24\times0.18\times0.12$ mm^3 was used for data collection. 1850 frames were collected, yielding 53411 reflections, of which 7392 were independent. Hydrogen positions were observed and refined. The dataset exhibited a rotated 180 degree twin about the (100) reciprocal axis, and corrections were made by use of CELL-NOW, SAINT-7, and TWINABS.[46,47] The twin component refined to 41% of the total diffraction. Within the coordination complex, Ni occupies a crystallographic inversion center. The asymmetric unit

Table 3. Crystal data.

	5	6	7	8′	9
Formula	$C_{24}H_{34}NiN_2O_4$	$C_{27}H_{32}NiN_4O_4$	$C_{44}H_{66}NiN_4O_4$	$C_{67}H_{83}BCuN_4O_3$	$C_{42}H_{59}ClZnN_4O_6$
M	473.24	535.28	773.72	1066.72	816.75
Space group	$P2_1/c$	$P\bar{1}$	$P2_1/c$	$P2_1/c$	$P\bar{1}$
a [Å]	14.8325(6)	9.4001(6)	13.864(3)	10.7795(5)	11.439(3)
b [Å]	7.0996(3)	11.7678(8)	12.596(3)	27.7798(10)	13.745(5)
c [Å]	22.2614(9)	11.8448(8)	12.297(3)	20.1353(9)	15.891(5)
α [°]		100.501(1)			96.456(8)
β [°]	94.382(2)	90.400(1)	105.450(4)	97.053(2)	110.106(5)
γ [°]		101.558(2)			108.547(4)
V [Å^3]	2337.38(17)	1260.9(2)	2069.8(7)	5983.9(4)	2154.3(11)
Z	4	2	2	4	2
T [K]	100(2)	213(2)	213(2)	100(2)	213(2)
λ [Å]	0.71073	0.71073	0.71073	0.71073	0.71073
$D_{calcd.}$ [g cm^{-3}]	1.345	1.410	1.241	1.184	1.259
μ [mm^{-1}]	0.862	0.810	0.515	0.413	0.681
$R(F)$ (%)[a]	3.43	3.87	3.59	4.70	7.47
$Rw(F)$ (%)	8.87	10.09	7.61	10.38	19.88

[a] $R(F) = \Sigma||F_o| - |F_c|| / \Sigma|F_o|$ for $I > 2\sigma(I)$; $Rw(F) = [\Sigma w(F_o^2 - F_c^2)^2/\Sigma w(F_o^2)^2]^{1/2}$ for $I > 2\sigma(I)$.

contains one half complex and one molecule of methanol solvate. $[Cu(C_{42}H_{59}N_4O_2)]\cdot B(C_6H_5)_4\cdot CH_3OH$ (**8′**) crystallized as square, purple plates. The sample mounted measured $0.24 \times 0.22 \times 0.03$ mm^3. 1397 frames were collected, yielding 51713 reflections, of which 14731 were unique. Hydrogen atoms were placed in observed or calculated positions. The asymmetric unit contains one cation, a tetraphenylborate anion and one equivalent of methanol solvent. $[Zn(C_{42}H_{59}N_4O_2)](ClO_4)$ (**9**) presents as yellow plates. The sample used was $0.4 \times 0.2 \times 0.05$ mm^3. 1850 frames yielded 11230 reflections, of which 8803 were unique. Hydrogen atoms were placed in observed or calculated positions. Partially occupied positions were assigned for disorder in the *tert*-butyl groups C15–17 and C36–38. In addition, C36–38 and C36′-38′ were kept isotropic during refinement. Typical large thermal parameters were displayed by the perchlorato anion.

Computational Calculations: Electronic Structure Calculations Methods. The B3LYP/6-31G(d) level of theory[48] was employed throughout. All calculations were done using the GAUSSIAN series of programs.[49] Geometries were fully minimized unless otherwise indicated, without symmetry constraints, using standard methods.[50] Cartesian coordinates of all optimized structures are provided as supporting material.

Syntheses

Preparation of the Ligands HL^A, HL^{tBu2A}, HL^{tBu2I}, and HL^{tBu2ODA}: The ligands were synthesized according to the literature.[17,20,21] Basic procedures are explained for the syntheses of the nickel, copper, and zinc complexes.

Preparation of the Metallosurfactant [Ni^{II}(L^{tBuODA})(OAc)] (1): A 10 mL MeOH solution of $Ni(OAc)_2\cdot 4H_2O$ (0.25 g, 1.0 mmol) was added dropwise to a 30 mL MeOH solution of HL^{tBuODA} (0.58 g, 1.0 mmol). The solution was stirred and gently refluxed for 2 h, and then filtered to eliminate unreacted solids. Slow solvent evaporation after concentration to one-third of its original volume yielded a waxy, dark green film layer. Yield 0.50 g, 72% for $[C_{41}H_{68}N_2O_3Ni_1]$ (1214.6). IR data (KBr): $\tilde{\nu}$ = 2933–2857 (alkyl chain and *tert*-butyl C–H stretches), 1609 (C=N from pyridine), 1574 (antisym. acetate stretch), 1480 (C–O from phenyl) cm^{-1}. MS data (ESI$^+$ in MeOH): m/z = 695.4 [Ni(L^{tBuODA})(OAc) + H]$^+$.

Preparation of the Metallosurfactants [Ni^{II}(L^{tBuODA})$_2$] (2), [Cu^{II}(HL^{tBuODA})(L^{tBuODA})]ClO$_4$ (3), and [Zn^{II}(HL^{tBuODA})$_2$](ClO$_4$)$_2$ (4)

CAUTION! *Although no difficulties were experienced, species **3–4** and **8–9** were isolated as their perchlorate salts, and therefore they should be handled as potentially explosive.*

A 10 mL MeOH solution containing the salts $Ni(ClO_4)_2\cdot 6H_2O$ (0.18 g, 0.5 mmol), $Cu(ClO_4)_2\cdot 6H_2O$ (0.185 g, 0.5 mmol), or $Zn(ClO_4)_2\cdot 6H_2O$ (0.186 g, 0.5 mmol) was added dropwise to a 30 mL MeOH solution containing HL^{tBuODA} (0.58 g, 1.0 mmol) and Et_3N (0.14 mL, 1.0 mmol). In each case the resulting solutions were stirred under mild reflux for 1–2 h and then filtered while warm. The solvent was removed by rotary evaporation and the crude products were dissolved in 50 mL dichloromethane and washed with 4×50 mL of saturated brine solution in a separation funnel. The dichloromethane phase was then dried with Na_2SO_4 and concentrated to one third of its origonal volume. Slow solvent evaporation yielded a brown thick oil for **2**, a brownish green waxy solid for **3** and an off-white solid for **4**.

2: Yield 0.42 g, 70% for $[C_{78}H_{130}N_4O_2Ni_1]$ (1214.6). IR data (KBr): $\tilde{\nu}$ = 2958–2854 (alkyl chain and *tert*-butyl C–H stretches), 1610 (C=N from pyridine), 1467 (C–O from phenyl) cm^{-1}. MS data (ESI$^+$ in MeOH): m/z = 1214 [Ni(L^{tBuODA})$_2$ + H]$^+$. The consistency of the material precludes elemental analysis.

3: Yield 0.46 g, 68%. $C_{79}H_{135}ClCuN_4O_7$ (1351.9): calcd. C 70.18, H 10.02, N 4.14; found C 69.66, H 9.84, N 3.97. IR data (KBr): $\tilde{\nu}$ = 2922–2856 (alkyl chain and *tert*-butyl C–H stretches), 1611 (C=N from pyridine), 1467 (C–O from phenyl), 1104 (Cl–O from ClO_4^-) cm^{-1}. MS data (ESI$^+$ in MeOH): m/z = 1219.0 [Cu(HL^{tBuODA})(L^{tBuODA})]$^+$.

4: Yield 0.50 g, 70%. $C_{78}H_{132}Cl_2N_4O_{10}Zn$ (1422.2): calcd. C 65.87, H 9.36, N 3.94; found C 66.12, H 9.34, N 4.00. IR data (KBr): $\tilde{\nu}$ = 2923–2851 (alkyl chain and *tert*-butyl C–H stretches), 1608 (C=N from pyridine), 1472 (C–O from phenyl), 1116 (Cl–O from ClO_4^-) cm^{-1}. MS data (ESI$^+$ in MeOH): m/z = 1220.0 [Zn(HL^{tBuODA})(L^{tBuODA})]$^+$ and 641.5 [($m/2$) + CH_3OH].

Preparation of the Archetype [Ni^{II}(L^{tBuI})(OAc)]·CH$_3$OH (5): The synthesis of this complex similarly follows that of **1**. The crude red powder product obtained after roto-evaporation was recrystallized using a 1:1 dichloromethane/methanol solvent combination to give needle-like crystals. Yield 0.65 g, 77%. $C_{24}H_{34}N_2NiO_4$ (473.2): calcd. C 60.81, H 7.24, N 5.92; found C 59.92, H 7.26, N 6.18. IR data (KBr): $\tilde{\nu}$ = 1600 (C=N from pyridine), 1570 (antisym. acetate

stretch) cm^{-1}. 1487 (C–O from phenyl), 2957–2869 (C–H). MS data (ESI^+ in MeOH): m/z = 413.4 $[Ni(L^{tBuI}) + CH_3OH]^+$.

Preparation of the Archetypes $[Ni^{II}(L^A)_2]\cdot H_2O\cdot CH_3OH$ (6), $[Ni^{II}(L^{tBuA})_2]\cdot 2CH_3OH$ (7), $[Cu^{II}(HL^{tBuA})(L^{tBuA})]ClO_4$ (8), $[Zn^{II}(HL^{tBuA})(L^{tBuA})]ClO_4$ (9): A general synthetic approach was followed for the archetypical complexes. A 10 mL solution of $Ni(ClO_4)_2\cdot 6H_2O$ (0.366 g, 1.0 mmol) for **6** and **7**, $Cu(ClO_4)_2\cdot 6H_2O$ (0.370 g, 1 mmol) for **8**, or $Zn(ClO_4)_2\cdot 6H_2O$ (0.372 g, 1 mmol) for **9** was added dropwise to a 30 mL MeOH solution containing 2.0 mmol of the appropriate ligand (HL^A for **6** and HL^{tBuODA} for **7**–**9**) and 2 equiv. of Et_3N (0.28 mL, 2.0 mmol). In each reaction, the resulting solution was stirred and warmed gently for 1 h. The metal complexes were recovered either by precipitation or by slow evaporation and were collected by filtration and washed with diethyl ether. Recrystallization in MeOH afforded suitable crystals for X-ray analysis for **6**, **7**, **8**, and **9** after slow solvent evaporation.

6: Yield 0.53 g, 79%. $C_{27}H_{32}N_4NiO_4$ (535.3): calcd. C 60.65, H 6.03, N 10.48; found C 60.23, H 6.17, N 10.21. IR data (KBr): $\tilde{\nu}$ = 3291 (N–H), 2924 (C–H stretches), 1606, 1593 (C=N from pyridine), 1486 (C–O from phenyl) cm^{-1}. MS data (ESI^+ in MeOH): m/z = 484.1 $[Ni(L^A)_2 + H]^+$.

7: Yield 0.59 g, 76%. $C_{44}H_{66}N_4NiO_4$ (773.7): calcd. C 68.35, H 8.61, N 7.25; found C 68.23, H 8.74, N 7.20. IR data (KBr): $\tilde{\nu}$ = 3322 (N–H), 2950 (C–H), 1607 (C=N from pyridine), 1469 (C–O from phenyl) cm^{-1}. MS data (ESI^+ in MeOH): m/z = 709.3 $[Ni(L^{tBuA})_2 + H]^+$.

8: Yield 0.68 g, 82%. $C_{42}H_{61}ClCuN_4O_7$ (832.9): calcd. C 60.56, H 7.38, N 6.73; found C 60.05, H 7.36, N 6.81. IR data (KBr): $\tilde{\nu}$ = 3439 (OH), 3259 (N–H), 2954 (C–H), 1603 (C=N from pyridine), 1443 (C–O from phenyl), 1120 (Cl–O from ClO_4^-) cm^{-1}. MS data (ESI^+ in MeOH): m/z = 714.4 $[Cu(HL^{tBuA})(L^{tBuA})]^+$. **Note:** X-ray quality crystals were generated through counterion exchange using a 3-fold excess of tetraphenylboron sodium salt in 50 mL methanol.

9: Yield 0.60 g, 73%. $C_{42}H_{59}ClN_4O_6Zn$ (816.8): calcd. C 61.76, H 7.28, N 6.86; found C 61.84, H 7.32, N 6.90. IR data (KBr): $\tilde{\nu}$ = 3290 (N–H), 2957–2869 (C–H), 1608 (C=N from pyridine), 1474 (C–O from phenyl), 1097 (Cl–O from ClO_4^-) cm^{-1}. MS data (ESI^+ in MeOH): m/z = 715.2 $[Zn^{II}(HL^{tBuA})(L^{tBuA})]^+$.

Supporting Information (see also the footnote on the first page of this article): Selected MOs for compound **9**, Cartesian coordinates for DFT calculations.

Acknowledgments

C. N. V. thankfully acknowledges the Wayne State University, the Donors of the ACS-Petroleum Research Fund (Grant No. 42575-G3), the Nano@Wayne initiative (Fund 11E420), and the National Science Foundation (Grant CHE-0718470) for financial support. F. D. L. acknowledges support from the WSU-Institute for Manufacturing Research. Computer time allocated at the WSU-Grid System to the DFT calculations is also acknowledged.

[1] J. Park, A. N. Pasupathy, J. I. Goldsmith, C. Chang, Y. Yaish, J. R. Petta, M. Rinkoski, J. P. Sethna, H. D. Abruna, P. L. McEuen, D. C. Ralph, *Nature* **2002**, *417*, 722.

[2] a) J. Zhang, B. W.-K. Chu, N. Zhu, V. W.-W. Yam, *Organometallics* **2007**, *26*, 5423; b) V. W.-w. Yam, B. Li, Y. Yang, B. W.-k. Chu, K. M.-c. Wong, K.-k. Cheung, *Eur. J. Inorg. Chem.* **2003**, 4035; c) B. W.-K. Chu, V. W.-W. Yam, *Inorg. Chem.* **2001**, *40*, 3324.

[3] a) K. Binnemans, K. Lodewyckx, B. Donnio, D. Guillon, *Chem. Eur. J.* **2002**, *8*, 1101; b) K. Binnemans, Y. G. Galyametdinov, R. Van Deun, D. W. Bruce, S. R. Collinson, A. P. Polishchuk, I. Bikchantaev, W. Haase, A. V. Prosvirin, L. Tinchurina, I. Litvinov, A. Gubajdullin, A. Rakhmatullin, K. Uytterhoeven, L. Van Meervelt, *J. Am. Chem. Soc.* **2000**, *122*, 4335.

[4] a) J.-M. Rueff, N. Masciocchi, P. Rabu, A. Sironi, A. Skoulios, *Eur. J. Inorg. Chem.* **2001**, 2843; b) J.-M. Rueff, N. Masciocchi, P. Rabu, A. Sironi, A. Skoulios, *Chem. Eur. J.* **2002**, *08*, 1813.

[5] J. B. Beck, S. J. Rowan, *J. Am. Chem. Soc.* **2003**, *125*, 13922.

[6] S. Hayami, K. Danjobara, Y. Shigeyoshi, K. Inoue, Y. Ogawa, Y. Maeda, *Inorg. Chem. Commun.* **2005**, *8*, 506.

[7] I. K. Lednev, M. C. Petty, *Adv. Mater.* **1996**, *8*, 615.

[8] F. W. Vergeer, X. Chen, F. Lafolet, L. De Cola, H. Fuchs, L. Chi, *Adv. Funct. Mater.* **2006**, *16*, 625.

[9] P. C. Griffiths, I. A. Fallis, T. Chuenpratoom, R. Watanesk, *Adv. Colloid Interf. Sci.* **2006**, *122*, 107; P. C. Griffiths, I. A. Fallis, D. J. Willock, A. Paul, C. L. Barrie, P. M. Griffiths, G. M. Williams, S. M. King, R. K. Heenan, R. Goergl, *Chem. Eur. J.* **2004**, *10*, 2022.

[10] X. Chen, S. Lenhert, M. Hirtz, N. Lu, H. Fuchs, L. Chi, *Acc. Chem. Res.* **2007**, *40*, 393.

[11] L. Yang, H. Peng, K. Huang, J. T. Mague, H. Li, Y. Lu, *Adv. Funct. Mater.* **2008**, *18*, 1526.

[12] C. J. Brabec, N. S. Sariciftci, J. C. Hummelen, *Adv. Funct. Mater.* **2001**, *11*, 15.

[13] a) D. A. Jaeger, M. F. Peacock, D. S. Bohle, *Langmuir* **2003**, *19*, 4859; b) N. Arulsamy, D. S. Bohle, P. A. Goodson, D. A. Jaeger, V. B. Reddy, *Inorg. Chem.* **2001**, *40*, 836.

[14] a) H. J. Choi, M. P. Suh, *Inorg. Chem.* **2003**, *42*, 1151; b) M. F. Ryan, R. A. Metcalfe, A. B. P. Lever, M.-a. Haga, *J. Chem. Soc., Dalton Trans.* **2000**, 2357; c) K. Wang, M.-a. Haga, H. Monjushiro, M. Akiba, Y. Sasaki, *Inorg. Chem.* **2000**, *39*, 4022.

[15] R. Shakya, P. H. Keyes, M. J. Heeg, A. Moussawel, P. A. Heiney, C. N. Verani, *Inorg. Chem.* **2006**, *45*, 7587.

[16] R. Shakya, S. S. Hindo, L. Wu, S. Ni, M. Allard, M. J. Heeg, S. R. P. da Rocha, G. T. Yee, H. P. Hratchian, C. N. Verani, *Chem. Eur. J.* **2007**, *13*, 9948.

[17] R. Shakya, S. S. Hindo, L. Wu, M. M. Allard, M. J. Heeg, H. P. Hratchian, B. R. McGarvey, S. R. P. da Rocha, C. N. Verani, *Inorg. Chem.* **2007**, *46*, 9808.

[18] S. S. Hindo, R. Shakya, N. S. Rannulu, M. M. Allard, M. J. Heeg, M. T. Rodgers, S. R. P. da Rocha, C. N. Verani, *Inorg. Chem.* **2008**, *47*, 3119.

[19] J. A. Driscoll, M. M. Allard, L. Wu, M. J. Heeg, S. R. P. da Rocha, C. N. Verani, *Chem. Eur. J.* **2008**, accepted.

[20] C. Imbert, H. P. Hratchian, M. Lanznaster, M. J. Heeg, L. M. Hryhorczuk, B. R. McGarvey, H. B. Schlegel, C. N. Verani, *Inorg. Chem.* **2005**, *44*, 7414.

[21] R. Shakya, C. Imbert, H. P. Hratchian, M. Lanznaster, M. J. Heeg, B. R. McGarvey, M. Allard, H. B. Schlegel, C. N. Verani, *Dalton Trans.* **2006**, 2517.

[22] R. Shakya, F. Peng, J. Liu, M. J. Heeg, C. N. Verani, *Inorg. Chem.* **2006**, *45*, 6263.

[23] O. Rotthaus, V. Labet, C. Philouze, O. Jarjayes, F. Thomas, *Eur. J. Inorg. Chem.* **2008**, 4215.

[24] A. A. Khandar, S. A. Hosseini-Yazdi, S. A. Zarei, *Inorg. Chim. Acta* **2005**, *358*, 3211.

[25] BMT stems for Bailar, Missler and Tarr notation, where ‹A1B2› indicates that A is *trans* to B, with A and B corresponding to the pyridine (Npy) amine (Nam), or phenolato (Ophen) groups. Subscripts 1 and 2 designate respectively the first and the second ligand. This concise notation saves space and was adapted by G. Miessler and D. Tarr, in *Inorganic Chemistry*, Pearson-Prentice Hall, p. 311–315, **2004** from the original work by John Bailar, Jr, *J. Chem. Educ.* 1957, **34**, 334 and 623. The link to Prof. Bailar's work has been explained by Prof. Miessler in a personal communication to C.N.V.

[26] O. Rotthaus, F. Thomas, O. Jarjayes, C. Philouze, E. Saint-Aman, J.-L. Pierre, *Chem. Eur. J.* **2006**, *12*, 6953.

[27] A. W. Addison, T. N. Rao, J. Reedijk, J. Van Rijn, G. C. Verschoor, *J. Chem. Soc., Dalton Trans.* **1984**, 1349.
[28] A. Neves, C. N. Verani, M. A. de Brito, I. Vencato, A. Mangrich, G. Oliva, D. D. H. F. Souza, A. A. Batista, *Inorg. Chim. Acta* **1999**, *290*, 207.
[29] J. Kaizer, J. Pap, G. Speier, L. Parkanyi, L. Korecz, A. Rockenbauer, *J. Inorg. Biochem.* **2002**, *91*, 190.
[30] H. Adams, N. A. Bailey, D. E. Fenton, Q.-Y. He, *J. Chem. Soc., Dalton Trans.* **1997**, 1533.
[31] M. Lanznaster, A. Neves, I. Vencato, A. J. Bortoluzzi, H. Gallardo, S. P. Machado, A. M. C. Assumpcao, *J. Braz. Chem. Soc.* **2006**, *17*, 289.
[32] A. dos Anjos, A. J. Bortoluzzi, B. Szpoganicz, M. S. B. Caro, G. R. Friedermann, A. S. Mangrich, A. Neves, *Inorg. Chim. Acta* **2005**, *358*, 3106.
[33] A. Neves, I. Vencato, C. N. Verani, *J. Braz. Chem. Soc.* **1997**, *8*, 265.
[34] A. B. P. Lever, *Inorganic Electronic Spectroscopy*, 2nd ed., Elsevier Science, Amsterdam, **1984**.
[35] S. Mukhopadhyay, D. Mandal, D. Ghosh, I. Goldberg, M. Chaudhury, *Inorg. Chem.* **2003**, *42*, 8439.
[36] H. Ohtsu, K. Tanaka, *Inorg. Chem.* **2004**, *43*, 3024.
[37] a) R. Viswanathan, M. Palaniandavar, T. Balasubramanian, P. T. Muthiah, *J. Chem. Soc., Dalton Trans.* **1996**, 2519; b) U. Rajendran, R. Viswanathan, M. Palaniandavar, M. Lakshminarayanan, *J. Chem. Soc., Dalton Trans.* **1992**, 3563.
[38] a) E. Bill, J. Mueller, T. Weyhermueller, K. Wieghardt, *Inorg. Chem.* **1999**, *38*, 5795; b) U. Auerbach, U. Eckert, K. Wieghardt, B. Nuber, J. Weiss, *Inorg. Chem.* **1990**, *29*, 938.
[39] a) B. A. Jazdzewski, P. L. Holland, M. Pink, V. G. Young Jr., D. J. E. Spencer, W. B. Tolman, *Inorg. Chem.* **2001**, *40*, 6097; b) J. A. Halfen, B. A. Jazdzewski, S. Mahapatra, L. M. Berreau, E. C. Wilkinson, L. Que Jr., W. B. Tolman, *J. Am. Chem. Soc.* **1997**, *119*, 8217.
[40] a) S. Carvalho, R. Delgado, M. G. B. Drew, V. Felix, *Dalton Trans.* **2007**, 2431; b) C. A. VanOrman, K. V. Reddy, L. M. Sayre, F. L. Urbach, *Polyhedron* **2001**, *20*, 541; c) E. L. Hegg, S. H. Mortimore, C. L. Cheung, J. E. Huyett, D. R. Powell, J. N. Burstyn, *Inorg. Chem.* **1999**, *38*, 2961.
[41] M. C. Petty, *Langmuir–Blodgett Films*, Cambridge University Press, New York, **1996**, pp. 65.
[42] a) S. Kundu, A. Datta, S. Hazra, *Phys. Rev. E: Stat., Nonlinear, Soft Matter Phys.* **2006**, *73*, 051608/051601–051608/051607; b) S. Kundu, A. Datta, S. Hazra, *Langmuir* **2005**, *21*, 5894.
[43] C. Ybert, W. Lu, G. Moller, C. M. Knobler, *J. Phys.: Condens. Matter* **2002**, *14*, 4753.
[44] H. E. Ries Jr., *Nature* **1979**, *281*, 287.
[45] J. Galvan-Miyoshi, S. Ramos, J. Ruiz-Garcia, R. Castillo, *J. Chem. Phys.* **2001**, *115*, 8178.
[46] *APEX-II*, SMART, SAINT, SAINT-7, SADABS and TWINABS collection and processing programs are distributed by the manufacturer. Bruker AXS, Inc., Madison WI, USA **2001**.
[47] a) H. Sheldrick, *SHELX-97 and CELL-NOW*, University of Göttingen, Germany, **1997**; b) G. M. Sheldrick, *Acta Crystallogr., Sect. A* **2008**, *64*, 112.
[48] a) R. Ditchfield, W. J. Hehre, J. A. Pople, *J. Chem. Phys.* **1971**, *54*, 724; b) W. J. Hehre, R. Ditchfield, J. A. Pople, *J. Chem. Phys.* **1972**, *56*, 2257; c) P. C. Hariharan, J. A. Pople, *Theor. Chim. Acta* **1973**, *28*, 213; d) P. C. Hariharan, J. A. Pople, *Mol. Phys.* **1974**, *27*, 209; e) M. S. Gordon, *Chem. Phys. Lett.* **1980**, *76*, 163; f) A. D. Becke, *Phys. Rev. A: Gen. Phys.* **1988**, *38*, 3098; g) C. Lee, W. Yang, R. G. Parr, *Phys. Rev. B: Condens. Matter* **1988**, *37*, 785; h) A. D. Becke, *J. Chem. Phys.* **1993**, *98*, 5648.
[49] M. J. Frisch, G. W. Trucks, H. B. Schlegel, G. E. Scuseria, M. A. Robb, J. R. Cheeseman, J. A. Montgomery, T. V. K. N. Kudin Jr., J. C. Burant, J. M. Millam, S. S. Iyengar, J. Tomasi, V. Barone, B. Mennucci, M. Cossi, G. Scalmani, N. Rega, G. A. Petersson, H. Nakatsuji, M. Hada, M. Ehara, K. Toyota, R. Fukuda, J. Hasegawa, M. Ishida, T. Nakajima, Y. Honda, O. Kitao, H. Nakai, M. Klene, X. Li, J. E. Knox, H. P. Hratchian, J. B. Cross, V. Bakken, C. Adamo, J. Jaramillo, R. Gomperts, R. E. Stratmann, O. Yazyev, P. Y. Ayala, K. Morokuma, G. A. Voth, P. Salvador, J. J. Dannenberg, V. G. Zakrzewski, S. Dapprich, A. D. Daniels, M. C. Strain, O. Farkas, D. K. Malick, A. D. Rabuck, K. Raghavachari, J. B. Foresman, J. V. Ortiz, Q. Cui, A. G. Baboul, S. Clifford, J. Cioslowski, B. B. Stefanov, G. Liu, A. Liashenko, P. Piskorz, I. Komaromi, R. L. Martin, D. J. Fox, T. Keith, M. A. Al-Laham, C. Y. Peng, A. Nanayakkara, M. Challacombe, P. M. W. Gill, B. Johnson, W. Chen, M. W. Wong, C. Gonzalez, J. A. Pople, *Gaussian 03, Revision D.01*, Gaussian, Inc., Wallingford CT, **2004**.
[50] H. B. Schlegel, *J. Comput. Chem.* **1982**, *3*, 214.

Received: July 31, 2008
Published Online: October 31, 2008

DOI: 10.1002/ejic.200800931

Facile Synthesis of *Bastnaesite*-Type $LaF[CO_3]$ and Its Thermal Decomposition to LaOF for Bulk and Eu^{3+}-Doped Samples

Oliver Janka[a] and Thomas Schleid*[a]

Keywords: Lanthanides / Fluorides / Oxo salts / Luminescence

Rare-earth metal(III) oxide fluorides with the composition MOF (M = La–Lu) seem to offer promising host lattices for luminescence applications by doping these materials with trivalent lanthanoid cations. Unfortunately, there was no simple and practicable way to synthesize the compounds in phase-pure quality with classical solid-state chemistry reactions. However, by using the rare-earth metal(III) fluoride oxocarbonates, $MF[CO_3]$, as solution-born precursor materials that crystallize with a *bastnaesite*-type structure, easy access is now possible by mild thermal decomposition. Synthetic details, investigations on the phase purity and the presence of the oxocarbonate anion $[CO_3]^{2-}$ proved by IR measurements as well as from X-ray powder diffraction data are given in this paper for the example of bulk $LaF[CO_3]$ and Eu^{3+}-doped samples. The latter ($LaF[CO_3]:Eu^{3+}$) shows a bright orange-red luminescence that is stronger than that of the product of its thermal decomposition: trimorphic $LaOF:Eu^{3+}$.

Introduction

Several ways to synthesize rare-earth metal(III) oxide fluorides with the composition MOF (M = Sc, Y, La; Ce–Lu) can be found in the literature.[1] Apart from pyrolysis of trifluorides in the flow of water or pyrolysis of sesquioxides in the flow of hydrogen fluoride, direct solid-state synthesis with the use of sesquioxides and trifluorides in equimolar ratios as reactants is most frequently quoted. Even thermal decomposition of *bastnaesite*-like rare-earth metal(III) fluoride oxocarbonates was introduced as a proper way to obtain MOF-type oxide fluorides.[1] Mann and Bevan were the first to refine the crystal structure of stoichiometric yttrium oxide fluoride (YOF)[2] synthesized from mixtures of Y_2O_3 and YF_3 by using X-ray powder diffraction data. Shortly afterwards, they published other yttrium oxide fluorides with various compositions, such as $Y_5O_4F_7$ and $Y_7O_6F_9$.[3] They not only mentioned the sharply defined stoichiometric molar ratios Y:O:F, but also stated that different so-called Vernier phases ($Y_{n+1}O_nF_{n+3}$) occur in the Y_2O_3–YF_3 system.[4] All these solid-state synthesis methods have the common problem that they seldom form phase-pure samples of 1:1:1-type rare-earth metal(III) oxide fluorides (MOF). The most cited way to synthesize *bastnaesite*-type precursors dates from 1959, where Jansen, Magin and Levin[5] dispersed $Ce_2O[CO_3]_2{\cdot}4H_2O$ in water under a CO_2 atmosphere and added some hydrofluoric acid. Fluoro-oxocarbonato complexes were also studied by Fridman and Gorokhov,[6] and they outlined the synthesis of $YF[CO_3]$ by precipitation from aqueous $Y(NO_3)_3$ solutions upon adding oxocarbonate and fluoride sources in addition to various alkali-metal derivatives. Later, other thermal investigations such as differential heating and thermogravimetric curves were published for various rare-earth metal(III) fluoride oxocarbonates.[7] Detailed information about this preparation method was published by Pleskova.[8] A comprehensive article on most of the different derivatives of rare-earth metal(III) fluorides by Batsanova[9] appeared in the same year. More recently, a review by Grice, Maisonneuve and Leblanc[10] was published, where not only an extensive compilation of different natural and synthetic fluoride oxocarbonates was given, but also magnetic and optical properties, mostly of alkali- or alkaline-earth metal derivatives. Although a lot of work on this topic was done in a 50-year period, no information about pure or doped *bastnaesite*-type $LaF[CO_3]$ and its thermal decay products (e.g., LaOF) has been described. The synthesis, as well as the thermal decomposition of $LaF[CO_3]$ proven by thermal analysis, X-ray powder diffraction and IR spectroscopy for bulk and Eu^{3+}-doped samples, is described in this work.

Results and Discussion

Structural Description

X-ray powder diffraction indicated that the microcrystalline precipitation obtained by adding F^- and HCO_3^- anions to La^{3+} cations in aqueous solution (see Experimental Section for details) is pure $LaF[CO_3]$, as compared to literature crystal structure data.[10] Thus, $LaF[CO_3]$ crystallizes with

[a] Institut für Anorganische Chemie, Universität Stuttgart, Pfaffenwaldring 55, 70569 Stuttgart, Germany
Fax: +49-711-685-64241
E-mail: schleid@iac.uni-stuttgart.de

the *bastnaesite*-type structure in the hexagonal space group $P\bar{6}2c$ (no. 190) with a = 709.4(4) pm and c = 485.9(3) pm (c/a = 0.685, Z = 6). The La^{3+} cations form hexagonal layers with both of the two crystallographic different fluoride anions within the *ab* plane (Figure 1). Both fluoride anions are threefold coordinated by La^{3+} cations, but whereas $(F1)^{-}$ resides in the same plane as the triangle, $(F2)^{-}$ is coordinated in a slightly nonplanar fashion, shifted away by 32 pm from the equilateral $(La^{3+})_3$ plane (Figure 2). A view of the complete crystal structure (Figure 3) indicates that two topologically different layers of oxocarbonate anions $[CO_3]^{2-}$ appear separating the hexagonal $^{2}_{\infty}\{[LaF_{3/3}]^{2+}\}$ monolayers, which can thus be written as $^{2}_{\infty}\{[La(F1)_{1/2}(F2)_{1/2}]^{2+}\}$. Each of the La^{3+} cations is coordinated by three fluoride and eight oxide anions with CN = 9 + 2. Typical distances in this structure are found at $d(La^{3+}–F^{-})$ = 241–243 pm and $d(La^{3+}–O^{2-})$ = 254–258 pm plus $2 \times d$(La–O2′) = 309 pm (Figure 4). Three forms of LaOF (Figure 5) were described earlier in the literature by Klemm and Klein, who recognized only the cubic form of LaOF.[11] Ten years later, Zachariasen published the data for the tetragonal and trigonal modification.[12] The tetragonal β-phase appears in space group $P4/nmm$ (no. 129) with a = 409.1(1) pm and c = 583.6(2) pm [c/a = 1.427, Z = 2; $d(La^{3+}–O^{2-})$ = 241.5 pm, $d(La^{3+}–F^{-})$ = 261.8 pm, 4 × each]. The trigonal γ-form of LaOF crystallizes in the space group $R\bar{3}m$ (no. 166) with Z = 6 with the unit-cell dimensions a = 405.1(1) pm and c = 2003.8(7) pm [c/a = 4.946; $d(La^{3+}–O^{2-})$ = 240–242 pm, $d(La^{3+}–F^{-})$ = 256–258 pm], whereas the cubic high-temperature α-modification is found with space group $Fm\bar{3}m$ (no. 225) and a = 575.6(3) pm [Z = 4; $d(La^{3+}–O^{2-}/F^{-})$ =

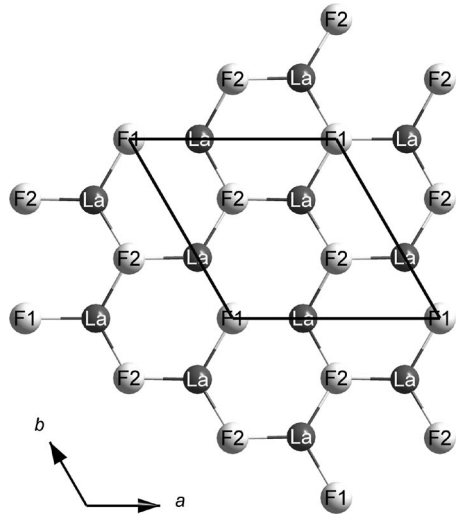

Figure 1. Hexagonal $^{2}_{\infty}\{[La(F1)_{1/2}(F2)_{1/2}]^{2+}\}$ layer parallel to the (001) plane in *bastnaesite*-type $LaF[CO_3]$.

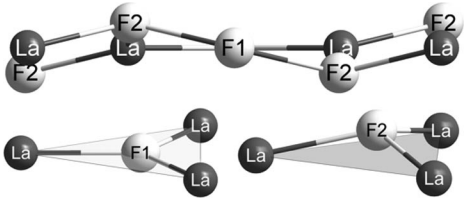

Figure 2. Coordination of the two different fluoride anions (F1 and F2, at bottom) in *bastnaesite*-type $LaF[CO_3]$ within the $^{2}_{\infty}\{[La(F1)_{1/2}(F2)_{1/2}]^{2+}\}$ layer (on top).

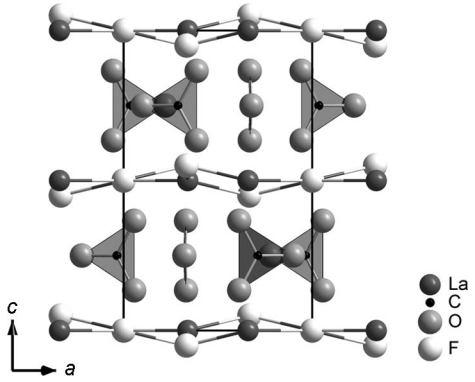

Figure 3. Crystal structure of *bastnaesite*-type $LaF[CO_3]$ presented as (110) section.

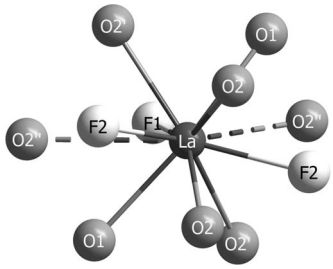

Figure 4. Polyhedron of coordination about the La^{3+} cation in *bastnaesite*-type $LaF[CO_3]$.

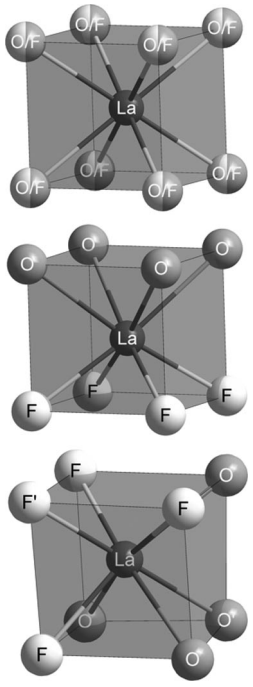

Figure 5. Coordination polyhedra about the La^{3+} cations in the three different structure types of LaOF: cubic phase (top), tetragonal phase (middle) and trigonal phase (bottom).

249.2 pm, 8 × each]. Both the tetragonal and the trigonal modification have a group–subgroup relationship with the cubic high-temperature fluorite-type modification. The relationship between the cubic and the tetragonal phase is shown in Figure 6. The first subgroup of the cubic α-phase ($Fm\bar{3}m$) is $I4/mmm$, which represents a "translationengleiche" subgroup of index 3. To obtain the subgroup of β-LaOF ($P4/nmm$) a "klassengleicher Übergang" of index 2 has to occur. In case of phase transition from the cubic to the trigonal phase, again a two-step descent takes place (Figure 7). In the first step, a "translationengleicher Übergang" again takes place, but this time with index 4 to give the direct subgroup $R\bar{3}m$ and afterwards a "klassengleicher Übergang" of index 2 to a unit cell with a doubled c axis occurs. In both Figures 6 and 7, the structures are shown in a layered assembly to clarify the arrangement of the anions (O^{2-} and F^-) situated in the tetrahedral vacancies of the cubic closest-packed La^{3+} cations in the ordered phases (β and γ). In the tetragonal β-phase the different anions alternate as square grids within the tetrahedral interlayer region, whereas in the trigonal γ-phase ordered sheets of the anions (O^{2-} and F^-) alternate as double layers between the La^{3+} cations in their *ccp* slabs. Both ordered modifications become identical when the differentiation of both kinds of anions is annihilated and the cubic CaF_2-type arrangement (CN = 8) of the high-temperature α-form occurs.

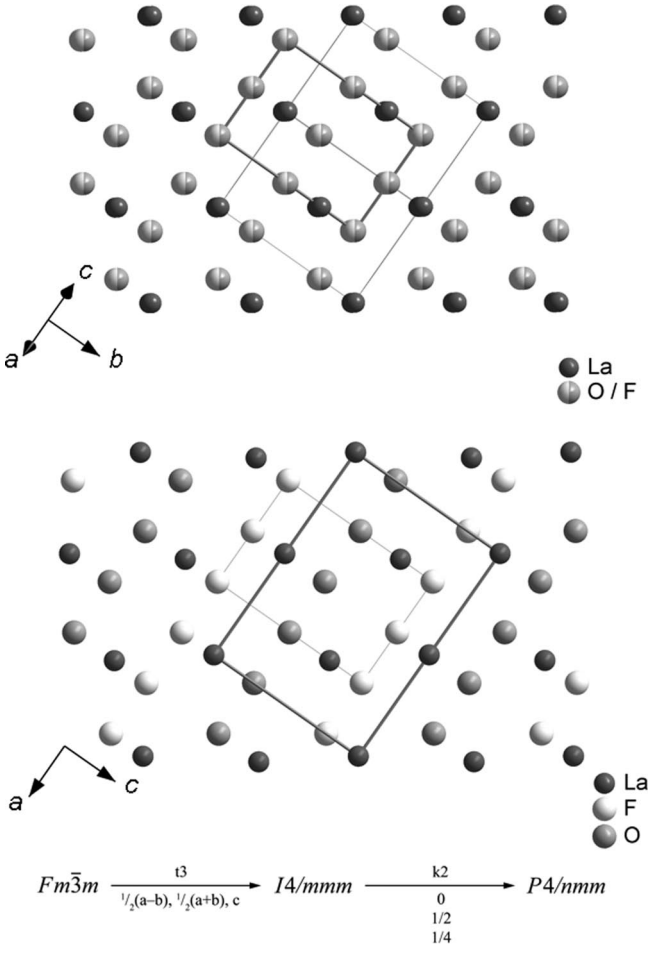

Figure 6. Group–subgroup relationship between the cubic α-phase of LaOF and the tetragonal γ-phase.

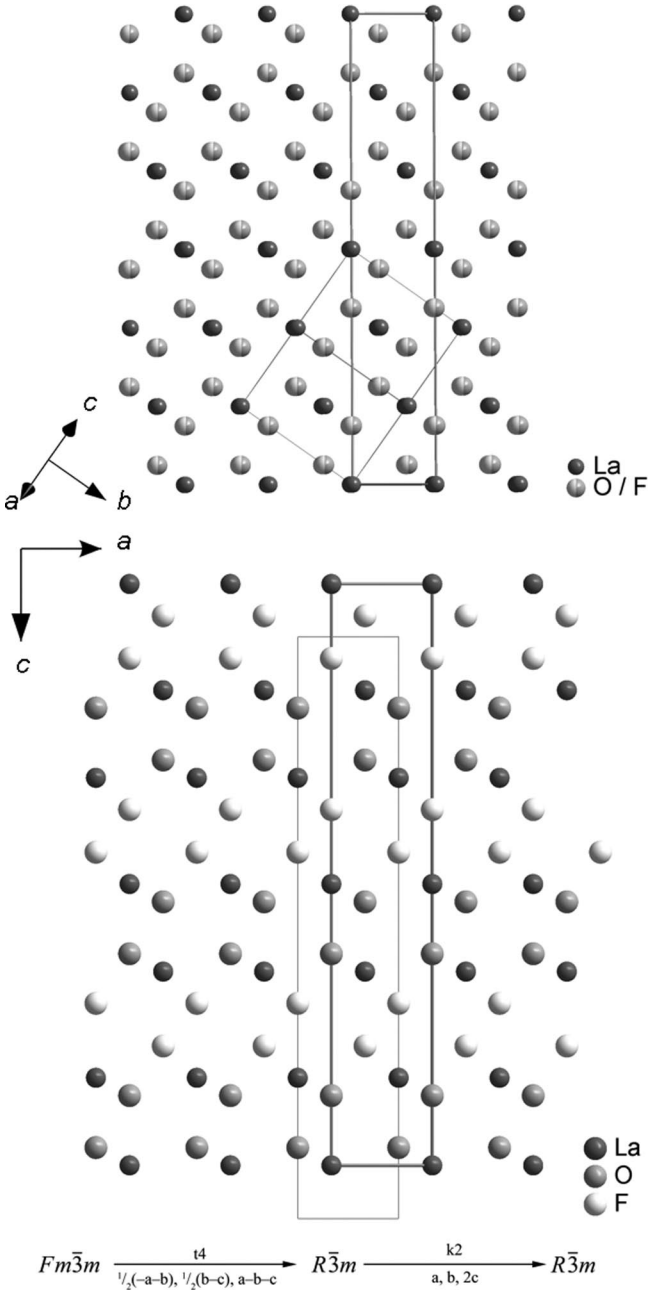

Figure 7. Group–subgroup relationship between the cubic α-phase of LaOF and the trigonal β-phase.

Thermal Stability Analysis

DTA and TG measurements with simultaneous mass spectroscopy (Figure 8) were done with a NETZSCH STA 409C machine by using finely powdered samples in order to prove the disposal of CO_2 from the LaF[CO_3] samples. Three steps are distinguishable in the TG curve. The first

mass loss occurs around 100 to 200 °C, which seems to be the loss of occlusion water according to the corresponding MS data. At temperatures of ca. 460 °C, the greatest loss of mass occurs in one step. Between 500 and 550 °C, a small mass loss of about 1% takes place, which we are unable to explain. The total mass loss of CO_2 is 16–18 wt.-%, which closely corresponds to the decomposition of $LaF[CO_3]$ to LaOF according to the equation $LaF[CO_3] \rightarrow LaOF + CO_2$ with a theoretical weight loss of 20.2%. Besides the decomposition of the samples from TG analyses, other samples were heated within 6 h in a muffle furnace to 550 °C, annealing for 24 h and cooling down afterwards within another 6 h. The third method used was a short thermal treatment of $LaF[CO_3]$ samples with a Bunsen burner at temperatures higher than 1300 °C under an argon atmosphere followed by rapid quenching down to ambient temperature.

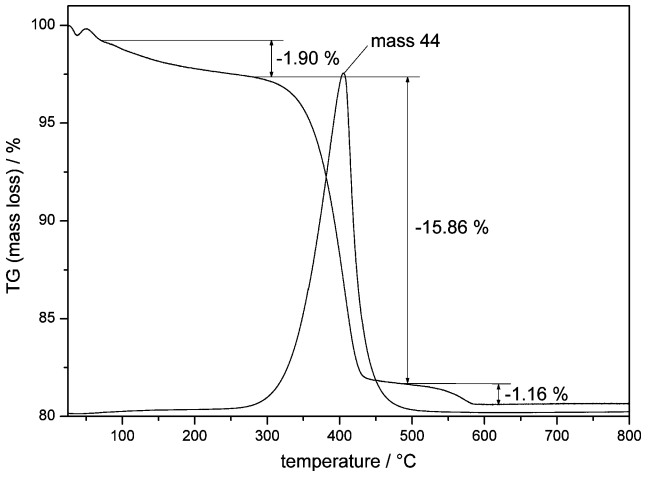

Figure 8. TG–MS measurements of the conversion of $LaF[CO_3]$ into LaOF showing the mass loss at 44 g mol^{-1}, which corresponds to the disposal of CO_2.

part of the tetragonal phase has to be fewer than 5%. Nevertheless, Rietveld refinements need to be performed in the future, which should give a quantitative indication of the fraction of the tetragonal phase impurity within the cubic samples. The colour of the luminescence of these samples differs drastically, however, as the cubic sample shows an orange emission upon UV excitation, whereas the tetragonal one exhibits red emission under the same conditions. Again, additional work will follow in collecting excitation and emission spectroscopic information caused by the effects of the different host lattices on the luminescence properties.[13] Samples of the precursor $LaF[CO_3]$ were also tested by X-ray powder diffraction (Figure 12) and these

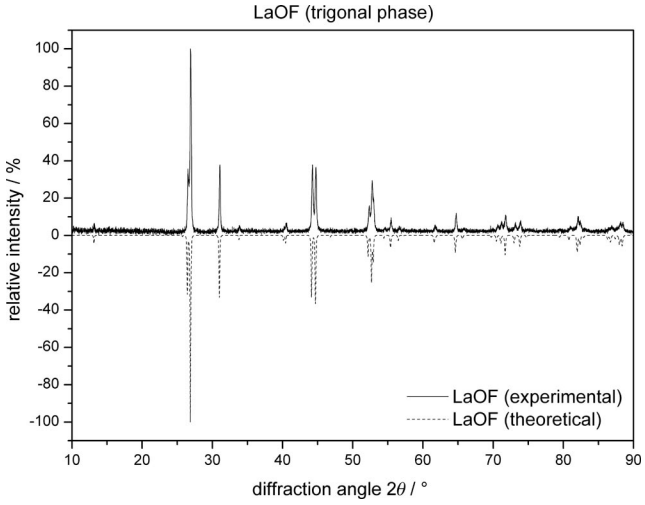

Figure 9. X-ray powder diffraction pattern of a LaOF sample in the trigonal γ-modification as compared to the theoretically calculated one (ICSD 76427).

Characterization of the Compounds

All samples were analyzed by X-ray powder diffraction with a STOE STADI P diffractometer. All three types of lanthanum oxide fluorides as decomposition products were characterized this way and in all three cases different powder patterns were obtained. By comparing each of these patterns with the data published in the literature, it becomes obvious that owing to the different methods of thermal treatment either one of the three different possible phases of LaOF can be obtained. Samples annealed in a muffle furnace at 550 °C form phase-pure LaOF crystallizing with the trigonal γ-phase (Figure 9), whereas the samples treated under DTA–TG conditions yield the tetragonal β-phase of LaOF (Figure 10). The cubic α-phase can be obtained under the most rigorous conditions, that is, by heating the samples with a Bunsen burner up to 1300 °C (Figure 11). In the case of the cubic α-phase, weak peaks around the regions of 38 and 55–60 ° indicate that there might be a small amount of the tetragonal β-phase present. Due to the marginal intensity of the peaks it can be assumed that the

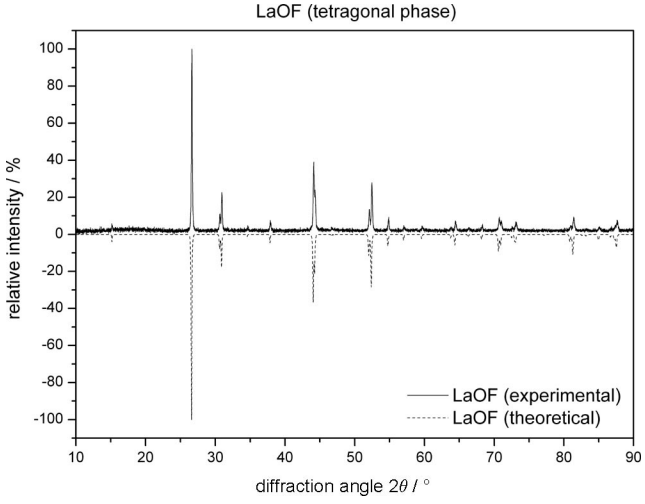

Figure 10. X-ray powder diffraction pattern of a LaOF sample in the tetragonal β-modification as compared to the theoretically calculated one (ICSD 30622).

samples were again phase pure. Additionally, solid-state IR spectroscopy was carried out (Figure 13) to ensure the presence of oxocarbonate anions. Four characteristic bands were found in the spectra, and could be identified as vibrations of the anionic $[CO_3]^{2-}$ unit in the *bastnaesite*-type structure. Juxtaposing the doped compounds of $LaF[CO_3]:Eu^{3+}$ and $LaOF:Eu^{3+}$ (β-phase), one can easily recognize that there is a significant difference in the luminescent behaviour. The oxocarbonate unit seems to have quenching effects on the luminescence properties, because the intensity of the red emission of the oxide fluoride appears to be drastically higher than that one of the fluoride oxocarbonate (Figure 14).

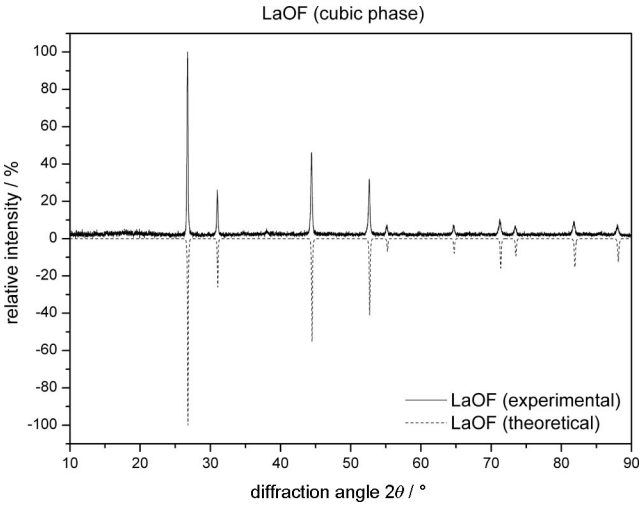

Figure 11. X-ray powder diffraction pattern of a LaOF sample in the cubic α-modification as compared to the theoretically calculated one (ICSD 38238).

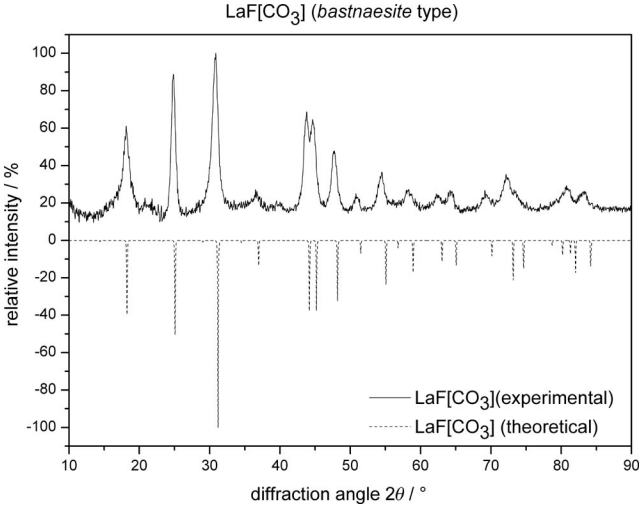

Figure 12. X-ray powder diffraction pattern of *bastnaesite*-type $LaF[CO_3]$ as compared to the theoretically calculated one (ICSD 26678).

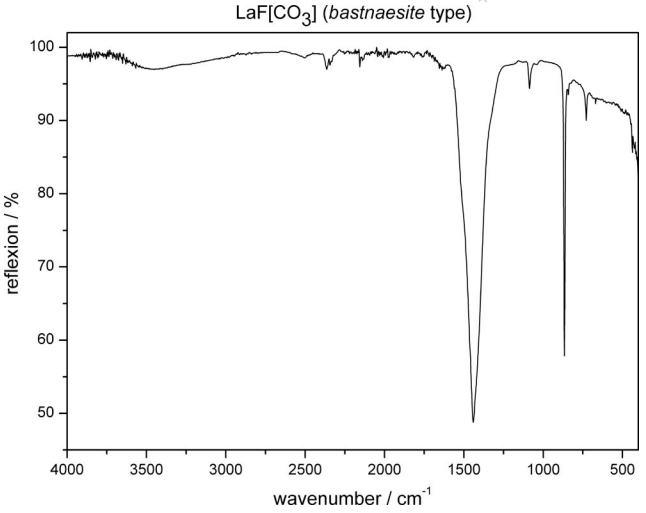

Figure 13. Solid-state infrared spectrum of $LaF[CO_3]$ showing the typical vibration and deformation bands of the $[CO_3]^{2-}$ unit.

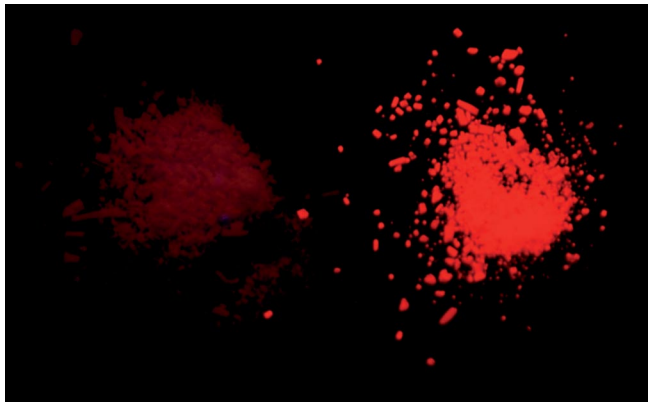

Figure 14. Samples of *bastnaesite*-type $LaF[CO_3]:Eu^{3+}$ (left) and trigonal β-type $LaOF:Eu^{3+}$ (right) showing weak (left) and strong red luminescence (right) upon irradiation with a UV lamp (excitation wavelength: λ = 254 nm).

Conclusions

Easy access to phase-pure bulk and Eu^{3+}-doped samples of LaOF is possible through a well-known precursor route of preparation by using precipitated samples of *bastnaesite*-type $LaF[CO_3]$ and thermally decomposing them subsequently to the single-phase LaOF material. Additionally, doping of these samples with Eu^{3+} already takes place in the very first step, where the lanthanum fluoride oxocarbonate precipitates. Small amounts of europium(III) nitrate in aqueous solution yield homogeneously doped samples of $LaF[CO_3]:Eu^{3+}$, which form stable $LaOF:Eu^{3+}$ after mild thermal decomposition (Figure 14). After the first few examinations of these samples by X-ray powder diffraction, IR spectroscopy, thermal DTA and TG analyses coupled with mass spectrometry more work has to be done in order to get better information about the luminescence properties

of the actual LaOF:Eu^{3+} modification. Absorption and emission spectroscopy may give more information about the luminescence efficiency of these materials. Another interesting question might be the dependence of the emission colour on the framework. From a structural point of view, it would be also interesting to establish a phase relationships between the three forms of LaOF, as its room-temperature molar volumes of 28.71(4) $cm^3 mol^{-1}$ for the cubic α-phase, 29.41(4) $cm^3 mol^{-1}$ for the tetragonal β-phase and 28.58(4) $cm^3 mol^{-1}$ for the trigonal γ-phase do not appear to be very indicative for a particular thermodynamic stability within a certain temperature range. Nevertheless, lanthanoid-doped samples in all of the three possible structures (trigonal, tetragonal and cubic) have to be prepared and examined further. Besides doping with Eu^{3+} cations other lanthanoid(III) cations and even co-doping should be tested in order to obtain materials with different and optimized properties. Ce^{3+}-doped samples, for example, could be possible scintillator materials, whereas Tb^{3+}-doped LaOF is considered to give an intense green luminescence.[13]

Experimental Section

Materials and Methods: All starting materials were purchased from E. Merck (Darmstadt, Germany), $La(NO_3)_3 \cdot 6H_2O$ with a purity of 99%, $NaHCO_3$ with purest quality and NaF with p.a. quality. X-ray powder diffraction patterns were recorded with a STOE STADI P powder diffractometer (Darmstadt, Germany).

Synthesis: To a continuously stirred solution of $La(NO_3)_3 \cdot 6H_2O$ (433 mg, 1 mmol) dissolved in H_2O (25 mL) was slowly added a solution of NaF (55 mg, 1.3 mmol) and $NaHCO_3$ (109 mg, 1.3 mmol) in water (50 mL). After stirring for 30 min, the mixture was left to stand for 2 h and then centrifuged. The residue was washed with distilled H_2O (3×) by using an ultrasonic bath to disperse the precipitate, followed by centrifugation. The aqueous precipitate was dried 12 h at 120 °C in an oven to obtain microcrystalline $LaF[CO_3]$. In order to prepare LaOF, $LaF[CO_3]$ was tempered for 12 h at 550 °C in MgO crucibles. Eu^{3+}-doped samples were prepared the same way by adding small amounts of $Eu(NO_3)_3 \cdot 6H_2O$ (65 mg, 0.05 mmol) to the solution of $La(NO_3)_3 \cdot 6H_2O$.

X-ray Crystallography: Only microcrystalline powders of $LaF[CO_3]$ and LaOF could be obtained and therefore used for X-ray powder diffraction with a STOE STADI P diffractometer (vide supra) by applying Johansson-monochromatized Cu-K_α radiation (λ = 154.04 pm).

IR Spectroscopy: The infrared spectra of both types of compounds were taken with a Nicolet 6700 FTIR spectrometer (Thermo Scientific; Karlsruhe, Germany), equipped with an ATR unit by using a diamond crystal, measuring the reflection of the powder samples.

Thermal Analysis (DTA, TG–MS): Differential thermoanalyses and thermogravimetry studies (DTA–TG) were performed with a STA-449C/CD machine from NETZSCH (Selb, Germany) followed by simultaneous mass spectrometry (MS) (vide infra).

Luminescence: Optical luminescence investigations of the Eu^{3+}-doped samples were performed with a commercial Desaga UV lamp (Sarstedt-Group; Nümbrecht, Germany) with λ = 254 and 355 nm as possible excitation wavelengths.

Acknowledgments

We thank CTA Christoph Schneck for thermoanalytic analysis, Dipl.-Chem. Markus Leboschka for the IR spectroscopic measurements and Sumati Panicker-Otto for language polishing. Furthermore, we gratefully acknowledge the Deutsche Forschungsgemeinschaft (Bonn) within the Priority Program SFB 1166 "Lanthanoid-spezifische Funktionalitäten in Molekül und Material" and the State of Baden-Württemberg (Stuttgart) for their financial support.

[1] R. J. Meyer (Ed.), GMELIN – *Handbuch der Anorganischen Chemie: Sc, Y, La–Lu (Selten-Erd-Elemente)*, Syst.-Nr. 39, C3: Fluoride, Oxidfluoride und zugehörige Alkalidoppelverbindungen, Springer, Berlin, **1976**, vol. 8, pp. 232–265.
[2] A. W. Mann, D. J. M. Bevan, *Acta Crystallogr., Sect. B* **1970**, *26*, 2129–2131
[3] A. W. Mann, D. J. M. Bevan, *Acta Crystallogr., Sect. B* **1975**, *31*, 1406–1411.
[4] D. J. M. Bevan, J. Mohyla, B. F. Hoskins, R. J. Steen, *Eur. J. Solid State Inorg. Chem.* **1990**, *27*, 451–465.
[5] G. J. Jansen, G. B. Magin, B. Levin, *Am. Mineral.* **1959**, *44*, 180.
[6] Y. D. Fridman, S. D. Gorokhov, *Russ. J. Inorg. Chem.* **1967**, *12*, 945–948.
[7] Y. D. Fridman, S. D. Gorokhov, *Russ. J. Inorg. Chem.* **1969**, *14*, 1440–1442.
[8] I. A. Pleskova, I. V. Shakhno, V. E. Plyushchev, M. N. Sotnikova, *Inorg. Mater. [USSR]* **1971**, *7*, 694–698.
[9] L. R. Batsanova, *Russ. Chem. Rev.* **1971**, *40*, 465–484.
[10] J. D. Grice, V. Maisonneuve, M. Leblanc, *Chem. Rev.* **2007**, *107*, 114–132.
[11] W. Klemm, H. A. Klein, *Z. Anorg. Allg. Chem.* **1941**, *248*, 167–171.
[12] W. H. Zachariasen, *Acta Crystallogr.* **1951**, *4*, 231–236.
[13] O. Janka, A. Krumpel, E. van der Kolk, P. Dorenbos, Th. Schleid, *J. Alloys Compd.* **2009**, manuscript in preparation.

Received: September 18, 2008
Published Online: December 9, 2008

DOI: 10.1002/ejic.200800646

Synthesis, Crystal Structures, and Thermal Properties of New [ZnX_2(2,5-dimethylpyrazine)] (X = Cl, Br, I) Coordination Compounds

Mario Wriedt,[a] Inke Jeß,[a] and Christian Näther*[a]

Keywords: Coordination compounds / N ligands / Synthesis design / Structure elucidation / Thermal reactivity

Eight new halidozinc(II) coordination compounds with 2,5-dimethylpyrazine as a ligand were prepared. The reaction of ZnX_2 (X = Cl, Br, I) and 2,5-dimethylpyrazine in methanol results in the formation of catena-(μ_2-2,5-dimethylpyrazine-*N*,*N*′)dichloridozinc(II) (**1**), catena-(μ_2-2,5-dimethylpyrazine-*N*,*N*′)dibromidozinc(II) (**3I** and **3II**), catena-(μ_2-2,5-dimethylpyrazine-*N*,*N*′)diiodidozinc(II) (**6**), and diiodidobis(2,5-dimethylpyrazine-*N*)zinc(II) (**7**). In addition, in a solvent-free reaction of ZnX_2 (X = Cl, Br) and 2,5-dimethylpyrazine, the ligand-rich compounds bis(dichlorido)bis(2,5-dimethylpyrazine-*N*)(μ_2-2,5-dimethylpyrazine-*N*,*N*′)dizinc(II) (**2**), bis(dibromido)bis(2,5-dimethylpyrazine-*N*)(μ_2-2,5-dimethylpyrazine-*N*,*N*′)dizinc(II) (**4**), and dibromidobis(2,5-dimethylpyrazine-*N*)zinc(II) 2,5-dimethylpyrazine solvate (**5**) were obtained. In the crystal structures of all compounds the zinc atoms are each coordinated by two halide atoms and two 2,5-dimethylpyrazine ligands within a distorted tetrahedron. The zinc atoms in the ligand-deficient 1:1 (1:1 = molar ratio of metal salt to ligand) compounds **1** and **6** and in the two polymorphic modifications **3I** and **3II** are linked by the N-donor ligands into chains. In contrast, the crystal structure of the 2:3 compounds **2** and **4** are built up of oligomeric discrete [(ZnX_2)$_2$(2,3-dimethylpyrazine)$_3$] units in which each ZnX_2 (X = Cl, Br) unit is coordinated by two halide atoms and one bridging and one terminal 2,5-dimethylpyrazine ligand. The structures of the ligand-rich 1:2 diiodido compound **7** and the 1:3 dibromido compound **5** consist of discrete monomeric tetrahedral building blocks. In the thermal decomposition reactions of the ligand-rich compounds **2**, **5**, and **7**, different mass steps are observed. In the first step, the ligand-deficient 1:1 compounds **1** and **6** are formed in quantitative yields from **2** and **7**, respectively, and **5** yields a mixture of **3I** and **3II**, and the second mass step leads to the formation of new ligand-deficient 2:1 compounds. On further heating of the compounds, the remaining ligands are discharged. This results in the formation of the zinc(II) halides, which vaporize on further heating. Solvent-mediated conversion experiments in methanol show that, irrespective of the ratio of zinc(II) halide and ligand, only the 1:1 compounds **1** and **3I** are formed and therefore represent the thermodynamically most stable compounds at room temperature. For ZnI_2 the 1:2 compound **7** is obtained at ratios of zinc(II) iodide to ligand larger than 1:3, whereas at lower ratios the 1:1 compound **6** is always obtained.

Introduction

Recently, the preparation of new coordination polymers and metal–organic frameworks has gained increasing interest.[1] In nearly all cases, these compounds were prepared in solution, which frequently leads to mixtures that have to be separated by hand. Moreover, in some cases, thermodynamically metastable compounds can easily be overlooked. Therefore, an alternative route for the discovery and preparation of new or known pure coordination polymers is essential.

Recently, we showed that thermal decomposition reactions of suitable ligand-rich precursor compounds of copper(I) halides or pseudohalides containing N-donor ligands can be widely used as a convenient preparative tool for the facile synthesis of novel coordination compounds.[2] To check the generality of such reactions for the preparation of new coordination polymers of other metals we started systematic investigations on zinc(II) halide compounds and N-donor ligands.[3,4] In addition to the tetrahedral coordination shown by copper(I) and zinc(II), they can also adopt octahedral geometry and hence a rich and diverse structural chemistry of zinc(II) compounds can be expected. Several of such compounds are known, but there has been no research on their thermal properties.[5–8] In earlier work we investigated compounds with pyrazine as ligands.[4] In the crystal structure of the ligand-rich 1:2 compounds of composition [ZnX_2(pyrazine)$_2$] (X = Cl,[4] Br[6]), the zinc atoms are each coordinated by two halide atoms and four pyrazine ligands within a distorted octahedron. The zinc atoms are connected by the pyrazine ligands into chains, which are further joined by ligands into layers. We found that, on heating, this 1:2 compounds transform quantitatively into

[a] Institut für Anorganische Chemie, Universität zu Kiel, Max-Eyth-Straße 2, 24098 Kiel, Germany
Fax: +49-431-8801520
E-mail: cnaether@ac.uni-kiel.de

Supporting information for this article is available on the WWW under http://www.eurjic.org or from the author.

the ligand-deficient 1:1 compounds. For ZnI_2, no ligand-rich 1:2 compound could be prepared. In the crystal structure of the 1:1 compounds of composition [ZnX_2(pyrazine)] (X = Cl,[6] Br,[5] I[7]), the zinc atoms are each coordinated by two halide atoms and two pyrazine ligands within a distorted tetrahedron, in which the ZnX_2 units are connected by the pyrazine ligands into chains. On further heating, the 1:1 compounds transform into the more ligand-deficient 2:1 compounds, which could not be prepared in solution.

In a continuation of this work, we investigated the reactions of zinc(II) halides with 2,5-dimethylpyrazine aimed at the characterization of new coordination compounds. This ligand was selected to study the influence of the bulky methyl substituents attached to the C atom adjacent to the N-donor atoms, on the structures and thermal reactivity of the products. Moreover, the N-donor atoms in 2,5-dimethylpyrazine should be better donors than those in pyrazine because of the inductive effect of the methyl group, which can also influence the reactivity. Herein, we report on the results of these investigations.

Results and Discussion

Crystal Structures

The 1:1 dichlorido compound **1** crystallizes in the orthorhombic space group *Pnma* with four formula units in the unit cell. The zinc atoms as well as the two crystallographically independent chlorine atoms are located on a mirror plane, whereas the 2,5-dimethylpyrazine ligand is situated on a center of inversion. In the crystal structure, the zinc atoms are each coordinated by two crystallographically independent chlorine atoms and two symmetry-related 2,5-dimethylpyrazine ligands within slightly distorted tetrahedra (Figure 1, top). The Zn–N distances amount to 2.1027(15) Å, and the angles around the zinc atoms range between 97.00(8) and 117.83(4)° (Table 1). The $ZnCl_2$ units are connected by the 2,5-dimethylpyrazine ligands by μ-*N*,*N*′ coordination into chains that elongate in the direction of the crystallographic *b* axis (Figure 1, bottom).

The 2:3 dichlorido compound **2** crystallizes in the triclinic space group $P\bar{1}$ with one formula unit in the unit cell and all atoms in general positions. In the crystal structure, discrete [$(ZnCl_2)_2$(2,5-dimethylpyrazine)$_3$] units are found, in which each of the two zinc atom is coordinated by two chlorine atoms and two nitrogen atoms of one terminal and one bridging 2,5-dimethylpyrazine ligand (Figure 2, top). These units are located on centers of inversion. The zinc atoms are bridged by the 2,5-dimethylpyrazine ligands through μ-*N*,*N* coordination. The Zn–N distances range between 2.085(4) and 2.091(4) Å, and the angles around the zinc atoms vary from 104.56(12) to 108.53(12)° (Table 1). In the crystal structure, the discrete complexes are connected through intermolecular C–H···Cl hydrogen bonds into chains [∠(C2–H2···Cl2) = 169.753(17)°, *d*(H2···Cl2) = 2.8391(4) Å]. The terminal 2,5-dimethylpyrazine rings are stacked in the direction of the crystallographic *a* axis, indicating π–π interactions (Figure 2, bottom).

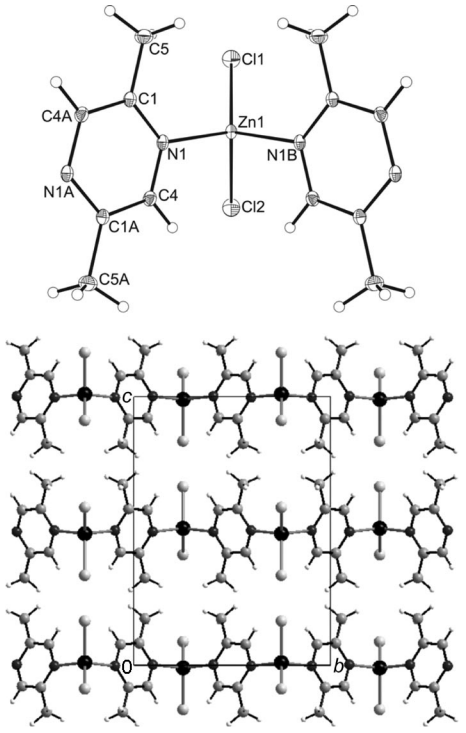

Figure 1. Crystal structure of the 1:1 compound **1** with a view of the coordination sphere of the zinc cations with labeling and displacement ellipsoids drawn at the 50% probability level (top) and a view of the structure in the direction of the crystallographic *a* axis (bottom). Symmetry codes: A = –*x* + 2, –*y* + 1, –*z* + 1; B = *x*, –*y* + 1/2, *z*.

Table 1. Selected bond lengths (in Å) and angles (in °) for compound **1** und **2**.[a]

Compound **1**			
Zn1–N1	2.1027(15)	Zn1–Cl1	2.2129(6)
N1–Zn1–N1B	97.00(8)	Zn1–Cl2	2.2312(6)
N1–Zn1–Cl1	117.83(4)	N1–Zn1–Cl2	103.99(4)
Cl1–Zn1–Cl2	113.80(2)		
Compound **2**			
Zn1–N1	2.085(4)	Zn1–Cl1	2.2148(14)
Zn1–N11	2.091(4)	Zn1–Cl2	2.2358(13)
N1–Zn1–N11	113.05(16)	N1–Zn1–Cl2	104.56(12)
N1–Zn1–Cl1	108.53(12)	N11–Zn1–Cl2	105.64(12)
N11–Zn1–Cl1	105.86(12)	Cl1–Zn1–Cl2	119.41(5)

[a] Symmetry codes: A = –*x* + 2, –*y* + 1, –*z* + 1; B = *x*, –*y* + 1/2, *z* for **1**.

The polymorphic 1:1 dibromido compound **3I** crystallizes in orthorhombic space group *Pnma* with four formula units in the unit cell and is isomorphous to the dichlorido compound **1** (Figure 3). The Zn–N distances amount to 2.110(4) Å, and the angles around the zinc atoms range between 97.5(2) and 118.20(11)° (Table 2).

The second modification of the 1:1 dibromido compound **3II** crystallizes in the monoclinic space group *C*2/*c* with four formula units in the unit cell. In the asymmetric unit of **3II**, the zinc atom is located on a twofold rotation axis, and the two bromine atoms are related by a twofold rotation axis, whereas the 2,5-dimethylpyrazine ligand is sit-

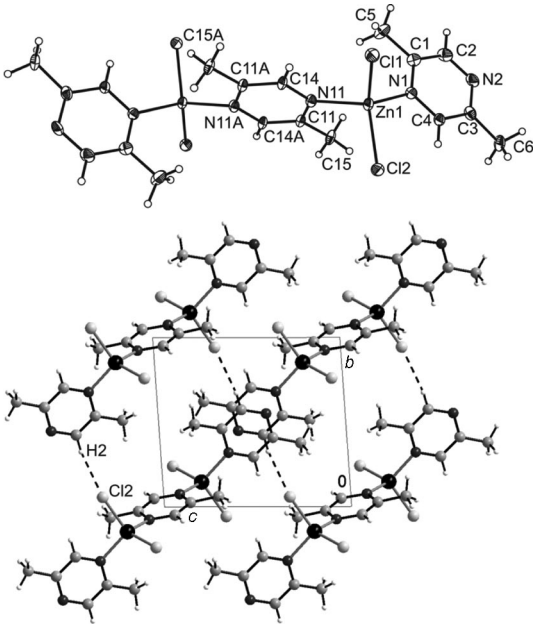

Figure 2. Crystal structure of the 2:3 compound **2** with a view of the coordination sphere of the zinc cations with labeling and displacement ellipsoids drawn at the 50% probability level (top) and a view of the structure in the direction of the crystallographic *a* axis (bottom). Intermolecular C–H···Cl hydrogen bonding is shown as dashed lines. Symmetry code: A = –*x* + 1, –*y* + 2,–*z*.

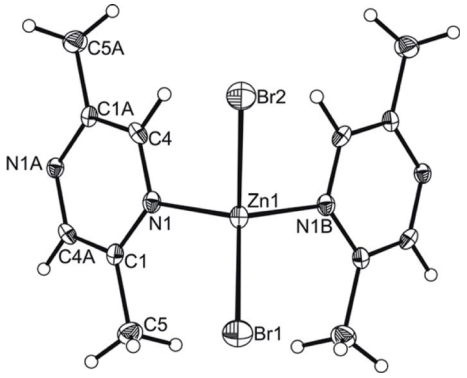

Figure 3. Crystal structure of the 1:1 compound **3I** with a view of the coordination sphere of the zinc cations with labeling and displacement ellipsoids drawn at the 50% probability level. Symmetry codes: A = –*x*, –*y* + 1, –*z* + 1; B = *x*, –*y* + 1/2, *z*.

uated on a center of inversion. In the crystal structure, the zinc atoms are each coordinated by two symmetry-related bromine atoms and two symmetry-related 2,5-dimethlpyrazine ligands within slightly distorted tetrahedra (Figure 4, top). The Zn–N distances amount to 2.121(2) Å, and the angles around the zinc atoms range between 93.57(13) and 119.86(7)° (Table 2). The $ZnCl_2$ units are connected by the 2,5-dimethylpyrazine ligands by μ-*N*,*N*′ coordination into chains that elongate in the direction of the crystallographic *b* axis (Figure 4, bottom). Thus, both modifications **3I** and **3II** are topologically identical.

The 2:3 dibromido compound **4** crystallizes in the triclinic space group $P\bar{1}$ with one formula unit in the unit cell and is isomorphous to the dichlorido compound **2** (Fig-

Table 2. Selected bond lengths (in Å) and angles (in °) for compounds **3I**, **3II**, **4**, and **5**.[a]

Compound **3I**			
Br1–Zn1	2.3510(10)	Zn1–N1	2.110(4)
Br2–Zn1	2.3711(10)	N1–Zn1–Br2	105.01(10)
N1B–Zn1–N1	97.5(2)	Br1–Zn1–Br2	111.05(4)
N1–Zn1–Br1	118.20(11)		
Compound **3II**			
Zn1–N1	2.121(2)	Zn1–Br1	2.3560(5)
N1B–Zn1–N1	93.57(13)	N1–Zn1–Br1B	119.86(7)
N1–Zn1–Br1	105.32(6)	Br1–Zn1–Br1B	112.38(3)
Compound **4**			
Zn1–N1	2.082(5)	Zn1–Br1	2.3534(10)
Zn1–N11	2.088(5)	Zn1–Br2	2.3801(10)
N1–Zn1–N11	113.6(2)	N1–Zn1–Br2	105.42(15)
N1–Zn1–Br1	107.88(15)	N11–Zn1–Br2	103.98(15)
N11–Zn1–Br1	106.79(15)	Br1–Zn1–Br2	119.37(4)
Compound **5**			
Zn1–N2	2.066(3)	Zn1–Br1	2.391(3)
Zn1–Br1′	2.323(4)	N2–Zn1–Br1A	104.26(11)
N2–Zn1–N2A	114.43(15)	Br1–Zn1–Br1A	124.5(4)
N2–Zn1–Br1′	111.9(3)	N2–Zn1–Br1	104.95(19)
N2–Zn1–Br1A′	106.33(18)	Br1′–Zn1–Br1A′	105.6(9)

[a] Symmetry codes: A = –*x*, –*y* + 1, –*z* + 1; B = *x*, –*y* + 1/2, *z* for **3I**; A = –*x* + 1, –*y*, –*z* + 1; B = –*x* + 1, *y*, –*z* + 1/2 for **3II**; A = –*x*, *y*, –*z* + 1/2; B = –*x*, –*y* + 2, –*z* for **5**.

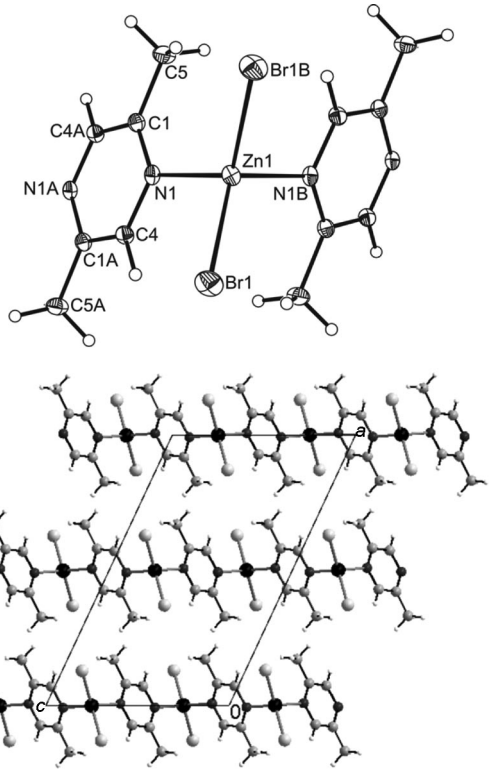

Figure 4. Crystal structure of the 1:1 compound **3II** with a view of the coordination sphere of the zinc cations with labeling and displacement ellipsoids drawn at the 50% probability level (top) and a view of the structure in the direction of the crystallographic *b* axis (bottom). Symmetry codes: A = –*x* + 1, –*y*, –*z* + 1; B = –*x* + 1, *y*, –*z* + 1/2.

ure 5). The Zn–N distances range between 2.082(5) and 2.085(5) Å, and the angles around the zinc atoms range between 106.79(15) and 119.37(4)° (Table 2). As in **2**, the discrete complexes are connected through intermolecular C–H···X (X = Br) hydrogen bonds into chains [∠(C2–H2···Br2) = 172.433(15)°, *d*(H2···Br2) = 2.9427(5) Å], and the terminal 2,5-dimethylpyrazine rings are stacked in the direction of the crystallographic *c* axis (Figure 5).

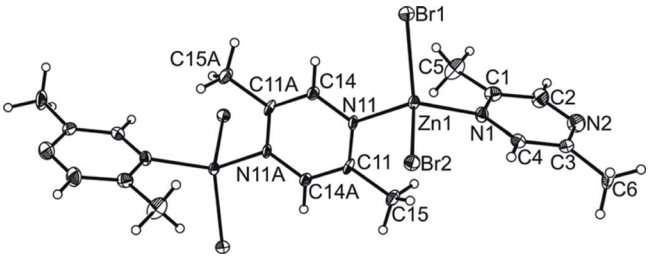

Figure 5. Crystal structure of the 2:3 compound **4** with a view of the coordination sphere of the zinc cations with labeling and displacement ellipsoids drawn at the 50% probability. Symmetry code: A = –*x* + 1, –*y* + 2, –*z*.

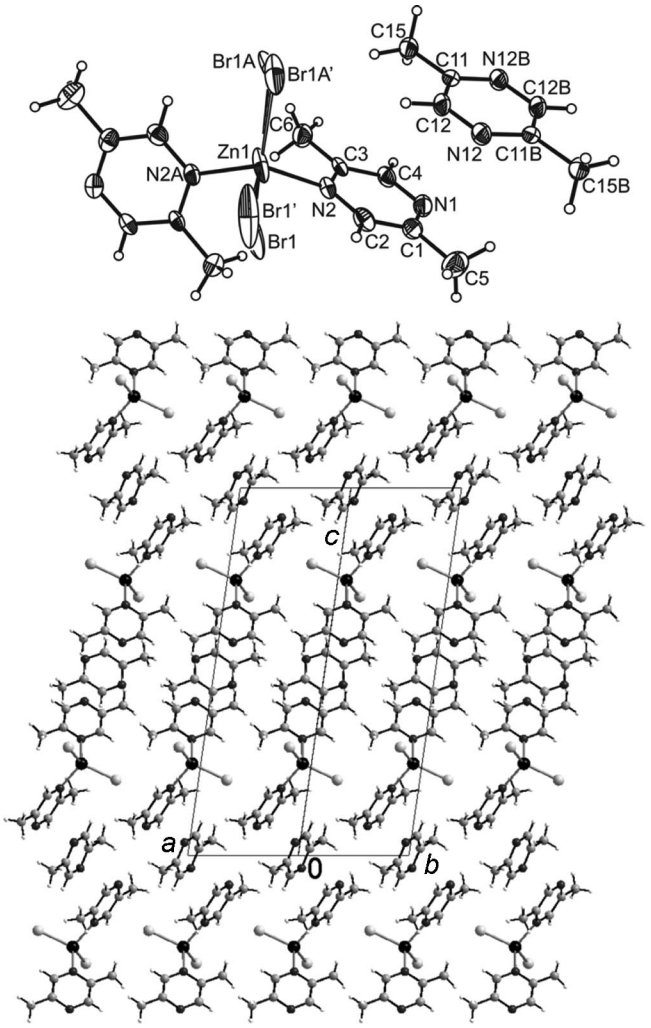

Figure 6. Crystal structure of the 1:3 compound **5** with a view of the coordination sphere of the zinc cations with labeling and displacement ellipsoids drawn at the 50% probability level (top) and a view of the structure along [110] (bottom). Symmetry codes: A = –*x*, *y*, –*z* + 1/2; B = –*x*, –*y* + 2, –*z*.

The 1:3 dibromido compound **5** crystallizes in the monoclinic space group *C*2/*c* with four formula units in the unit cell. The zinc atoms are located on a twofold rotation axis, whereas the two bromine atoms are located on general positions and are related by a twofold rotation axis. The 2,5-dimethylpyrazine ligand is situated on a center of inversion and one further ligand occupies a general position. In the crystal structure, discrete $[(ZnBr_2)(2,5\text{-dimethylpyrazine})_2]\cdot$(2,5-dimethylpyrazine) units are found, in which the zinc atoms are each coordinated by two symmetry-related bromine atoms and two symmetry-related 2,5-dimethlpyrazine ligands within slightly distorted tetrahedra (Figure 6, top, and Table 2). The additional 2,5-dimethylpyrazine ligand is not connected with the zinc atom (Figure 6, bottom).

The 1:2 diiodido compound **6** crystallizes in the monoclinic space group *C*2/*c* with four formula units in the unit cell and is isomorphous to the bromine compound **3II** (Figure 7). The Zn–N distances amount to 2.132(2) Å, and the angles around the zinc atoms range between 93.65(12) and 120.32(7)° (Table 3).

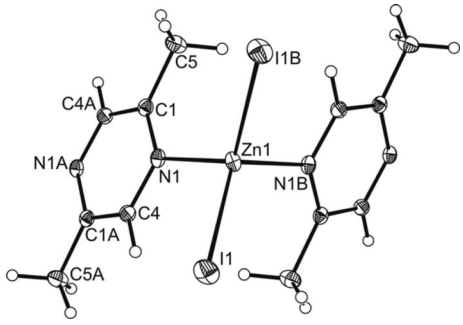

Figure 7. Crystal structure of compound **6** with a view of the coordination sphere of the zinc cations with labeling and displacement ellipsoids drawn at the 50% probability level. Symmetry codes: A = –*x* + 1, –*y*, –*z* + 1; B = –*x* + 1, *y*, –*z* + 1/2.

Table 3. Selected bond lengths (in Å) and angles (in °) for compounds **6** and **7**.[a]

Compound **6**			
Zn1–N1	2.132(2)	Zn1–I1	2.5568(4)
N1B–Zn1–N1	93.65(12)	N1–Zn1–I1B	120.32(7)
N1–Zn1–I1	105.91(6)	I1–Zn1–I1B	110.60(2)
Compound **7**			
Zn1–N1	2.092(3)	Zn1–I1	2.5600(5)
Zn1–N11	2.100(3)	Zn1–I2	2.5744(5)
N1–Zn1–N11	101.81(12)	N1–Zn1–I2	105.85(9)
N1–Zn1–I1	110.42(9)	N11–Zn1–I2	117.59(9)
N11–Zn1–I1	103.69(9)	I1–Zn1–I2	116.517(19)

[a] Symmetry codes for **6**: A = –*x* + 1, –*y*, –*z* + 1; B = –*x* + 1, *y*, –*z* + 1/2.

The ligand-rich 1:2 diiodido compound **7** crystallizes in the monoclinic space group $P2_1/c$ with four formula units in the unit cell and all atoms in general positions. In the crystal structure, discrete complexes are found, in which the

zinc atoms are coordinated by two iodine atoms and two nitrogen atoms of the 2,5-dimethylpyrazine ligands within distorted tetrahedra (Figure 8, top). The Zn–N distances vary from 2.092(3) to 2.100(3) Å, and the angles around the zinc atoms range between 101.81(12) and 116.517(19)° (Table 3). In the crystal structure, the discrete complexes are connected by weak intermolecular C–H···I hydrogen bonds into a two-dimensional network (Figure 8, bottom, and Table 4).

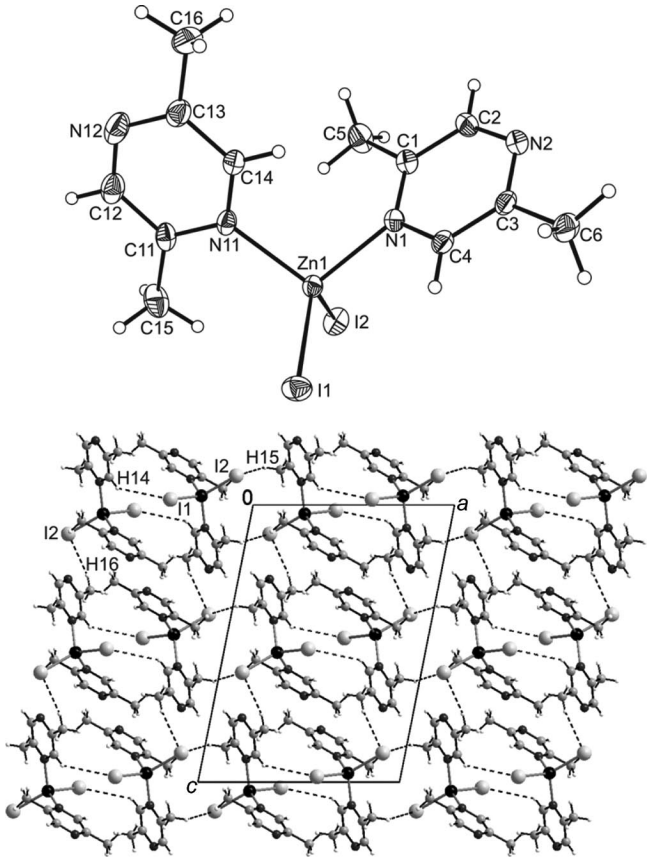

Figure 8. Crystal structure of the 1:2 compound **7** with a view of the coordination sphere of the zinc cations with labeling and displacement ellipsoids drawn at the 50% probability level (top) and a view of the structure in the direction of the crystallographic *b* axis (bottom). Intermolecular C–H···I hydrogen bonding is shown as dashed lines.

Table 4. Distances and angles of the intermolecular hydrogen-bonding interactions of compound **7**.

	Distance (H···I) /Å	Angle (C–H···I) /°
C14–H14···I1	3.3873(2)	139.687(4)
C15–H15···I2	3.8614(3)	116.753(4)
C16–H16···I2	3.5735(2)	153.832(5)

Thermoanalytic Investigations

On heating the ligand-rich 2:3 chlorine compound **2** to 500 °C, two well-resolved mass steps are observed in the thermogravimetric (TG) curve that are accompanied by endothermic events in the differential thermal analysis (DTA) curve (Figure 9, left). The MS trend scan curve reveals that only the N-donor ligand (*m*/*z* = 108) is released during these mass steps. The mass loss of 18.1% in the first step is in perfect agreement with that calculated for the removal of one third (1 mol; 18.1%) of the ligands. The mass loss of 18.7% in the second step is in good agreement with that calculated for the removal of an additional one third (1 mol; 18.1%) of the ligands. On the basis of the observed mass losses, it can be confirmed that in the first step a 1:1 compound and in the second step a ligand-deficient 2:1 compound are formed. Heating the complex further causes the remaining ligands to be released, leading to the formation of $ZnCl_2$, which vaporizes on further heating (Figure 9, left).

For the ligand-rich 1:3 dibromido compound **5**, very similar thermal behavior as for compound **2** is observed. The mass loss of 36.8% in the first step is in rough agreement with that calculated for the removal of two thirds (2 mol; 39.4%) of the ligands. Hence, it can be confirmed that in this step a ligand-deficient 1:1 compound has been formed. For the first TG step, two endothermic events in the DTA curve are observed, which might correspond to the formation of a 2:3 intermediate compound (Figure 9, middle). However, heating-rate-dependent measurements do not show an additional TG step (see the Supporting Information). The experimental mass loss of 10.0% observed in the second TG step is in reasonable agreement with that expected for the removal of one sixth (0.5 mol; 9.8%) of the ligands, which may lead to a new ligand-deficient 2:1 compound of composition [$(ZnBr_2)_2$(2,5-dimethylpyrazine)]. On further heating, the remaining ligands are discharged, and the final product was identified as $ZnBr_2$, which vaporizes on further heating (Figure 9, middle).

The TG curve of the ligand-rich 1:2 compound **7** exhibits three well-resolved mass steps (Figure 9, right). The mass loss of 20.2% in the first step is in perfect agreement with that calculated for the removal of half of the ligands (1 mol; 20.2%), and the second TG step of 13.5% is in exact agreement with that expected for the removal of one third of the ligands (0.67 mol; 13.5%). Therefore, it can be inferred that in the first TG step a 1:1 compound is formed, which decomposes on further heating into a new ligand-deficient 3:1 compound of composition [$(ZnI_2)_3$(2,5-dimethylpyrazine)]. On further heating, the 3:1 compound transforms into ZnI_2.

The DTA/TG/MS measurements indicate that the ligand-rich compounds **2**, **5**, and **7** decompose in the first step into 1:1 compounds and in the second step into new ligand-deficient 2:1 or 3:1 intermediate compounds. To verify the nature of the intermediates formed, additional TG measurements with heating rates of 4 K min^{-1} were performed and stopped after the first and second TG step, respectively. Afterward, the residues were investigated by X-ray powder diffraction (XRPD) and elemental analysis.

The powder pattern of the residue obtained after the first TG step of the ligand-rich 2:3 chlorine compound **2** is in perfect agreement with that calculated for the 1:1 compound **1** from single-crystal data (compare A with B in Fig-

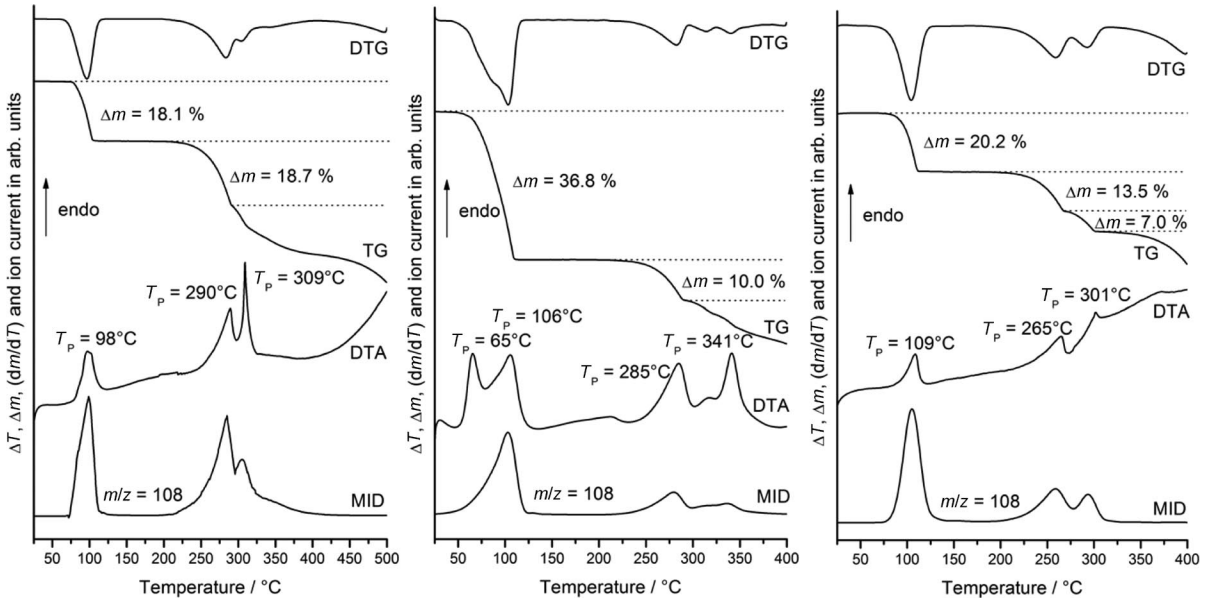

Figure 9. DTA, TG, DTG, and MS trend scan curves for the ligand-rich compounds **2** (left), **5** (middle), and **7** (right). Heating rate = 4 K min^{-1}; m/z = 108 (2,5-dimethylpyrazine); given are the mass changes (%) and the peak temperatures T_P (in °C).

ure 10). Hence, this phase is produced in a very pure form in the thermal decomposition reaction. The powder pattern of the intermediate formed after the second TG step is different from that of the pristine material (compare C with A in Figure 10). A detailed analysis shows that there are still some reflections of the 1:1 compound **1** and $ZnCl_2$. All our efforts to obtain this intermediate compound in phase-pure form by stopping the TG experiment at different temperatures after the second TG step were not fruitful. Consequently elemental analysis of the intermediate is only in reasonable agreement with that calculated for a ligand-deficient 2:1 compound (see the Experimental Section).

Comparison of the powder X-ray diffraction pattern of the residue obtained after the first TG step in the thermal decomposition reaction of the ligand-rich 1:3 dibromido compound **5** with that calculated for 1:1 compounds **3I** and **3II** from single-crystal data reveals that these phases were formed as a mixture (compare A with B and C in Figure 11). The powder X-ray diffraction pattern of the residue after the second TG step indicates the formation of a new ligand-deficient 2:1 compound. However, there are still some additional reflections of the 1:1 compounds and $ZnBr_2$ (compare D with B and C in Figure 11), and therefore the elemental analysis is only in reasonable agreement

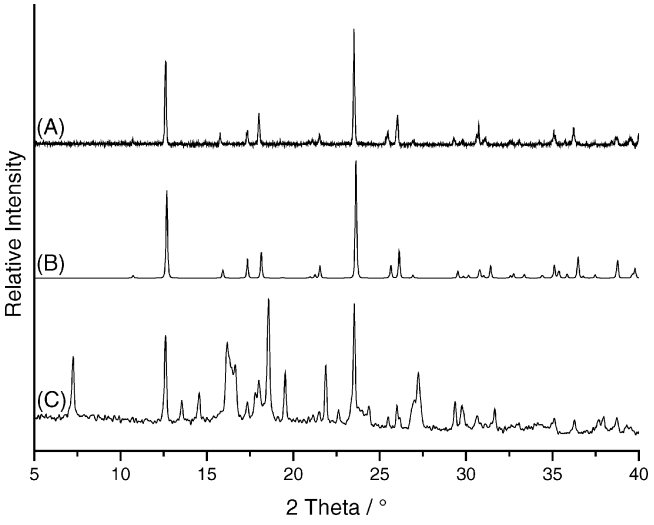

Figure 10. Experimental XRPD patterns of the residue obtained after the first (A) and second (C) TG step in the thermal decomposition reaction of compound **2** and calculated XRPD pattern for the 1:1 compound **1** (B).

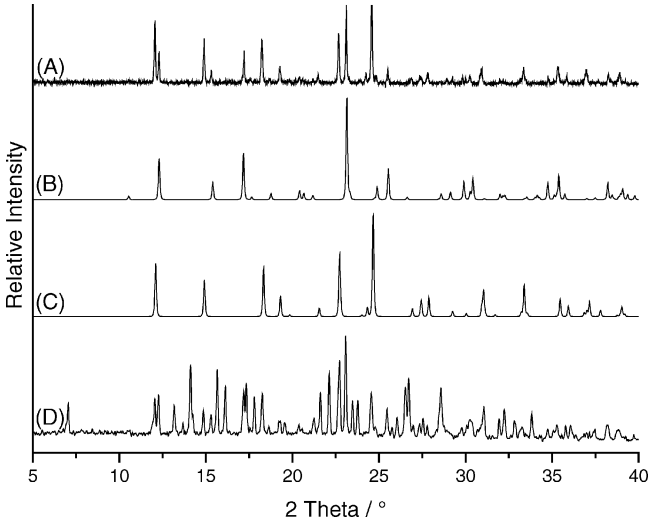

Figure 11. Experimental XRPD patterns of the residue obtained after the first (A) and second (D) TG step in the thermal decomposition reaction of compound **5**, and calculated XRPD patterns for the 1:1 compounds **3I** (B) and **3II** (C).

with that calculated (see the Experimental Section). In addition, the X-ray powder diffraction patterns gave evidence that the ligand-deficient dichlorido and dibromido intermediates are isomorphous (compare C in Figure 10 with D in Figure 11).

The powder X-ray diffraction pattern of the residue obtained after the first TG step in the thermal decomposition reaction of the ligand-rich 1:2 diiodido compound **7** is in exact agreement with that calculated for the 1:1 compound **6** from single-crystal data (compare A with B in Figure 12). Interestingly, the powder X-ray diffraction pattern of the residue obtained after the second TG step is identical to that formed in the first step (compare C with B in Figure 12). Therefore, we stopped the reaction at different temperatures and all residues investigated by X-ray powder diffraction and elemental analysis. In these investigations we only isolated residues that consist of the 1:1 intermediate or a compound that is amorphous to X-rays. The IR spectra of all residues show clearly differences, and the results of elemental analysis are in good agreement with that calculated for a 3:1 compound (see the Experimental Section). Thus, we do not have any explanation for this unusual observation.

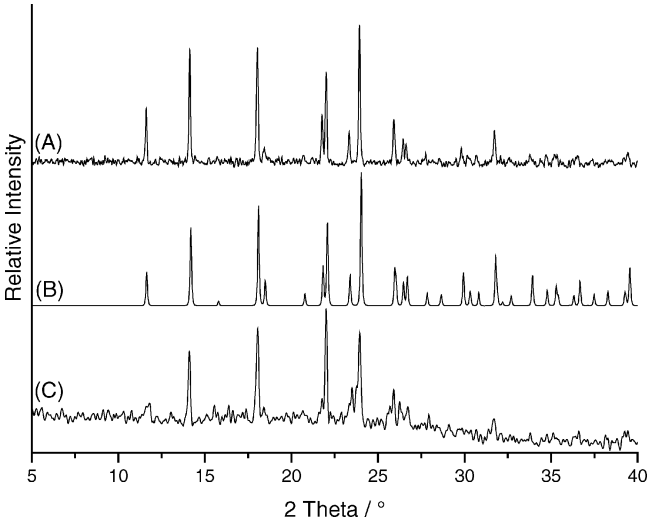

Figure 12. Experimental XRPD patterns of the residue obtained after the first (A) and second (C) step in the thermal decomposition reaction of compound **7**, and calculated XRPD pattern for the 1:1 compounds **6** (B).

Synthetic Aspects

The formation and stability of these compounds was investigated in solution by solvent-mediated conversion experiments. In these experiments, an excess of metal salt and N-donor ligand were mixed in different stoichiometric ratios in methanol, resulting in a precipitate, which was stirred for three days to obtain the thermodynamically most stable form. Afterwards, the products were investigated by X-ray powder diffraction (Table 5).

These experiments clearly show that only compound **1**, **3I**, **6**, and **7** are stable and can also be prepared in solution.

Table 5. Results of the crystallization experiments in methanol as a function of the molar ratio between metal and ligand (2,5-dimethylpyrazine).

	1:6	1:4	1:3	1:2	2:3	1:1	3:2	2:1	4:1
X = Cl	**1** (1:1)								
X = Br	**3I** (1:1)								
X = I	**7** (1:2)			**6** (1:1)					

However, it should be noted that compound **7** cannot be prepared simply by mixing the reactants stoichiometrically as given by the formula. The reaction of ZnI_2 and 2,5-dimethylpyrazine in 1:2 molar ratio results in the formation of the 1:1 compound **6**, whereas in the case of $ZnCl_2$ and $ZnBr_2$ only the 1:1 compounds are formed irrespective of the stoichiometric ratios. Moreover, the 2:3 bromine compound **2** and 1:3 bromine compound **5** can only be prepared in a solvent-free reaction, whereas compound **4** cannot be prepared phase-pure either in solution or in a solvent-free reaction.

To verify which of the two polymorphic modifications **3I** and **3II** represents the thermodynamically most stable form at room temperature, equivalent amounts of both forms were stirred in methanol solution. After three days, only modification **3I** was present, showing that **3I** is the stable modification, whereas **3II** is metastable (Figure 13).

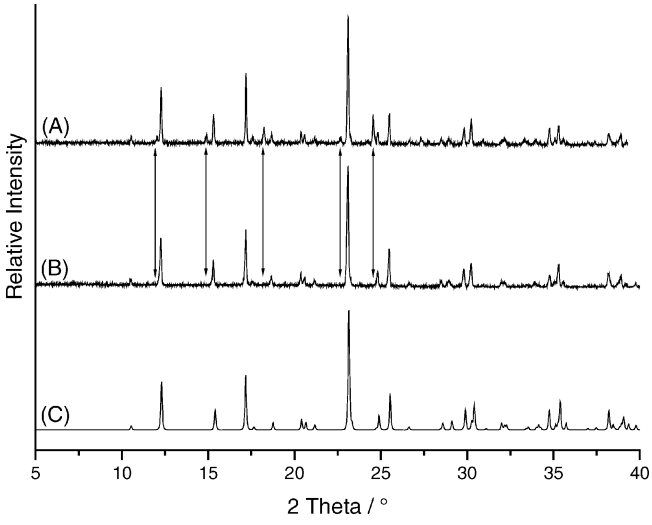

Figure 13. Experimental XRPD patterns of a mixture of the polymorphic 1:1 bromine compounds **3I** and **3II** before (A) and after (B) stirring for three days in methanol solution, together with calculated XRPD pattern for the 1:1 bromine compound **3I** (C). The arrows indicate the position of the reflections of compound **3II**.

Additional differential scanning calorimetry (DSC) investigations in combination with X-ray powder diffraction do not show any transition between the two modifications, and the heat flow cannot be precisely extracted from the DSC curve. Therefore, it cannot be decided if the two forms behave enantiotropically or monotropically.

Comparison of [ZnX_2(pyrazine)] and [ZnX_2(2,5-dimethylpyrazine)] (X = Cl, Br, I)

As mentioned above, for the corresponding coordination compounds with pyrazine as a ligand, a variety of ligand-rich and ligand-deficient compounds were found.[4–7] In the ligand-rich 1:2 compounds with $ZnCl_2$ and $ZnBr_2$, each zinc atom is coordinated by two halide atoms and four pyrazine ligands within slightly distorted octahedra. In the crystal structures, the zinc atoms are connected by the ligands into layers. In contrast, in all 2,5-dimethylpyrazine compounds the metal atoms are only tetrahedrally coordinated by two halide atoms and two N-donor ligands. For the ligand-rich compounds, this difference leads to oligomers in compounds **2** and **4** and to discrete building blocks in compound **5** and **7**. The presence of the more sterically demanding methyl groups attached to the carbon atoms adjacent to the N atoms is responsible for this deviating behavior. Interestingly, a ligand-rich 1:2 compound with zinc(II) iodine was only obtained with 2,5-dimethylpyrazine as ligand, and there is no simple explanation for this unusual behavior.

In contrast, in practically all crystal structures of the ligand-deficient 1:1 compounds, topologically identical coordination networks are found, in which the ZnX_2 units are connected by the pyrazine or 2,5-dimethylpyrazine ligands into chains, with the exception of the crystal structure of the 1:1 dichlorido pyrazine compound,[6] in which the metal centers are octahedrally coordinated. The zinc(II) atoms are connected by the chlorine atoms sharing common edges into chains, which are further linked by the N-donor ligands into layers.

The thermal reactivity of all ligand-rich compounds with pyrazine or 2,5-dimethylpyrazine is similar. On heating, they transform in two steps into ligand-deficient 2:1 compounds via the 1:1 compounds as intermediates. Therefore, these results show clearly that there is no simple relationship between their crystal structure and their thermal behavior.

Conclusion

We have presented eight new coordination compounds including one pair of polymorphic modifications prepared by the reaction of zinc(II) halides and 2,5-dimethylpyrazine, some of which show new [ZnX_2] substructures. Comparison of their crystal structures with those of the corresponding pyrazine compounds reported recently show differences that originate clearly from the additional methyl groups attached to the neighboring C atoms of the N donor atoms in 2,5-dimethylpyrazine. Steric and inductive effects of the methyl group clearly influence the structural diversity. None of these compounds are isotypic to the corresponding pyrazine coordination polymers. In addition, our thermal investigations show that thermal decomposition of the ligand-rich precursor compounds is an adequate alternative for the preparation of new coordination polymers. Even in such cases where all ligand-deficient 1:1 compounds can be prepared in solution, like in the present work, such investigations can help to discover new compounds, such as we have recently shown. Therefore, for the further discovery of new coordination compounds and their polymorphs, also typical solid-state reactions such as the thermal decomposition presented above should be used. In future, we expect more insight into the chemical reactivity and mechanisms of the thermal reactions by comparing the thermal behavior of coordination polymers based on other aromatic N-donor ligands.

Experimental Section

Synthesis: Compounds **1**, **3I**, **3II**, **6**, and **7** were prepared by stirring the reactants in methanol for 3 days at room temperature. The residues were filtered off and washed with diethyl ether. Compounds **2**, **4**, and **5** were prepared in a solvent-free reaction by simply adding the liquid ligand to ZnX_2. The reaction mixtures were kept without stirring for a week at room temperature. The powders obtained contained a large number of single crystals and were used without further purification. Compound **4** could not be prepared phase-pure as described above. The purity of these compounds was checked by X-ray powder diffraction and elemental analysis.

Synthesis of Compound 1: The crystalline powder was prepared by the reaction of $ZnCl_2$ (272.6 mg, 2.0 mmol) and 2,5-dimethylpyrazine (216.3 mg, 2.0 mmol) in methanol (1.0 mL). Yield: 411.5 mg (84.2%). $C_6H_8Cl_2N_2Zn$ (244.41): calcd. C 29.48, H 3.30, N 11.46; found C 29.41, H 3.29, N 10.86. IR (KBr): $\tilde{\nu}$ = 3127 (w), 3040 (m), 2929 (w), 1827 (w), 1624 (w), 1508 (s), 1451 (m), 1381 (w), 1346 (s), 1273 (w), 1165 (m), 1078 (s), 1037 (m), 992 (w), 903 (w), 754 (w), 527 (w), 446 (m) cm^{-1}. Single crystals were prepared by the reaction of $ZnCl_2$ (68.1 mg, 0.5 mmol), 2,5-dimethylpyrazine (108.1 mg, 1.0 mmol), and methanol (2 mL) in a closed test tube at 100 °C for 1 day. Colorless crystals were obtained on cooling.

Synthesis of Compound 2: The crystalline powder was prepared by the solvent-free reaction of $ZnCl_2$ (136.3 mg, 1.0 mmol) and 2,5-dimethylpyrazine (648.9 mg, 6.0 mmol). $C_{18}H_{24}Cl_4N_6Zn_2$ (596.97): calcd. C 36.21, H 4.05, N 14.08; found C 36.50, H 4.00, N 14.13. IR (KBr): $\tilde{\nu}$ = 3105 (w), 3042 (m), 2954 (w), 2918 (w), 2859 (w), 1982 (w), 1830 (w), 1635 (w), 1497 (s), 1445 (s), 1382 (m), 1335 (s), 1268 (w), 1233 (w), 1158 (s), 1077 (s), 1060 (s), 1039 (m), 979 (m), 894 (w), 751 (w), 453 (s), 425 (s) cm^{-1}. Single crystals were prepared by the solvent-free reaction of $ZnCl_2$ (68.2 mg, 0.5 mmol) and 2,5-dimethylpyrazine (108.1 mg, 1.0 mmol). Colorless crystals were obtained within about a week.

Synthesis of Compound 3I and 3II: The crystalline powder of compound **3I** was prepared by the reaction of $ZnBr_2$ (450.4 mg, 2.0 mmol) and 2,5-dimethylpyrazine (216.3 mg, 2.0 mmol) in methanol (1.0 mL). Yield: 542.7 mg (81.4%). $C_6H_8Br_2N_2Zn$ (333.33): calcd. C 21.62, H 2.42, N 8.40; found C 21.59, H 2.32, N 8.48. IR (KBr): $\tilde{\nu}$ = 3124 (w), 3035 (m), 2926 (w), 1816 (w), 1615 (w), 1506 (s), 1445 (m), 1389 (m), 1343 (s), 1272 (m), 1164 (s), 1078 (s), 1035 (m), 987 (m), 897 (w), 753 (w), 525 (w), 425 (m) cm^{-1}. The crystalline powder of compound **3II** was obtained by fast evaporation without stirring of the solvent and initial injection of single crystals of compound **3II**. $C_6H_8Br_2N_2Zn$ (333.33): calcd. C 21.62, H 2.42, N 8.40; found C 21.35, H 2.20, N 8.59. IR (KBr): $\tilde{\nu}$ = 3126 (w), 3039 (m), 1818 (w), 1616 (w), 1500 (s), 1438 (m), 1384 (m), 1339 (s), 1270 (m), 1163 (s), 1080 (s), 1033 (m), 973 (w), 893 (w), 750 (w), 528 (w), 432 (s) cm^{-1}. Single crystals were prepared by the reaction of $ZnBr_2$ (112.6 mg, 0.5 mmol) and 2,5-dimethylpyrazine

(54.1 mg, 0.5 mmol) in methanol (2.0 mL). After slow evaporation of the solvent at room temperature, colorless crystals of both polymorphic modifications were obtained within about a week.

Synthesis of Compound 4: Single crystals were prepared by the solvent-free reaction of $ZnBr_2$ (28.1 mg, 0.125 mmol) and 2,5-dimethylpyrazine (108.1 mg, 1.0 mmol). Colorless crystals were obtained within about a week.

Synthesis of Compound 5: The crystalline powder and single crystals were prepared by the solvent-free reaction of $ZnBr_2$ (450.4 mg, 2.0 mmol) and 2,5-dimethylpyrazine (1297.7 mg, 12.0 mmol). Colorless crystals were obtained within about a week. $C_{18}H_{24}Br_2N_6Zn$ (549.62): calcd. C 39.34, H 4.40, N 15.29; found C 39.35, H 4.38, N 15.25. IR (KBr): $\tilde{\nu}$ = 3039 (w), 2921 (w), 2363 (w), 1819 (w), 1635 (w), 1499 (s), 1446 (m), 1383 (m), 1337 (s), 1270 (m), 1163 (s), 1081 (s), 1039 (m), 972 (w), 891 (w), 751 (w), 669 (w), 508 (w), 430 (m) cm^{-1}.

Synthesis of Compound 6: The crystalline powder was prepared by the reaction of ZnI_2 (1276.7 mg, 4.0 mmol) and 2,5-dimethylpyrazine (432.6 mg, 4.0 mmol) in methanol (1.0 mL). Yield: 542.7 mg (81.4%) on the basis of ZnI_2. $C_6H_8I_2N_2Zn$ (427.31): calcd. C 16.86, H 1.89, N 6.56; found C 16.82, H 1.83, N 6.54. IR (KBr): $\tilde{\nu}$ = 3118 (w), 3031 (m), 1813 (w), 1497 (s), 1438 (m), 1378 (w), 1337 (m), 1268 (m), 1159 (m), 1077 (s), 1030 (m), 891 (w), 750 (w), 526 (w), 433 (m) cm^{-1}. Single crystals were prepared by the reaction of ZnI_2 (159.6 mg, 0.5 mmol) and 2,5-dimethylpyrazine (54.1 mg, 0.5 mmol) in methanol (2.0 mL). After slow evaporation of the solvent, colorless crystals were obtained within about a week.

Synthesis of Compound 7: The crystalline powder was prepared by the reaction of ZnI_2 (1276.7 mg, 4.0 mmol) and 2,5-dimethylpyrazine (2595.4 mg, 24.0 mmol) in methanol (1.0 mL). Yield: 542.7 mg (81.4%) based on ZnI_2. $C_{12}H_{16}I_2N_4Zn$ (535.46): calcd. C 26.92, H 3.01, N 10.46; found C 27.04, H 3.04, N 10.90. IR (KBr): $\tilde{\nu}$ = 2911 (w), 1804 (w), 1628 (w), 1501 (s), 1436 (m), 1384 (m), 1333 (s), 1268 (w), 1239 (w), 1162 (m), 1062 (s), 1035 (m), 971 (w), 883 (w), 749 (w), 672 (w), 429 (s) cm^{-1}. Single crystals were prepared by the solvent-free reaction of ZnI_2 (75.8 mg, 0.25 mmol) and 2,5-dimethylpyrazine (108.1 mg, 1.0 mmol). Colorless crystals were obtained within about a week.

Elemental Analysis of the Residues Obtained in the Thermal Decomposition: (A) Isolated after first heating step for 2:3 chlorine compound **2**. For 1:1 compound **1**: calcd. C 29.48, H 3.30, N 11.46; found C 29.74, H 3.19, N 11.63. (B) Isolated after second heating step for 2:3 chlorine compound **2**. For 2:1 compound: calcd. C 18.93, H 2.12, N 7.36; found C 18.43, H 2.25, N 7.26. (C) Isolated after first heating step for 1:3 bromine compound **5**. For 1:1 compound: calcd. C 21.62, H 2.42, N 8.40; found C 21.81, H 2.24, N 8.23. (D) Isolated after second heating step for 1:3 bromine compound **5**. For 2:1 compound: calcd. C 12.90, H 1.44, N 5.02; found C 12.33, H 1.53, N 5.59. (E) Isolated after first heating step for 1:2 iodine compound **7**. For 1:1 compound: calcd. C 16.86, H 1.89, N 6.56; found C 16.95, H 1.86, N 6.70. (F) Isolated after second heating step for 1:2 iodine compound **7**. For 3:1 compound: calcd. C 6.76, H 0.76, N 2.63; found C 6.88, H 0.72, N 2.72.

Single-Crystal Structure Analysis: All investigations were performed with an imaging plate diffraction system (IPDS-1) with Mo-K_α-radiation from STOE & CIE. The structure solutions were performed with direct methods by using SHELXS-97,[9] and structure refinements were performed against F^2 by using SHELXL-97.[10] For all compounds, numerical absorption correction was applied with X-Red[11] and X-Shape[12] (**1**, **3I**, **3II**, **5**, **6**, and **7**) or Platon[13] (**2** and **4**). All non-hydrogen atoms were refined with anisotropic displacement parameters. All hydrogen atoms were positioned with idealized geometry (methyl groups were allowed to rotate but not to tip) and were refined with fixed isotropic displacement parameters [U_{eq}(H) = –1.5·U_{eq}(C)] for methyl H atoms and

Table 6. Selected crystal data and details of the structure determinations.

Compound	**1**	**2**	**3I**	**3II**	**4**	**5**	**6**	**7**
Formula	$C_6H_8Cl_2N_2Zn$	$C_{18}H_{24}Cl_4N_6Zn_2$	$C_6H_8Br_2N_2Zn$	$C_6H_8Br_2N_2Zn$	$C_{18}H_{24}Br_4N_6Zn_2$	$C_{18}H_{24}Br_2N_6Zn$	$C_6H_8I_2N_2Zn$	$C_{12}H_{16}I_2N_4Zn$
Ratio ZnX_2/L	1:1	2:3	1:1	1:1	2:3	1:3	1:1	1:2
MW/g mol^{-1}	244.41	596.97	333.33	333.33	774.81	549.62	427.31	535.46
Crystal system	orthorhombic	triclinic	orthorhombic	monoclinic	triclinic	monoclinic	monoclinic	monoclinic
Space group	*Pnma*	$P\bar{1}$	*Pnma*	*C*2/*c*	$P\bar{1}$	*C*2/*c*	*C*2/*c*	$P2_1/c$
a/Å	6.0621(4)	7.2149(10)	6.2698(6)	16.1453(18)	7.2840(8)	8.5956(9)	16.6286(13)	12.2908(8)
b/Å	10.2156(8)	9.1905(11)	10.3167(7)	6.4913(6)	9.4775(16)	11.4237(7)	6.8351(4)	8.2723(7)
c/Å	13.9518(8)	10.1410(13)	14.3842(9)	9.8755(10)	10.1762(11)	23.1531(16)	10.0199(8)	17.2054(13)
α/°		79.973(15)°			81.004(13)			
β/°		70.138(15)°		115.096(11)	72.489(12)	100.174(10)	113.947(9)	101.266(8)
γ/°		70.264(15)°			71.306(12)			
V/Å^3	864.01(10)	593.94(13)	930.42(12)	937.29(17)	633.21(14)	2237.7(3)	1040.81(13)	1715.6(2)
T/K	170	170	170	170	170	170	170	170
Z	4	1	4	4	1	4	4	4
$D_{calcd.}$/g cm^{-3}	1.879	1.669	2.380	2.362	2.032	1.631	2.727	2.073
μ /mm^{-1}	3.393	2.487	11.166	11.084	8.222	4.683	8.237	5.024
Transmission range	0.521–0.869	0.753–0.831	0.361–0.722	0.249–0.521	0.403–0.621	0.571–0.751	0.411–0.785	0.582–0.735
θ_{max}/°	28	28	28	28	28	28	28	28
Measured reflections	9309	5213	7814	4836	5880	7691	5219	12810
Unique reflections	1092	2740	1164	1134	2991	2368	1240	3671
Reflections [$F_o > 4\sigma(F_o)$]	1026	2050	985	982	2473	1649	1109	3022
Parameters	57	140	57	53	140	137	53	173
R_{int}	0.0350	0.0529	0.1052	0.0378	0.0548	0.0622	0.0300	0.0480
R_1[a] [$F_o > 4\sigma(F_o)$]	0.0241	0.0496	0.0431	0.0271	0.0525	0.0425	0.0208	0.0300
wR_2[b] [all data]	0.0648	0.1369	0.0524	0.0707	0.1526	0.0992	0.0524	0.0773
GOF	1.072	1.074	1.063	0.999	1.078	0.995	1.051	0.979
Residual electron density /e Å^{-3}	0.544/–0.562	0.890/–1.195	1.006/–1.795	0.840/–0.755	1.706/–1.335	0.483/–0.699	0.654/–0.864	0.745/–0.846

[a] $R_1 = \sum||F_o| - |F_c||/\sum|F_o|$. [b] $wR_2 = [\sum w(F_o^2 - F_c^2)^2/\sum w(F_o^2)^2]^{1/2}$.

[U_{eq}(H) = –1.2·U_{eq}(C)] for aromatic H atoms using a riding model with $d_{C–H}$ = 0.95 Å for methyl and $d_{C–H}$ = 0.98 Å for aromatic H atoms. The bromine atom in compound **5** is disordered over two positions and was refined by using a split model (s.o.f. = 0.5). Details of the structure determination are given in Table 6 and in the Supporting Information.

CCDC-705375 (**1**), -705376 (**2**), -705377 (**3I**), -705378 (**3II**), -705379 (**4**), -705380 (**5**), -705381 (**6**), and -705382 (**7**) contain the supplementary crystallographic data for this paper. These data can be obtained free of charge from the Cambridge Crystallographic Data Centre via www.ccdc.cam.uk/data_request.cif.

X-ray Powder Diffraction (XRPD): XRPD experiments were performed with a STOE DF4 transmission powder diffractometer with Cu-K_α radiation (λ = 154.0598 pm) that is equipped with a position-sensitive detector (scan range: 5–45°) from STOE & CIE.

Differential Thermal Analysis, Thermogravimetry, and Mass Spectroscopy (DTA/TG/MS): The heating-rate-dependent DTA/TG measurements were performed in a nitrogen atmosphere (purity: 5.0) in Al_2O_3 crucibles with a STA-409CD instrument from Netzsch. The DTA/TG/MS measurements were performed with the same instrument, which was connected to a quadrupole mass spectrometer from Balzers by Skimmer coupling from Netzsch. The MS measurements were performed in analog and trend-scan mode in Al_2O_3 crucibles in a dynamic helium atmosphere (purity: 5.0) at heating rates of 4 K min^{-1}. All measurements were performed with a flow rate of 75 mL min^{-1} and were corrected for buoyancy and current effects. The instrument was calibrated with standard reference materials.

Differential Scanning Calorimetry (DSC): DSC investigations were performed with a DSC 204/1/F device from Netzsch. The measurements were performed in aluminum pans at heating rates of 3 K min^{-1}. The instrument was calibrated with standard reference materials.

Elemental Analysis: C,H,N analysis was performed with an EURO EA elemental analyzer, fabricated by EURO VECTOR Instruments and Software.

Spectroscopy: Fourier transform IR spectra were recorded with a Genesis series FTIR spectrometer by ATI Mattson in KBr pellets.

Supporting Information (see footnote on the first page of this article): Experimental and calculated X-ray powder diffraction patterns as well as IR spectra of compounds **1**, **2**, **3I**, **3II**, **4**, **6**, and **7**. DTA/TG/MS measurements for compounds **1**, **3I**, **3II**, and **6**, heating-rate-dependent TG measurements of compounds **1**, **2**, **3I**, **5**, **6**, and **7** as well as DSC measurements of the polymorphic modifications **3I** and **3II**.

Acknowledgments

We gratefully acknowledge financial support by the State of Schleswig-Holstein and the Deutsche Forschungsgemeinschaft (Project NA 720/1-1). We thank Professor Dr. Wolfgang Bensch for the use of his experimental facility.

[1] a) S. R. Batten, R. Robson, *Angew. Chem. Int. Ed.* **1998**, *37*, 1460–1494; b) R. Robson, B. F. Abrahams, S. R. Batten, R. W. Grable, B. F. Hoskins, J. Liu in *Supramolecular Architecture*, ACS publications, Washington DC, **1992**; c) D. Braga, L. Maini, M. Polito, L. Scaccianoce, G. Cojazzi, F. Grepioni, *Coord. Chem. Rev.* **2001**, *216*, 225–248; d) W. Chen, H.-M. Yuan, J.-Y. Wang, Z.-Y. Liu, J.-J. Xu, M. Yang, J.-S. Chen, *J. Am. Chem. Soc.* **2003**, *125*, 9266–9267; e) P. J. Hagrman, D. Hagrman, J. Zubieta, *Angew. Chem. Int. Ed.* **1999**, *38*, 2638–2684; f) B. Moulton, M. J. Zaworotko, *Chem. Rev.* **2001**, *101*, 1629–1658; g) S. Muthu, J. H. K. Yip, J. J. Vittal, *J. Chem. Soc., Dalton Trans.* **2001**, 3577–3584; h) R. Robson in *Comprehensive Supramolecular Chemistry*, Pergamon, New York, **1996**, p. 733; i) C.-D. Wu, W. Lin, *Inorg. Chem.* **2005**, *44*, 1178–1180; j) A. J. Blake, N. R. Champness, P. Hubberstey, W.-S. Li, M. A. Withersby, M. Schröder, *Coord. Chem. Rev.* **1999**, *183*, 117–138.

[2] a) C. Näther, I. Jeß, J. Greve, *Polyhedron* **2001**, *20*, 1017–1022; b) C. Näther, I. Jeß, H. Studzinski, *Z. Naturforsch. B* **2001**, *56*, 997–1002; c) C. Näther, I. Jeß, *Monatsh. Chem.* **2001**, *132*, 897–910; d) C. Näther, M. Wriedt, I. Jeß, *Z. Anorg. Allg. Chem.* **2002**, *628*, 394–400; e) C. Näther, J. Greve, I. Jeß, *Solid State Sci.* **2002**, *4*, 813–820; f) C. Näther, I. Jeß, *Z. Naturforsch. B* **2002**, *57*, 1133–1140; g) C. Näther, I. Jeß, *J. Solid State Chem.* **2002**, *169*, 103–112; h) C. Näther, M. Wriedt, I. Jeß, *Inorg. Chem.* **2003**, *42*, 2391–2397; i) C. Näther, I. Jess, *Inorg. Chem.* **2003**, *42*, 2968–2976; j) C. Näther, I. Jeß, N. Lehnert, D. Hinz-Hübner, *Solid State Sci.* **2003**, *5*, 1343–1357; k) C. Näther, I. Jeß, M. Bolte, *Z. Naturforsch. B* **2003**, *58*, 1105–1111; l) T. Kromp, W. S. Sheldrick, C. Näther, *Z. Anorg. Allg. Chem.* **2003**, *629*, 45–54.

[3] a) G. Bhosekar, I. Jeß, Z. Havlas, C. Näther, *Cryst. Grow. Des.* **2007**, *7*, 2627–2634; b) G. Bhosekar, I. Jeß, N. Lehnert, C. Näther, *Eur. J. Inorg. Chem.* **2008**, 605–611; c) G. Bhosekar, I. Jeß, C. Näther, *Z. Naturforsch. B* **2006**, *61*, 721–726; d) C. Näther, G. Bhosekar, I. Jeß, *Eur. J. Inorg. Chem.* **2007**, 5353–5359; e) C. Näther, G. Bhosekar, I. Jess, *Inorg. Chem.* **2007**, *46*, 8079–8087.

[4] G. Bhosekar, I. Jess, C. Näther, *Inorg. Chem.* **2006**, *45*, 6508–6515.

[5] S. A. Bourne, M. Kilkenny, L. R. Nassimbeni, *J. Chem. Soc., Dalton Trans.* **2001**, 1176–1179.

[6] B. Staub, J. Pickardt, *Z. Naturforsch. B* **1996**, *51b*, 947–952.

[7] Y. Song, Y. Niu, H. Hou, Y. Zhu, *J. Mol. Struct.* **2004**, *689*, 69–74.

[8] a) E. Dubler, G. Haenggi, H. Schmalle, *Inorg. Chem.* **1992**, *31*, 3728–3736; b) C. A. Grapperhaus, T. Tuntulani, J. H. Reibenspies, M. Y. Darensbourg, *Inorg. Chem.* **1998**, *37*, 4052–4058; c) E. Sahin, S. Ide, A. Atac, S. Yurdakul, *J. Mol. Struct.* **2002**, *616*, 253–258; d) U. Siemeling, I. Scheppelmann, B. Neumann, A. Stammler, H.-G. Stammler, J. Frelek, *Chem. Commun.* **2003**, 2236–2237; e) F. Pezet, I. Sasaki, J.-C. Daran, J. Hydrio, H. Aït-Haddou, G. Balavoine, *Eur. J. Inorg. Chem.* **2001**, 2669–2674; f) Y. D. M. Champouret, J.-D. Maréchal, I. Dadhiwala, J. Fawcett, D. Palmer, K. Singh, G. A. Solan, *Dalton Trans.* **2006**, 2350–2361; g) C. Hu, U. Englert, *Angew. Chem. Int. Ed.* **2005**, *44*, 2281–2283.

[9] G. M. Sheldrick, *SHELXS-97, Program for Crystal Structure Solution*, University of Göttingen, Göttingen, Germany, **1997**.

[10] G. M. Sheldrick, *SHELXL-97, Program for the Refinement of Crystal Structures*, University of Göttingen, Göttingen, Germany, **1997**.

[11] *X-Red, Version 1.11, Program for Data Reduction and Absorption Correction*, STOE & CIE GmbH, Darmstadt, Germany, **1998**.

[12] *X-Shape, Version 1.03, Program for the Crystal Optimization for Numerical Absorption Correction*, STOE & CIE GmbH, Darmstadt, Germany, **1998**.

[13] A. L. Spek, Utrecht University, Utrecht, Netherlands, **2005**.

Received: June 26, 2008
Published Online: December 15, 2008

DOI: 10.1002/ejic.200800812

(1,3,4-Oxadiazole)copper(II) Compounds: Dimensionality, Magnetism and Nuclease Activity

Patricia Gómez-Saiz,[a] Rubén Gil-García,[a] Miguel A. Maestro,[b] Francisco J. Arnaiz,[a] Luis Lezama,[c] Teófilo Rojo,[c] José Luis Pizarro,[c] María Isabel Arriortúa,[c] Marta González-Álvarez,[d] Joaquín Borrás,[d] Virginia Diez-Gómez,[e] and Javier García-Tojal*[a]

Keywords: Copper / DNA cleavage / Magnetic properties / Oxadiazole / Structure elucidation

The work presented here describes the synthesis of new copper(II) complexes derived from 2-amino-5-(pyridin-2-yl)-1,3,4-oxadiazole (L^1) and 2-methylamino-5-(pyridin-2-yl)-1,3,4-oxadiazole (L^2) which also incorporate azido (N_3^-), thiocyanato (NCS^-), cyanato (NCO^-), dicyanamido [$N(CN)_2^-$, dca] and malonato ($C_3H_2O_4^{2-}$, mal) coligands. Structures of the $[Cu(L^2)(mal)(H_2O)]\cdot 2H_2O$ (**1**), $[\{Cu(L^2)(mal)\}_2]$ (**2**), $[Cu(L^2)_2(NCS)_2]$ (**3**), $[Cu(L^1)(NCS)_2]_n$ (**4**) and $[\{Cu(L^2)\}_2(dca)_2](ClO_4)_2\cdot 2H_2O$ (**5**) compounds show the dependence of the dimensionality on parameters such as the type of oxadiazole and coligand utilised, solvents or reaction times. In this sense, **1** and **3** are mononuclear complexes, **2** contains centrosymmetric dinuclear entities, **4** is a 1D compound in which thiocyanato groups act as end-to-end bridges and **5** shows a 2D arrangement of dinuclear motifs linked through dicyanamido spacers. The copper(II) ions acquire distorted octahedral (**3** and **4**), square-pyramidal (**1** and **2**) and trigonal bipyramidal (**5**) geometries. Stacking π–π interactions and hydrogen bonds stabilise the crystal frameworks. Water tetramers are present in **1**. Spectroscopic (infrared, UV/Vis absorption and electron spin resonance) studies have also been developed for **1**–**5** and for the $Cu(L^2)(dca)_2(H_2O)$ (**6**), $Cu(L^2)(NCO)_2$ (**7**) and $Cu(L^2)_2(N_3)_2(H_2O)_2$ (**8**) complexes. The studies suggest the coordination of oxadiazole and coligands in all cases. Magnetic measurements show antiferromagnetic coupling for compound **5**, ferromagnetic interactions for compound **2** and paramagnetic behaviour in compound **4**. The susceptibility data were fitted by using the Bleaney–Bowers′ equation for the copper(II) dimers derived from $H = -2JS_1S_2$. The resultant J/k values are +2.15 and –38.3 K for compounds **2** and **5**, respectively. Magneto-structural correlations are discussed and extended to more than 30 published dinuclear $Cu(NN)_2Cu'$ diazole-only bridged compounds. All these systems show J values close to or greater than those given by the expression $J \approx -90 + 3\,\Delta\beta$ (where $\Delta\beta$ is the difference between the Cu–N–N and Cu–N′–N′ angles). The artificial nuclease activity of **1**, **2**, **3** and **5** in the presence of mercaptopropionic acid or glutathione has also been analysed and compared with that exhibited by $[Cu(L^2)_2(H_2O)_2](NO_3)_2$ and $CuSO_4$.

Introduction

1,3,4-Oxadiazole derivatives show a wide range of properties such as luminescence phenomena, semiconductor behaviour or biological activity which has prompted research on these compounds for diverse applications from light-emitting diodes and electrochromic devices[1a–j] to antimalarial,[1k] antinflammatory,[1l,1m] antibacterial,[1n] anti-HIV,[1o] antifungal[1p,1q] and antitumoral substances.[1r] In particular, important efforts have been focused on the study of coordination compounds where the oxadiazole ligands link copper(II) ions. Most of these complexes incorporate oxadiazole moieties joined to two or more substituents containing chelating centres (i.e. two pyridine rings) generating bis(hydroxyphenyl) (see Scheme 1, part a),[2] bis(anilyl) (part b)[3] and, more often, bis(pyridyl-1,3,4-oxadiazole) ligands (parts c–e).[4] The research has given rise to systems exhibiting original architectures and interesting magnetic, electric and luminescent properties. Surprisingly, studies on the biological applications of metal-containing oxadiazole derivatives are lacking, despite the promising properties of some related compounds.[5]

[a] Departamento de Química, Universidad de Burgos,
Plaza Misael Bañuelos s/n, 09001 Burgos, Spain
Fax: +34-947-258831
E-mail: qipgatoj@ubu.es
[b] Departamento de Química Fundamental, Universidade da Coruña,
Campus da Zapateira s/n, 15071 A Coruña, Spain
[c] Departamentos de Química Inorgánica y de Mineralogía y Petrología,
Universidad del País Vasco, Aptdo. 644, 48080 Bilbao, Spain
[d] Departamento de Química Inorgánica, Facultad de Farmacia,
Universidad de Valencia, Vicent Andres Estelles s/n,
46100 Burjassot (Valencia), Spain
[e] Instituto de Ciencia de Materiales, Sor Juana Inés de la Cruz 3,
28049, Madrid, Spain
Supporting information for this article is available on the WWW under http://www.eurjic.org/ or from the author.

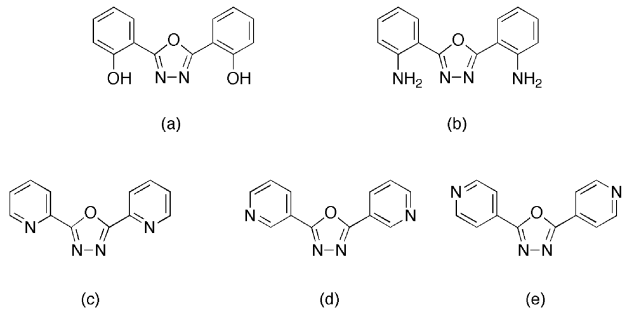

Scheme 1.

Recently, we obtained new 1,3,4-oxadiazole derivatives from the oxidative cyclisation of thiosemicarbazones and their copper(II) complexes in the presence of bromate and iodate.[6] In this case, a pyridine ring is the only coordinating substituent apart from the oxadiazole moiety,[7] as is shown in Scheme 2.

L^1 L^2

Scheme 2.

This paper deals with the synthesis, structures and magnetic properties of copper(II) compounds containing 2-amino-5-(pyridin-2-yl)-1,3,4-oxadiazole (L^1) or 2-methylamino-5-(pyridin-2-yl)-1,3,4-oxadiazole (L^2) together with pseudohalide [azido N_3^-, thiocyanato NCS^-, cyanato NCO^-, dicyanamido $N(CN)_2^-$ dca] or malonato (mal) ancillary ligands. The corresponding formulae are $[Cu(L^2)(mal)(H_2O)]\cdot 2H_2O$ (**1**), $[\{Cu(L^2)(mal)\}_2]$ (**2**), $[Cu(L^2)_2(NCS)_2]$ (**3**), $[Cu(L^1)(NCS)_2]_n$ (**4**), $[\{Cu(L^2)\}_2(dca)_2](ClO_4)_2\cdot 2H_2O$ (**5**), $Cu(L^2)(dca)_2(H_2O)$ (**6**), $Cu(L^2)(NCO)_2$ (**7**) and $Cu(L^2)_2(N_3)_2(H_2O)_2$ (**8**). We report, for the first time, the nuclease activity of some of these compounds in the presence of thiols as reducing agents.

Results and Discussion

Synthesis

The procedures which lead to the attainment of the title oxadiazolecopper(II) derivatives incorporating pseudohalide ligands are very sensitive to different experimental parameters. Firstly, the kind of oxadiazole ligand (L^1 or L^2) used influences the stoichiometries of the final products, as is the case of compounds **3** and **4** belonging to the Cu^{II}–L^1/L^2–NCS system. Besides, thiocyanato Cu^{II}–L^2 derivatives can adopt a single 1D chain in as in $[Cu(L^2)(NCS)_2]_n$[7b] or a monomeric octahedral structure (compound **3**) depending on the reaction time: 5 and 1 h, respectively. This suggests that **3** is a kinetically favoured intermediate and $[Cu(L^2)(NCS)_2]_n$ represents the most thermodynamically stable product. On the other hand, the synthesis of the cyanato complex requires strict pH control.

The preparation of the malonato complexes is affected by pH, concentration of reactants, temperature and the Cu^{II}/malonato molar ratio as has been pointed out previously.[8] These influences are particularly noticeable in the synthesis of **2**, where the presence of water and the lack of base can lead to the formation of other compounds such as **1**, $[Cu(L^2)_2(H_2O)_2](NO_3)_2$ or Cu^{II}/malonato species. Two synthetic approaches have been combined for the syntheses of **1** and **2**: the use of 1,3,4-oxadiazolecopper(II) precursors as starting materials and the reaction with $[Cu(mal)_2]^{2-}$ dianionic species.[9]

Crystal Structures

Crystal Structures of the Malonato Derivatives

The crystal structure of **1** contains monomeric units as represented in Figure 1 and solvent molecules. The coordination around the metal centre is a distorted square-pyramidal topology ($\tau = 0.09$).[10] Two oxadiazole nitrogen atoms and two oxygen carboxylato atoms complete the basal plane and one water molecule occupies the apical position with bonds given in Table 1. Adjacent monomers are close with Cu···O(2)^{i} (i: $-x + 1, -y + 1, -z + 1$) distances of 2.923(2) Å which could be interpreted as a (5+1) pseudo-coordination giving rise to pseudo-dimers where copper(II) ions are 3.6349(3) Å away.

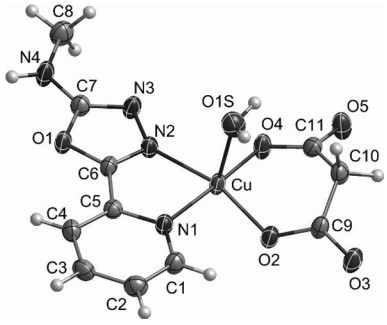

Figure 1. ORTEP drawing of the monomeric $[Cu(L^2)(mal)(H_2O)]$ entities in **1**. Thermal ellipsoids are drawn at the 50% probability level.

In the case of **2**, the structure consists of discrete centrosymmetric dinuclear $[\{Cu(L^2)(mal)\}_2]$ entities as shown in Figure 2. The copper(II) ions are located in a square-pyramidal environment ($\tau = 0.02$). The oxadiazole shows bidentate behaviour through the N(1) and N(2) atoms which form the basal plane together with the malonato O(2) and O(4) atoms. A longer bond length separates the metal centre from the apical O(3)^{ii} atom (ii: $-x + 1, -y + 1, -z + 1$), see Table 1. The Cu···Cu^{ii} intradimeric distance is 4.7266(3) Å while the closest metal ions from different dimers are separated by 5.4210(4)^{iii} Å (iii: $-x + 2, -y + 2, -z$). It is well established that the malonato dianion exhibits coordination modes different from those observed in other

Table 1. Selected bond lengths [Å] and angles [°] for **1**, **2**, **3**, **4** and **5**.

	1	2	3	4	5
Cu–N(1)	2.047(2)	2.050(2)	2.039(1)	2.083(2)	2.033(4)
Cu–N(2)	2.022(2)	2.041(2)	2.422(1)	1.999(2)	2.159(4)
Cu–O(1S)/O(3)′/N(5)/S(1)′	2.366(2)	2.336(2)[ii]	1.959(2)	2.952(1)[x]	2.028(5)
Cu–O(2)/N(8)/N(6)	1.920(2)	1.915(2)	–	1.934(2)	1.957(5)
Cu–O(4)/N(9)	1.921(2)	1.917(2)	–	1.943(2)	–
Cu–N(3)′/S(2)′	–	–	–	3.048(1)[ix]	1.964(4)[xv]
N(1)–Cu–N(2)	80.13(8)	80.36(7)	76.91(5)	79.19(8)	78.4(2)
N(1)–Cu–O(4)/N(3)′/N(1)′/N(9)	174.23(7)	169.2(7)	180.0(1)	173.00(9)	170.9(2)
N(2)–Cu–O(2)/N(2)′/N(8)/N(6)	162.95(8)	168.61(7)	180.00(7)[xiv]	171.78(9)	129.5(2)
N(2)–Cu–O(1S)/O(3)′/N(5)/S(1)′	96.62(8)	88.66(6)[ii]	88.08(6)	84.78(6)	110.0(2)

Symmetry transformations: ii: $-x + 1, -y + 1, -z + 1$; ix: $-x + 2, -y, -z$; x: $-x, -y + 2, -z + 1$; xiv: $-x, -y, -z$; xv: $-x - 1, -y, -z + 1$.

carboxylato anions[11] and that they allow the metal centres to link other ligands giving rise to high dimensionality structures.[12] This versatile behaviour is graphically summarised in Scheme 3. Bidentate chelate and (monodentate + bidentate) modes are present in compounds **1** and **2**, respectively (Scheme 3, a and b). The malonato bridges give rise to chair-shaped eight-membered rings in **2**. Previous studies have reported chelate,[13] and (monodentate + bidentate) abilities[14] and collections of compounds exhibiting both kinds of coordinating behaviours.[15] However, we have found in the literature only one reference in which a (monodentate + bidentate) malonato ligand acts as a double-linker between the copper ions in a dinuclear entity analogous to compound **2**.[16] Concerning the carboxylato bridges in **2**, *syn-anti* modes are present (see Scheme 4).

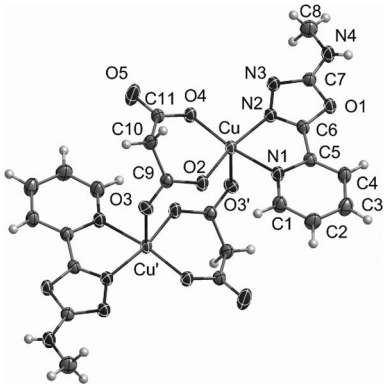

Figure 2. ORTEP drawing of the molecular structure of the $[\{Cu(L^2)(mal)\}_2]$ dimers in **2**. Thermal ellipsoids are drawn at the 50% probability level.

Cyclic planar water tetramers with a parallelogram shape are formed in **1** through two hydrogen bonds linking the O(12)···O(11) and O(11)···O(12)[iv] atoms (iv: $-x + 2, -y + 1, -z$) at 2.934(4) and 2.805(4) Å, respectively, with angles of 81.78 and 98.22°. The symmetry of the parallelograms is C_i (D_{2h} considering only the oxygen atoms). Four-membered water clusters already published show C_4, S_4 and C_s symmetries which are depicted in Scheme 5.[17] However, in past years, several analogous C_i cycles have been discovered.[18] In this sense, the geometry of the tetramer in **1** shows an excellent agreement with that predicted by Schütz and coworkers using ab intio methods.[19] The average O···O distance of the tetramers in **1** is 2.870 Å which is longer

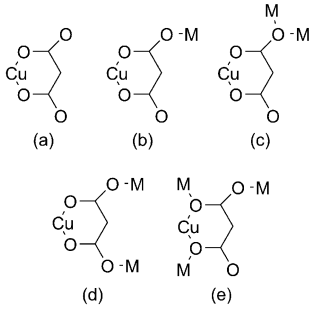

Scheme 3.

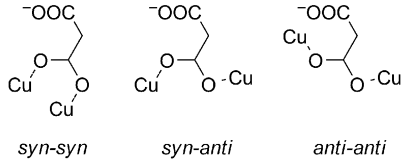

Scheme 4.

than that measured for the water tetramer using far-infrared vibration-rotation-tunnelling spectroscopy (FIR-VRT, 2.78 Å).[20] However, this O···O length is close to the experimentally determined distance in liquid water at 298 K (2.85 Å)[21] while that in hexagonal ice (I_h) at 183 K is 2.759 Å.[22] These O···O distances fall inside the range obtained by quantum mechanical and semiempirical methods for four-membered water cycles (2.70–2.94 Å, mainly depending on the calculation methods and geometries assumed).[23] A net of hydrogen bonds involving O(12), O(10) and the carboxylato O(5) and O(3) atoms (Figure S1 in Supporting Information) gives rise to chains along the [–10–1] direction very similar to those described by other authors.[24]

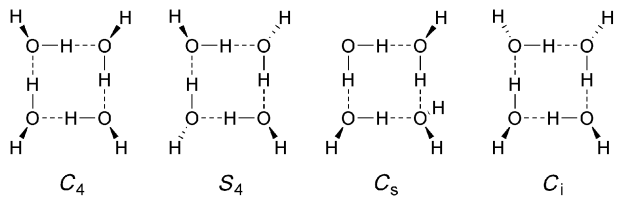

Scheme 5.

Crystal Structures of the Thiocyanato Derivatives

Compound **3** consists of $[Cu(L^2)_2(NCS)_2]$ monomers with tetragonal elongated copper(II) ions joined to two bidentate oxadiazole and two *N*-bonded thiocyanato ligands, all of them occupying *trans* positions. The long axis of the distorted octahedron lies along the Cu–N(2) bonds. The molecular entities are connected through noncovalent interactions in which the thiocyanato sulfur atom is directed towards the oxadiazole ring with minimum distances of 3.18 Å [S···O(1)^{vi}] and 3.25 Å, [S···centroid^{vi} (vi: $-x + 1$, $-y$, $-z$, Figure 3)]. Pseudochains along the x axis are formed. The closest Cu···Cu^{vii} distances are 8.502(4) Å (vii: $-x$, $-y + 1$, $-z$) and metal ions are aligned along the [010] direction. The linearity of the Cu–N–C–S fragments results in important steric hindrance which manifests itself in the large distances between monomers hindering them from establishing strong interactions. It also gives rise to a peculiar arrowhead arrangement (Figure S2).

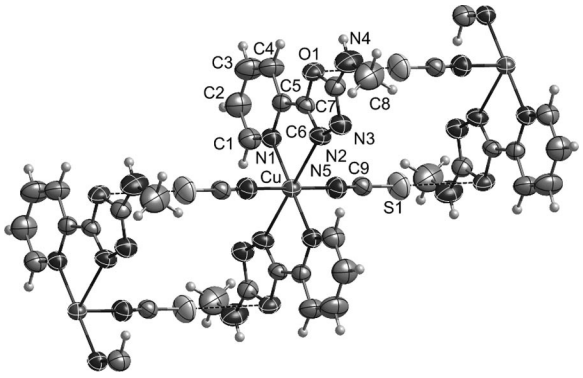

Figure 3. ORTEP drawing of the molecular structure of the $[Cu(L^2)_2(NCS)_2]$ entity in **3** and the connectivity through the S1···O(1) atoms represented by dashed lines. Thermal ellipsoids are drawn at the 50% probability level.

A portion of the 1D complex **4** is depicted in Figure 4. It consists of $[Cu(L^1)]^{2+}$ building blocks double-bridged by μ-1,3 equatorial-axial thiocyanato ligands to give zig-zag chains running parallel to the [001] direction. The coordination sphere around the copper(II) ion is a (4+2) distorted octahedron. Four nitrogen atoms form the equatorial plane, two of them belong to an oxadiazole group and the others originate from thiocyanato groups. The axial positions are occupied by weakly bonded sulfur thiocyanato atoms with Cu–S(1)^{viii} and Cu–S(2)^{ix} distances of 2.952(1) and 3.048(1) Å, respectively (viii: $-x + 2$, $-y$, $-z + 1$; ix: $-x + 2$, $-y$, $-z$). The shortest intrachain Cu···Cu distances are 5.573(1)^{x} (x: $-x$, $-y + 2$, $-z + 1$) and 5.877(1)^{ix} Å while the closest copper ions from different chains are 7.185(1)^{xi} Å apart (xi: $-x + 1$, $-y$, $-z$).

The structural differences between **4** and the chain with single end-to-end thiocyanato bridges in $[Cu(L^2)(NCS)_2]_n$ must also be pointed out.[7b] This last complex represented the first structural evidence of that particular coordination

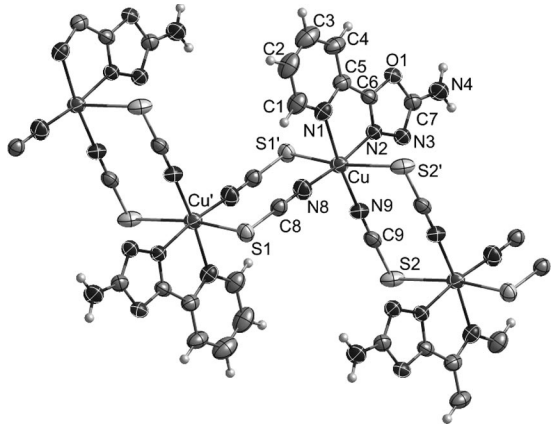

Figure 4. ORTEP drawing of **4**. Thermal ellipsoids are drawn at the 50% probability level.

mode together with other compounds simultaneously published.[25] Such differences could be due to the presence of the methyl group in the 1D $[Cu(L^2)(NCS)_2]_n$ compound which hinders the establishment of strong π-π stacking. Structural relationships and conversion from $[Cu(L^2)(NCS)_2]_n$ into **3** and **4** are visualised in Figure 5.

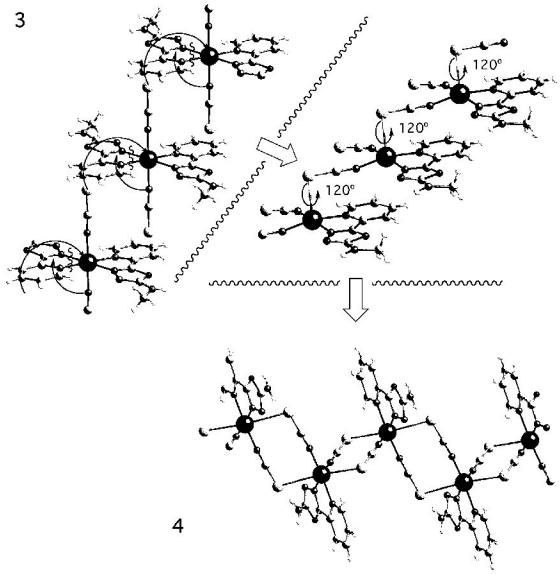

Figure 5. Thiocyanato-containing oxadiazole-copper(II) derivatives. A reorganisation of the thiocyanato groups around the metal ion in **3** together with the evolution of one oxadiazole ligand gives rise to the thermodynamically more stable $[Cu(L^2)(NCS)_2]_n$ compound. Doubly bridged zig-zag chains of **4** can be obtained by turning about 120° around the Cu–S_{axial} bonds in $[Cu(L^2)(NCS)_2]_n$.

More than 550 crystal structures of thiocyanatocopper complexes have been reported. Around 60 of them contain double μ-1,3 thiocyanato systems. However, 1D polymeric compounds incorporating $Cu(NCS)_2Cu'$ moieties with doubly-bridging thiocyanato as the unique linker between ligand-copper(II) fragments are relatively scarce.[26]

Crystal Structure of the Dicyanamido Derivative

The lattice of compound **5** is made up of centrosymmetric $[\{Cu(L^2)\}_2]^{4+}$ dinuclear entities where the oxadiazole rings act as bridges between the copper(II) ions. Four dicyanamido (dca) ligands connect each of the $[\{Cu(L^2)\}_2]^{4+}$ fragments to four adjacent dimeric $[\{Cu(L^2)\}_2]^{4+}$ cations (Figure 6) giving rise to a 2D structure in which water molecules of crystallisation and perchlorate counterions are accommodated in elliptical channels along the [100] direction (Figure 7).

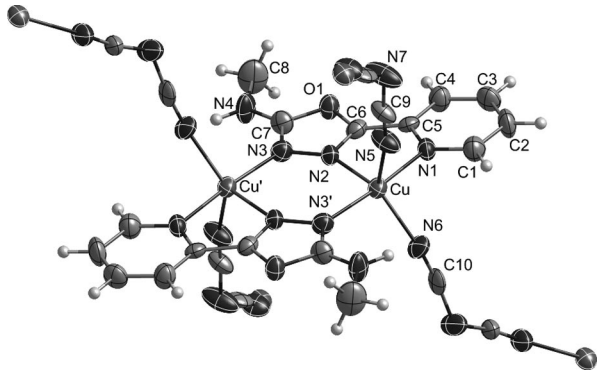

Figure 6. ORTEP drawing of the $[\{Cu(L^2)\}_2(dca)_2]^{2+}$ dimeric units that form the 2D structure in **5**. Perchlorate ions and water molecules are omitted for clarity. Thermal ellipsoids are drawn at the 50% probability level.

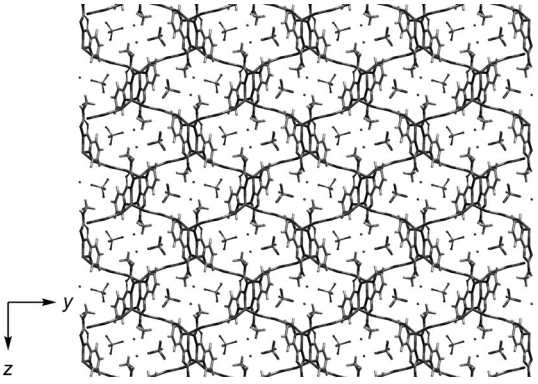

Figure 7. Channels in the structure of **5** contain the perchlorate ions and the water molecules. The approximate maximum dimensions are 13.5 × 9.3 Å. Hydrogen atoms from water molecules are omitted.

The copper(II) ions are five-coordinate with a geometry close to trigonal bipyramidal (τ = 0.69). Five nitrogen atoms sit around the metal centre: two of them from the respective dca ligands, two from a bidentate oxadiazole ligand and the last one belongs to the other intradimeric oxadiazole bridge. Copper ions inside the dimer are spaced at 4.2193(9)[xii] Å (xii: $-x + 1, -y, -z + 1$) and the shortest interdimeric Cu···Cu′ distance is 7.301(1)[xiii] Å (xiii: $-x, -y, -z + 1$). Perspective views are given in Figure S3.

The use of dca in coordination chemistry mainly rests on three relevant features: (i) a great coordinating ability which gives rise to very stable complexes with copper(II) ions, (ii) a multidentate character with the donor atoms properly positioned to enable the ligand to act as a bridge between metal centres and (iii) a long enough chain to warrant a suitable separation between the oxadiazolecopper(II) entities, minimising steric hindrance. In fact, dca is a very versatile ligand.[27–33] In our case, a μ-1,5 system is present (mode c in Scheme 6). Approximately 150 crystal structures of dicyanamidocopper(II) derivatives are known, the dimensionality of which ranges from monomers to 1D, 2D or 3D frameworks. As far as we are aware, 2D copper(II) compounds incorporating dca ligands are unusual .[34–40]

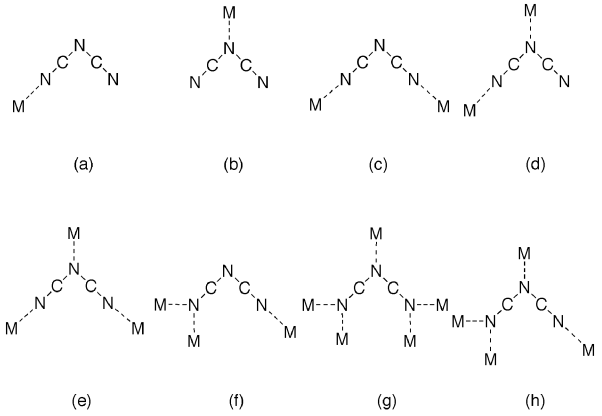

Scheme 6.

Features Which Are Common to All the Structures: Oxadiazole Ligands and Noncovalent Interactions

The N(1) and N(2) atoms in the free L^2 ligand exhibit a *syn* conformation with respect to the C(5)–C(6) bond.[6] In the same way, N(3) and C(8) are *syn* to the C(7)–N(4) linkage. This conformational behaviour is retained in the complexes, except in **5**, $[\{Cu(L^2)(H_2O)_2(SO_4)\}_2]\cdot 2H_2O$[6b] and $[Cu(L^2)(NCS)_2]_n$.[7b] In these compounds, the terminal methyl group flips, rendering the N(3) and C(8) atoms *anti*. The bidentate behaviour of the L^1 ligand enforces a *syn* conformation for N(1) and N(2) in all its complexes. The C–C and C–N bond lengths in these complexes are quite similar to those observed for the free L^2 ligand (the structure of L^1 is unknown). The most divergent parameters are given in Table S1. The dihedral angle between the pyridine and oxadiazole rings (δ) decrease on complexation which reveals that coordination induces high planarity in the ligand. In fact, maximum shifts from the pyridine plane correspond to the C(8) atoms which deviate by 0.245, 0.285 and 0.286 Å in **1**, **2** and **3**, respectively, 0.058 Å for N(4) in **4** and 0.071 Å for N(3) in **5**. The exception is compound **3** with a δ value greater than that observed in the free ligand which could be related to spatial requirements due to the largest Cu–N(2) bond length of the studied compounds. It must be also noticed that the C(5)–C(6)–N(2) angle decreases upon coordination. Detailed information about hydrogen bonds and π-π stacking interactions in these complexes is given in Tables S2–S5.

Spectroscopic Studies

An unequivocal assignment of the bands in the IR spectra of these compounds is a very difficult task due to the high electronic delocalisation, the existence of different configurations and conformations, the presence of hydrogen bonds, stacking and lattice influences and the effects of coordination and distortions. Notwithstanding this, we present here a tentative proposal for selected bands which is complementary to the assignments given in the Exp. Sect. for the coligands. Briefly, the following assignments have been made: absorptions around 3500–3100 cm^{-1} [$\nu(NH_2)$, ν(NH) and ν(OH) water modes], above 1650 cm^{-1} [$\nu(C{=}N)_{oxadiazole}$ and $\nu(C{=}N)_{pyridine}$], 1635–1300 cm^{-1} [$\delta(NH_2)$, $\nu(C{=}C)_{pyridine}$ together with $\delta(H_2O)$ vibrations and combinations of oxadiazole ν(CC/CN) and δ(NH/CH) modes], 1200–1000 cm^{-1} [combinations of C–O, C–N, C–H and N–H stretching and bending modes], 800–600 cm^{-1} [$\rho_s(CH_3)$, $\delta(CH)_{pyridine}$ and $\gamma(C{-}C{-}C/N)_{pyridine}$] and slightly higher than 415 cm^{-1} [$\gamma(CH)_{oop}$ modes]. The results suggest the coordination of the oxadiazole ligand in the title compounds is in good accordance with the crystal structures obtained. In the same way, the positions and shapes of the bands corresponding to the malonato and pseudohalide anions point to the linkage to the metal centre in all cases. In particular, the IR spectrum of compound **6** exhibits more dicyanamido bands than observed in **5**, suggesting the presence of dicyanamido ligands with different coordination modes in **6**. Finally, the spectrum of **7** is very similar to that reported for $[Cu(L^2)(NCS)_2]_n$[7b] which supports possible structural analogies.

The diffuse reflectance spectra of the oxadiazole complexes are characterised by the presence of bands in the 225–230 and 255–310 nm regions corresponding to intraligand $\pi\rightarrow\pi^*$ and $n\rightarrow\pi^*$ transitions, respectively (see Table 2). The bands observed in solid samples around 360–485 nm can be attributed to ligand-to-metal $N/O\rightarrow Cu^{II}$ charge transfer (LMCT) while those arising at 630–780 nm are characteristic of d→d transitions. It is worth mentioning the resemblances between the energies of the d→d bands in **3** and **4** which support the similarities in their distorted octahedral polyhedra. LMCT bands are usually absent in the UV/Vis spectra recorded in aqueous solutions of all these compounds probably because the LMCT transitions shift to higher energies thereby overlapping with the intense and broad intraligand absorptions.[7a] The highest energy absorptions in **1** and **2** are very similar to those found in $[\{Cu(L^2)(H_2O)_2(SO_4)\}_2]\cdot 2H_2O$.[6] However, d→d transitions are slightly shifted. This fact agrees with the conductivity measurements given in the Exp. Sect. suggesting that the coordination of the malonato ligand to the copper(II) ion is retained in solution while sulfate is liberated in $[\{Cu(L^2)(H_2O)_2(SO_4)\}_2]\cdot 2H_2O$ giving rise to a 1:1 electrolyte. In spite of the uncertainty inherent in interpreting the broad and weak d→d maxima, aqueous solutions of **3**, **5**, **6**, **7**, $[Cu(L^2)(NCS)_2]_n$ and $[\{Cu(L^2)(H_2O)_2(SO_4)\}_2]\cdot 2H_2O$ show the same spectra and 1:2 electrolyte character so that the existence of the same cationic entities in water after removing the pseudohalides can be proposed.

Table 2. UV-visible spectroscopic data: λ [nm], ε ($M^{-1}\,cm^{-1}$). Unpublished results of compound $[Cu(L^2)(NCS)_2]_n$[7b] are also included for comparison.

Compounds	Absorptions
1[a]	≈ 257 (sh), ≈ 360 (sh), ≈ 440 (sh), 686 (sh)
1[b]	226 (sh, 6000), 295 (14100), 728 (31)
2[b]	227 (sh, 6250), 297 (13550), ≈ 731 (30)
3[a]	228 (sh), 310 (sh), 386 (sh), 638 (sh)
3[b]	225 (sh, 12600), 296 (27500), ≈ 747 (b, 35)
$[Cu(L^2)(NCS)_2]_n$[a]	228 (sh), 307 (sh), 375 (sh), ≈ 471 (sh), 533 (sh), 667 (sh)
$[Cu(L^2)(NCS)_2]_n$[b]	225 (sh, 9100), 296 (14000), 759 (27)
4[a]	226 (sh), 307 (sh), ≈ 427 (sh), ≈ 483 (sh), ≈ 636 (sh)
5[b]	296 (14500), 763 (12)
6[b]	296 (13900), 764 (13)
7[b]	296 (11350), 769 (28)

[a] Solid. [b] In aqueous solution (6×10^{-5} M and 10^{-3} M).

The X-band EPR spectra on powdered samples of **4**, **7** and **8** are characteristic of a $d_{x^2-y^2}$ ground state orbital, due to both the shapes of the lines and the values of the *R* parameter. $R = (g_2 - g_3)/(g_1 - g_2)$ for $g_1 > g_2 > g_3$, $R > 1$ implies a d_{z^2} ground state, while *R* is < 1 for a $d_{x^2-y^2}$ state (Table 3, Figures S4–S10).[41] In the case of compounds **1** and **2**, axial EPR signals can be observed which leads to *G* values, $G = (g_\parallel - 2)/(g_\perp - 2)$, of 4.7 and 4.5, respectively, falling in the 3.5–5.0 region which predicts small exchange couplings and meaningful *g* values.[42] The latter are characteristic of $S = \frac{1}{2}$ systems with a $d_{x^2-y^2}$ ground state. The value of *G* for **1** points to possible magnetic exchange pathways through the Cu···O(2)^i bond or some of the hydrogen bonds. Compound **3** shows an axial-like pattern and different fits of the signal are possible. One of them is obtained through a rhombic symmetry introducing a hyperfine coupling constant $A_z = 163\times10^{-4}\,cm^{-1}$ (155 G) which corresponds to a partial resolution of the hyperfine structure of the parallel component. This fit agrees well with the structural results which indicate closest Cu···Cu distances of 8.5 Å indicating that the chromophores are relatively isolated. However, a broadening of g_1 due to the presence of exchange interactions between magnetically nonequivalent centres instead of hyperfine coupling cannot be completely disregarded. A broad asymmetric signal can be observed in **5** at room temperature the shape and intensity of which do not show appreciable changes upon lowering the tempera-

Table 3. Experimental EPR parameters.

Complex	g_1	g_2	g_3	*R*
1[a]	$g_\parallel$ = 2.282	$g_\perp$ = 2.060		0
2[a]	$g_\parallel$ = 2.291	$g_\perp$ = 2.065		0
3[a]	2.280	2.075	2.047	0.14
4[a]	$g_\parallel$ = 2.284	$g_\perp$ = 2.058		0
5[a]	2.210	2.180	2.050	4.33
6[a]	2.258	2.078	2.065	0.07
7[b]	$g_\parallel$ = 2.254	$g_\perp$ = 2.070		0
7[c]	2.257	2.076	2.062	0.08
8[a]	2.194	2.094	2.049	0.45

[a] No variation in the *g* values from room temperature to 120 K. [b] At room temperature. [c] At 120 K.

ture to 120 K. This aspect is reminiscent of an inverted-axial signal in spite of it being fitted as rhombic. The shape of the spectrum is characteristic of an exchange coupled system and, therefore, the parameters given in Table 3 for **5** probably do not reflect the molecular topology. Complex **6** also exhibits an apparent axial signal which is better resolved using a rhombic pattern and suggests the presence of magnetic interactions.

Magnetic Properties

Plots of the molar susceptibility (χ_m), together with the $\chi_m T$ vs. T curves for compounds **2** and **5** are given in Figure 8. The plot corresponding to complex **4** is characteristic of paramagnetic behaviour over the range of temperatures considered (Figure S11). The magnetic measurements obey the Curie–Weiss law at temperatures higher than 50 K and 100 K for **2** and **5**, respectively. The Weiss temperatures are +1.28 (**2**) and –13.09 K (**5**). The C_m experimental values are 0.43 and 0.40 $cm^3 K mol^{-1}$ and the calculated μ_{eff} values at room temperature are 1.86 and 1.76 BM for **2** and **5**, respectively. In the case of **5**, the χ_m values increase with decreasing temperature reaching a maximum at 50 K (0.045 $cm^3 mol^{-1}$) whilst the $\chi_m T$ value continuously decreases on lowering the temperature. These features indicate the presence of antiferromagnetic interactions in **5**. However, measurements on compound **2** are characteristic of ferromagnetic behaviour.

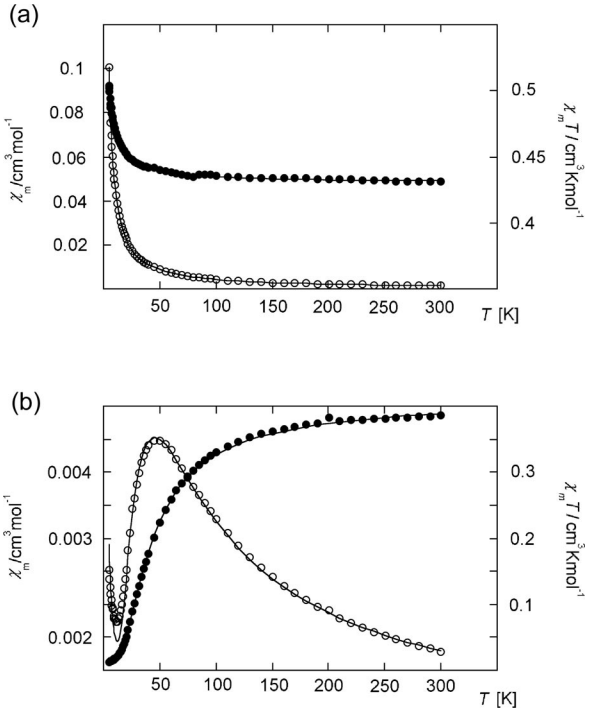

Figure 8. Thermal variation of the molar susceptibility (○○○) and $\chi_m T$ (●●●) for (a) **2** and (b) **5**. Solid lines represent the best fit.

Taking into account the structure of these complexes, we fitted the susceptibility data by the expression given by Bleaney and Bowers for copper(II) dinuclear compounds[43] that is derived from the Heisenberg isotropic spin Hamiltonian ($H = -2\,J\,S_1S_2$) for two coupled $S = ½$ ions.

$$\chi_m = \frac{Ng^2\beta^2}{kT}\left(\frac{2(1-\rho)}{\left(3+\exp\left(\frac{-2J}{kT}\right)\right)}+\frac{\rho}{2}\right)+N\alpha \quad (1)$$

In this formula we have considered the possibility of a certain amount of paramagnetic impurities (ρ) and temperature-independent paramagnetism (TIP, $N\alpha$) where N is Avogadro's number, β = the Bohr magneton and k = Boltzmann's constant. An $N\alpha$ value of 300×10^{-6} $cm^3 mol^{-1}$ per copper(II) ion was considered in the case of **2** and we had to take into account 3.5% of paramagnetic impurities in **5**. The best least-square fitting was obtained from the parameters J/k = +2.15(1) K (+1.49 cm^{-1}, **2**) and –38.3(3) K (–26.60 cm^{-1}, **5**). The calculated g values are 2.14(1) and 2.11(1) for **2** and **5**, respectively, values which are in good agreement with those of 2.14 (**2**) and 2.13 (**5**) obtained from EPR experiments. Calculations carried out using the molecular field approach to evaluate the influence of intermolecular exchange pathways did not improve the fittings.

Compound **2** is the first complex containing L^1/L^2 ligands that shows ferromagnetic interactions. This could be related to the role of the malonato ligand as a magnetic pathway between the copper(II) ions. This ligand is coordinated in an asymmetric fashion, as was pointed out in the structural section of this article. The existence of malonato basal-apical bridges (see Supporting Information, Scheme S1) prevents the overlapping of the $d_{x^2-y^2}$ magnetic orbitals and so reduces the antiferromagnetic contribution (J_{AF}) to the magnetic exchange ($J = J_{AF} + J_F$). This behaviour is relatively usual for other malonato-copper(II) dimeric derivatives, in particular those exhibiting a (monodentate + bidentate) chelating character and *syn-anti* carboxylato bridges. In the opposite way, *anti-anti* conformations give rise to antiferromagnetic interactions.[11] An analogous argument can explain the lack of appreciable magnetic interactions in **4** in which the magnetic coupling takes place through thiocyanato bridges almost perpendicular to the basal plane containing the magnetic $d_{x^2-y^2}$ orbitals. Several polynuclear copper(II) complexes containing N(basal)–S(axial) thiocyanate bridges exhibit very small or negligible J values.[7b,44]

The magnetic coupling observed in **5** can be attributed to intradimer interactions propagated through the oxadiazole moiety which give rise to Cu–N–N–Cu superexchange pathways. The role of the dicyanamido linkers is mainly structural in **5**, being nearly irrelevant in the propagation of the magnetic interactions. Indeed, most of the copper(II) complexes with dicyanamido bridges described in the literature show zero or weak antiferromagnetic[29,34] and ferromag-

netic[35] interactions. In a few examples, significant couplings can be observed due to the presence of good couplers such as pyrimidines,[30,39] pyrazines,[31] radicals[32,36] or others.[33,40]

Most of the published magnetic studies on 1,3,4-oxadiazolecopper(II) complexes describe systems where the metal ions are not coordinated to the oxadiazole moiety but only to the pyridine substituents (see Supporting Information, Scheme S2b). These latter compounds show Cu···Cu distances larger than in **5** (Scheme S2a) and $d_{x^2-y^2}$ magnetic orbitals perpendicular to the oxadiazole ligand. These features induce weak antiferromagnetic[4f,4j,4m] and ferromagnetic[4a] behaviour and even zero interactions.[4d,4h,4n] Some exceptional systems show strong antiferromagnetism which mainly propagates through the coligands (e.g. carboxylato, pseudohalide, bipyridine, etc.).[4f,4l] Thus, in the cases referenced, the actual influence of the oxadiazole ligand as a coupler between paramagnetic centres is almost negligible. The few compounds analogous to **5** where the oxadiazole ring itself acts as a bridge between the copper(II) ions show J values of –2.75 and –2.78 K (–1.91 and –1.93 cm^{-1}),[6b] values which are significantly lower than that in **5**. This can be due to an axial-to-equatorial orientation involving $d_{x^2-y^2}$ magnetic orbitals which corresponds to their elongated octahedral geometries (Scheme S3b). On the contrary, copper(II) ions in **5** exhibit a topology close to trigonal bipyramid and the d_{z^2} magnetic orbitals lie along the N1···N3 direction directly pointing to the oxadiazole bridges (Scheme S3a). The weak magnetic interactions in oxadiazole-copper(II) complexes contrast with the magnitude of those interactions in most analogous $Cu(NN)_2Cu'$ systems such as triazoles where $J \approx -90 - (-200)$ cm^{-1}.[45] In those cases, the copper(II) $d_{x^2-y^2}$ orbitals point directly to the nitrogen atoms of the heterocyclic ring giving rise to an appreciable overlap with the ligand orbitals thereby increasing the antiferromagnetic interactions. Notwithstanding this, compounds with structural distortions leading to weak antiferromagnetic[46] and even ferromagnetic[47] interactions have also been reported.

In order to gain the general scope of the magneto-structural relationships in compounds analogous to **5**, we have compared some structural parameters with the magnetic exchange constant (J) for several diazole-copper(II) dinuclear compounds[6,45a–d,48–63] containing $Cu(NN)_2Cu'$ fragments as the only bridges between the metal centres. The results are summarised in Table S6. A more complete list is given in Table S7. Some of the parameters used in these tables are depicted in Scheme 7.

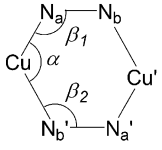

Scheme 7.

It has been proposed that, roughly speaking, antiferromagnetic interactions in $Cu(NN)_2Cu$ symmetric systems are more intense than those in asymmetric ones. Hanot et al.[49] have considered the difference between the Cu–N–N and Cu–N′–N′ angles ($\Delta\beta$) as a measure of the asymmetry in the $Cu(NN)_2Cu$ bridge. A plot of $\Delta\beta$ vs. J for all the complexes in Table S6 is given in Figure 9. One surprising structural feature is the existence of a $\Delta\beta$ gap in the 5–10° range, although some copper(I) complexes exhibit this difference in their CuNN angles.[64] Several compounds with $\Delta\beta > 2°$ indicate that the greater $\Delta\beta$ the weaker the antiferromagnetic interactions. The values for these complexes fall around a straight line ($J \approx -90 + 3\ \Delta\beta$; estimated maximum deviations of ± 10 cm^{-1}). For instance, it can be suggested for $\Delta\beta = 10°$ that J is at least –60 cm^{-1} or –50 cm^{-1} if we consider the deviations in the formula. Note that the predictive validity of this equation could imply the cancellation of the antiferromagnetic interactions at $\Delta\beta$ values above 30° and then paramagnetic or even ferromagnetic behaviour for these highly asymmetric systems. Unfortunately, a greater dispersion is observed for $\Delta\beta < 2°$ and J values bigger than |–100 cm^{-1}|. In such cases, we have not found a function to represent $\Delta\beta$ vs. J.

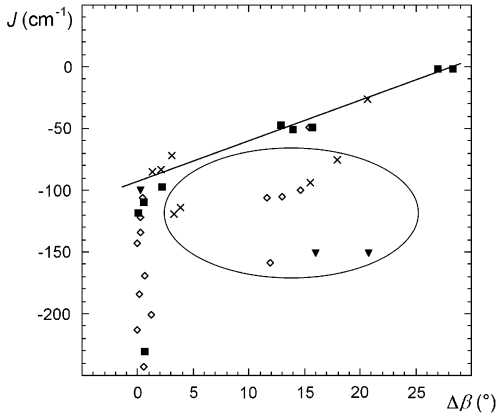

Figure 9. Relationships between $\Delta\beta$ and J for the compounds mentioned in Table S6. An ellipse frames those points which do not follow the general trend. Geometries: square-planar (▼), octahedral (■), square-pyramidal (✧) and trigonal bipyramidal (×).

All the octahedral $Cu(NN)_2Cu$ diazole complexes follow the trends mentioned before for the entire $\Delta\beta$ range, together with all the triazole and oxadiazole derivatives. This behaviour is also found in diazole-copper(II) complexes not shown in the Table S6[65] with only one exception.[66] However, the data for nine pyrazole derivatives fall out of the two-slope plot which represents the general trend. They show more intense antiferromagnetic interactions than those in the straight line. This fact could be due to an improvement of the superexchange interactions. Most of these nine complexes contain coordinating substituents linked to the pyrazole ring. Furthermore, they share some structural characteristics: (1) they have large and small β (CuNN) angles in the 135–140° and 120–125° ranges; (2) the most divergent compounds, e.g. $[\{Cu(bpzt)\}_2]\cdot 3H_2O$ and $[Cu(4\text{-mepzdoxim})Cl]_2\cdot 2H_2O$, exhibit α ($N_aCuN_{b'}$) angles between

97 and 99°, (CuN_aN_b)–($CuN_{a'}N_{b'}$) angles of 0°, pz−pz angles of 0° and CuN_2Cu'–$CuN_2'Cu'$ dihedral angles of 0°.

DFT calculations performed on imidazolate-bridged copper(II) complexes with $d_{x^2-y^2}$ magnetic orbitals[67] indicate that the greater the Cu–N–C(imidazole) angles the stronger the magnetic coupling. The β(Cu–N–N) angles for the compounds shown in Table S6 are in a range of 128–130° and induce very strong antiferromagnetism as observed for $[Cu(Smepz)(ClO_4)(CH_3OH)]_2$ and $[Cu(Smepz)(NO_3)]_2{\cdot}CH_3OH$ ($|-J| > 230\ cm^{-1}$). In the same way, β angles greater than 142° lead to relatively weak antiferromagnetic interactions ($|-J| < 30\ cm^{-1}$). Apart from these limits, a clear relationship between β and J is not observed. These results could be related to the δ vs. J relationship proposed by Hanot et al.[49] They considered an optimum Cu–N–N′ angle of 130.8° arising from structural and magnetic studies reported by Kamiusuki et al. for a diazole-bridged copper(II) compound with $J = -214\ cm^{-1}$.[65a]

$$\delta(CuNN) = ½\ (|CuNN - CuNN_{opt}| + |CuN'N' - CuNN_{opt}|) \quad (2)$$

Unfortunately, plots of δ vs. J for $CuNN_{opt}$ = 128, 129, 130 and 130.8° did not show any clear relationship. Other parameters and their combinations have been studied [e.g. N–Cu–N′, Cu–N–N–Cu′, (CuNN)−(CuNN)′, pz−pz, pz−(CuNNCu′) angles, etc.] but the results did not enable us to estimate their influence in the magnitude of the exchange constant (see Supporting Information).

Finally, it must be noted that the signs of the magnetic interactions in all the described [2-amino-5-(pyridin-2-yl)-1,3,4-oxadiazole]copper(II) complexes are consistent with a spin-polarisation model: J values are positive for Cu–O–C–O–Cu and negative for Cu–N–N–Cu pathways. It is difficult to evaluate the actual contribution of this mechanism to the exchange interaction in these systems. In fact, particular caution should be taken into account to avoid overestimation of the influence of this mechanism usually neglected in most of the magneto-structural discussions on analogous diazole and carboxylato systems. However, copper(II) compounds containing highly π-conjugated bis(3-pyridyl)-1,3,4-oxadiazole ligands and nonorthogonal magnetic orbitals also follow spin-polarisation mechanisms by the N–N oxadiazole route (even when both nitrogen atoms are not coordinated to the metal).

Nuclease Activity of the Complexes

The activity of the complexes **1**, **2**, **3**, **5** and $[Cu(L^2)_2(H_2O)_2](NO_3)_2$ as chemical nucleases has been studied using supercoiled pUC18 DNA in cacodylato buffer (pH 6.0) with mercaptopropionic acid and glutathione as reducing agents. The efficiencies of the complexes have been compared with that of the copper salt under the same conditions. If the compounds present nuclease activity then the DNA that appears initially as supercoiled plasmid (form I) will be converted into the nicked circular (form II) and/or linear (form III) forms through single-strand cleavage events.

Complexes **1**, **2** and $[Cu(L^2)_2(H_2O)_2](NO_3)_2$ exhibited high activity when we used mercaptopropionic acid (MPA) as a reducing agent (Figures 10 and 11). Complex **1** (Figure 10) and $[Cu(L^2)_2(H_2O)_2](NO_3)_2$ (Figure 11) at 12 μM (lanes 8) produced partial conversion of supercoiled DNA (form I) into its open circular form (form II). When the concentration was 18 μM or higher, the compounds induced complete degradation of the supercoiled form to yield circular (form II) and linear (form III) forms (lanes 9, 10 and 11). Form III resulted from multiple cleavage of form II and appeared only when full cleavage of form I was practically achieved. In contrast, the activity of complex **2** diminished when the complex concentration was increased.

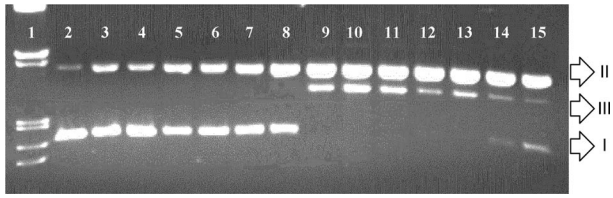

Figure 10. Agarose gel electrophoresis of pUC18 plasmid DNA treated with the copper salt or the complexes **1** and **2** and a 50-fold excess of mercaptopropionic acid. Incubation time 60 min (37 °C). Forms I, II and III are indicated. 1: λDNA/EcoR1+HindIII marker; 2: control; 3: pUC18 + mercaptopropionic acid; 4: $CuSO_4$ 12 μM; 5: $CuSO_4$ 18 μM; 6: $CuSO_4$ 24 μM; 7: $CuSO_4$ 30 μM; 8: complex **1** 12 μM; 9: complex **1** 18 μM; 10: complex **1** 24 μM; 11: complex **1** 30 μM; 12: complex **2** 12 μM; 13: complex **2** 18 μM; 14: complex **2** 24 μM; 15: complex **2** 30 μM.

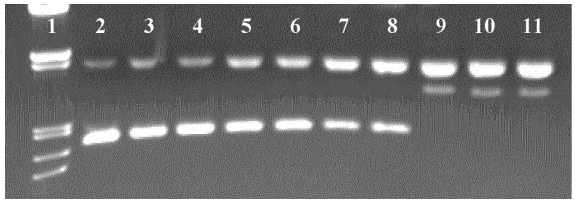

Figure 11. Agarose gel electrophoresis of pUC18 plasmid DNA treated with the copper salt or the complex $[Cu(L^2)_2(H_2O)_2](NO_3)_2$ and a 50-fold excess of mercaptopropionic acid. Incubation time was 60 min (37 °C). 1: λDNA/EcoR1+HindIII marker; 2: control; 3: pUC18 + mercaptopropionic acid; 4: $CuSO_4$ 12 μM; 5: $CuSO_4$ 18 μM; 6: $CuSO_4$ 24 μM; 7: $CuSO_4$ 30 μM; 8: complex $[Cu(L^2)_2(H_2O)_2](NO_3)_2$ 12 μM; 9: complex $[Cu(L^2)_2(H_2O)_2](NO_3)_2$ 18 μM; 10: complex $[Cu(L^2)_2(H_2O)_2](NO_3)_2$ 24 μM; 11: complex $[Cu(L^2)_2(H_2O)_2](NO_3)_2$ 30 μM.

The progression of the cleavage reaction with the increasing concentrations is given in lanes 12 to 15 of Figure 10. Complex **2** at 12 or 18 μM was able to cleave DNA to linear and nicked forms (lanes 12 and 13), at 24 μM and 30 μM the three forms are present (I, II and III) (lanes 14 and 15) and at 30 μM the amount of supercoiled material is higher. Little activity was observed for $CuSO_4$ under the same conditions (see lanes 5, 6 and 7). It is noteworthy that complex **2** exhibits less nuclease activity at higher concentrations. This is probably derived from the chelating activity of the thiol.[68] In the case of MPA, Veal et al.[69] have reported that the $Cu(phen)_2^+$ complex is less of a nuclease agent in the presence of MPA due to the competition between the chelating

ability of MPA and phen which gives rise to the ternary mixed $[Cu^{I}(phen)(MPA)_n]$ complex that exhibits only a little affinity for DNA. Results obtained with our compounds in the presence of mercaptopropionic acid are better than those reported in the literature[70,71] and similar to results for other complexes published previously by our group.[72]

Assays of the activities of the complexes **1**, **2** and $[Cu(L^2)_2(H_2O)_2](NO_3)_2$ using glutathione as the reducing agent show that the complexes display little activity under these conditions (data not shown). The difference between MPA and glutathione is remarkable taking into account the higher reducing potential of the latter (–0.262 V for the glutathione and –0.275 V for MPA). The higher ability as a chelating ligand for the glutathione with respect to MPA is probably the reason for this behaviour.[73] Complexes **3** and **5** were not able to cleave the DNA in the presence of MPA, glutathione or dithiothreitol (data not shown).

In order to know the complex species responsible of the nuclease activity, we carried out ESI experiments in aqueous solution. From these, we have deduced the presence of the following entities: $[Cu(L^2)(mal)(H_2O)]\cdot 2H_2O\cdot H_2OH^+$ (m/z^+ = 415) for compound **1**, $[Cu(L^2)(mal)(OH)]\cdot H_2OH^+$ (m/z^+ = 378) for **2** and $[Cu(L^2)(mal)(H_3O)]^+$ (m/z^+ = 361) and $[Cu(L^2)(mal)]^+$ (m/z^+ = 342) for both malonato complexes. In the case of the $[Cu(L^2)_2(H_2O)_2](NO_3)_2$ compound, we observed peaks corresponding to $[Cu(L^2)_2(H_2O)_2](NO_3)^+$ (m/z^+ = 513) and $[Cu(L^2)_2(OH)_2]\cdot H_2O^+$, ($m/z^+$ = 467). All these data, together with the UV/Vis spectra and the conductivity measurements, allow us to suggest that the oxadiazole and malonato ligands remain coordinated in aqueous solution.

The existence of diffusible radical species in the nuclease mechanism can be inferred by monitoring the quenching of DNA cleavage in the presence of alternative H-atom donors which would scavenge radicals in solution. To this end, a new electrophoresis study was carried out including standard scavengers of reactive oxygen intermediates. Figure 12 shows the results for complex **1**. The behaviour of the other two complexes is similar and is not shown for brevity.

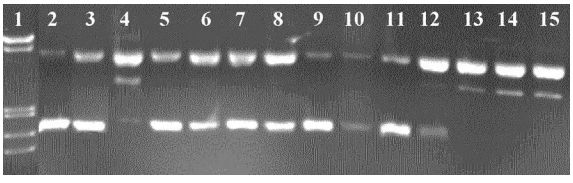

Figure 12. Agarose gel electrophoresis of pUC18 plasmid treated with complex **1** 30 μM and a 50-fold excess of mercaptopropionic acid in presence of potential inhibiting agents. 1: λDNA/EcoR1+HindIII Marker; 2: control (pUC18); 3: pUC18 + reducing agent; 4: complex; 5: complex + dmso (0.4 M); 6. complex + *tert*-butyl alcohol (0.4 M); 7: complex + sodium formate (0.4 M); 8: complex + potassium iodide (0.4 M); 9: complex + NaN_3 (100 mM); 10: complex + 2,2,6,6 tetramethylpiperidone (100 mM); 11: complex + tiron (10 mM); 12: complex + SOD (15 units); 13: complex + neocuproine (1 mM); 14. complex + distamycin (8 μM); 15: complex + methyl green (2.5 μL of a 0.01 mg mL^{-1} solution).

The presence of the hydroxyl radical scavengers DMSO, *tert*-butyl alcohol, sodium formate and potassium iodide (lanes 5, 6, 7 and 8 of Figure 12) significantly inhibits the chemical nuclease activity of the complexes. We can therefore suggest a cleavage pathway involving the formation of the reactive hydroxyl radical. Sodium azide and 2,2,6,6-tetramethylpiperidone (lanes 9 and 10) inhibit, to the same extent, DNA cleavage by the compounds indicating the participation of singlet oxygen-like entities in the reaction. Lanes 11 and 12 show a significant reduction of the DNA cleavage of the complexes in the presence of tiron and SOD (superoxide dismutase enzyme) which indicates that the O_2^- anion is one of the reactive species that actually breaks the DNA. The presence of neocuproine produces little reduction of DNA strand scission mediated by the complex (lane 13). This is probably due to the competition between the chelating ability of the phen, the oxadiazole ligands and MPA. The presence of a minor groove binder, distamycin does not produce an important inhibition of the DNA damage for the complex (lane 14). In the presence of the major groove binder, methyl green (lane 15), no apparent inhibition of DNA damage was observed, suggesting that there are no major binding preferences for the complexes.

These studies reveal possible involvement of hydroxyl radical and/or copper bound oxo/hydroxo-like singlet oxygen species[74,75] in the oxidative cleavage of DNA in the presence of MPA. All the results lead us to propose, not the mechanisms, but the pathways or sequential events by which the DNA cleavage by the complexes takes place (Scheme 8).

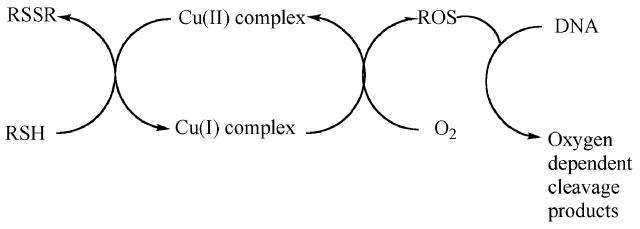

Scheme 8.

Conclusions

The composition, structures and properties of some oxadiazole-copper(II) compounds can be drastically modified by means of an appropriate selection of the ligands and some experimental parameters such as the ratio of the starting materials, reaction time, pH and solvent. In this sense, the use of good spacers as coligands (e.g. dca), long reaction times and nonaqueous solvents (DMF in **2**) seem to increase the nuclearity/dimensionality of these systems. Thus, a great variety of structural arrangements can be obtained ranging from monomers to 2D complexes. The planarity of the oxadiazole ligands gives rise to π–π stacking interactions which stabilise the crystal structures together with the hydrogen bonding. The latter can order the solvent molecules to form cyclic water tetramers in **1**.

Moderate antiferromagnetic interactions are present in compound **5**, in good accordance with the orientation of

the d_{z^2} magnetic orbitals. A comparison with other bis(diazole)-bridged copper(II) compounds shows that the magnitude of the magnetic exchange interaction constant (*J*) mainly depends on the difference between the Cu–N–N and Cu–N′–N′ angles (the so called $\Delta\beta$ parameter): the greater $\Delta\beta$, the smaller *J*. On the other hand, the malonato derivative **2** exhibits ferromagnetic behaviour while the separation and position of the orbitals lead to paramagnetism in **4**.

Complexes **1**, **2** and $[Cu(L^2)_2(H_2O)_2](NO_3)_2$ exhibited high activity when we used mercaptopropionic acid as a reducing agent. The involvement of the hydroxyl radical and/or copper bound oxo/hydroxo-like singlet oxygen species in the oxidative cleavage of DNA in the presence of mercaptopropionic acid has been shown.

Experimental Section

Materials: Copper(II) sulfate pentahydrate, copper(II) nitrate trihydrate, copper(II) perchlorate hexahydrate, sodium hydroxide, malonic acid, potassium cyanate, potassium thiocyanate, sodium azide, sodium dicyanamide, *N*,*N*-dimethylformamide (DMF) and ethanol were purchased from commercial sources and used as received. Published methods were employed to synthesise $L^2{\cdot}3H_2O$,[6] $[Cu(L^2)_2(H_2O)_2](NO_3)_2$,[7a] $[\{Cu(L^2)(H_2O)_2(SO_4)\}_2]{\cdot}2H_2O$[6] and $[\{Cu(L^1)(H_2O)_3\}_2](SO_4)_2$.[6b] All operations should be carried out in a fume cupboard.

CAUTION: Perchlorate and azide salts and their respective metal complexes can be explosive. Although we have not experienced any accidents following the methods described below, it is strongly recommended to handle only small amounts of these salts.

Preparation of the Compounds

Compound 1: A suspension obtained from the reaction of $CuSO_4{\cdot}5H_2O$ (0.100 g, 0.40 mmol) with an aqueous solution of malonic acid (0.080 g, 0.80 mmol) adjusted to pH ≈ 8 by addition of NaOH was poured into a solution of the $[\{Cu(L^2)(H_2O)_2(SO_4)\}_2]{\cdot}2H_2O$ complex (0.156 g, 0.20 mmol) in distilled water (40 mL). The resultant turquoise solution was stirred at room temperature for 1 h and filtered. Two months later, slow evaporation of the mother liquor had yielded blue crystals of **1** suitable for X-ray diffraction measurements (yield 0.055 g, 35%). $C_{11}H_{16}CuN_4O_8$ (395.82): calcd. C 33.4, H 4.1, N 14.2; found C 32.9, H 4.0, N 13.9. Molar conductivity of 5×10^{-4} M solutions in water (DMF) at 25 °C: Λ_M = 27 (not soluble) $\Omega^{-1}cm^2mol^{-1}$. IR (KBr pellet): $\tilde{\nu}$ = 3391 (br. m), 3220 (m), 3054 (w), 2920 (w), 2816 (w), 1666 (vs); $\tilde{\nu}(OCO)_{as}$ = 1614 (vs), 1576 (vs), 1493 (w); $\tilde{\nu}(OCO)_s$ = 1433 (s) and 1369 (w), 1400 (m), 1330 (w), 1160 (m), 1113 (w), 1080 (m), 1020 (w), 966 (m), 819 (w), 810 (m); δ (OCO) = 753 (w) and 700 (w), 725 (m), 680 (m) cm^{-1}.

Compound 2: Three solutions containing $Cu(NO_3)_2{\cdot}3H_2O$ (0.097 g, 0.4 mmol), $L^2{\cdot}3H_2O$ (0.090 g, 0.40 mmol) and malonic acid (0.080 g, 0.80 mmol), were separately prepared using DMF (7–8 mL). Next, the malonic solution was added with stirring to the copper(II) solution and, immediately, the oxadiazole ligand was added too. Some minutes later, 2 drops of NaOH 5 M were added and small amounts of a blue precipitate were filtered off. The green solution was kept for slow evaporation at room temperature. Two weeks later, green crystals of **2** were collected (yield 0.048 g, 35%). $C_{11}H_{10}CuN_4O_5$ (341.77): calcd. C 38.7, H 3.0, N 16.4; found C 38.8, H 3.1, N 16.6. Molar conductivity of 5×10^{-4} M solutions in water (DMF) at 25 °C: Λ_M = 17 (not soluble) $\Omega^{-1}cm^2mol^{-1}$. IR (KBr pellet): $\tilde{\nu}$ = 3425 (b,w), 3039 (w), 3008 (w), 2903 (w), 2790 (w), 1666 (vs), $\tilde{\nu}(OCO)_{as}$ = 1608 (vs). and 1580 (vs), 1486 (w), $\tilde{\nu}(OCO)_s$ = 1451 (w) and 1422 (vs) and 1340 (w), 1405 (vs), 1322 (m), 1300 (m), 1273 (m), 1257 (m), 1166 (m), 1137 (m), 1060 (m), 1048 (m), 1017 (m), 966 (w), 942 (w), 933 (w), 813 (m), $\tilde{\nu}$ (OCO) = 769 (w) and 700–690 (w), 723 (m), 700 (m), 680 (m) cm^{-1}.

Compound 3: Two aqueous solutions containing KNCS (0.039 g, 0.40 mmol) and $[\{Cu(L^2)(H_2O)_2(SO_4)\}_2]{\cdot}2H_2O$ (0.078 g, 0.10 mmol) were mixed together. The reaction was stirred for 1 h and then **3** was filtered off as a green precipitate (yield 0.017 g, 32%). This procedure is almost the same used for the attainment of $[Cu(L^2)(NCS)_2]_n$[7b] the only difference being the reaction time of 5 h for $[Cu(L^2)(NCS)_2]_n$. A week after slow evaporation of the mother liquor, single crystals of both **3** and $[Cu(L^2)(NCS)_2]_n$ were obtained. $C_{18}H_{16}CuN_{10}O_2S_2$ (532.07): calcd. C 40.6, H 3.0, N 26.3, S 12.0; found C 40.2, H 3.1, N 25.9, S 12.1. Molar conductivity of 5×10^{-4} M solutions in water (DMF) at 25 °C: Λ_M = 187 (42) $\Omega^{-1}cm^2mol^{-1}$. IR (KBr pellet): $\tilde{\nu}$ = 3330 (br. m), $\tilde{\nu}(NCS)_{as}$ = 2102 (vs), 1649 (vs, sh), 1611 (s), 1573 (m), 1550 (m), 1416 (s), 1433 (m), 1366 (m), 1289 (w), 1272 (w), 1255 (m), 1156 (m), 1086 (m), 1041 (s), 1023 (m), 950 (w), 783 (m), 750 (w), 730 (m), 706 (w), 680 (m), 430 (m) cm^{-1}.

Compound 4: A solution with an excess of KNCS (0.080 g, 0.80 mmol) in a minimum volume of water was added to an aqueous solution of $[\{Cu(L^1)(H_2O)_3\}_2](SO_4)_2$ (0.075 g, 0.10 mmol) and the mixture was stirred for 1 h. A light-green solid of **4** was then filtered off, washed with cold water and dried (yield 0.036 g, 53%). An excess of pseudohalide is necessary because of the high solubility of **4** in water. $C_9H_6CuN_6OS_2$ (341.86): calcd. C 31.6, H 1.8, N 24.6, S 18.8; found C 31.2, H 1.9, N 24.9, S 18.9. Molar conductivity of 5×10^{-4} M solutions in water (DMF) at 25 °C: Λ_M = 288 (51) $\Omega^{-1}cm^2mol^{-1}$. IR (KBr pellet): $\tilde{\nu}$ = 3336 (m,b), 3246 (m), 3093 (m,b), $\tilde{\nu}(NCS)_{as}$ = 2129 (vs) and 2108 (vs), 1672 (vs), 1623 (m), 1560 (s), 1496 (m), 1431 (s), 1346 (m), 1300 (m), 1266 (m), 1124 (s), 1050 (w), 1016 (m), 786 (m), 726 (m), 702 (w), 683 (m), 496 (w) cm^{-1}.

Compound 5: A solution of sodium dicyanamide (0.180 g, 2.00 mmol) in water (10 mL) was added to an aqueous solution of $Cu(ClO_4)_2{\cdot}6H_2O$ (0.185 g, 0.50 mmol) in the minimum volume of solvent. A few minutes later, a solution of L^2 (0.090 g, 0.50 mmol) in ethanol (10 mL) was poured over the mixture and the blue solution became green. The reaction was maintained with stirring for 2 h and then filtered. After a day, green crystals of **5** were collected (yield 0.085 g, 40%). $C_{10}H_{10}ClCuN_7O_6$ (423.24): calcd. C 28.4, H 2.4, N 23.2; found C 28.3, H 2.2, N 23.7. Molar conductivity of 5×10^{-4} M solutions in water (DMF) at 25 °C: Λ_M = 186 (117) $\Omega^{-1}cm^2mol^{-1}$. IR (KBr pellet): $\tilde{\nu}$ = 3511 (sh,b,m), 3103 (m), [$\tilde{\nu}(C{\equiv}N)_{as}$ + $\tilde{\nu}(C{\equiv}N)_s$] = 2351 (m), $\tilde{\nu}(C{\equiv}N)_{as}$ = 2270 (s), $\tilde{\nu}(C{\equiv}N)_s$ = 2205 (vs, br.), 1688 (vs), 1631 (s), 1583 (s), 1403 (m), 1344 (w), 1302 (w), 1269 (w), 1163 (sh, s), $\tilde{\nu}_3(ClO_4)$ = 1108 (vs), 1012 (m), $\tilde{\nu}(C–N)_s$ = 969 (w), 930 (w), 927 (w), 788 (w), 780 (w), 722 (sh, s), 677 (w), 624 (s), 590 (w), 510 (w), 460 (w), 430 (w) cm^{-1}.

Compound 6: The procedure is analogous to the previous one but utilises $CuSO_4{\cdot}5H_2O$ (0.120 g, 0.50 mmol) instead of $Cu(ClO_4)_2{\cdot}6H_2O$ (yield 0.112 g, 60%). Sometimes, the last two syntheses concerning dicyanamide derivatives gave rise to white precipitates that had to be removed. In several attempts, cocrystallisation of **5** and **6** was achieved from a given solution. Unfortunately, however, we have not been able to obtain good quality single crystals of **6** suitable for X-ray structural analysis. $C_{12}H_{10}CuN_{10}O_2$ (373.82): calcd. C 37.0, H 2.6, N 35.9; found C 36.2, H 2.4, N 35.8. Molar conductivity of 5×10^{-4} M solutions in water (DMF) at 25 °C: Λ_M = 201

(107) $\Omega^{-1}cm^2mol^{-1}$. IR (KBr pellet): $\tilde{\nu}$ = 3377 (m), 3226 (w), 3132 (w), 2992 (w), 2923 (w), [$\tilde{\nu}$ $(C\equiv N)_{as}$ + $\tilde{\nu}$ $(C\equiv N)_s$] = 2308 (m), $\tilde{\nu}$ $(C\equiv N)_{as}$ = 2243 s, $\tilde{\nu}$ $(C\equiv N)_s$ = 2190 (vs) and 2183 (vs, sh) and 2168 vs, 1676 s, 1668 s, 1572 m, 1556 w, 1486 w, 1416 m, 1397 w, 1385 w, 1276 w, 1257 w, 1151 m, 1112 (w), 1090 (w), 1073 (w), 1047 (w), 1020 (w), $\tilde{\nu}$ $(C–N)_s$ = 945 (w), 786 (w), 767 (w), 747 (w), 724 (w), 673 (w), 638 (w), 515 (w), 446 (w) cm^{-1}.

Compound 7: A green solution of $[\{Cu(L^2)(H_2O)_2(SO_4)\}_2]\cdot 2H_2O$ (0.078 g, 0.10 mmol) in water (40 mL) was placed in an ice-bath and an aqueous solution of KCNO (0.096 g, 1.20 mmol) was slowly added dropwise (10 mL). Once the colour of the solution turned greenish-blue the pH of the reaction was adjusted to 5 and maintained around this value.[76] Ten minutes later, a light green precipitate of **7** appeared which was filtered off, washed with water and dried (0.030 g, 47%). $C_{10}H_8CuN_6O_3$ (323.76): calcd. C 37.1, H 2.5, N 26.0; found C 37.5, H 2.7, N 25.2. IR (KBr pellet): $\tilde{\nu}$ = 3496 (m,b), 3430 (m, br.), 3275 (sh, m), 3066 (w), $\tilde{\nu}$ $(NCO)_{as}$ = 2221 (vs) and 2172 (vs), 1661 (vs), 1622 (m), 1573 (w), 1555 (w), 1416 (m), 1401 (m), 1338 (w), 1297 (w), $\tilde{\nu}$ $(CO)_{pseudosym}$ = 1276 (w) and 1256 (w), 1152 (m), 1137 (w), 1102 (w), 1063 (m), 1017 (w), 933 (w), 791 (m), 728 (w), 617 (w), 604 (w) cm^{-1}.

Compound 8: A solution of NaN_3 (0.020 g, 0.30 mmol) dissolved in the minimum volume of water was slowly added to a solution of $[Cu(L^2)_2(H_2O)_2](NO_3)_2$ (0.086 g, 0.15 mmol) in water (20 mL). A yellowish-green solid immediately appeared. After 1 h the precipitate was filtered off, washed with water and dried (yield 0.040 g, 50%).[77] $C_{16}H_{20}CuN_{14}O_4$ (535.98): calcd. C 35.9, H 3.8, N 36.6; found C 35.5, H 3.8, N 36.4. Molar conductivity of 5×10^{-4} M solutions in water (DMF) at 25 °C: Λ_M = not soluble (8) $\Omega^{-1}cm^2mol^{-1}$. IR (KBr pellet): $\tilde{\nu}$ = 3307 (m, br.), 323 (m,b), 3144 (w), 3027 (m), $\tilde{\nu}$ $(NNN)_{as}$ = 2036 (vs), 1654 (vs, sh), 1610 (m), 1550 (m), 1483 (m), 1421 (s), 1366 (m), 1293 (w), 1161 (m), 1150 (m), 1041 (m), 1025 (m), 784 (m), 750 (m), 730 (m), 613 (w), 569 (w) cm^{-1}.

Physical Measurements: Microanalyses were performed with a LECO CHNS-932 analyser. Conductivity and pH measurements were made using a CRISON 522 conductimeter and a CRISON micropH 2002 instrument, respectively. IR spectra were recorded on samples prepared as KBr pellets in the 400–4000 cm^{-1} region on a Nicolett Impact 410 FTIR spectrophotometer. Reflectance spectra were measured on a Cary 2415 spectrometer in the 200–2000 nm range. For UV/Vis solution measurements, a Varian UV/Vis/NIR spectrophotometer was employed (200–900 nm). X-band EPR spectra were recorded on a Bruker EMX spectrometer, equipped with a standard Oxford continuous-flow cryostat. Magnetic measurements of powdered samples were carried out in the temperature range 5–300 K using a Quantum Design MPMS-7 SQUID magnetometer and operating with a magnetic field of 0.5 T. Diamagnetic corrections were estimated from Pascal tables. ESI mass (+ mode) analyses were performed on a Bruker Esquire 3000 plus LC-MS system.

X-ray Crystallographic Studies: Crystal data collections were carried out using a Bruker Smart CCD area detector equipped single crystal diffractometer. Absorption corrections were made using the SADABS program.[78] Direct methods (SHELXS-97)[79] were employed to solve the structures which were then refined by full-matrix least-squares methods using the SHELXL-97 computer program.[80] All non-hydrogen atoms were assigned anisotropic thermal parameters. Nearly all the hydrogen positions were determined by difference Fourier syntheses and introduced in calculations using the riding model. However, some hydrogen atoms were refined isotropically: H10D, H10C, H11A, H11B, H12A and H12B in **1**, all the hydrogen atoms in **2**, H1, H2, H3, H4A and H4B in **3** and H4N in **5**. The scattering factors and anomalous dispersion coefficients were taken from the International Tables of X-ray Crystallography.[81] Refinements were made on F_0^2 for all reflections. Crystallographic details for the five crystal structures are shown in Table 4.

CCDC-685580 (for **1**), -685581 (for **2**), -685582 (for **3**), -685583 (for **4**), -685584 (for **5**) contain the supplementary crystallographic data for this paper. These data can be obtained free of charge from The Cambridge Crystallographic Data Centre via www.ccdc.cam.ac.uk/data_request/cif.

pUC18 DNA Cleavage: Reactions were undertaken by mixing cacodylate buffer (pH 6.0, 7 μL of 0.1 M), pUC18 (0.25 $\mu g\mu L^{-1}$, 1 μL),

Table 4. Crystallographic data for compounds **1**–**5**.

	1	**2**	**3**	**4**	**5**
Formula	$C_{11}H_{16}CuN_4O_8$	$C_{11}H_{10}CuN_4O_5$	$C_{18}H_{16}CuN_{10}O_2S_2$	$C_9H_6CuN_6OS_2$	$C_{10}H_{10}ClCuN_7O_6$
M	395.82	341.77	532.07	341.86	423.24
System	triclinic	triclinic	monoclinic	triclinic	monoclinic
Space group	$P\bar{1}$	$P\bar{1}$	$P2_1/n$	$P\bar{1}$	$P2_1/n$
a [Å]	7.7590(17)	8.077(1)	8.8312(7)	8.4678(13)	8.1852(6)
b [Å]	10.2410(19)	8.725(1)	8.5018(7)	8.8856(10)	14.7701(11)
c [Å]	10.8851(18)	10.271(1)	15.7679(13)	9.6090(14)	14.1703(10)
α [°]	93.425(19)	65.629(1)	90	80.691(11)	90
β [°]	104.948(18)	85.031(1)	104.013(1)	69.057(14)	106.469(7)
γ [°]	111.486(14)	68.466(1)	90	74.066(12)	90
V [Å^3]	766.1(3)	611.52(9)	1148.64(16)	647.66(16)	1642.9(2)
Z	2	2	2	2	4
D_c [g cm^{-3}]	1.716	1.856	1.538	1.753	1.711
μ [mm^{-1}]	1.476	1.816	1.170	2.008	1.537
F_{000}	406	346	542	342	852
2θ range [°]	2–25	2–28	2–26	3–24	3–24
Measured reflections	7446	3967	6494	3773	9358
Independent reflections	2687	2792	2344	1965	2504
GOF	1.175	1.053	1.057	0.977	0.908
R_1	0.0367	0.0335	0.0330	0.0347	0.1123
$R_1[I > 2\sigma(I)]$	0.0328	0.0290	0.0269	0.0293	0.0466
wR_2	0.1064	0.0784	0.0776	0.0724	0.0850
$wR_2[I > 2\sigma(I)]$	0.0941	0.0757	0.0738	0.0705	0.0700

a solution of the test complex at increasing concentrations (6 μL) to obtain final concentrations between 12 μM and 30 μM and reducing agent (mercaptopropionic acid or glutathione, 6 μL) in cacodylate buffer. The mixtures were allowed to stand for 60 min at 37 °C after which a loading buffer solution consisting of 0.25% bromophenol blue, 0.25% xylene cyanole and 30% glycerol was added (3 μL). The solution was then subjected to electrophoresis on a 0.8% agarose gel in 0.5 × TBE buffer (0.045 M tris, 0.045 M boric acid and 1 mM EDTA) containing a solution of ethidium bromide (10 mg mL^{-1}, 2 μL 100 mL^{-1}) at 80 V for about 2 h. The gel was photographed on a capturing gel printer plus TDI.

To test for the presence of reactive oxygen species (ROS) generated during strand scission, reactive oxygen intermediate scavengers were added alternatively to the reaction mixtures. These scavengers were DMSO (0.4 M), *tert*-butyl alcohol (0.4 M), sodium formate (0.4 M), potassium iodide (0.4 M), sodium azide (100 mM), 2,2,6,6-tetramethyl-4-piperidone (100 mM), tiron (10 mM) and SOD (15 units). Assays in the presence of the minor groove binder distamycin (8 μM), the major groove binder methyl green (2.5 μL of a 0.01 mg mL^{-1} solution) or the stabiliser of copper(I) forms (neocuproine 1 mM) were also performed. Samples were treated as described above.

Supporting Information (see footnote on the first page of this article): Perspective views, selected structural parameters to compare L^1 and L^2 derivatives, tables of hydrogen bonds and π−π stacking parameters, EPR spectra, molar magnetic susceptibility vs. temperature data for compound **4** and structural parameters used to analyse the magneto-structural correlations in bisdiazole-copper(II) systems.

Acknowledgments

We thank Dr. J. J. Delgado (SCAI, Universidad de Burgos, Spain) for the elemental analyses and Prof. R. Olazcuaga and Dr. F. Guillen (CNRS, Pessac, France) for the reflectance measurements. This work was financially supported by the Junta de Castilla y León (BU033A06) and Ministerio de Ciencia y Tecnología (MCYT) [CTQ2007-63690 (ERDF(EU)-DGI-MCYT)]. P. G.-S. thanks the Universidad de Burgos for a Doctoral Fellowship.

[1] a) J. F. Wang, G. E. Jabbour, E. A. Mash, J. Anderson, Y. Zhang, P. A. Lee, N. R. Armstrong, N. Peyhgambarian, B. Kippelen, *Adv. Mater.* **1999**, *11*, 1266–1269; b) J. Wang, R. Wang, J. Yang, Z. Zheng, M. D. Carducci, T. Cayou, N. Peyhgambarian, G. E. Jabbour, *J. Am. Chem. Soc.* **2001**, *123*, 6179–6180; c) C. Wang, A. S. Batsanov, M. R. Bryce, *Chem. Commun.* **2004**, 578–579; d) A. Van Dijken, J. J. A. M. Bastiaansen, N. M. M. Kiggen, B. M. W. Langeveld, C. Rothe, A. Monkman, I. Bach, P. Stössel, K. Brunner, *J. Am. Chem. Soc.* **2004**, *126*, 7718–7727; e) S.-H. Jin, M.-Y. Kim, J. Y. Kim, K. Lee, Y.-S. Gal, *J. Am. Chem. Soc.* **2004**, *126*, 2474–2480; f) A. S. Fisyuk, R. Demadrille, C. Querner, M. Zargorska, J. Bleuse, A. Pron, *New J. Chem.* **2005**, *29*, 707–713; g) C. Wang, L.-O. Palsson, A. S. Batsanov, M. R. Bryce, *J. Am. Chem. Soc.* **2006**, *128*, 3789–3799; h) X.-b. Zhang, B.-c. Tang, P. Zhang, M. Li, W.-j. Tian, *J. Mol. Struct.* **2007**, *846*, 55–64; i) F. Emmerling, I. Orgzall, G. Reck, B. Dietzel, B. W. Schulz, G. Reck, B. Schulz, *J. Mol. Struct.* **2007**, *832*, 124–131; j) L. Chen, H. You, C. Yang, D. Ma, J. Qin, *Chem. Commun.* **2007**, 1352–1354; k) K. Ersmark, M. Nervall, E. Hamelink, L. K. Janka, J. C. Clemente, B. M. Dunn, M. J. Blackman, B. Samuelsson, J. Åqvist, A. Hallberg, *J. Med. Chem.* **2005**, *48*, 6090–6106; l) F. A. Omar, N. M. Mahfouz, M. A. Rahman, *Eur. J. Med. Chem.* **1996**, *31*, 819–825; m) S. G. Küçükgüzel, I. Küçükgüzel, E. Tatar, S. Rollas, F. Sahin, M. Güllüce, E. De Clercq, L. Kabasakal, *Eur. J. Med. Chem.* **2007**, *42*, 893–901; n) G. Navarrete-Vázquez, G. M. Molina-Salinas, Z. V. Duarte-Fajardo, J. Vargas-Villarreal, S. Estrada-Soto, F. González-Salazar, E. Hernández-Núñez, S. Said-Fernández, *Bioorg. Med. Chem.* **2007**, *15*, 5502–5508; o) T. Sakamoto, M. D. Cullen, T. L. Hartman, K. M. Watson, R. W. Buckheit, C. Pannecouque, E. De Clercq, M. Cushman, *J. Med. Chem.* **2007**, *50*, 3314–3321; p) Y.-P. Luo, G.-F. Yang, *Bioorg. Med. Chem.* **2007**, *15*, 1716–1724; q) X. Zou, Z. Zhang, G. Jin, *J. Chem. Res. (S)* **2002**, 228–230; r) H.-Z. Zhang, S. Kasibhatla, J. Kuemmerle, W. Kemnitzer, K. Ollis-Mason, L. Qiu, C. Crogan-Grundy, B. Tseng, J. Drewe, S. X. Cai, *J. Med. Chem.* **2005**, *48*, 5215–5223.

[2] Y.-B. Dong, T. Sun, J.-P. Ma, X.-X. Zhao, R.-Q. Huang, *Inorg. Chem.* **2006**, *45*, 10613–10628.

[3] C. Incarvito, A. L. Rheingold, C. J. Qin, A. L. Gavrilova, B. Bosnich, *Inorg. Chem.* **2001**, *40*, 1386–1390.

[4] a) X.-H. Bu, H. Liu, M. Du, L. Zhang, Y.-M. Guo, M. Shionoya, J. Ribas, *Inorg. Chem.* **2002**, *41*, 1855–1861; b) Y.-B. Dong, J.-P. Ma, M. D. Smith, R.-Q. Huang, B. Tang, D. Chen, H.-C. zur Loye, *Solid State Sci.* **2002**, *4*, 1313–1320; c) Y.-B. Dong, J.-P. Ma, R.-Q. Huang, F.-Z. Liang, M. D. Smith, *Dalton Trans.* **2003**, 1472–1479; d) M. Du, X.-H. Bu, Y.-M. Guo, H. Liu, S. R. Batten, J. Ribas, T. C. W. Mak, *Inorg. Chem.* **2002**, *41*, 4904–4908; e) M. Du, S.-T. Chen, X.-H. Bu, J. Ribas, *Inorg. Chem. Commun.* **2002**, *5*, 1003–1006; f) M. Du, X.-H. Bu, Z. Huang, S.-T. Chen, Y.-M. Gu, C. Diaz, J. Ribas, *Inorg. Chem.* **2003**, *42*, 552–559; g) M. Du, C. K. Lam, X. H. Bu, T. C. W. Mak, *Inorg. Chem. Commun.* **2004**, *7*, 315–318; h) M. Du, Y.-M. Guo, S.-T. Chen, X.-H. Bu, S. R. Batten, J. Ribas, S. Kitagawa, *Inorg. Chem.* **2004**, *43*, 1287–1293; i) M. Du, X.-J. Zhao, J.-H. Guo, *Inorg. Chem. Commun.* **2005**, *8*, 1–5; j) M. Du, X.-J. Jiang, X.-J. Zhao, H. Cai, J. Ribas, *Eur. J. Inorg. Chem.* **2006**, 1245–1254; k) A. Gueddi, B. Mernari, M. Giorgi, M. Pierrot, *Acta Crystallogr., Sect. C* **2000**, *56*, e426-e428; l) H. Hou, L. Xie, G. Li, T. Ge, Y. Fan, Y. Zhu, *New J. Chem.* **2004**, *28*, 191–199; m) Z. Huang, H.-B. Song, M. Du, S.-T. Chen, X.-H. Bu, *Inorg. Chem.* **2004**, *43*, 931–944; n) M. Lagrenee, S. Sueur, J. P. Wignacourt, B. Mernari, A. Boukhan, *J. Chim. Phys.* **1991**, *88*, 2075–2082; o) J.-P. Ma, Y.-B. Dong, R.-Q. Huang, M. D. Smith, C.-Y. Su, *Inorg. Chem.* **2005**, *44*, 6143–6145; p) P. Wang, Y.-B. Dong, J.-P. Ma, R.-Q. Huang, M. D. Smith, *Inorg. Chem. Commun.* **2005**, *8*, 596–599; q) J. P. Wignacourt, S. Sueur, M. Lagrenée, *Acta Crystallogr., Sect. C* **1990**, *46*, 394–396.

[5] a) H. Singh, V. K. Srivastava, S. N. Shukla, M. K. Srivastava, M. K. Upahyay, *Indian J. Chem. Sect. A* **1994**, *33*, 350–353; b) L. Mishra, V. K. Singh, *Synth. React. Inorg. Met.-Org. Chem.* **1994**, *24*, 95–115; c) , K. H. Al-Obaidi, B. F. Ali, R. Abu-El-Halawa, A. Abo-Amer, *Transition Met. Chem.* **2004**, *29*, 804–811; d) Z.-D. Xu, H. Liu, S.-L. Xiao, M. Yang, X.-H. Bu, *J. Inorg. Biochem.* **2002**, *90*, 79–84.

[6] a) P. Gómez-Saiz, J. García-Tojal, M. A. Maestro, F. J. Arnaiz, T. Rojo, *Inorg. Chem.* **2002**, *41*, 1345–1347; b) P. Gómez-Saiz, J. García-Tojal, M. A. Maestro, J. Mahía, F. J. Arnáiz, L. Lezama, T. Rojo, *Eur. J. Inorg. Chem.* **2003**, 2639–2650.

[7] a) P. Gómez-Saiz, J. García-Tojal, M. A. Maestro, F. J. Arnáiz, T. Rojo, *Polyhedron* **2002**, *21*, 2257–2263; b) P. Gómez-Saiz, J. García-Tojal, F. J. Arnáiz, M. A. Maestro, L. *Lezama*, T. Rojo, *Inorg. Chem. Commun.* **2003**, *6*, 558–560; c) P. Gómez-Saiz, F. J. Arnáiz, J. García-Tojal, *Rev. Soc. Quím. Perú* **2005**, *71*, 107–113.

[8] C. Ruiz-Pérez, J. Sanchiz, M. Hernández-Molina, F. Lloret, M. Julve, *Inorg. Chem.* **2000**, *39*, 1363–1370.

[9] J. Sanchiz, Y. Rodríguez-Martín, C. Ruiz-Pérez, A. Mederos, F. Lloret, M. Julve, *New J. Chem.* **2002**, *26*, 1624–1628.

[10] A. W. Addison, T. N. Rao, J. Reedijk, J. van Rijn, G. C. Verschoor, *J. Chem. Soc., Dalton Trans.* **1984**, 1349–1356.

[11] C. Ruiz-Pérez, Y. Rodríguez-Martín, M. Hernández-Molina, F. S. Delgado, J. Pasán, J. Sanchiz, F. Lloret, M. Julve, *Polyhedron* **2003**, *22*, 2111–2123.

[12] a) I. Gil de Muro, F. A. Mautner, M. Insausti, L. Lezama, M. I. Arriortua, T. Rojo, *Inorg. Chem.* **1998**, *37*, 3243–3251; b) T. F. Liu, H.-L. Sun, S. Gao, S.-W. Zhang, T.-C. Lau, *Inorg. Chem.* **2003**, *42*, 4792–4794; c) S. Sain, T. K. Maji, G. Mostafa, T.-H. Lu, N. R. Chaudhuri, *New J. Chem.* **2003**, *27*, 185–187; d) I. G. de Muro, L. Lezama, M. Insausti, T. Rojo, *Polyhedron* **2004**, *23*, 929–936; e) H.-L. Liu, H.-Y. Mao, H.-Y. Zhang, C. Xu, Q.-A. Wu, G. Li, Y. Zhu, H.-W. Hou, *Polyhedron* **2004**, *23*, 943–948; f) M. Liang, Q.-L. Wang, L.-H. Yu, D.-Z. Liao, Z.-H. Jiang, S.-P. Yan, P. Cheng, *Polyhedron* **2004**, *23*, 2203–2208; g) K. L. Yao, J. Q. Zhang, Z. L. Liu, G. Y. Gao, Y. L. Li, D. Xi, Q. Ning, *J. Magn. Magn. Mater.* **2008**, *320*, 458–462.

[13] a) S. K. Chawla, M. Arora, K. Nättinen, K. Rissanen, J. V. Yakhmi, *Polyhedron* **2004**, *23*, 3007–3019; b) M. Hemamalini, P. T. Muthiah, R. J. Butcher, D. E. Lynch, *Inorg. Chem. Commun.* **2006**, *9*, 1155–1160; c) X.-J. Zhao, Q. Wang, M. Du, *Inorg. Chim. Acta* **2007**, *360*, 1970–1976.

[14] a) C. Ruiz-Pérez, M. Hernández-Molina, P. Lorenzo-Luis, F. Lloret, J. Cano, M. Julve, *Inorg. Chem.* **2000**, *39*, 3845–3852; b) Y. Rodríguez-Martín, C. Ruiz-Pérez, J. Sanchiz, F. Lloret, M. Julve, *Inorg. Chim. Acta* **2001**, *318*, 159–165; c) F. S. Delgado, J. Sanchiz, C. Ruiz-Pérez, F. Lloret, M. Julve, *Inorg. Chem.* **2003**, *42*, 5938–5948; d) S. Konar, P. S. Mukherjee, M. G. B. Drew, J. Ribas, N. R. Chaudhuri, *Inorg. Chem.* **2003**, *42*, 2545–2552; e) J. Pasán, J. Sanchiz, C. Ruiz-Pérez, F. Lloret, M. Julve, *New J. Chem.* **2003**, *27*, 1557–1562; f) A. Cuevas, R. Chiozzone, C. Kremer, L. Suescun, A. Mombrú, D. Armentaro, G. De Munno, F. Lloret, J. Cano, J. Faus, *Inorg. Chem.* **2004**, *43*, 7823–7831; g) C. Gkioni, A. K. Boudalis, Y. Sanakis, C. P. Raptopoulou, *Polyhedron* **2007**, *26*, 2536–2542; h) M. R. Montney, R. L. LaDuca, *Inorg. Chem. Commun.* **2007**, *10*, 1518–1522.

[15] a) C. Ruiz-Pérez, J. Sanchiz, M. Hernández-Molina, F. Lloret, M. Julve, *Inorg. Chem.* **2000**, *39*, 1363–1370; b) J. Sanchiz, Y. Rodríguez-Martín, C. Ruiz-Pérez, A. Mederos, F. Lloret, M. Julve, *New J. Chem.* **2002**, *26*, 1624–1628; c) J. Pasán, F. S. Delgado, Y. Rodríguez-Martín, M. Hernández-Molina, C. Ruiz-Pérez, J. Sanchiz, F. Lloret, M. Julve, *Polyhedron* **2003**, *22*, 2143–2153.

[16] G.-H. Cui, J.-R. Li, T.-L. Hu, X.-H. Bu, *J. Mol. Struct.* **2005**, *738*, 183–187.

[17] a) S. Supriya, S. Manikumari, P. Raghavaiah, S. K. Das, *New J. Chem.* **2003**, *27*, 218–220; b) S. Supriya, S. K. Das, *New J. Chem.* **2003**, *27*, 1568–1574; c) N. S. Oxtoby, A. J. Blake, N. R. Champness, C. Wilson, *Chem. Eur. J.* **2005**, *11*, 4643–4654; d) M. Zuhayra, W. U. Kampen, E. Henze, Z. Soti, L. Zsolnai, G. Huttner, F. Oberdorfer, *J. Am. Chem. Soc.* **2006**, *128*, 424–425; e) J. Yang, J.-F. Ma, Y.-Y. Liu, J.-C. Ma, H.-Q. Jia, N.-H. Hu, *Eur. J. Inorg. Chem.* **2006**, 1208–1215; f) Y.-g. Sun, E.-j. Gao, D.-z. Wei, *Inorg. Chem. Commun.* **2007**, *10*, 467–470; g) H. Wang, J.-Q. Liu, Y.-N. Zhang, Y.-Y. Wang, G.-L. Wen, C.-Y. Guo, Q.-Z. Shi, *Inorg. Chem. Commun.* **2008**, *11*, 129–133.

[18] a) J. Tao, Z.-J. Ma, R.-B. Huang, L.-S. Zheng, *Inorg. Chem.* **2004**, *43*, 6133–6135; b) L.-S. Long, Y.-R. Wu, R.-B. Huang, L.-S. Zheng, *Inorg. Chem.* **2004**, *43*, 3798–3800; c) J. Q. Sun, J. Zang, Z. F. Ju, G. Y. Yang, *Aust. J. Chem.* **2005**, *58*, 572–577; d) Z.-G. Li, J.-W. Xu, H.-Q. Jia, N.-H. Hu, *Inorg. Chem. Commun.* **2006**, *9*, 969–972; e) P. Raghavaiah, S. Supriya, S. K. Das, *Chem. Commun.* **2006**, 2762–2764; f) M. N. Kopylovich, E. A. Tronova, M. Haukka, A. M. Kirillov, V. Y. Kukushkin, J. J. R. Fraústo da Silva, A. J. L. Pombeiro, *Eur. J. Inorg. Chem.* **2007**, 4621–4627; g) M. Shao, M.-X. Li, H. Dai, W.-C. Lu, *J. Mol. Struct.* **2008**, *875*, 316–321.

[19] M. Schütz, W. Klopper, H.-P. Luthi, *J. Chem. Phys.* **1995**, *103*, 6114.

[20] a) J. D. Cruzan, L. B. Braly, K. Liu, M. G. Brown, J. G. Loeser, R. J. Saykally, *Science* **1996**, *271*, 59–62; b) J. D. Cruzan, M. G. Brown, K. Liu, L. B. Braly, R. J. Saykally, *J. Chem. Phys.* **1996**, *105*, 6634–6644; c) J. D. Cruzan, M. R. Viant, M. G. Brown, R. J. Saykally, *J. Phys. Chem. A* **1997**, *101*, 9022–9031.

[21] A. H. Narten, W. E. Thissen, L. Blum, *Science* **1982**, *217*, 1033–1034.

[22] S. W. Peterson, H. A. Levy, *Acta Crystallogr.* **1957**, *10*, 70–76.

[23] a) S. S. Xantheas, T. H. Dunning Jr., *J. Chem. Phys.* **1993**, *99*, 8774–8792; b) S. S. Xantheas, *J. Chem. Phys.* **1994**, *100*, 7523–7534; c) S. S. Xantheas, *J. Chem. Phys.* **1995**, *102*, 4505–4517; d) R. Ludwig, *Angew. Chem. Int. Ed.* **2001**, *40*, 1808–1827; e) M. Masella, N. Gresh, J.-P. Flament, *J. Chem. Soc. Faraday Trans.* **1998**, *94*, 2745–2753; f) J. Dolenc, J. Koller, *Acta Chim. Slov.* **2006**, *53*, 229–237.

[24] G. Beobide, O. Castillo, A. Luque, U. García-Couceiro, J. P. García-Terán, P. Román, *Inorg. Chem.* **2006**, *45*, 5367–5382.

[25] L. Li, D. Liao, S. Liu, Z. Jiang, S. Yan, *Inorg. Chem. Commun.* **2003**, *6*, 225–228.

[26] a) M. Kabesova, M. Dunaj-Junco, J. Soldanova, *Inorg. Chim. Acta* **1987**, *130*, 105–111; b) Z. Koziskova, J. Kozisek, M. Kabesova, *Polyhedron* **1990**, *9*, 1029–1034; c) G. De Mundo, G. Bruno, F. Nicolo, M. Julve, J. A. Real, *Acta Crystallogr., Sect. C Cryst. Struct. Comun.* **1993**, *49*, 457–460; d) M. Julve, M. Verdaguer, G. De Munno, J. A. Real, G. Bruno, *Inorg. Chem.* **1993**, *32*, 795–802; e) J. A. R. Navarro, M. A. Romero, J. M. Salas, M. Quirós, E. R. T. Tiekink, *Inorg. Chem.* **1997**, *36*, 4988–4991; f) G. Chen, Z.-P. Bai, S.-J. Qu, *Acta Crystallogr., Sect. E, Struct. Rep. Online* **2005**, *61*, m2718.

[27] S. R. Batten, K. S. Murray, *Coord. Chem. Rev.* **2003**, *246*, 103–130.

[28] See for instance the following articles, those in the next footnotes on this point and references cited therein: a) M. Liang, D. Z. Liao, Z. H. Jiang, S. P. Yan, P. Cheng, *Inorg. Chem. Commun.* **2004**, *7*, 173–175; b) J. A. Schlueter, J. L. Manson, U. Geiser, *C. R. Chim.* **2007**, *10*, 101–108; c) X.-J. Zhao, Q. Wang, M. Du, *Inorg. Chim. Acta* **2007**, *360*, 1970–1976.

[29] a) I. Riggio, G. A. van Albada, D. D. Ellis, A. L. Spek, J. Reedijk, *Inorg. Chim. Acta* **2001**, *313*, 120–124; b) J. Carranza, C. Brennan, J. Sletten, F. Lloret, M. Julve, *J. Chem. Soc., Dalton Trans.* **2002**, 3164–3170; c) F. Thétiot, S. Triki, J. S. Pala, S. Golhen, *Inorg. Chim. Acta* **2003**, *350*, 314–320; d) W. Gu, H.-D. Bian, J.-Y. Xu, Z.-Q. Liu, P. Cheng, S.-P. Yan, D.-Z. Liao, Z.-H. Jiang, *Inorg. Chem. Commun.* **2003**, *6*, 966–970; e) J. Carranza, J. Sletten, F. Lloret, M. Julve, *Inorg. Chim. Acta* **2004**, *357*, 3304–3316; f) R. Karmakar, C. R. Choudhury, D. L. Hughes, G. P. A. Yap, M. S. El Fallah, C. Desplanches, J.-P. Sutter, S. Mitra, *Inorg. Chim. Acta* **2006**, *359*, 1184–1192; g) D. Mal, J.-P. Tuchagues, S. Chakraborty, A. K. Mukherjee, R. Sen, S. Koner, *Inorg. Chim. Acta* **2006**, *359*, 4431–4435; h) D. Ghoshal, A. D. Jana, T. K. Maji, G. Mostafa, *Inorg. Chim. Acta* **2006**, *359*, 690–694; i) G. A. Van Albada, M. G. Van der Horst, I. Mutikainen, U. Turpeinen, J. Reedijk, *Inorg. Chem. Commun.* **2007**, *10*, 1014–1018; j) S. Sen, S. Mitra, D. L. Hughes, G. Rosair, C. Desplanches, *Inorg. Chim. Acta* **2007**, *360*, 4085–4092; k) J. A. Schlueter, J. L. Manson, K. A. Hyzer, U. Geiser, *Polyhedron* **2007**, *26*, 2264–2272; l) D. Mal, C. Adhikary, E. Rentschler, Y. Miyashita, K.-I. Okamoto, S. Koner, *Polyhedron* **2007**, *26*, 736–740; m) M. Biswas, G. M. Rosair, G. Pilet, S. Mitra, *Inorg. Chim. Acta* **2007**, *360*, 695–699; n) M. Biswas, G. M. Rosair, G. Pilet, M. S. El Fallah, J. Ribas, S. Mitra, *Polyhedron* **2007**, *26*, 123–132; o) S. Sen, S. Mitra, D. L. Hughes, G. Rosair, C. Desplanches, *Inorg. Chim. Acta* **2007**, *360*, 4085–4092.

[30] a) S. Martín, M. G. Barandika, J. I. Ruiz de Larramendi, R. Cortés, M. Font-Bardia, L. Lezama, Z. E. Serna, X. Solans, T. Rojo, *Inorg. Chem.* **2001**, *40*, 3687–3692; b) B. Vangdal, J. Carranza, F. Lloret, M. Julve, J. Sletten, *J. Chem. Soc., Dalton Trans.* **2002**, 566–574.

[31] a) W.-F. Yeung, S. Gao, W.-T. Wong, T.-C. Lau, *New J. Chem.* **2002**, *26*, 523–525; b) J. Carranza, C. Brennan, J. Sletten, J.-M. Clemente-Juan, F. Lloret, M. Julve, *Inorg. Chem.* **2003**, *42*,

8716–8727; c) J. L. Manson, J. A. Schlueter, H.-J. Koo, M.-H. Whangbo, *Inorg. Chem.* **2004**, *43*, 4007–4011; d) G.-Y. Hsu, C.-W. Chen, S.-C. Cheng, S.-H. Lin, H.-H. Wei, C.-J. Lee, *Polyhedron* **2005**, *24*, 487–494.

[32] C.-X. Zhang, Z.-Q. Liu, D.-Z. Liao, Z.-H. Jiang, S.-P. Yan, *Inorg. Chim. Acta* **2004**, *357*, 376–380.

[33] Q. Shi, M.-L. Hu, H.-P. Xiao, X.-H. Li, *Inorg. Chem. Commun.* **2005**, *8*, 1169–1172.

[34] a) P. Jensen, S. R. Batten, G. D. Fallon, D. C. R. Hockless, B. Moubaraki, K. S. Murray, R. Robson, *J. Solid State Chem.* **1999**, *145*, 387–393; b) G. A. Van Albada, M. E. Quiroz-Castro, I. Mutikainen, U. Turpeinen, J. Reedijk, *Inorg. Chim. Acta* **2000**, *298*, 221–225; c) P. Jensen, S. R. Batten, B. Moubaraki, K. S. Murray, *J. Chem. Soc., Dalton Trans.* **2002**, 3712–3722; d) A. Mohamadou, G. A. van Albada, H. Kooijman, B. Wieczorek, A. L. Spek, J. Reedijk, *New J. Chem.* **2003**, *27*, 983–988; e) S. Konar, S. Dalai, J. Ribas, M. G. B. Drew, E. Zangrando, N. R. Chaudhuri, *Inorg. Chim. Acta* **2004**, *357*, 4208–4214; f) L. F. Jones, L. O'Dea, D. A. Offermann, P. Jensen, B. Moubaraki, K. S. Murray, *Polyhedron* **2006**, *25*, 360–372.

[35] J. Luo, M. Hong, J. Weng, Y. Zhao, R. Cao, *Inorg. Chim. Acta* **2002**, *329*, 59–65.

[36] I. Dasna, S. Golhen, L. Ouahab, M. Fettouhi, O. Pena, N. Daro, J.-P. Sutter, *Inorg. Chim. Acta* **2001**, *326*, 37–46.

[37] a) M. Hvastijova, J. Kohout, J. Kozisek, J. G. Diaz, L. Jäger, M. Mrozinski, *Z. Anorg. Allg. Chem.* **1998**, *624*, 349–354; b) S. R. Batten, B. F. Hoskins, R. Robson, *Chem. Eur. J.* **2000**, *6*, 156–161; c) Z.-M. Wang, J. Luo, B.-W. Sun, C.-H. Yan, S. Gao, C.-S. Liao, *Acta Crystallogr., Sect. C* **2000**, *56*, 786–788; d) M. Liang, D. Z. Liao, Z. H. Jiang, S. P. Yan, P. Cheng, *Inorg. Chem. Commun.* **2004**, *7*, 173–175; e) J. A. Schlueter, J. L. Manson, U. Geiser, *C. R. Chim.* **2007**, *10*, 101–108; f) X.-J. Zhao, Q. Wang, M. Du, *Inorg. Chim. Acta* **2007**, *360*, 1970–1976.

[38] A. Mohamadou, G. A. van Albada, H. Kooijman, B. Wieczorek, A. L. Spek, J. Reedijk, *New J. Chem.* **2003**, *27*, 983–988.

[39] J. L. Manson, J. Gu, J. A. Schlueter, H.-H. Wang, *Inorg. Chem.* **2003**, *42*, 3950–3955.

[40] M. S. El Fallah, F. Badyne, R. Vicente, A. Escuer, X. Solans, M. Font-Bardia, *Dalton Trans.* **2006**, 2934–2942; Z.-G. Gu, X.-H. Zhou, Y.-B. Jin, R.-G. Xiong, J.-L. Zuo, X.-Z. You, *Inorg. Chem.* **2007**, *46*, 5462–5464.

[41] a) B. J. Hathaway, D. E. Billing, *Coord. Chem. Rev.* **1970**, *5*, 143–207; b) D. E. Billing, B. J. Dudley, R. J. Hathaway, A. A. G. Tomlinson, *J. Chem. Soc. A* **1971**, 691–696; c) B. Macías, I. Garcia, M. V. Villa, J. Borrás, M. González-Alvarez, A. Castiñeiras, *Inorg. Chim. Acta* **2003**, *353*, 139–144.

[42] B. J. Hathaway, *J. Chem. Soc., Dalton Trans.* **1972**, 1196–1199.

[43] B. Bleaney, K. D. Bowers, *Proc. R. Soc. London Ser. A* **1952**, *214*, 451–465.

[44] a) S. Ferlay, G. Fracese, H. W. Schmalle, S. Decurtins, *Inorg. Chim. Acta* **1999**, *286*, 108–113; b) M. A. S. Goher, L. A. Al-Shatti, F. A. Mautner, *Polyhedron* **1997**, *16*, 889–895; c) M. Julve, M. Verdaguer, G. De Munno, J. A. Real, G. Bruno, *Inorg. Chem.* **1993**, *32*, 795–802; d) Z. E. Serna, R. Cortés, M. K. Urtiaga, M. G. Barandika, L. Lezama, M. I. Arriortua, T. Rojo, *Eur. J. Inorg. Chem.* **2001**, 865–872; e) S. Sen, S. Mitra, D. L. Hughes, G. Rosair, C. Desplanches, *Polyhedron* **2007**, *26*, 1740–1744; f) F. A. Mautner, R. Vicente, S. S. Massoud, *Polyhedron* **2006**, *25*, 1673–1680; g) S. Youngme, J. Phatchimkun, U. Suksangpanya, C. Pakawatchai, G. A. van Albada, M. Quesada, J. Reedijk, *Inorg. Chem. Commun.* **2006**, *9*, 242–247; h) H. Xu, C. He, Y.-X. Sui, X.-M. Ren, L.-M. Guo, Y.-G. Zhang, S. Nishihara, Y. Hosokoshi, *Polyhedron* **2007**, *26*, 4463–4469.

[45] a) R. Prins, P. J. M. W. L. Birker, J. G. Haasnoot, G. C. Verschoor, J. Reedijk, *Inorg. Chem.* **1985**, *24*, 4128–4133; b) W. M. E. Koomen-Van Oudenniel, R. A. G. De Graaff, J. G. Haasnoot, R. Prins, J. Reedijk, *Inorg. Chem.* **1989**, *28*, 1128–1133; c) P. M. Slangen, P. J. Van Doningsbrugen, J. G. Haasnoot, J. Jansen, S. Gorter, J. Reedijk, H. Kooijman, W. J. J. Smeets, A. L. Spek, *Inorg. Chim. Acta* **1993**, *212*, 289–301; d) P. M. Slangen, P. J. Van Koningsbruggen, K. Goubitz, J. G. Haasnoot, J. Reedijk, *Inorg. Chem.* **1994**, *33*, 1121–1126; e) S. S. Tandon, L. Chen, L. K. Thompson, J. N. Bridson, *Inorg. Chem.* **1994**, *33*, 490–497; f) S. Ferrer, P. J. Van Koningsbruggen, J. G. Haasnoot, J. Reedijk, H. Kooijman, A. L. Spek, L. Lezama, A. M. Arif, J. S. Miller, *J. Chem. Soc., Dalton Trans.* **1999**, 4269–4276.

[46] a) Y. García, P. J. Van Koningsbruggen, G. Bravic, D. Guionneau, D. Chasseau, G. L. Cascarano, J. Moscovici, K. Lambert, A. Michalowicz, *Inorg. Chem.* **1997**, *36*, 6357; b) J.-L. Song, Z.-C. Dong, H.-Y. Zeng, W.-B. Zhou, T. Naka, Q. Wei, J.-G. Mao, G.-C. Guo, J.-S. Huang, *Inorg. Chem.* **2003**, *42*, 2136–2140; c) B. Ding, Y. Q. Huang, Y. Y. Liu, W. Shi, P. Cheng, *Inorg. Chem. Commun.* **2007**, *10*, 7–10; d) J.-R. Li, Q. Yu, E. C. Sañudo, Y. Tao, X.-H. Bu, *Chem. Commun.* **2007**, 2602–2604.

[47] Y. García, P. J. Van Koningsbruggen, G. Bravic, D. Chasseau, O. Kahn, *Eur. J. Inorg. Chem.* **2003**, 356–362.

[48] J. C. Bayón, P. Esteban, G. Net, P. G. Rasmussen, K. N. Baker, C. W. Hahn, M. M. Gumz, *Inorg. Chem.* **1991**, *30*, 2572–2574.

[49] V. P. Hanot, T. D. Robert, J. Kolnaar, J. G. Haasnoot, J. Reedijk, H. Kooijman, A. L. Spek, *J. Chem. Soc., Dalton Trans.* **1996**, 4275–4281.

[50] P. J. Van Koningsbruggen, J. G. Haasnoot, R. A. G De Graaff, J. Reedijk, S. Slingerland, *Acta Crystallogr., Sect. C* **1992**, *48*, 1923.

[51] J. Teichgraber, G. Leibeling, S. Dechert, F. Meyer, *Z. Anorg. Allg. Chem.* **2005**, *631*, 2613–2618.

[52] V. Mishra, F. Lloret, R. Mukherjee, *Eur. J. Inorg. Chem.* **2007**, 2161–2170.

[53] T.-L. Hu, J.-R. Li, C.-S. Liu, X.-S. Shi, J.-N. Zhou, X.-H. Bu, J. Ribas, *Inorg. Chem.* **2006**, *45*, 162–173.

[54] P. King, R. Clérac, C. E. Anson, C. Coulon, A. K. Powell, *Dalton Trans.* **2004**, 852–861.

[55] H. Matsushima, H. Hamada, K. Watanabe, M. Koikawa, T. Tokii, *J. Chem. Soc., Dalton Trans.* **1999**, 971–977.

[56] C. Miranda, R. Escarti, L. Lamarque, E. García-España, P. Navarro, J. Latorre, F. Lloret, H. R. Jiménez, M. J. R. Yunta, *Eur. J. Inorg. Chem.* **2005**, 189–208.

[57] B. Mernari, F. Abraham, M. Lagrenee, M. Drillon, P. Legoll, *J. Chem. Soc., Dalton Trans.* **1993**, 1707–1711.

[58] D. J. De Geest, A. Noble, B. Moubaraki, K. S. Murray, D. S. Larsen, S. Brooker, *Dalton Trans.* **2007**, 467–475.

[59] M. Du, S.-T. Chen, Y.-M. Guo, X.-H. Bu, J. Ribas, *J. Mol. Struct.* **2005**, *737*, 17–21.

[60] R. Krämer, I. O. Fritsky, H. Pritzkow, L. A. Kovbasyuk, *J. Chem. Soc., Dalton Trans.* **2002**, 1307–1314.

[61] M. K. Ehlert, S. J. Rettig, A. Storr, R. C. Thompson, J. Trotter, *Can. J. Chem.* **1992**, *70*, 2161–2173.

[62] S. Tanase, I. A. Koval, E. Bowman, R. de Gelder, J. Reedijk, *Inorg. Chem.* **2005**, *44*, 7860–7865.

[63] E. Spodine, A. M. Atria, J. Valenzuela, J. Jalocha, J. Manzur, A. M. García, M. T. Garland, O. Peña, J.-Y. Saillard, *J. Chem. Soc., Dalton Trans.* **1999**, 3029–3034.

[64] a) G. A. Ardizzoia, S. Cenini, G. La Monica, N. Masciocchi, A. Maspero, M. Moret, *Inorg. Chem.* **1998**, *37*, 4284–4292; b) K. Singh, J. R. Long, P. Stavropoulos, *Inorg. Chem.* **1998**, *37*, 1073–1079.

[65] a) T. Kamiusuki, H. Ökawa, N. Matsumoto, S. Kida, *J. Chem. Soc., Dalton Trans.* **1990**, 195–198; b) J. Pons, X. Lopez, J. Casabo, F. Teixidor, A. Caubet, J. Rins, C. Miravitlles, *Inorg. Chim. Acta* **1992**, *195*, 61–66; c) F. Degang, W. Guoxiong, Z. Zongyuan, Z. Xiangge, *Transition Met. Chem.* **1994**, *19*, 592–594.

[66] T. Kamiusuki, H. Ökawa, N. Matsumoto, M. Kodera, S. Kida, *J. Coord. Chem.* **1991**, *23*, 201–221.

[67] Y.-M. Sun, C.-B. Liu, X.-J. Lin, S.-W. Bi, *New J. Chem.* **2004**, *28*, 270–274.

[68] D. S. Sigman, R. Landgrave, D. M. Perrin, L. Pearson in *Nucleic Acid Chemistry of the Cuprous Complexes of 1,10-Phenanthroline and Derivatives*, Chapter 16 in *Metal Ions in Biological*

Systems (Eds.: H. Sigel, A. Sigel), Marcel Dekker Inc., New York, **1996**; vol. 33.
[69] J. M. Vaal, K. Mechant, R. L. Rill, *Nucleic Acid Res.* **1991**, *19*, 3383–3388.
[70] P. A. N. Reddy, M. Nethaji, A. R. Chakarvarty, *Eur. J. Inorg. Chem.* **2004**, 1440–1446.
[71] S. Dhar, M. M. Nethaji, A. R. Chakarvarty, *Inorg. Chim. Acta* **2005**, *358*, 2437–2444.
[72] P. Gómez-Saiz, R. Gil-García, M. A. Maestro, J. L. Pizarro, M. I. Arriortua, L. Lezama, T. Rojo, M. González-Álvarez, J. Borrás, J. García-Tojal, *J. Inorg. Biochem.* **2008**, *102*, 1910–1920.
[73] K. K. Millis, K. H. Weaver, D. L. Rabenstein, *J. Org. Chem.* **1993**, *58*, 4144–4146.
[74] D. S. Sigman, A. Mazumder, D. M. Perrin, *Chem. Rev.* **1993**, *93*, 2295–2316.
[75] W. K. Pogozelski, T. D. Tullius, *Chem. Rev.* **1998**, *98*, 1017–1089.
[76] It is very important to keep the reaction at low temperature and pH = 5 because other conditions yield a cottony brown solid that we have not been able to characterise.
[77] An interesting variation of this method led to very different results. A solution of $L^2 \cdot 3H_2O$ (0.060 g, 0.26 mmol) in DMF (2 mL) was added to a solution of $CuSO_4 \cdot 5H_2O$ (0.065 g, 0.26 mmol) in the same solvent (2 mL). An aqueous solution of NaN_3 (0.033 g, 0.51 mmol) was then added to the green solution. The colour immediately turned red and bubbling was observed with evolution of a colourless gas. A brown solid precipitated but we were not able to characterise it. This reaction was not observed in other solvents such as water or ethanol and the presence of azide ions was always required.
[78] R. H. Blessing, *Acta Crystallogr., Sect. A* **1995**, *51*, 33–38.
[79] G. M. Sheldrick, SHELXS-97, *Program for Crystal Structure Solution*; University of Göttingen, Göttingen, Germany, **1997**.
[80] G. M. Sheldrick, SHELXL-97, *Program for the Refinement of Crystal Structures from Diffraction Data*; University of Göttingen, Göttingen, Germany, **1997**.
[81] *International Tables for Crystallography*, Kluwer Academic Publishers, Dordrecht, The Netherlands, **1992**.

Received: August 14, 2008
Published Online: December 12, 2008

DOI: 10.1002/ejic.200800913

Conformational Analysis of β-Lactam-Containing Ferrocene Peptides

Veronika Kovač,[a] Katarina Radolović,[b] Ivan Habuš,[b] Daniel Siebler,[c] Katja Heinze,*[c] and Vladimir Rapić*[a]

Keywords: Conformation analysis / Density functional calculations / Hydrogen bonds / Metallocenes / Molecular modeling

The homochiral 3-amino-1-(4-methoxyphenyl)-4-phenyl-β-lactam (≡ Alm) was conjugated with Boc-Ala to give Ala-Alm (**9**) after Boc deprotection (Boc = *tert*-butoxycarbonyl, Ala = alanine). Coupling of Fc-COOH (**1**) and Boc-Fca (**10**) with "dipeptide" **9** resulted in the formation of Fc-CO-Ala-Alm (**12**) and the trisamide Boc-Fca-Ala-Alm (**13**), respectively (Fc = ferrocenyl, Fca = 1′-aminoferrocene-1-carboxylic acid). The reactions were accomplished by the HOBt/EDC procedure, and the products were obtained in good yields [HOBt = 1-hydroxybenzotriazole, EDC = *N*-(3-dimethylaminopropyl)-*N*′-ethylcarbodiimide hydrochloride]. Symmetrically 1,1′-disubstituted "tetrapeptide" Fn(CO-Ala-Alm)$_2$ (**14**) was prepared by reaction of ferrocene chloride **11** with **9** (Fn = 1,1′-ferrocenediyl). Spectroscopic and theoretical analyses revealed that compounds **12**, **13**, and **14** are stabilized in solution by medium-strong intramolecular hydrogen bonds. In all dominant conformations (DFT calculations) intrachain bonds spanning CO_{Fc} and NH_{Alm} are present (γ-turns). Additional interchain hydrogen bonds $NH_{Ala}\cdots CO_{Boc}$ (**13**) and $NH_{Ala}\cdots CO_{Ala}/NH_{Ala}\cdots CO_{Alm}$ (**14**) give rise to ordered helical conformations of the ferrocene moieties.

Introduction

The β-lactam skeleton has attracted significant interest among synthetic and medicinal chemists, mainly because it is the core structure of natural and synthetic β-lactam antibiotics.[1,2] The potential of β-lactams to serve as intermediates for eventual access to α- and β-amino acid derived peptides has gained tremendous attention.[3–6] Enantiopure 3-amino-[7,8] and 3-hydroxy-β-lactams[9] are key intermediates for the synthesis of peptides and peptidomimetics. A variety of 3-amino- and 3-hydroxy-β-lactams with excellent enantiopurities can be obtained through chiral ester enolate/imine cyclocondensation.[4,6,10] Hydrolysis of 3-amino- and 3-hydroxy-β-lactams affords the corresponding α,β-diamino and α-hydroxy-β-amino acids.[11] This forms the foundation for applications of these β-lactams to asymmetric synthesis of nonprotein amino acids, peptides, dipeptide isosteres, and peptidomimetics that are not easily prepared by conventional methods. α,β-Diamino acids (nonprotein amino acids) are often components of peptidic antibiotics such as lavendomycin or glumamycin,[12] whereas α-hydroxy-β-amino acids (isoserines) are key components of a large number of therapeutically important compounds.[13–17]

β-Lactams containing a ferrocene moiety[7,18–21] at C-4 are important, because they are ideal candidates for drug design due to their low toxicity[22] and due to the ability of ferrocene to modify the β-lactam molecule in the third dimension by bringing the bulky metal complex in close proximity to the β-lactam ring without disturbing the molecule profile, which is necessary for antibiotic activity.[23] Besides their potential as antibacterial agents and potent enzyme inhibitors, nowadays a very attractive aspect of ferrocenyl-substituted compounds is their potential role as electrochemical markers in biological processes.[24–26]

Turns are ubiquitous elements in the secondary structure of proteins that have become important targets in medicinal chemistry.[27–29] A common strategy to impart a specific secondary structure to a peptide/protein backbone is the use of molecular scaffolds.[30] The particular choice of the ferrocene scaffold influences the ability to form hydrogen-bonded assemblies. For example, conjugates of ferrocenecarboxylic acid with amino acids (Scheme 1, type I) often give rise to 1D hydrogen-bonded chains in the solid state. Symmetrically substituted bioconjugates of ferrocene-1,1′-dicarboxylic acid (Fcd) with 1–2 amino acids per substituent have been extensively studied.[31–41] In the solid state, the majority of these compounds form two intramolecular hydrogen bonds (independent of the number and

[a] Department of Chemistry and Biochemistry, Faculty of Food Technology and Biotechnology,
Pierottijeva 6, 10000 Zagreb, Croatia
Fax: +385-4836-082
E-mail: vrapic@pbf.hr
[b] Ruđer Bošković Institute,
Bijenička c. 54, P. O. Box 180, 10002 Zagreb, Croatia
[c] Institute of Inorganic and Analytical Chemistry, Johannes Gutenberg University of Mainz
Duesbergweg 10–14, 55128 Mainz, Germany
Fax: +49-6131-3927277
E-mail: katja.heinze@uni-mainz.de

Supporting information for this article is available on the WWW under http://www.eurjic.org or from the author.

type of the amino acid incorporated). This results in the formation of two 10-membered rings (Scheme 1, type II; β-turn-like "Herrick conformation"). Usually, these intramolecular hydrogen bonds are sufficiently strong to retain this C_2-symmetrical conformation in chloroform solution.[31–41] As a result of their constitution, type II conjugates can only form *parallel* peptide strands.

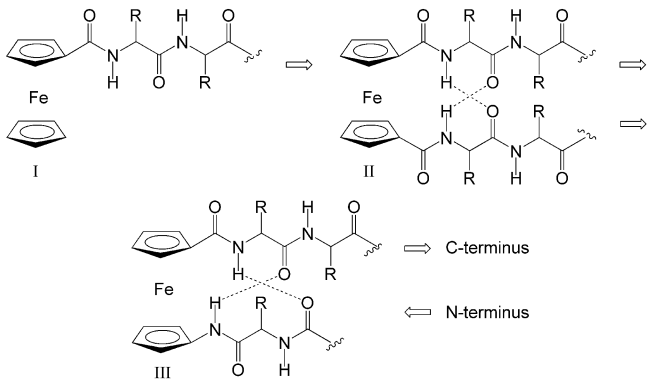

Scheme 1. Oligopeptides derived from ferrocenecarboxylic acid, ferrocene-1,1′-dicarboxylic acid (Fcd), and 1′-aminoferrocene-1-carboxylic acid (Fca) [arrows are directed from the N-terminus to the C-terminus of the peptide chains].

The feature of natural peptides to form turns by juxtapositioning their chains in an *antiparallel* way can be mimicked by bioorganometallics that include 1′-aminoferrocene-1-carboxylic acid (Fca[42]) coupled with natural amino acids or peptides (Scheme 1, type III). In several of our previous studies the syntheses and conformational analyses of a number of such oligopeptides (including various L- and D-amino acids) were described.[43–47] It was shown that, unlike previous metallocene turn structures found in conjugates II, these compounds are the first true ferrocene turn mimetics, maintaining an *antiparallel orientation* of the peptide strands and a helical chirality (conformational enantiomerism) based on intramolecular hydrogen bonds. Short Fca-containing peptides (incorporating 1–2 natural amino acids) establish a single hydrogen bond and exist as an ensemble of conformers in solution. The longer oligopeptides of type III contain two strong intramolecular hydrogen bonds forming an 11-membered ring (β-turn-like) and a 9-membered ring (reverse β-turn-like) as depicted in Scheme 1. These conformers, which can be considered as β-sheet models, are found in the solid state, and it appears from spectroscopic data that they prevail (like Herrick conformations) in solution as well. There are many examples of Fcd-derived oligopeptides (Scheme 1, type II) that include heterocycles (e.g., pyridine or the pyrrolidine part of Pro) incorporated into the peptide strands.[37–40,48–52] Participation of the heterocyclic nitrogen atom (as hydrogen acceptor) in the formation of hydrogen bonds has not been described so far. Instead, in such systems the expected β-turn-like Herrick double intramolecular hydrogen bonds are found. Fn(CO-Pro-Ala-NHPy)$_2$ is an interesting exception to this general finding. Here, the ferrocene scaffold induces an antiparallel β-sheet (two 10-membered interchain intramolecular hydrogen-bonded rings between CO_{Fc} and NH_{Ala}) and an inverse γ-turn-like structure (two 7-membered intrachain intramolecular hydrogen bonded rings including CO_{Pro} and NH_{Py}).[53] Previously, we described homochiral *trans*-(+)-(3*S*,4*S*)-3-amino-4-ferrocenyl-1-(4-methoxyphenyl)azetidin-2-one. The crystal structure determination of this ferrocene β-lactam system showed that two conformers are present in the unit cell. In both of these conformers, the molecules are associated by two intermolecular hydrogen bonds between the carboxamido functions of the β-lactam rings.[7] To the best of our knowledge, conjugates of 3-amino-β-lactams with naturally occurring amino acids and oligopeptides have not been described so far. Having in mind the interesting characteristics and diversities in hydrogen-bonding capabilities and motifs found in ferrocene bioconjugates of types I–III and the 3-amino-β-lactam,[7] we decided to construct and investigate β-lactam-containing ferrocene peptides and expected participation of the heterocyclic amide function in hydrogen-bond formation.

Results and Discussion

Synthesis of Compounds 8, 12, 13, and 14

As an initial approach to the title compounds, we planned the condensation of ferrocenecarboxylic acid (**1**), 1′-aminoferrocene-1-carboxylic acid, or ferrocene-1,1′-dicarboxylic acid with Ala-OMe and the subsequent coupling of the intermediates obtained with *trans*-(–)-(3*R*,4*R*)-3-amino-1-(4-methoxyphenyl)-4-phenylazetidin-2-one (**2**; Scheme 2). Homochiral 3-amino-1-(4-methoxyphenyl)-4-phenyl β-lactam (≡ Alm) **2** was prepared by chiral ester enolate/imine cyclocondensation according to a literature procedure with >99% enantiomeric purity.[8] Compound **2** can be considered a cyclic amide of the corresponding α,β-diamino acid, and we supposed that the remaining "α-amino" group can be coupled with the C-terminus of *N*-substituted alanine by the HOBt/EDC protocol appropriate for the preparation of dipeptides [HOBt = 1-hydroxybenzotriazole, EDC = *N*-(3-dimethylaminopropyl)-*N*′-ethylcarbodiimide hydrochloride]. In a first experiment, Fc-COOH (**1**) was coupled with Ala-OMe resulting in the formation of Fc-CO-Ala-OMe (**3**; Scheme 2). Basic hydrolysis of this intermediate gave Fc-CO-Ala-OH (**5**), which was coupled to Alm to produce Fc-CO-Ala-Alm (**6**). However, on the basis of NMR spectroscopy, racemization of the Ala subunit in this "dipeptide" was observed, which is rationalized by the mechanism[54] presented in Scheme 2. Under the basic conditions employed, deprotonation of the amide group (in its tautomeric imido form) occurs, which leads to the formation of oxazolone **4a**. Further deprotonation/protonation gives enantiomeric oxazolone **4c**, which is in equilibrium with **4a** via enolate **4b**. Opening of the oxazolone ring by hydroxide gives *rac*-**5**, which is converted into diastereomeric mixture *"rac"*-**6** (Scheme 2).

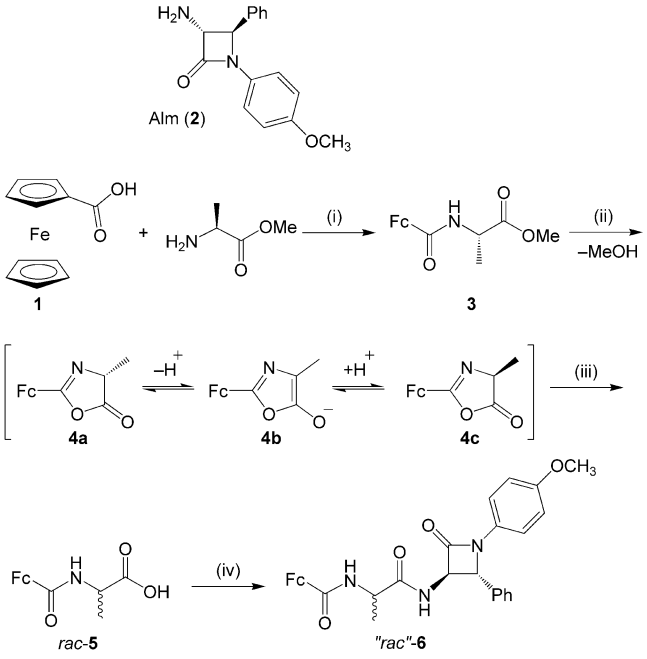

Scheme 2. Attempted synthesis of enantiomerically pure β-lactam-containing ferrocene peptides and mechanism of racemization of the Ala subunit. Reagents and conditions: (i) HOBt/EDC/CH_2Cl_2; (ii) NaOH/dioxane, H_2O; (iii) 1. NaOH/H_2O, 2. HCl/H_2O, pH 1–2; (iv) 1. HOBt/EDC/CH_2Cl_2, 2. **2**/CH_2Cl_2.

Therefore, we developed a different strategy (Scheme 3). Commercially available Boc-Ala (**7**) was coupled with homochiral Alm (**2**) by the HOBt/EDC method and 81% of Boc-Ala-Alm (**8**) was obtained (Scheme 3). Intermediate **8** was deprotected by the action of gaseous HCl in ethyl acetate. The resulting hydrochloride was treated with an excess amount of NEt_3 to give the rather unstable amine **9**. Reaction of **9** with ferrocenecarboxylic acid (**1**) by using the HOBt/EDC technique yielded 40% of optically pure Fc-CO-Ala-Alm (**12**) (Scheme 3). In a similar way, trisamide Boc-Fca-Ala-Alm (**13**) was obtained in 49% yield by starting from Boc-protected **10** (Scheme 3).[42a] In previous attempts to couple HOBt/EDC activated ferrocene-1,1′-dicarboxylic acid with various natural amino acids, only very low yields were obtained. Therefore, ferrocene-1,1′-(dicarbonyl chloride) (**11**)[55] was employed, which upon treatment with Ala-Alm gave 30% of "tetrapeptide" **14**. The relatively poor yield of product **14** might be due to steric hindrance during coupling with two bulky Ala-Alm substituents. However, prolonged reaction times led to decomposition of starting dichloride **7** into unidentified products. Compounds **12**–**14** were characterized by IR (Table 1), NMR (Tables 2, 3, and 4), and CD spectroscopy, as well as by elemental analyses and high-resolution mass spectrometry (Experimental Section).

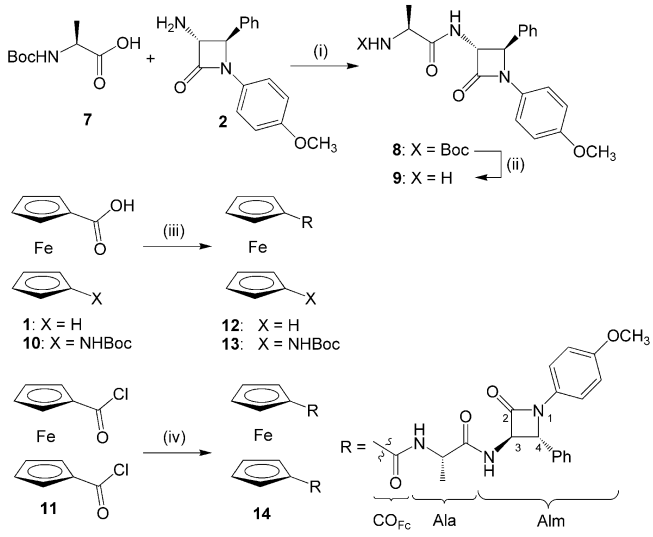

Scheme 3. Synthesis of β-lactam-containing ferrocene peptides **12**, **13**, and **14**. Reagents and conditions: (i) HOBt/EDC/CH_2Cl_2; (ii) 1. EtOAc/HCl(g), 2. Et_3N, pH 9–10/CH_2Cl_2; (iii) 1. HOBt/EDC/CH_2Cl_2, 2. **9**/CH_2Cl_2; (iv) **9**/CH_2Cl_2.

Table 2. 300 MHz ^{1}H NMR [δ / ppm] data of **8**, **12**, **13**, and **14**.[a]

	δ_{NH} ($CDCl_3$)			δ_{NH} ([D_6]DMSO)			$\Delta\delta$ ([D_6]DMSO/$CDCl_3$)		
8	7.98	5.43	–	8.74	7.05	–	0.76	1.62	–
12	8.21	6.79	–	8.81	7.87	–	0.60	1.08	–
13	8.26	7.33	6.82	8.79	7.85	8.46	0.53	0.52	1.64
14	8.53	8.01	–	9.15	8.15	–	0.62	0.14	–

[a] All values are given in the sequence NH_{Alm}, NH_{Ala}, and NH_{Boc}.

IR, NMR, and CD Spectroscopic Analysis of 12, 13, and 14

To elucidate preferred conformations of compounds **12**–**14**, detailed IR and NMR spectroscopic analyses were performed (Tables 1 and 2). The IR spectra of **8** and **12**–**14** display absorptions for the NH groups around 3310 and 3425 cm^{-1} in CH_2Cl_2 ($c \approx 10^{-2}$ M), which suggests the simultaneous presence of hydrogen-bonded and free NH groups. The ratio of these two NH bands remained unchanged when the solution was diluted to $c \approx 10^{-3}$ M, which is strongly indicative of intramolecular hydrogen bonds in these conjugates. However, a detailed assignment to individual NH groups is impossible by IR spectroscopic methods.

Table 1. IR spectroscopic data of **8**, **12**, **13**, and **14** in CH_2Cl_2 ($c \approx 10^{-2}$ M).

	ν_{NH}(free) / cm^{-1}	ν_{NH}(bonded) / cm^{-1}	ν_{CO}(Alm) / cm^{-1}	ν_{CO}(Boc) / cm^{-1}	ν_{CO}(Ala) / cm^{-1}	ν_{CO}(Fc) / cm^{-1}
8	3428	3321	1755		1694	
12	3421	3283	1756		1688	1637
13	3428	3309	1755	1709	1692	1632
14	3425	3320	1755		1683	1642

Table 3. 300 MHz ^{1}H NMR data [δ / ppm] of **8**, **12**, **13**, and **14** in $CDCl_3$.

	8	**12**	**13**	**14**
NH_{Alm}	7.98 (br. d, ^3J = 5.47 Hz, 1 H)	8.21 (d, ^3J = 7.55 Hz, 1 H)	8.26 (d, ^3J = 7.64 Hz, 1 H)	8.53 (d, ^3J = 7.95 Hz, 2 H)
NH_{Ala}	5.43 (d, ^3J = 7.68 Hz, 1 H)	6.79 (d, ^3J = 7.66 Hz, 1 H)	7.34–7.32 (m, 1 H + 5 Ph)	8.01 (d, ^3J = 7.29 Hz, 2 H)
NH_{Boc}	–	–	6.82 (s, 1 H)	–
CH_{Ala}	4.35 (m, 1 H)	4.83 (m, 1 H)	4.75 (m, 1 H)	4.76–4.73 (m, 2 H + Cp)
3-CH_{Alm}	4.75 (d, ^3J = 6.17 Hz, 1 H)	4.70–4.66 (m, 1 H + Cp)	4.79 (dd, ^3J = 2.04, 2.10 Hz, 1 H)	4.93–4.90 (m, 2 H)
4-CH_{Alm}	4.91 (br. s, 1 H)	4.94 (br. s, 1 H)	4.93 (d, ^3J = 1.96 Hz, 1 H)	5.30 (d, ^3J = 1.85 Hz, 2 H)
$C(CH_3)_3/CH_3$	1.39 [m, 12 H, $(CH_3)_3$ + CH_3]	1.54 (d, ^3J = 6.89 Hz, 3 H)	1.49 (s, 9 H), 1.54 (d, ^3J = 7.09 Hz, 3 H)	1.38 (d, ^3J = 7.15 Hz, 6 H)
OCH_3	3.70 (s, 3 H)	3.70 (s, 3 H)	3.71 (s, 3 H)	3.71 (s, 6 H)
Cp-H	–	4.70–4.66 (m, 2 H),4.29–4.26 (m, 2 H),4.18 (m, 5 H)	4.70 (m, 1 H), 4.59 (m, 1 H), 4.45 (m, 1 H), 4.38 (m, 2 H), 4.32 (m, 1 H), 4.07 (m, 1 H), 3.96 (m, 1 H)	4.76–4.73 (m, 4 H), 4.43 (br. s, 2 H), 4.23 (br. s, 2 H)
Ph (5 H)	7.36–7.30 (m, 5 H)	7.34–7.28 (m, 5 H)	7.34–7.32 (m, 5 H + NH_{Alm})	7.36–7.31 (m, 10 H)
Ph (H2-H6	7.13 (d, ^3J = 8.80 Hz, 2 H)	7.13 (d, ^3J = 8.75 Hz, 2 H),	7.14 (d, ^3J = 9.02 Hz, 2 H),	7.18 (d, ^3J = 8.92 Hz, 4 H)
H3-H5)	6.67 (d, ^3J = 8.82 Hz, 2 H)	6.67 (d, ^3J = 8.79 Hz, 2 H)	6.68 (d, ^3J = 9.03 Hz, 2 H)	6.71 (d, ^3J = 8.98 Hz, 4 H)

Table 4. 300 MHz ^{1}H NMR data [δ / ppm] of **8**, **12**, **13**, and **14** in [D_6]DMSO.

	8	**12**	**13**	**14**
NH_{Alm}	8.74 (d, ^3J = 8.27 Hz, 1 H)	8.81 (d, ^3J = 8.18 Hz, 1 H)	8.79 (d, ^3J = 8.17 Hz, 1 H)	9.15 (d, ^3J = 8.28 Hz, 2 H)
NH_{Ala}	7.05 (d, ^3J = 8.97 Hz, 1 H)	7.87 (d, ^3J = 7.72 Hz, 1 H)	7.85 (d, ^3J = 7.54 Hz, 1 H)	8.15 (d, ^3J = 7.84 Hz, 2 H)
NH_{Boc}	–	–	8.46 (s, 1 H)	–
CH_{Ala}	3.98 (m, 1 H)	4.50 (m, 1 H)	4.49–4.41 (m, 1 H + Cp)	4.51 (m, 2 H)
3-CH_{Alm}	4.66 (dd, ^3J = 2.15, 2.16 Hz, 1 H)	4.69 (dd, ^3J = 2.29, 2.31 Hz, 1 H)	4.68 (dd, ^3J = 1.89, 1.81 Hz, 1 H)	4.83–4.80 (m, 2 H + Cp)
4-CH_{Alm}	4.99 (br. s, 1 H)	5.04 (d, ^3J = 2.31 Hz, 1 H)	5.05 (d, ^3J = 1.97 Hz, 1 H)	5.06 (d, ^3J = 2.11 Hz, 2 H)
$CH_3/C(CH_3)_3$	1.20 (d, ^3J = 7.12 Hz, 3 H) 1.39 (s, 9 H)	1.36 (d, ^3J = 7.17 Hz, 3 H)	1.38 (d, ^3J = 7.11 Hz, 3 H) 1.45 (s, 9 H)	1.21 (d, ^3J = 7.28 Hz, 6 H)
OCH_3	3.68 (s, 3 H)	3.67 (s, 3 H)	3.67 (s, 3 H)	3.67 (s, 6 H)
Cp-H	–	4.88 (br. s, 2 H), 4.36–4.35 (m, 2 H), 4.19 (m, 5 H)	4.76 (br. s, 2 H), 4.49–4.41 (m, 2 H + 1 H CH_{Ala}), 4.26 (br. s, 2 H), 3.93 (br. s, 2 H)	4.83–4.80 (m, 2 H + 2 CH_{Alm}), 4.75 (m, 2 H), 4.45 (m, 2 H), 4.36 (m, 2 H)
Ph (5 H)	7.37–7.33 (m, 5 H)	7.40–7.35 (m, 5 H)	7.39–7.33 (m, 5 H)	7.40–7.35 (m, 10 H)
Ph (H2-H6	7.15 (d, ^3J = 8.96 Hz, 2 H)	7.16 (d, ^3J = 8.99 Hz, 2 H)	7.16 (d, ^3J = 8.86 Hz, 2 H)	7.18 (d, ^3J = 8.99 Hz, 4 H)
H3-H5)	6.87 (d, ^3J = 8.97 Hz, 2 H)	6.87 (d, ^3J = 9.01 Hz, 2 H)	6.87 (d, ^3J = 8.88 Hz, 2 H)	6.88 (d, ^3J = 9.02 Hz, 4 H)

In the ^{1}H NMR spectra of conjugate **13** the NH_{Boc} proton is easily assigned, as it shows a singlet without any coupling pattern in contrast to NH_{Alm} and NH_{Ala} (for atom numbering see Scheme 3). Both the latter amide protons are observed as doublets in the 1D ^{1}H NMR spectra due to ^3J coupling to the neighboring CH protons.

To assign NH_{Alm} and NH_{Ala} of **12**, **13**, and **14** unambiguously, 2D NMR experiments were conducted. Long-range couplings between the NH_{Ala} and $CH_{3,Ala}$ groups (TOCSY experiments; for **14** see Figure 1, top) and NOE cross peaks between NH_{Ala}/CH_{Ala} and NH_{Alm}/3-CH_{Alm}/4-CH_{Alm}/CH_{Ala} (NOESY experiments; for **14** see Figure 1, bottom) allow the assignment of the resonances to individual NH_{Ala} and NH_{Alm} groups. Similarly, the NH_{Alm} and NH_{Ala} groups of **13** and **14** were conclusively assigned.

To address the question of which NH group is preferentially engaged in hydrogen bonds, NH chemical shifts δ_{NH} were measured in different solvents. Chemical shift variation from [D_6]DMSO (forming strong hydrogen bonds to NH groups) to $CDCl_3$ ($\Delta\delta$) provides a measure of the extent to which an amide proton is engaged in hydrogen bonding. If the shift variation of a particular NH proton is medium small the NH proton is considered to be involved in a strong hydrogen bond in $CDCl_3$ solution. Medium shifts are representative for weaker hydrogen bonds, whereas large shifts are compatible with rather weak or no hydrogen bonds. On the basis of our previous investigation of the ferrocene peptides Boc-Ala_n-Fn-Ala_m-OMe (n = 0–2; m = 1–2) related to those described in the present study, we define approximate ranges of $\Delta\delta$ decisive for the estimation of specific hydrogen bonds: $\Delta\delta < 0.6$ ppm suggest (very) strong hydrogen bonds, $\Delta\delta$ = 0.6–0.9 ppm indicate medium strong bonds and $\Delta\delta > 1$ are designated non-hydrogen-bonded NH groups. These data were corroborated by ^{1}H NMR variation ratio measurements and CD spectroscopy.[44a] The correlation between $\Delta\delta$ and the strength of an intramolecular hydrogen bond NH···OC (i.e., the population of conformations involving such bonds) is described elsewhere.[44b,61]

The ^{1}H NMR spectra of **8** and **12**–**14** suggest that the proton of the NH_{Alm} group is involved in hydrogen bonds in all cases, as these protons resonate at fields well below δ = 7 ppm in $CDCl_3$, and according to the previous statement the shift variations $\Delta\delta$ = 0.76 (for **8**), 0.60 (for **12**), 0.53 (for **13**), and 0.62 (for **14**) ppm indicate medium strong hydrogen bonds (Table 2). Furthermore, the resonances are only weakly dependent on the concentration (Figures 2 and 3), which thus suggests participation of NH_{Alm} in intramolecu-

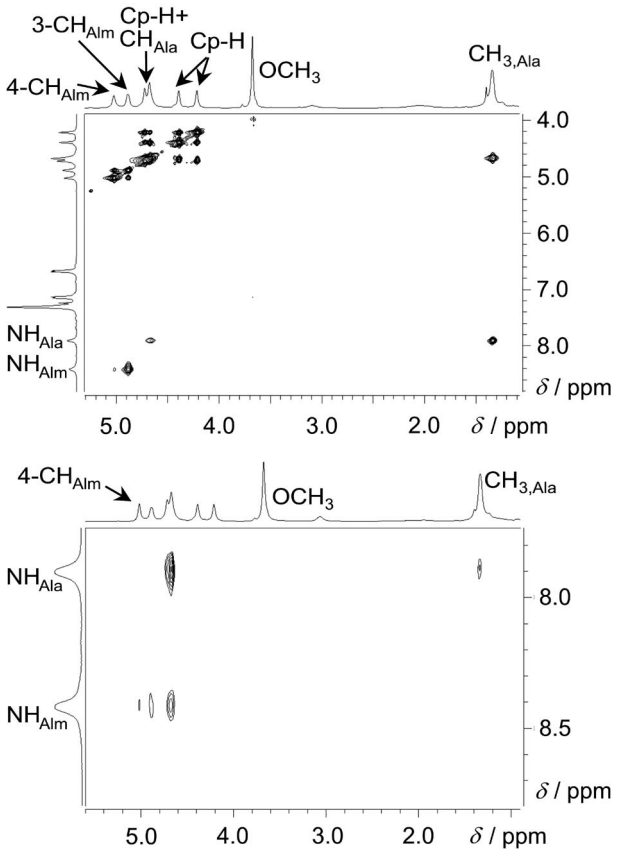

Figure 1. Partial TOCSY (top) and NOESY (bottom) NMR spectra (400 MHz) of compound **14** (for atom numbering see Scheme 3).

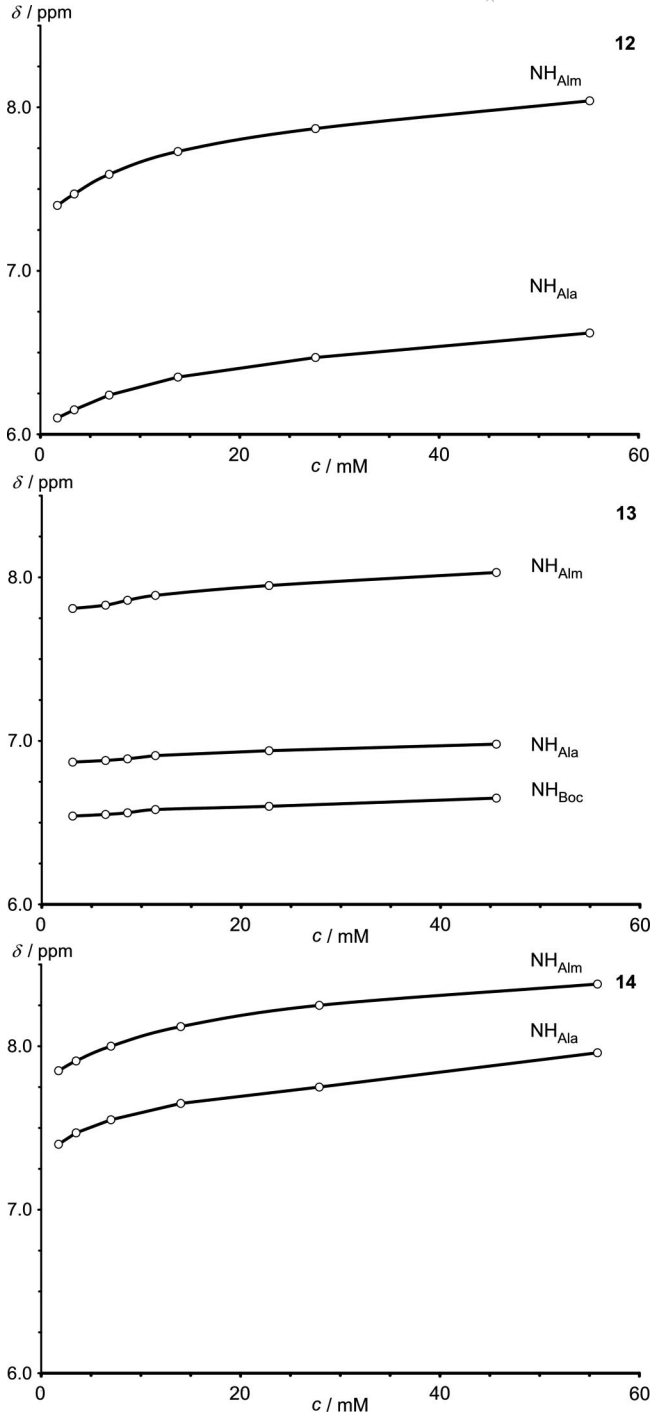

Figure 2. Plots of the concentration-dependent ^{1}H NMR chemical shifts (200 MHz) of amide protons of **12**, **13**, and **14** in $CDCl_3$ (the lines are a guide to the eye).

lar hydrogen bonds in molecules **8** and **12**–**14**. The same arguments apply for the NH_{Ala} protons of **13** and **14** but not for **8** and **12**. The chemical shift variation of NH_{Ala} in **14** is small ($\Delta\delta$ = 0.14 ppm) relative to that of **13** ($\Delta\delta$ = 0.52 ppm), which thus implies stronger hydrogen bonds in **14** involving this NH group. In addition, the data of the NH_{Boc} proton of **13** suggest that this proton practically does not participate in hydrogen bonds.

Possible helical conformations of the ferrocene units of **12**, **13**, and **14** were probed by using CD spectroscopy (Figures 4, 5, 6, and 7). In dichloromethane, disubstituted ferrocenes **13** and **14** display a positive Cotton effect around the ferrocene absorption (λ = 450–500 nm), whereas **12** is nearly "CD-silent" in this spectral region suggesting ordered (*P*)-helical conformations of **13** and **14** in CH_2Cl_2 solution but nonordered ferrocene conformations of **12**. Even in the presence of 10% DMSO (Figures 5 and 6) as a strongly hydrogen-bond accepting solvent these ordered structures are retained (at least partly for **13**; fully for **14**). In the solid state, the CD data of **13** and **14** suggest (*P*)-helical conformations as well, whereas the CD data of **12** suggest an (*M*)-helical conformation, which is most likely due to packing forces and intermolecular hydrogen bonds only (Figure 7).

The combined experimental data suggest that in chloroform or dichloromethane solution **8** and **12** display simple intramolecular hydrogen bonds from the NH_{Alm} group to the CO_{Boc} (**8**) and CO_{Fc} (**12**) units, respectively (γ-turns[56]). In contrast, 1,1′-disubstituted ferrocene derivatives **13** and **14** display, in addition to that γ-turn, hydrogen-bond contacts *between* the 1-substituent and the 1′-substituent involving the NH_{Ala} moiety. These interchain hydrogen bonds also result in ordered arrangements of the ferrocene unit in

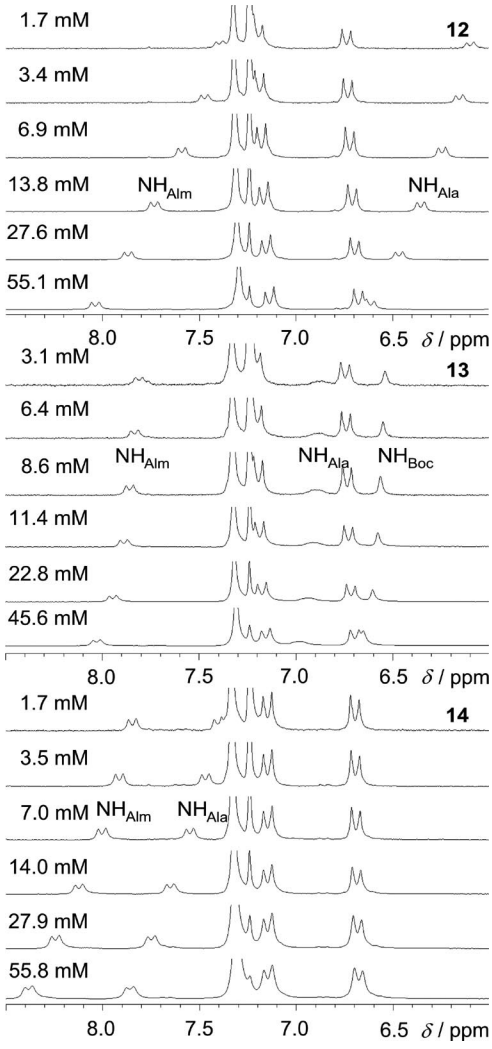

Figure 3. Concentration-dependent ^{1}H NMR spectra of **12**, **13**, and **14** in $CDCl_3$ (200 MHz).

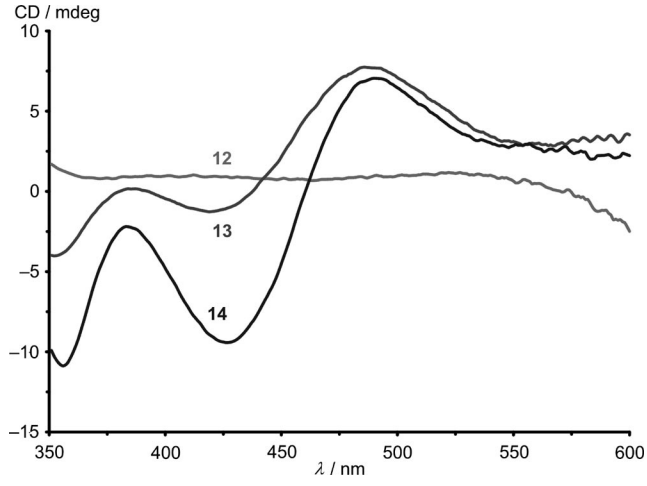

Figure 4. CD spectra of **12**, **13**, and **14** in CH_2Cl_2 ($c = 6\times10^{-4}$ M).

13 and **14** with positive helical orientations of the Cp rings, which gives rise to the observed positive Cotton effects in the CD spectra, whereas no ordered helical structure is ob-

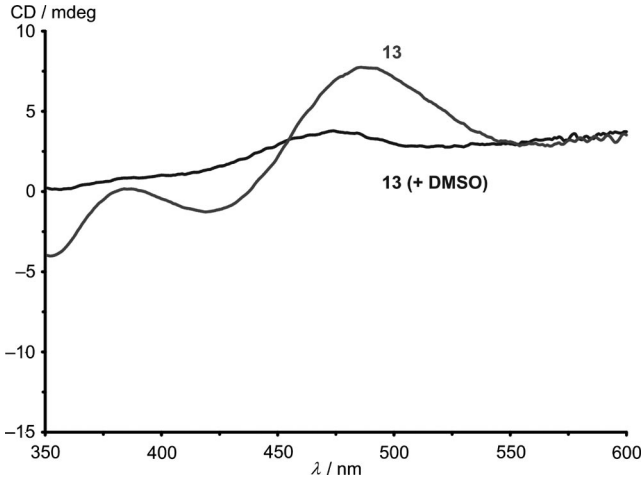

Figure 5. CD spectra of **13** in CH_2Cl_2 ($c = 6\times10^{-4}$ M) and CH_2Cl_2/DMSO (10%).

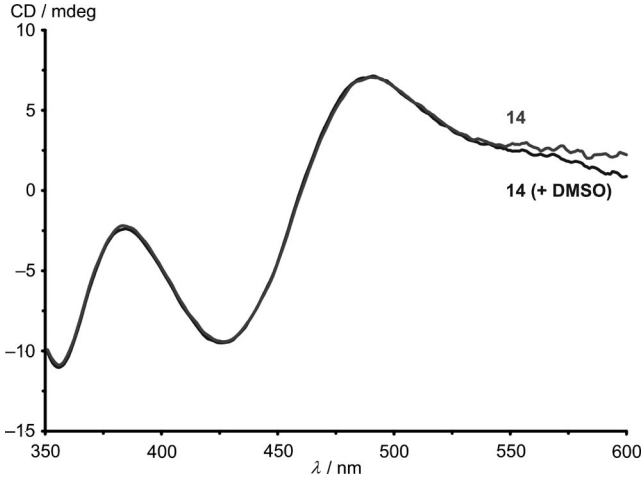

Figure 6. CD spectra of **14** in CH_2Cl_2 ($c = 6\times10^{-4}$ M) and CH_2Cl_2/DMSO (10%).

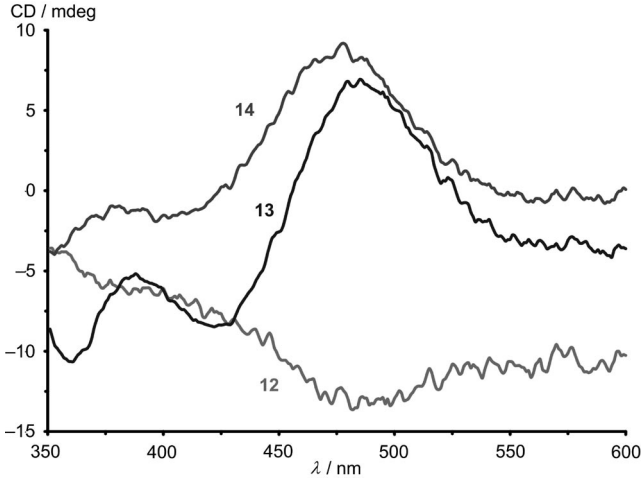

Figure 7. CD spectra of **12**, **13**, and **14** in the solid state.

served for **12**. The CD spectra of **13** and **14** in CH_2Cl_2 and in CH_2Cl_2/DMSO (10%) additionally corroborate the higher stability of the ordered structure of **14** relative to that of **13** in accordance with the NMR spectroscopic data ($\Delta\delta$ of NH_{Ala}). To further shed light on the possible conformations of **13** and **14** in solution, DFT calculations (B3LYP, LanL2DZ[57]) were performed on truncated models of **12**, **13**, and **14** (all aryl groups were replaced by hydrogen atoms). The B3LYP, LanL2DZ methodology was applied previously to elucidate conformations of ferrocene bioconjugates and ferrocene oligoamides.[42e–42g,45,58–62]

DFT Modeling of 12

The geometry-optimized structure of **12** is shown in Figure 8. Ferrocene-lactam conjugate **12** displays an intramolecular hydrogen bond from NH_{Alm} to CO_{Fc} (γ-turn; distance O···H 1.89 Å, Scheme 4). This finding is fully consistent with the experimental NMR spectroscopic data (vide supra). Additionally, the observed vicinal coupling constant $^3J(NH_{Ala}, CH_{Ala})$ = 7.66 Hz and the derived CO_{Fc}–NH_{Ala}–CH_{Ala}–CO_{Ala} torsion angle of –154° fits reasonably well to the DFT calculated torsion angle of –147°.[63] This NH_{Alm}···CO_{Fc} hydrogen bond does not promote any helicity of the ferrocene unit, which is also compatible with the negligible Cotton effect of **12** in the CD spectrum (Figure 4).

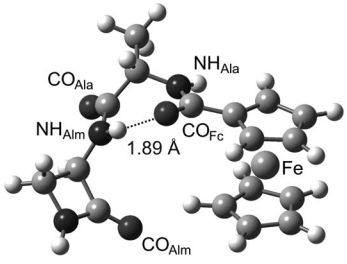

Figure 8. DFT-optimized geometry of **12**.

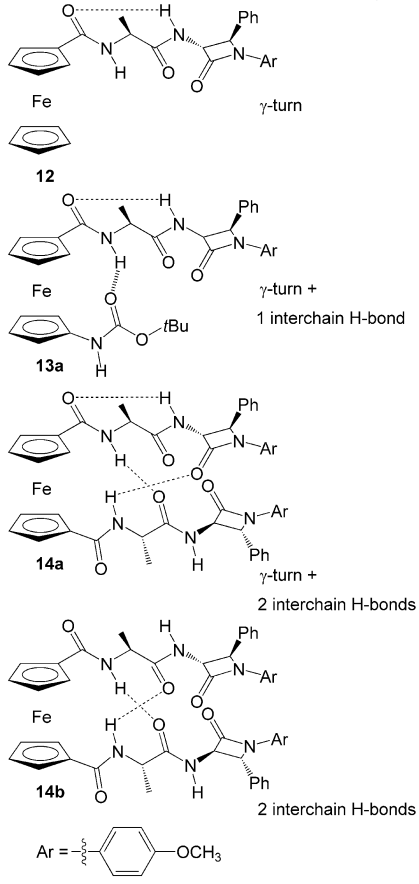

Scheme 4. Schematic representations of the most stable hydrogen-bonding arrangements in **12**, **13**, and **14**.

DFT Modeling of 13

Several local minima were located on the energy landscape of **13** (Figure 9, Table 5). The NH_{Alm}···CO_{Fc} (γ-turn) hydrogen bond displayed by **12** is also observed in conformations **13a**(*M*,*P*), **13g**′, and **13h**′. Additional hydrogen bonds between the substituents of the type NH_{Boc}···CO_{Ala} or NH_{Boc}···CO_{Fc} are observed in **13b**(*M*,*P*)/**13d**(*M*,*P*) and **13c**(*M*,*P*)/**13f**(*M*,*P*), respectively, whereas the most stable conformers **13a**(*M*,*P*) display additional hydrogen bonds between NH_{Ala} and CO_{Boc} (Figure 9). Conformations without hydrogen bonds between the substituents (**13g**, **13g**′, **13h**, and **13h**′) are destabilized relative to hydrogen-bonded systems. Thus, the calculations support the experimental finding that the most stable hydrogen bonds are the interchain H-bonds formed by NH_{Ala} and the intrachain H-bonds by NH_{Alm} (γ-turn), whereas NH_{Boc} is only marginally involved in hydrogen bonding. Furthermore, the (*P*)-helical conformation **13a**(*P*) is calculated to be more stable than its pseudo mirror image **13a**(*M*) in full agreement with the observed positive Cotton effect [indicative of (*P*)-helical ferrocene] of **13** in the CD spectra. Thus, the most stable conformation of **13** is represented by **13a**(*P*) with one γ-turn and one interchain H-bond (Scheme 4).

DFT Modeling of 14

For Fcd-amino acid conjugates, it has been shown that two interchain hydrogen bonds NH_{Ala}···CO_{Ala} (β-turn-like, type II, Scheme 1) are exceptionally stable.[31–41] Indeed, this is also computed as a stable conformation of **14** with a (*P*)-helical ferrocene moiety (conformer **14b**; NH_{Ala}···CO_{Ala} 1.98 and 1.94 Å). However, additional stable conformations of **14** (Figure 10, Scheme 4, **14a** and **14c**) have been observed during the geometry optimizations that feature *three* hydrogen bonds, namely one γ-turn (NH_{Alm}···CO_{Fc} 1.89 Å), one interchain H-bond NH_{Ala}···CO_{Ala} (1.86 Å), and one interchain hydrogen bond NH_{Ala}···CO_{Alm} (2.03 Å) in **14a** and two γ-turns (NH_{Alm}···CO_{Fc} 1.87 and 2.08 Å) and one interchain H-bond NH_{Ala}···CO_{Fc} (1.99 Å) in **14c**. In **14b**, γ-turns are not feasible, as this would disturb the planarity of the amide bonds between Ala and Alm.

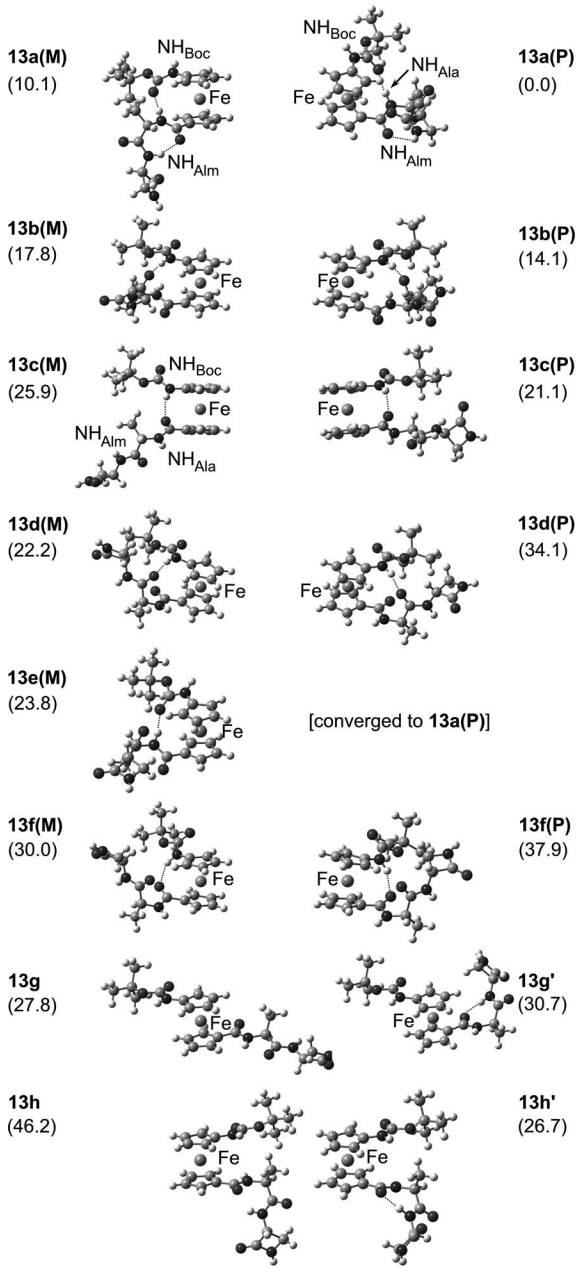

Figure 9. DFT-optimized geometries of **13** along with their relative energies (in kJ mol^{-1}) in parentheses.

Table 5. DFT-calculated relative energies and (N)H···O distances of hydrogen bonds of conformers of **13**.

	E_{rel} / kJ mol^{-1}	NH_{Boc}···CO_{Ala} / Å	NH_{Boc}···CO_{Fc} / Å	NH_{Ala}···CO_{Boc} / Å	NH_{Alm}···CO_{Fc} / Å
13a(*M*)	10.1			1.86	1.94
13a(*P*)	0.0			1.87	1.86
13b(*M*)	17.8	1.81			
13b(*P*)	14.1	1.86			
13c(*M*)	25.9		2.08		
13c(*P*)	21.1		2.17		
13d(*M*)	22.2	1.91			
13d(*P*)	34.1	1.92			
13e(*M*)	23.8			1.84	
13f(*M*)	30.0		2.06		
13f(*P*)	37.9		1.96		
13g	27.8				
13g′	30.7				1.86
13h	46.2				
13h′	26.7				1.86

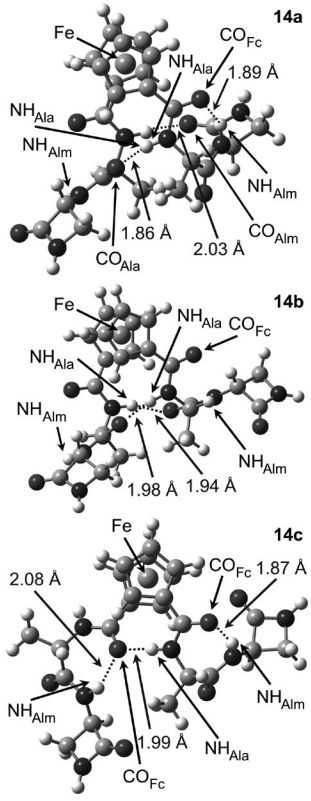

Figure 10. DFT-optimized geometries of **14**.

The additional hydrogen bonds in conformers **14a** and **14c** stabilize **14a** by 21.9 kJ mol^{-1} and **14c** by 4.1 kJ mol^{-1} relative to the energy of **14b**. Thus, intrachain γ-turns can override the expected double interchain β-turn-like hydrogen bond system (Schemes 1 and 4). The high stabilization energy of **14a** relative to that of **14b** is much more than the expected energy gain from a single isolated hydrogen bond. Thus, in **14a** the three hydrogen bonds represent a cooperative network system. This is also substantiated by the experimentally observed higher stability of the interchain NH_{Ala}···CO hydrogen bond in **14** relative to that of **13** (NMR, Table 2) and the higher stability of the (*P*)-helical ferrocene conformation in **14** (CD, Figures 5 and 6).

Conclusions

For the first time ferrocene conjugates with β-lactam rings including alanine spacers were synthesized. Their conformational preferences were elucidated on the basis of spectroscopic techniques in solution and theoretical methods with the use of DFT calculations. The compounds prepared are analogues of Fc-CO(AA)$_n$OMe (Scheme 1, type I; AA = amino acid), Fn[CO(AA)$_n$OMe]$_2$ (Scheme 1, type II), and Boc-Fca-(AA)$_n$OMe (Scheme 1, type III). It was found that similarly as in type II and type III conjugates, Fn[CO-Ala-Alm]$_2$ (**14**) and Boc-Fca-Ala-Alm (**13**) feature

medium strong hydrogen bonds spanning NH_{Ala} or NH_{Boc} with CO groups of the juxtaposed strand. In addition, these compounds are stabilized by intrachain $NH_{Alm}\cdots CO_{Fc}$ interactions (γ-turns). This is especially evident for the preferred conformation of **14**, for which a novel cooperative three-hydrogen-bond network initiated by an intrachain γ-turn is proposed (Scheme 4, **14a**). The interchain hydrogen bonds in bioconjugates **13** and **14** induce a (*P*)-helical arrangement of the ferrocene moiety, which is particularly stable in **14**.

Experimental Section

General Considerations: The syntheses were carried out under an atmosphere of argon. CH_2Cl_2 used for synthesis and FTIR spectroscopy was dried (P_2O_5), distilled from CaH_2, and stored over molecular sieves (4 Å). EDC, HOBt, and Boc-L-alanine (**1**) (Aldrich) were used as received. Products were purified by preparative thin-layer chromatography on silica gel (Merck, Kieselgel 60 HF_{254}) by using EtOAc and EtOAc/CH_2Cl_2 as eluents, as well as by recrystallization from CH_2Cl_2/petroleum ether. Melting points were determined with a Reichert Thermovar apparatus. IR spectra were recorded as CH_2Cl_2 solutions with a Bomem MB 100 mid FTIR spectrophotometer. ^1H and ^{13}C NMR spectra were recorded with a Varian Gemini 300 spectrometer in $CDCl_3$ and [D_6]DMSO solutions with Me_4Si as the internal standard or with a Varian Unity Plus 400 or a Bruker AX 200 spectrometer. MS and HRMS (FAB) were recorded with a JEOL JMS-700. CD spectra were recorded as CH_2Cl_2 solutions and CH_2Cl_2 solutions with 10% of DMSO with CD spectrophotometer Jasco-810. Elemental analyses were performed using a Perkin–Elmer 2400 series II CHNS/O analyzer.

tert-Butyl 1′-carboxy-1-ferrocenecarbamate (**10**) and ferrocene-1,1′-(dicarbonyl chloride) (**11**) were prepared according to the literature.[42a,55] *trans*-(–)-(3*R*,4*R*)-3-Amino-1-(4-methoxyphenyl)-4-phenylazetidin-2-one (**2**) was prepared according to the literature.[8]

Computational Method: Density functional calculations were carried out with the Gaussian03/DFT[57] series of programs. The B3LYP formulation of density functional theory was used by employing the Lanl2DZ basis set.[57] All points were characterized as minima (N_{imag} = 0) by frequency analysis.

Boc-Ala-Alm (8): To a suspension of **7** (31.7 mg, 0.168 mmol) in dry dichloromethane (2 mL) was added HOBt (31.7 mg, 0.168 mmol). After cooling to 0 °C, EDC was added (64.26 mg, 0.3354 mmol), and the reaction mixture was stirred for 3 h at room temperature. Thereafter, **2** (30 mg, 0.112 mmol) was added, and the solution was stirred for 72 h, washed with a saturated solution of $NaHCO_3$, 10% aqueous citric acid, and brine, dried with Na_2SO_4, and evaporated in vacuo. TLC purification (EtOAc/CH_2Cl_2, 5:1) of the crude product gave **8** (49.1 mg, 81%) in the form of white crystals. M.p. 71–73 °C. IR (CH_2Cl_2): $\tilde{\nu}$ = 3426 (m, NH_{free}), 3322 (w, NH_{assoc}), 2934, 2839 (w, CH_{aliph}), 1755 (s, C=O_{Alm}), 1699 (s, C=O), 1694 (s, C=O), 1513 (s, amide II) cm^{-1}. ^{13}C NMR (75 MHz, $CDCl_3$): δ = 17.97 (CH), 27.83 (3×CH_3), 49.42 (CH_3), 54.84 (OCH_3), 63.08 (4-*C*H_{Alm}), 64.84 (3-*C*H_{Alm}), 79.75 [O*C*(CH_3)$_3$], 113.62 (C-3, C-5, PhN), 118.19 (C-2, C-6, *Ph*N), 125.58 (C-2, C-6, *Ph*C), 128.26 (C-4, *Ph*C), 128.66 (C-3, C-5, *Ph*C), 129.91 (C-1, *Ph*C), 135.53 (C-1, PhN), 155.25 (COO), 155.66 (C-4, PhN), 163.27 (CO), 172.94 (*C*OCH) ppm. HRMS (FAB+): calcd. for $C_{24}H_{29}N_3O_5$ 439.2107; found 439.2070.

Ala-Alm (9): A suspension of **8** (86 mg, 0.196 mol) in ethyl acetate (6 mL) was cooled to 0 °C and treated with gaseous HCl for 2 h. The reaction mixture was washed with water and 10% aqueous citric acid. After removal of the organic layer, Et_3N was added to the aqueous layer (pH 9–10), and the solution was extracted with dichloromethane. The organic layer was dried with Na_2SO_4 and evaporated in vacuo. TLC purification (EtOAc/CH_2Cl_2, 5:1) of the crude product gave **9** (31.5 mg, 47%). IR (CH_2Cl_2): $\tilde{\nu}$ = 3362 (m, NH_{assoc}), 2958, 2933, 2839 (w, CH_{aliph}), 1755 (s, C=O_{Alm}), 1681 (s, C=O), 1513 (s, amide II) cm^{-1}. Amine **9** is very unstable and reliable NMR spectroscopic data could not be obtained.

Fc-CO-Ala-Alm (12): To a solution of ferrocenecarboxylic acid (**1**; 46 mg, 0.20 mmol) in dry dichloromethane (3 mL) was added HOBt (41.7 mg, 0.30 mmol), and the mixture was cooled to 0 °C. Thereafter, EDC was added (57.5 mg, 0.30 mmol), and the reaction mixture was stirred for 1 h at room temperature. After the addition of **9** [0.112 mmol; obtained from **8** by successive treatment with HCl(g) in ethyl acetate, evaporation of solvent and addition of Et_3N to pH 10 in CH_2Cl_2], the solution was stirred for 24 h. The mixture was worked up as described for compound **8**. TLC purification (EtOAc/CH_2Cl_2, 5:2) of the crude product gave orange crystals of **12** (22.6 mg, 40%). M.p. 114–116 °C (CH_2Cl_2/petroleum ether). IR (CH_2Cl_2): $\tilde{\nu}$ = 3421 (m, NH_{free}), 3283 (w, NH_{assoc}), 3090 (w, CH_{arom}), 2935, 2839 (m, CH_{aliph}), 1756 (s, C=O_{Alm}), 1688 (s, C=O), 1637 (s, C=O), 1513 (s, amide II) cm^{-1}. ^{13}C NMR (75 MHz, $CDCl_3$): δ = 18.71 (CH), 48.90 (CH_3), 55.52 (OCH_3), 63.51 (4-*C*H_{Alm}), 65.79 (3-*C*H_{Alm}), 68.34 (Cp), 68.71 (Cp), 70.03 (5 C, $Cp_{unsubst}$), 71.01 (2 C, Cp), 75.04 (C-1, Cp), 114.37 (C-3, C-5, PhN), 118.90 (C-2, C-6, PhN), 126.34 (C-2, C-6, *Ph*C), 128.89 (C-4, *Ph*C), 129.33 (C-3, C-5, *Ph*C), 130.78 (C-1, *Ph*C), 136.42 (C-1, PhN), 156.39 (C-4, PhN), 163.80 (CO), 171.09 (*C*OCH), 173.43 (*C*OCp) ppm. HRMS (FAB+): calcd. for $C_{30}H_{29}N_3O_4Fe$ 551.1507; found 551.1476. $C_{30}H_{29}FeN_3O_4$ (551.42): calcd. C 65.35, H 5.30, N 7.62; found C 65.16, H 5.70, N 7.47.

Boc-Fca-Ala-Alm (13): To a solution of **10** (81.04 mg, 0.235 mmol) in dry dichloromethane (6 mL) was added HOBt (49.04 mg, 0.352 mmol). After cooling to 0 °C, EDC (67.5 mg, 0.352 mmol) was added, and the reaction mixture was stirred for 1 h at room temperature. Compound **9** [0.117 mmol; obtained from **8** by successive treatment with HCl(g) in ethyl acetate, evaporation of solvent and addition of Et_3N to pH 10 in CH_2Cl_2] was added, and the solution was stirred for an additional 48 h. The usual work-up (as described for compound **8**) gave the crude product, which was purified by TLC (EtOAc/CH_2Cl_2, 5:2) to afford orange crystals of **13** (33.2 mg, 49%). M.p. 106–108 °C (CH_2Cl_2/petroleum ether). IR (CH_2Cl_2): $\tilde{\nu}$ = 3428 (m, NH_{free}), 3309 (w, NH_{assoc}), 3012 (w, CH_{arom}), 2934 (w, CH_{aliph}), 1755 (m, C=O_{Alm}); 1709 (s, C=O), 1692 (s, C=O), 1632 (s, C=O), 1513 (s, amide II) cm^{-1}. ^{13}C NMR (75 MHz, $CDCl_3$): δ = 17.41 (CH), 28.50 (3×CH_3), 49.21 (CH_3), 55.50 (OCH_3), 63.94 (4-*C*H_{Alm}), 65.54 (3-*C*H_{Alm}), 62.42, 63.19, 65.61, 66.04, 69.62, 69.88, 71.46 and 71.56 (8 C, Cp), 76.44 (C-1, Cp), 80.61 (C-1′, Cp), 97.33 [O*C*(CH_3)$_3$], 114.34 (C-3, C-5, PhN), 118.94 (C-2, C-6, PhN), 126.35 (C-2, C-6, *Ph*C), 128.84 (C-4, *Ph*C), 129.26 (C-3, C-5, *Ph*C), 130.71 (C-1, *Ph*C), 136.40 (C-1, PhN), 153.92 (COO), 156.39 (C-4, PhN), 164.06 ($CO_{β\text{-lact.}}$), 171.40 (*C*OCH), 173.62 (*C*OCp) ppm. HRMS (FAB+): calcd. for $C_{35}H_{38}N_4O_6Fe$ 666.2141; found 666.2177. $C_{35}H_{38}FeN_4O_6$ (666.56): calcd. C 63.07, H 5.75, N 8.41; found C 62.67, H 5.55, N 8.01.

Fn(CO-Ala-Alm)$_2$ (14): To a cooled solution (0 °C) of **9** [1.480 mmol; obtained from **8** by successive treatment with HCl(g) in ethyl acetate, evaporation of solvent and addition of Et_3N to pH 10 in CH_2Cl_2] in dry dichloromethane (10 mL) was dropwise added

a solution of ferrocene-1,1′-(dicarbonyl chloride) (**11**; 205 mg, 0.660 mmol) in the same solvent (10 mL). The reaction mixture was stirred for 3 d at room temperature, washed with a 5% aqueous $NaHCO_3$ and brine, dried with Na_2SO_4, and evaporated in vacuo. TLC purification (EtOAc) of the crude product gave orange crystals of **14** (181.5 mg, 30%). M.p. 161–163 °C (CH_2Cl_2/petroleum ether). IR (CH_2Cl_2): $\tilde{\nu}$ = 3425 (m, NH_{free}), 3320 (w, NH_{assoc}), 3010 (w, CH_{arom}), 2934, 2839 (w, CH_{aliph}), 1755 (s, $C{=}O_{Alm}$); 1683 (m, C=O), 1642 (m, C=O), 1513 (s, amide II) cm^{-1}. ^{13}C NMR (75 MHz, $CDCl_3$): δ = 17.44 (CH), 49.03 (CH_3), 55.30 (OCH_3), 63.51 (4-*C*H_{Alm}), 65.52 (3-*C*H_{Alm}), 70.08, 70.81, 71.28 and 71.83 (8 C, Cp), 76.31 (C-1, C-1′, Cp), 114.11 (C-3, C-5, C-3′, C-5′, PhN), 118.74 (C-2, C-6, C-2′, C-6′, PhN), 126.00 (C-2, C-6, C-2′, C-6′, *Ph*C), 128.68 (C-4, C-4′, *Ph*C), 129.11 (C-3, C-5, C-3′, C-5′, *Ph*C), 130.61 (C-1, C-1′, *Ph*C), 136.31 (C-1, C-1′, PhN), 156.24 (C-4, C-4′, PhN), 164.15 (CO), 170.20 (2 × *C*OCH), 174.36 (2 × *C*OCp) ppm. HRMS (FAB+): calcd. for $C_{50}H_{48}N_6O_8Fe$ 916.2883; found 916.2900. $C_{50}H_{48}FeN_6O_8$ (916.81)·$2H_2O$: calcd. C 63.03, H 5.50, N 8.82; found C 62.88, H 5.88, N 8.55.

Supporting Information (see footnote on the first page of this article): DFT-calculated Cartesian coordinates of conformers of **12**, **13**, and **14**.

Acknowledgments

We thank the Ministry of Science, Education and Sport of Croatia for support through grants No. 058-1191344-3122 and No. 098-0982915-2948 and the Deutsche Forschungsgemeinschaft for financial support.

[1] G. S. Singh, *Tetrahedron* **2003**, *59*, 7631–7649.
[2] G. I. Georg, *The Organic Chemistry of β-Lactams*, VCH, New York, **1992**, and references therein.
[3] T. C. Maier, J. Podleck, *Eur. J. Org. Chem.* **2004**, 4379–4386.
[4] M. Liu, M. P. Sibi, *Tetrahedron* **2002**, *58*, 7991–8035.
[5] C. Palomo, J. M. Aizpurua, I. Ganboa, M. Oiarbide, *Amino Acids* **1999**, *16*, 321–343.
[6] I. Ojima, F. Delaloge, *Chem. Soc. Rev.* **1997**, *26*, 377–386.
[7] T. Poljak, K. Molčanov, A. Višnjevac, I. Habuš, V. Kovač, V. Rapić, *J. Mol. Struct.* **2005**, *751*, 60–64.
[8] I. Ojima, I. Habuš, *Tetrahedron Lett.* **1990**, *31*, 4289–4292.
[9] I. Ojima, I. Habuš, M. Zhao, G. I. Georg, L. R. Jayasinghe, *J. Org. Chem.* **1991**, *56*, 1681–1683.
[10] D. J. Hart, D.-C. Ha, *Chem. Rev.* **1989**, *89*, 1447–1465.
[11] I. Ojima, *Acc. Chem. Res.* **1995**, *28*, 383–389.
[12] M. J. Jung in *Chemistry and Biochemistry of Amino Acids* (Ed.: G. C. Barrett), Chapman and Hall, New York, **1985**, p. 227.
[13] I. Ojima, I. Habuš, M. Zhao, M. Zucco, Y. H. Park, C. M. Sun, T. Brigaud, *Tetrahedron* **1992**, *48*, 6985–7012.
[14] *Taxane Anticancer Agents: Basic Science and Current Status* (Eds.: G. I. Georg, T. T. Chen, I. Ojima, D. M. Vyas), ACS, Washington, DC, **1995**.
[15] M. Suffness, *Taxol: Science and Applications*, CRC Press, New York, **1995**.
[16] S. Thaisrivongs, D. T. Pals, L. T. Kroll, S. R. Turner, F.-S. Han, *J. Med. Chem.* **1987**, *30*, 976–982.
[17] J. R. Huff, *J. Med. Chem.* **1991**, *34*, 2305–2314.
[18] M. A. Sierra, M. J. Mancheno, R. Vicente, M. Gomez-Gallego, *J. Org. Chem.* **2001**, *66*, 8920–8925.
[19] A. Ghatak, F. F. Becker, B. K. Banik, *Heterocycles* **2000**, *53*, 2769–2773.
[20] Y.-Y. Tong, J. J. R. Frausto da Silva, A. J. L. Pobiero, G. Wagner, R. J. Hermann, *J. Organomet. Chem.* **1998**, *552*, 17–21.
[21] E. I. Edwards, R. Epton, G. Marr, *J. Organomet. Chem.* **1976**, *107*, 351–357.
[22] K. M. Hassan, *Z. Naturforsch.* **1978**, *33*, 1508–1514.
[23] E. I. Edwards, R. Epton, G. Marr, *J. Organomet. Chem.* **1975**, *85*, C23–C25.
[24] K. Di Gleria, H. A. O. Hill in *Advances in Biosensors Vol. 2* (Ed.: A. P. F. Turner), JAI Press, Greenwich, **1992**, p. 53.
[25] H. A. O. Hill, N. J. Hunt, *Methods Enzymol.* **1993**, *227*, 501–522.
[26] K. Di Gleria, C. M. Halliwell, C. Jacob, H. A. O. Hill, *FEBS Lett.* **1997**, *400*, 155–157.
[27] a) G. Hölzemann, *Kontakte (Darmstadt)* **1991**, *1*, 3–13; b) G. Hölzemann, *Kontakte (Darmstadt)* **1991**, *2*, 56–64.
[28] D. Obrecht, M. Altorfer, J. A. Robinson, *Adv. Med. Chem.* **1999**, *4*, 1–68.
[29] K. S. Kee, S. D. S. Jois, *Curr. Pharm. Des.* **2003**, *9*, 1209–1224.
[30] T. Moriuchi, T. Hirao, *Chem. Soc. Rev.* **2004**, *33*, 294–301.
[31] a) S. Chowdhury, G. Schatte, H.-B. Kraatz, *Angew. Chem.* **2008**, *120*, 7164–7167; *Angew. Chem. Int. Ed.* **2008**, *47*, 7056–7059; b) S. Chowdhury, D. A. R. Sanders, G. Schatte, H.-B. Kraatz, *Angew. Chem.* **2006**, *118*, 765–768; *Angew. Chem. Int. Ed.* **2006**, *45*, 751–754.
[32] T. Moriuchi, T. Nagai, T. Hirao, *Org. Lett.* **2005**, *7*, 5265–5268.
[33] S. I. Kirin, D. Wissenbach, N. Metzler-Nolte, *New J. Chem.* **2005**, *29*, 1168–1173.
[34] S. Chowdhury, G. Schatte, H.-B. Kraatz, *Dalton Trans.* **2004**, 1726–1730.
[35] F. E. Appoh, T. C. Sutherland, H.-B. Kraatz, *J. Organomet. Chem.* **2004**, *689*, 4669–4677.
[36] T. Moriuchi, K. Yoshida, T. Hirao, *Org. Lett.* **2003**, *5*, 4285–4288.
[37] T. Moriuchi, A. Nomoto, K. Yoshida, T. Hirao, *Organometallics* **2001**, *20*, 1008–1013.
[38] T. Moriuchi, A. Nomoto, K. Yoshida, A. Ogawa, T. Hirao, *J. Am. Chem. Soc.* **2001**, *123*, 68–75.
[39] T. Moriuchi, A. Nomoto, K. Yoshida, T. Hirao, *J. Organomet. Chem.* **1999**, *589*, 50–58.
[40] A. Nomoto, T. Moriuchi, S. Yamazaki, A. Ogawa, T. Hirao, *Chem. Commun.* **1998**, 1963–1964.
[41] R. S. Herrick, R. M. Jarret, T. P. Curran, D. R. Dragoli, M. B. Flaherty, S. E. Lindyberg, R. A. Slate, L. C. Thornton, *Tetrahedron Lett.* **1996**, *37*, 5289–5292.
[42] a) L. Barišić, V. Rapić, V. Kovač, *Croat. Chem. Acta* **2002**, *75*, 199–210; b) G. Pavlović, L. Barišić, V. Rapić, I. Leban, *Acta Crystallogr., Sect. E* **2002**, *58*, m13–15; c) G. Pavlović, L. Barišić, V. Rapić, V. Kovač, *Acta Crystallogr., Sect. C* **2003**, *59*, m55–57; d) L. Barišić, V. Rapić, H. Pritzkow, G. Pavlović, I. Nemet, *J. Organomet. Chem.* **2003**, *682*, 131–142; e) K. Heinze, M. Schlenker, *Eur. J. Inorg. Chem.* **2004**, 2974–2988; f) K. Heinze, M. Schlenker, *Eur. J. Inorg. Chem.* **2005**, 66–71; g) K. Heinze, U. Wild, M. Beckmann, *Eur. J. Inorg. Chem.* **2007**, 617–623.
[43] L. Barišić, M. Dropučić, V. Rapić, H. Pritzkow, S. I. Kirin, N. Metzler-Nolte, *Chem. Commun.* **2004**, 2004–2005.
[44] a) L. Barišić, M. Čakić, K. A. Mahmoud, Y. Liu, H.-B. Kraatz, H. Pritzkow, S. I. Kirin, N. Metzler-Nolte, V. Rapić, *Chem. Eur. J.* **2006**, *12*, 4965–4980; b) B. Ishimoto, K. Tonan, S. Ikawa, *Spectrochim. Acta Part A* **1999**, *56*, 201–209.
[45] K. Heinze, M. Beckmann, *Eur. J. Inorg. Chem.* **2005**, 3450–3457.
[46] L. Barišić, V. Rapić, N. Metzler-Nolte, *Eur. J. Inorg. Chem.* **2006**, *20*, 4019–4021.
[47] M. Čakić-Semenčić, D. Siebler, K. Heinze, V. Rapić, manuscript in preparation.
[48] T. Moriuchi, K. Yoshida, T. Hirao, *Organometallics* **2001**, *20*, 3101–3105.
[49] T. Moriuchi, K. Yoshida, T. Hirao, *J. Organomet. Chem.* **2001**, *637–639*, 75–79.
[50] T. Moriuchi, K. Yoshida, T. Hirao, *J. Organomet. Chem.* **2003**, *668*, 31–34.
[51] Y. Xu, P. Saweczko, H.-B. Kraatz, *J. Organomet. Chem.* **2001**, *637–639*, 335–342.

[52] H.-B. Kraatz, D. M. Leek, A. Houmam, G. D. Enright, J. Lusztyk, D. D. M. Wayner, *J. Organomet. Chem.* **1999**, *589*, 38–49.
[53] T. Moriuchi, T. Nagai, T. Hirao, *Org. Lett.* **2006**, *8*, 31–34.
[54] W. C. Chan, P. D. White, *Fmoc Solid Phase Peptide Synthesis*, Oxford University Press, Oxford, **2000**.
[55] F. W. Knobloch, W. H. Rauscher, *J. Polym. Sci.* **1961**, *54*, 651.
[56] E. Vass, M. Hollósi, F. Besson, R. Buchet, *Chem. Rev.* **2003**, *103*, 1917–1954.
[57] M. J. Frisch, G. W. Trucks, H. B. Schlegel, G. E. Scuseria, M. A. Robb, J. R. Cheeseman, J. A. Montgomery Jr, T. Vreven, K. N. Kudin, J. C. Burant, J. M. Millam, S. S. Iyengar, J. Tomasi, V. Barone, B. Mennucci, M. Cossi, G. Scalmani, N. Rega, G. A. Petersson, H. Nakatsuji, M. Hada, M. Ehara, K. Toyota, R. Fukuda, J. Hasegawa, M. Ishida, T. Nakajima, Y. Honda, O. Kitao, H. Nakai, M. Klene, X. Li, J. E. Knox, H. P. Hratchian, J. B. Cross, C. Adamo, J. Jaramillo, R. Gomperts, R. E. Stratmann, O. Yazyev, A. J. Austin, R. Cammi, C. Pomelli, J. W. Ochterski, P. Y. Ayala, K. Morokuma, G. A. Voth, P. Salvador, J. J. Dannenberg, V. G. Zakrzewski, S. Dapprich, A. D. Daniels, M. C. Strain, O. Farkas, D. K. Malick, A. D. Rabuck, K. Raghavachari, J. B. Foresman, J. V. Ortiz, Q. Cui, A. G. Baboul, S. Clifford, J. Cioslowski, B. B. Stefanov, G. Liu, A. Liashenko, P. Piskorz, I. Komaromi, R. L. Martin, D. J. Fox, T. Keith, M. A. Al-Laham, C. Y. Peng, A. Nanayakkara, M. Challacombe, P. M. W. Gill, B. Johnson, W. Chen, M. W. Wong, C. Gonzalez, J. A. Pople, *Gaussian 03*, Revision B.03, Gaussian, Inc., Pittsburgh, PA, **2003**.
[58] S. Djaković, D. Siebler, M. Čakić-Semenčić, K. Heinze, V. Rapić, *Organometallics* **2008**, *27*, 1447–1453.
[59] J. Lapić, G. Pavlović, D. Siebler, K. Heinze, V. Rapić, *Organometallics* **2008**, *27*, 726–735.
[60] K. Heinze, M. Beckmann, *J. Organomet. Chem.* **2006**, *691*, 5588–5596.
[61] G. Lapić, D. Siebler, K. Heinze, V. Rapić, *Eur. J. Inorg. Chem.* **2007**, 2014–2024.
[62] K. Heinze, D. Siebler, *Z. Anorg. Allg. Chem.* **2007**, *633*, 2223–2233.
[63] V. F. Bystrov, *Prog. Nucl. Magn. Reson. Spectrosc.* **1976**, *10*, 41–81.

Received: September 12, 2008
Published Online: December 10, 2008

DOI: 10.1002/ejic.200800928

Anion Coordination Effect on the Nuclearity of Co^{II}, Ni^{II}, Cu^{II}, and Zn^{II} Complexes with a Benzimidazole Pendant-Armed Crown

Lea Vaiana,[a] David Esteban-Gómez,*[a] Marta Mato-Iglesias,[a] Carlos Platas-Iglesias,[a] Andrés de Blas,[a] and Teresa Rodríguez-Blas*[a]

Keywords: Macrocyclic ligands / Crown compounds / X-ray diffraction / N,O ligands / Transition metals

The study presented in this paper provides a rare example of a macrocyclic receptor allowing the formation of mono- or binuclear complexes on the same first-row transition-metal guest cation depending on the nature of the counterion present. Reaction of *N*,*N*′-bis(benzimidazol-2-ylmethyl)-4,13-diaza-18-crown-6 (L^4) with Co^{II}, Ni^{II}, Cu^{II}, or Zn^{II} perchlorates leads to the formation of the expected mononuclear complexes with the metal ion showing a distorted octahedral coordination environment. In these complexes, the metal ion is placed at one end of the macrocyclic cavity, and two of the oxygen atoms of the crown ether moiety remain uncoordinated. ^1H and ^{13}C NMR spectroscopic studies on the diamagnetic $[Zn(L^4)]^{2+}$ complex indicate that the asymmetric coordination of the metal ion inside the macrocyclic cavity is maintained in acetonitrile solution, but translocation of the Zn^{II} ion from one end of the macrobicyclic cavity to the second one occurs. However, reaction of L^4 with Co^{II}, Ni^{II}, or Cu^{II} perchlorates in the presence of chloride anions results in the formation of binuclear complexes where the metal ion is either five-coordinate in a distorted trigonal bipyramidal coordination environment (Co or Cu) or six-coordinate in a distorted octahedral geometry (Ni), and a chloride anion coordinates to each of the two metal ions in all cases. The Zn^{II} ion behaves in a different way, and addition of chloride anions to the Zn^{II} perchlorate in the presence of L^4 does not lead to the formation of a binuclear complex. The formation of these binuclear systems was followed by spectrophotometric titrations of the mononuclear $[M(L^4)](ClO_4)_2$ complexes with $[nBu_4N]Cl$ in acetonitrile solution indicating the formation of a $[M_2(L^4)(Cl)]^{2+}$ intermediate species, followed by the formation of the binuclear complex $[M_2(L^4)(Cl)_2]^{2+}$ (M = Co, Ni, or Cu).

Introduction

The rational control of the nuclearity of first-row transition-metal complexes is important, as the nuclearity of metalloenzyme active sites and synthetic catalysts often determines their reactivity. Often in binuclear complexes the two metal ions interact cooperatively at a catalyst binding site, which results in a catalytic rate acceleration far in excess from recruitment of only a single metal ion.[1,2] Moreover, some bimetallic first-row transition-metal complexes present unusual chemical reactivities.[3] Bi- or polymetallic systems are often made from complex reaction systems containing metal ions, ligand(s), solvent molecules, and even trace amounts of moisture. Each component of the reaction mixture, as well as other variables such as temperature and ionic strength of the solution, may influence the final product. Therefore, the rational control of the nuclearity of metal complexes remains a challenge for coordination chemists.[4]

We recently demonstrated that the pendant-armed crown ethers *N*,*N*′-bis(2-aminobenzyl)-1-10-diaza-15-crown-5 (L^1, Scheme 1)[5,6] and *N*,*N*′-bis(benzimidazol-2-yl-methyl)-1,10-diaza-15-crown-5 (L^3)[7] form mononuclear complexes in acetonitrile solution with divalent first-row transition-metal ions that represent unusual examples of structurally characterized seven-coordinate (pentagonal bipyramidal) complexes.[8] Particularly interesting are also the coordinative properties towards these divalent metal ions of the larger related receptor *N*,*N*′-bis(2-aminobenzyl)-4-13-diaza-18-crown-6 (L^2). We observed that this receptor only forms binuclear complexes of Co^{II}, Ni^{II}, and Cu^{II} in acetonitrile

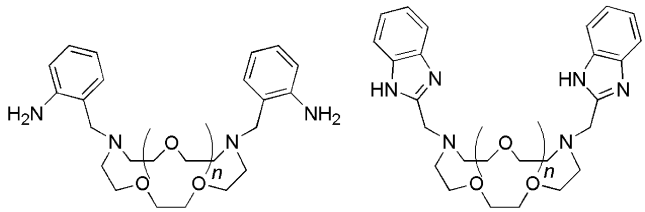

L^1: $n = 1$
L^2: $n = 2$
L^3: $n = 1$
L^4: $n = 2$

Scheme 1.

[a] Dpto. Química Fundamental, Facultade de Ciencias, Campus da Zapateira s/n, Universidade da Coruña,
15071 A Coruña, Spain
Fax: +34-981-167065
E-mail: mayter@udc.es

Supporting information for this article is available on the WWW under http://www.eurjic.org/ or from the author.

with the metal ions being five- or six-coordinate,[9] whereas the corresponding mononuclear complexes could not be isolated. In the case of the Co^{II} complex, the presence of a hydroxido bridge allows antiferromagnetic exchange in this compound. However, this receptor only forms mononuclear complexes with Zn^{II}[10] and Mn^{II} in acetonitrile,[11] but not binuclear ones. We showed that the presence of a poorly coordinating anion such as perchlorate results in endocyclic coordination of Zn^{II}, whereas the presence of a more-coordinating anion such as nitrate gives rise to exocyclic coordination of this metal ion.

Herein we report the coordinative properties of the related *N*,*N*′-bis(benzimidazol-2-ylmethyl)-4,13-diaza-18-crown-6 (L^4, Scheme 1) towards divalent first-row transition-metal ions. The study presented in this paper provides a new example of a ligand allowing the formation of mono- or binuclear complexes on the same first-row transition-metal guest cation depending on the nature of the counterion present.[12] Spectrophotometric titrations in acetonitrile solution were used to study the formation of the complexes and to understand the factors influencing the formation of mono- or binuclear complexes.

Results and Discussion

Spectrophotometric Titrations

The coordination of L^4 to Co^{II}, Ni^{II}, Cu^{II}, and Zn^{II} perchlorates was studied by spectrophotometric titrations in the absence and presence of chloride anions. The UV/Vis spectrum of L^4 recorded in CH_3CN solution shows two bands at 276 and 284 nm (Figure 1), which can be assigned as $\pi^*\leftarrow\pi$ singlet–singlet transitions[13] ($^1L_a\leftarrow S_0$ and $^1L_b\leftarrow S_0$, where the two excited states are labeled by ^1L_a and ^1L_b following the suggestion of Platt).[14] Upon addition of the corresponding metal perchlorates, both absorption bands shift towards shorter wavelengths as their intensity slightly increases (Figure 1). These spectral changes indicate the coordination of the benzimidazole substituents to the corresponding metal ion and allowed us to monitor the formation of the complexes in solution. In all cases, a 1:1 reaction stoichiometry was ascertained, as the data displayed a single inflection point when the M/ligand molar ratio is close to 1, in agreement with the formation of mononuclear $[M(L^4)]^{2+}$ (M = Co, Ni, Cu, or Zn) complexes in solution. The steep curvature of the titration profiles correspond to an especially high equilibrium constant ($\log K > 7$). In particular, the *p* parameter (*p* = [concentration of complex]/[maximum possible concentration of complex]) was found to be higher than 0.8 in both cases, a condition which does not permit the determination of a reliable equilibrium constant.[15]

Figure 2 shows the spectral changes of a 10^{-4} M solution of L^4 in the presence of two equivalents of Co^{II}, Ni^{II}, or Cu^{II} perchlorates upon addition of tetrabutylammonium chloride. Upon addition of Cl^-, the intensity of the absorption bands of the mononuclear complexes at ca. 272 and 278 nm increases, whereas the spectral region between 220 and 260 nm shows a more complicated variation, especially in the case of the Ni^{II} and Cu^{II} complexes. Addition of Cl^- anions to solutions of the Ni^{II} mononuclear complex results in the formation of a new band at ca. 300 nm that can be assigned to a charge-transfer band of the $[Ni_2(L^4)(Cl)_2]^{2+}$ complex.[16] Similarly, the binuclear species $[Cu_2(L^4)(Cl)_2]^{2+}$ shows rather intense bands at 308 and 461 nm that can be also assigned to charge-transfer bands. In the case of the titrations in the presence of Ni^{II} and Cu^{II}, the titration profiles display two inflection points at Cl^-/ligand molar ratios close to 1 and 2, indicating the stepwise coordination of two Cl^- ligands to the metal ion. Furthermore, the presence of new isosbestic points at 245 and 302 nm [M = Cu^{II}] and at 240 nm [M = Ni^{II}] after the Cl^-/M^{2+} (1:1) molar ratio also confirms the existence of two equilibrium processes in both cases. However, no inflection point is observed for the titration in the presence of Co^{II} at Cl^-/Co^{2+} (1:1) molar ratio. These results can be interpreted in terms of the following equilibria:

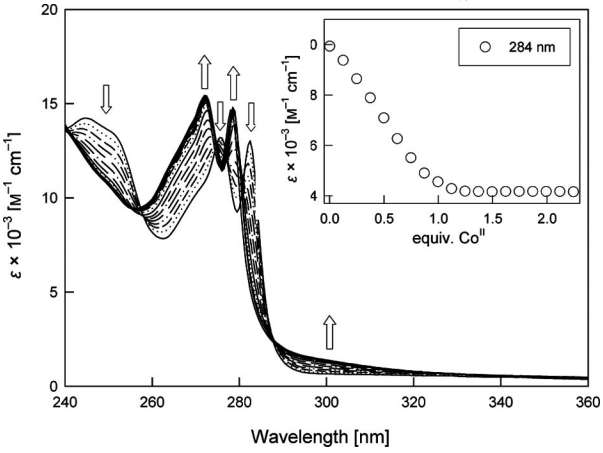

Figure 1. UV/Vis spectrum of L^4 in a CH_3CN solution and spectral changes upon addition of aliquots of a solution of $Co(ClO_4)_2{\cdot}6H_2O$ in the same solvent.

$$[M(L^4)]^{2+} + M^{2+} + Cl^- \leftrightarrows [M_2(L^4)(Cl)]^{3+},\ \log\beta_{111} \quad (1)$$

$$[M_2(L^4)(Cl)]^{3+} + Cl^- \leftrightarrows [M_2(L^4)(Cl)_2]^{2+},\ \log\beta_{112} \quad (2)$$

where M = Co, Ni, or Cu. Nonlinear least-squares fit of the experimental data allowed us to determine the constants given in Table 1. In all cases the *p* parameter calculated for each complex species was found to be lower than 0.8, a condition that allows a reliable determination of equilibrium constants. Our results indicate that the stability of both binuclear complex species increases in the following order: Cu > Ni > Co. Species distribution diagrams obtained with the $\log\beta$ values listed in Table 1 indicate a stepwise formation of the $[M_2(L^4)(Cl)]^{3+}$ and $[M_2(L^4)(Cl)_2]^{2+}$ complexes in solution when M = Ni or Cu (Figure 2). The concentrations of the intermediate $[M_2(L^4)(Cl)]^{3+}$ species upon addition of one equivalent of Cl^- anions are ca. 80% (Ni) and 66% (Cu); however, in the case of the Co^{II} complex the maximum concentration of the intermediate species is only 1.3%.

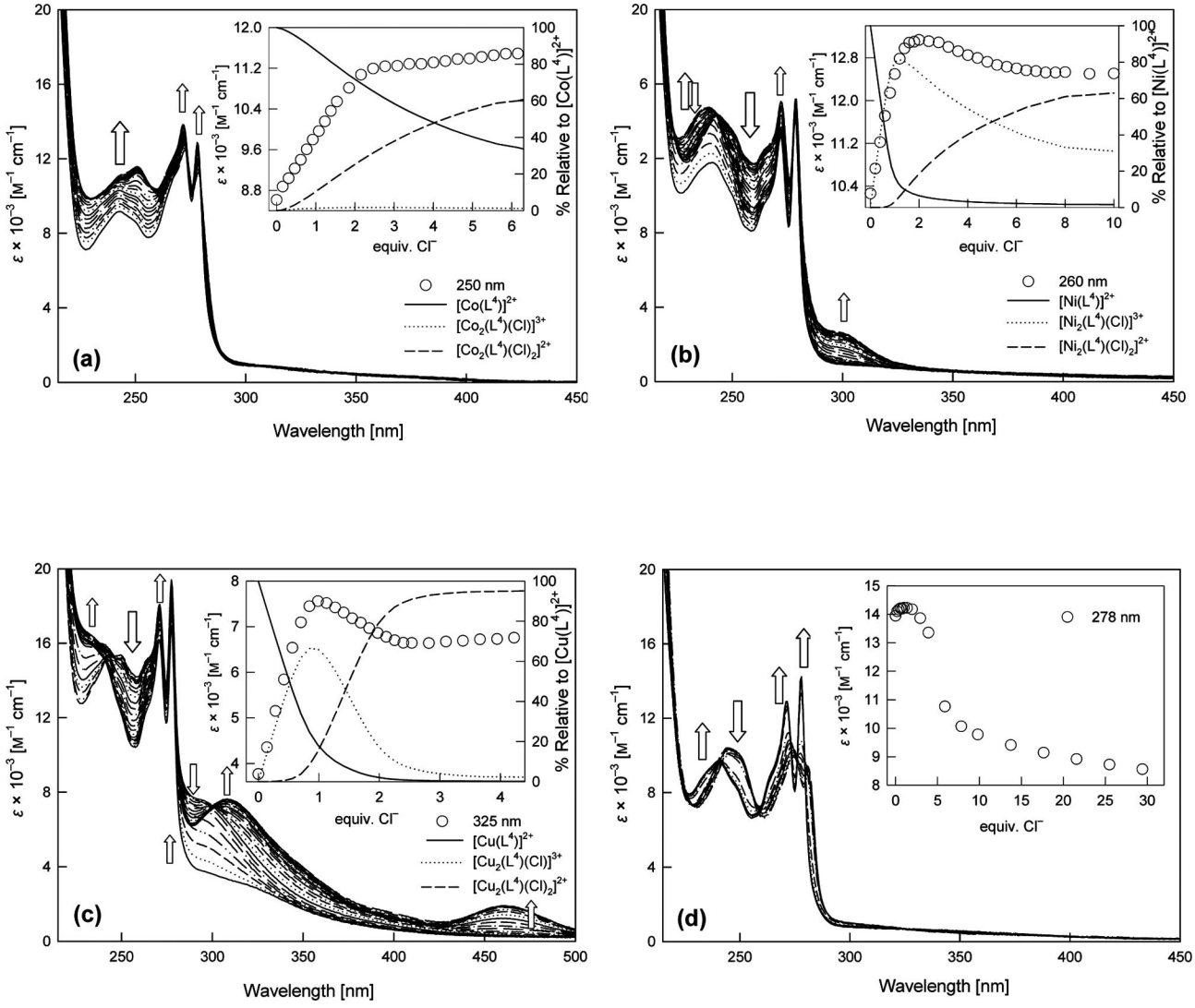

Figure 2. Family of UV/Vis spectra taken during the course of the titrations of L^4 (5×10^{-5} M in CH_3CN) and M^{2+} (1×10^{-4} M in CH_3CN) [Co^{2+} (a); Ni^{2+} (b); Cu^{2+} (c); Zn^{2+} (d)] with a standard solution of [nBu$_4$N]Cl at 25 °C. Insets: titration profiles at selected wavelengths vs. equivalents of chloride (left scale vertical axis) and species distribution diagram (right scale vertical axis).

Table 1. Equilibrium constants defined in Equations (1) and (2) (see text) obtained from spectrophotometric titrations in CH_3CN solutions at 25 °C.[a]

	Co	Ni	Cu
$\log\beta_{111}$	6.96(3)	10.92(9)	11.93(9)
$\log\beta_{112}$	12.28(7)	14.67(8)	17.61(13)

[a] The errors given correspond to one statistical deviation.

The mononuclear $[Zn(L^4)]^{2+}$ perchlorate complex shows a different behavior, and addition of Cl^- to a 10^{-4} M solution of L^4 in the presence of two equivalents of Zn^{II} does not provoke substantial changes in the UV/Vis absorption spectrum at Cl^-/L^4 molar ratios <2 (Figure 2). From this point, the two absorption bands of the $[Zn(L^4)]^{2+}$ complex experience a blueshift as their intensity increase, and the spectra recorded at Cl^-/L^4 molar ratios >2 are identical to that of the free ligand. These results indicate that the addition of Cl^- anions to the $[Zn(L^4)](ClO_4)_2$ complex does not result in the formation of binuclear species, as observed for the Co^{II}, Ni^{II}, and Cu^{II} analogues. By contrast, addition of an excess amount of Cl^- anions to this zinc complex provokes its dissociation.

Mononuclear Complexes

Reaction of L^4 with the appropriate hydrated perchlorate salt under the conditions described in the Experimental Section led to compounds of formula $[M(L^4)](ClO_4)_2 \cdot nC_3H_8O$ with M = Co (**1**), Ni (**2**), Cu (**3**), or Zn (**4**) in good yield (68–85%). The IR spectra (KBr disks) show a band at ca. 1550 cm^{-1} due to the ν(C=C) stretching frequency of the benzimidazole groups. This band is shifted by 15–21 cm^{-1} to higher wavenumbers with respect to their position in the spectra of the free ligand. Bands corresponding

to the ν_{as}(Cl–O) stretching and δ_{as}(O–Cl–O) bending modes of the ionic perchlorate groups appear at ca. 1086 and 626 cm^{-1}, respectively.[17] The mass spectra (FAB) of these complexes display an intense peak (100% BPI) due to $[M(L^4 - H)]^+$, which confirms the formation of the complexes. The molar conductivity values, as measured in $\approx 10^{-3}$ M acetonitrile solutions of the complexes, fall in the range generally accepted for 2:1 electrolytes in this solvent (220–300 $cm^2 \Omega^{-1} mol^{-1}$),[18] suggesting that the perchlorate anions are not coordinated to the metal ion in solution. Reaction of L^4 with two equivalents of the corresponding perchlorate salt did not result in the formation of the expected binuclear complexes.

The solid-state structures of compounds **1**–**4** were determined by single-crystal X-ray diffraction analyses. Crystals contain the cations $[M(L^4)]^{2+}$ (M = Co, Ni, Cu, or Zn) and two perchlorate anions that are hydrogen bonded to the NH groups of the benzimidazole units (see Figure 3 caption), as previously observed for related complexes.[19] Table 2 summarizes selected bond lengths and angles of the metal coor-

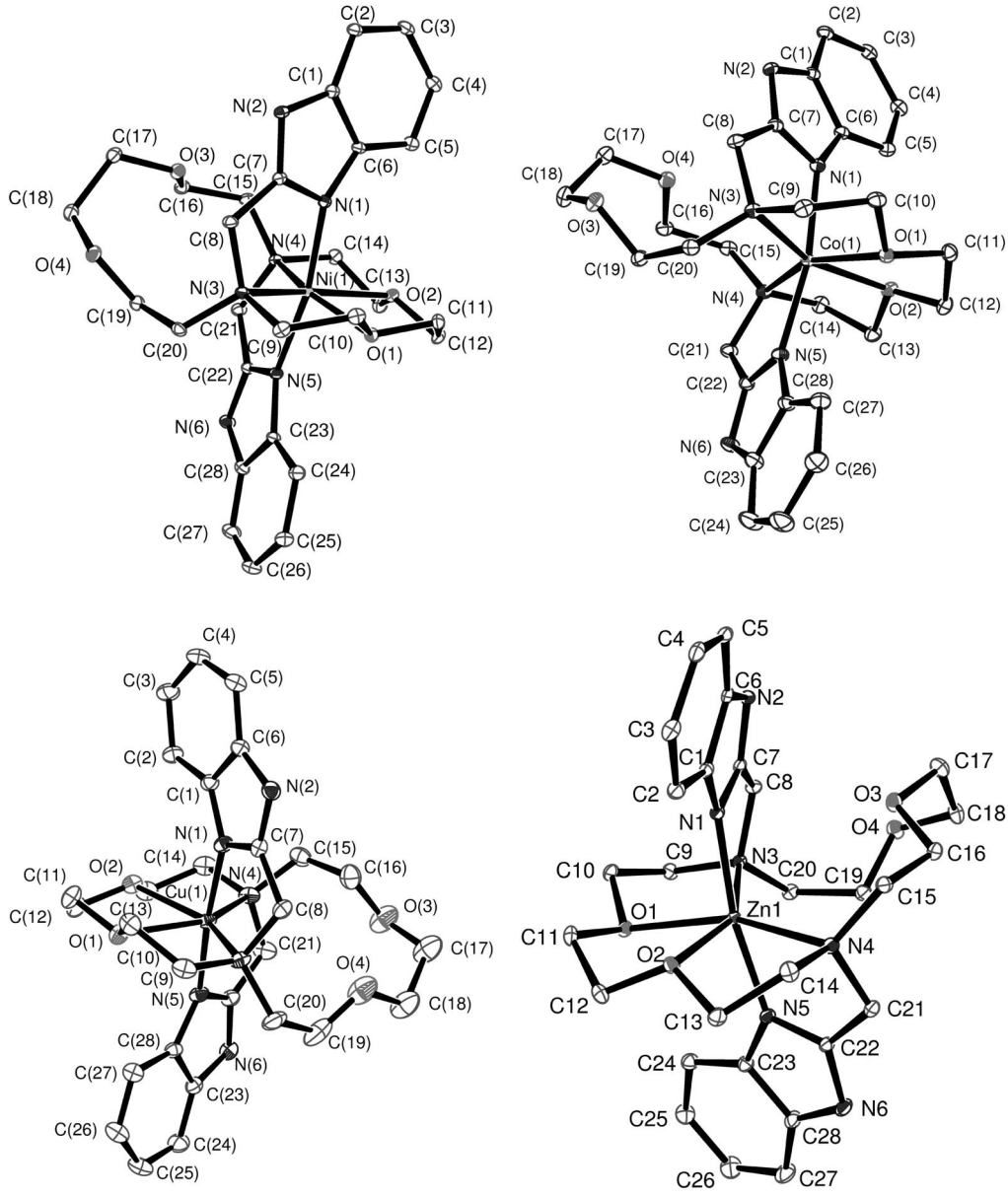

Figure 3. X-ray crystal structure of the cations $[M(L^4)]^{2+}$ (M = Co, Ni, Cu, or Zn) in compounds **1**–**4** with atom labeling; hydrogen atoms are omitted for simplicity. The ORTEP plots are drawn at the 30% probability level. Hydrogen-bonding data, compound **1**: N(2)···H(2N) 0.87(3) Å, H(2N)···O(10) 2.04(3) Å, N(2)···O(10) 2.898(2) Å, N(2)–H(2N)–O(10) 174(2)°; N(6)···H(6N) 0.87(3) Å, H(6N)···O(8) 2.03(3) Å, N(6)···O(8) 2.877(3) Å, N(6)–H(6N)–O(8) 164(3)°; compound **2**: N(2)···H(2N) 0.81(3) Å, H(2N)···O(7) 2.10(3) Å, N(2)···O(7) 2.897(2) Å, N(2)–H(2N)–O(7) 171(3)°; N(6)···H(6N) 0.88(3) Å, H(6N)···O(11) 2.02(3) Å, N(6)···O(11) 2.879(2) Å, N(6)–H(6N)–O(11) 165(3)°; compound **3**: N(6)···H(6N) 0.79(4) Å, H(6N)···O(7) 2.09(5) Å, N(6)···O(7) 2.859(4) Å, N(6)–H(6N)–O(7) 165(4)°; compound **4**: N(2)···H(2N) 0.88 Å, H(2N)···O(6) 2.03 Å, N(2)···O(6) 2.888(3) Å, N(2)–H(2N)–O(7) 165.6°; N(6)···H(6N) 0.88 Å, H(6N)···O(10) 2.03 Å, N(6)···O(10) 2.869(3) Å, N(6)–H(6N)–O(11) 159.7°.

dination environments, whereas the structures of the cations are depicted in Figure 3. The macrocyclic ligand adopts an *anti* conformation in the complexes and the two pendant arms are disposed on opposite sides of the crown moiety. In the $[M(L^4)]^{2+}$ cations, the metal ion is asymmetrically placed inside the crown moiety hole, being bound to six of the eight donor atoms of the ligand: two oxygen atoms of the crown moiety [O(1) and O(2)], the two pivotal nitrogen atoms [N(3) and N(4)], and the two nitrogen atoms of the benzimidazole groups [N(1) and N(5)]. The coordination polyhedron around the metal coordination environment may be described as a distorted octahedron, where the two oxygen atoms of the crown moiety, the pivotal nitrogen atoms, and the metal ion form one of the equatorial planes [mean deviation from planarity: 0.089(3) (**1**), 0.107(2) (**2**), 0.059(3) (**3**), and 0.058(6) Å (**4**)]. The *trans* angles N(1)–M(1)–N(5) [169.03(7), 169.73(7), 173.3(1), and 170.02(7)° for **1**, **2**, **3**, and **4**, respectively] deviate by ca. 10° from the expected value for a regular octahedron (180°). Three of the *cis* angles of the equatorial plane are considerably smaller than the ideal value of 90°, whereas the fourth *cis* angle of the equatorial plane is considerably larger [N(3)–M(1)–N(4) 126.74(6), 124.20(6), 135.88(1), and 129.84(6)° for **1**, **2**, **3**, and **4** respectively]. However, this is not surprising considering that coordination of the pivotal nitrogen atoms N(3) and N(4) results in the formation of an eleven-membered chelate ring. Finally, the vectors defined by the metal ion and the axial donors N(1) and N(5) form angles close to 90° with the vectors containing the metal ion and the equatorial donor atoms, as expected for an octahedral coordination environment. The M–N(1) and M–N(5) distances are close to those observed in other six-coordinate first-row transition-metal complexes with ligands containing benzimidazole groups.[20] In the case of the Cu^{II} complex, the distances between the metal ion and oxygen atoms of the crown moiety are ca. 0.7 Å shorter than those observed in six-coordinate Cu^{II} complexes derived from diaza-18-crown-6 containing phenolic pendant arms.[21] It is also interesting to note that whereas in the structure of complex $[Zn(L^4)]^{2+}$ the metal ion is six-coordinate, in the case of $[Zn(L^2)]^{2+}$ the metal ion is only four-coordinate.[10] These results indicate that the substitution of the aniline pendants of L^2 by benzimidazole groups has an important effect on the structure of the corresponding Zn^{II} complexes. This can be attributed to the different size of the chelate rings formed upon coordination of the pendant arms in L^2 and L^4. Indeed, coordination of the aniline pendants in L^2 results in the formation of six-membered chelate rings, whereas coordination of the pendant arms of L^4 forms five-membered chelate rings.

The ^{1}H NMR spectrum of the diamagnetic compound $[Zn(L^4)](ClO_4)_2{\cdot}2H_2O$ (**4**) recorded in CD_3CN solution at 298 K shows broad signals for the CH_2 protons of the ligand backbone. However, the spectrum recorded at 234 K is well resolved and consistent with the presence of a single species in solution with an effective C_2 symmetry in solution (Table 3). This is confirmed by the ^{13}C NMR spectrum, which shows 14 signals for the 28 carbon nuclei of the ligand backbone at 234 K. These results suggest that the $[Zn(L^4)]^{2+}$ complex presents a structure in solution similar to that observed in the solid state (vide supra). A partial assignment of the ^{1}H and ^{13}C NMR spectra recorded at 234 K was achieved with the aid of 2D COSY, HSQC, and HMBC experiments (Table 3). The most complicated region of the ^{1}H NMR spectrum is that where the ethylene and methylene proton signals are observed. The coordination to the metal ion increases the rigidity of the ligand, limiting conformational exchange processes, so that the geminal $–CH_2–$ protons are no longer equivalent. Because assignments to specific axial/equatorial CH_2 protons were not possible on the basis of the 2D NMR spectra, they were carried out by using the stereochemically dependent proton shift effects, resulting from the polarization of the C–H bonds by the electric field generated by the charge of the cation.[22] This polarization results in deshielding of the equatorial protons, which point away from the metal ion. The H8 methylene protons show an AB pattern ($^2J_{8a,8b}$ = 18.2 Hz), in which the protons labeled as H8b are again deshielded, because they are pointing away from the metal ion. Specific assignment of several pairs of NMR signals (1–6, 2–5, 3–4, 9–12, 10–13 and 11–14) was not possible on the basis of the 2D spectra (see Table 3 for numbering scheme).

In order to obtain information about the solution structure of the $[Zn(L^4)]^{2+}$ complex we performed DFT calculations by using the B3LYP model. On the grounds of our previous experience,[6,7,10] full geometry optimizations of the $[Zn(L^4)]^{2+}$ system were performed in vacuo by using the standard 6-31G(d) basis on the ligand atoms and Ahlrichs' valence triple-ζ (VTC) on Zn. The latter basis was shown to provide accurate molecular structures for several first-row transition-metal complexes.[23] The most relevant geo-

Table 2. Selected bond lengths [Å] and angles [°] for compounds **1**–**4**.

	1	**2**	**3**	**4**
M(1)–N(1)	2.049(2)	2.025(2)	1.939(3)	2.036(2)
M(1)–N(5)	2.052(2)	2.027(2)	1.948(3)	2.033(2)
M(1)–O(1)	2.126(2)	2.087(2)	2.279(2)	2.170(2)
M(1)–O(2)	2.131(2)	2.096(1)	2.283(2)	2.174(2)
M(1)–N(3)	2.279(2)	2.243(2)	2.266(3)	2.286(2)
M(1)–N(4)	2.352(2)	2.330(2)	2.249(3)	2.391(2)
N(1)–M(1)–N(5)	169.03(7)	169.73(7)	175.3(1)	170.02(7)
N(1)–M(1)–O(1)	92.88(6)	93.00(6)	88.9(1)	92.74(6)
N(5)–M(1)–O(1)	96.63(6)	96.06(6)	94.6(1)	96.51(6)
N(1)–M(1)–O(2)	94.34(6)	93.66(6)	93.5(1)	93.40(6)
N(5)–M(1)–O(2)	93.18(6)	93.02(6)	90.7(1)	92.61(7)
O(1)–M(1)–O(2)	76.63(5)	77.47(5)	71.62(9)	75.08(6)
N(1)–M(1)–N(3)	79.50(6)	80.22(6)	80.9(1)	79.51(7)
N(5)–M(1)–N(3)	96.92(6)	96.57(6)	96.8(1)	98.63(7)
O(1)–M(1)–N(3)	79.03(6)	80.06(6)	76.2(1)	78.56(6)
O(2)–M(1)–N(3)	154.54(6)	156.36(6)	147.5(1)	152.33(6)
N(1)–M(1)–N(4)	95.82(6)	95.14(6)	97.8(1)	95.92(7)
N(5)–M(1)–N(4)	77.91(6)	78.51(6)	81.0(1)	77.65(7)
O(1)–M(1)–N(4)	153.92(6)	155.40(6)	147.8(1)	151.39(6)
O(2)–M(1)–N(4)	78.23(6)	78.87(6)	76.5(1)	77.22(6)
N(3)–M(1)–N(4)	126.74(6)	124.20(6)	135.88(1)	129.84(6)

Table 3. ^1H and ^{13}C NMR shifts (ppm with respect to TMS) for compound **4**.[a]

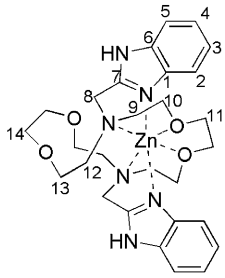

^1H	$\delta_{i,exp}$[a]	^{13}C	$\delta_{i,exp}$[a]	$\delta_{i,calcd}$[b]
H2	8.04 (dd, 2 H)	C1	138.3	145.5
H3	7.44 (m, 2 H)	C2	118.2	123.1
H4	7.47 (m, 2 H)	C3	125.0	137.1
H5	7.73 (dd, 2 H)	C4	125.6	139.4
H8a	3.95 (m, 2 H)	C5	113.6	121.4
H8b	5.30 (d, 2 H)	C6	134.9	141.3
H9ax	3.07 (m, 2 H)	C7	156.0	160.6
H9eq	3.56 (m, 2 H)	C8	52.4	58.1
H10ax	3.00 (m, 2 H)	C9	63.1	68.1
H10eq	3.92 (m, 2 H)	C10	66.9	72.3
H11ax	3.34 (m, 2 H)	C11	69.1	74.7
H11eq	3.93 (m, 2 H)	C12	59.3	64.0
H12	2.30 (m, 2 H)	C13	70.4	75.0
	3.02 (m, 2 H)	C14	70.7	77.0
H13	3.24 (m, 2 H)			
	3.61 (m, 2 H)			
H14	3.40 (m, 2 H)			
	3.61 (m, 2 H)			
NH	12.33 (br., 2 H)			

[a] Conditions: Assignment supported by 2D H,H COSY, HMQC, and HMBC experiments at 234 K, CD_3CN, 300 MHz, $^2J_{8a,8b} = {}^2J_{8b,8a} = 18.2$ Hz; $^3J_{2,3} = 7.8$ Hz; $^4J_{2,4} = 1.3$ Hz; $^3J_{5,4} = 7.3$ Hz; $^4J_{5,3} = 1.7$ Hz. [b] Values calculated in vacuo at the B3LYP/6-311G** level by using the GIAO method.

metrical parameters calculated for $[Zn(L^4)]^{2+}$ are given in Table S1 (Supporting Information). The calculated structure for the $[Zn(L^4)]^{2+}$ complex is very similar to that observed in the solid state. The calculated bond lengths for $[Zn(L^4)]^{2+}$ are in excellent agreement with those observed experimentally for compound **4**, as evidenced by the excellent agreement factor obtained ($AF_i = [\Sigma(exp - calcd)^2/\Sigma(exp)^2]^{1/2} = 0.036$, where *exp* and *calcd* denote calculated and experimental values, respectively).[24]

To aid the experimental NMR assignments, the ^{13}C NMR shielding constants of $[Zn(L^4)]^{2+}$ were calculated on the DFT-optimized structure (vide supra) by using the GIAO method. This method was shown to provide theoretical ^{13}C NMR shifts in good agreement with the experimental values for different coordination compounds,[25] including Zn^{II} complexes.[26] The main results of these calculations together with the experimental values are given in Table 3. Our calculations provide ^{13}C NMR chemical shifts in good agreement with the experimental values, thereby confirming the spectral assignments. These results also indicate that the calculated structure for $[Zn(L^4)]^{2+}$ provides a good model for the structure of the complex in solution. Once the ^{13}C NMR signals were assigned on the basis of the GIAO calculations a full assignment of the ^1H NMR signals was obtained from the cross peaks observed in the 2D HSQC experiment.

Upon increasing the temperature above 234 K, the ^{13}C NMR signals corresponding to the carbon nuclei of the crown moiety gradually broaden, whereas the remaining carbon signals are not affected (Figure 4). This reflects the presence in solution of an intramolecular conformational exchange process. When the temperature is increased to ca. 298 K, coalescence of the peaks due to C9 and C12, C10 and C13, and C11 and C14 is observed (see Table 3 for numbering scheme). As a result, the ^{13}C NMR spectrum recorded shows three resonances attributable to the carbon nuclei of the macrocyclic moiety at $\delta = \frac{1}{2}[\delta_1 + \delta_2]$, where δ_1 and δ_2 are the shifts observed for the pair of signals C9 and C12, C10 and C13, or C11 and C14. These results are consistent with the presence of a single species in solution with C_{2h} symmetry at high temperature. The dynamic behavior observed in acetonitrile solution can be attributed to a translocation of the Zn^{II} ion from one end of the macrocyclic cavity to the second one, as it was previously observed for a Pb^{II} complex with a macrobicyclic ligand containing a 1,10-diaza-15-crown-5 moiety.[27] If it is assumed that the exchange process associated with this line broadening (before coalescence) is slow on the NMR timescale, then

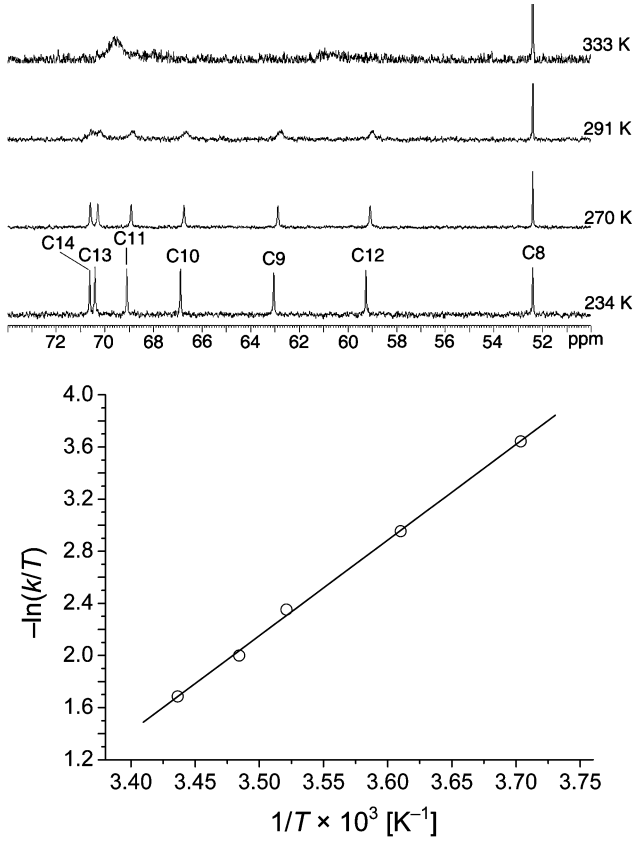

Figure 4. Top: partial ^{13}C NMR spectra of $[Zn(L^4)]^{2+}$ recorded at different temperatures in CD_3CN solution. Bottom: Eyring plot for the translocation of Zn^{II} in $[Zn(L^4)]^{2+}$ based upon line-broadening data for C12.

the exchange rate for this dynamic process (k) can be calculated from the observed linewidths at half-height ($\Delta\nu_{1/2}$): $k = \pi\{\Delta\nu_{1/2} - \Delta\nu_{1/2}(0)$, where $\Delta\nu_{1/2}(0)\}$ is the linewidth in the absence of exchange. A band-shape analysis was carried out on the C12 resonance over the 270–291 K temperature range in order to calculate the activation parameters for the translocation process. A plot ($R^2 > 0.999$, Figure 4) of $\ln(k/T)$ vs. $1/T$ [$k = (k_bT/h)\exp(\Delta S^{\#}/R - \Delta H^{\#}/RT)$, where k_b is the Boltzmann constant, T is the absolute temperature, k is the rate constant, $\Delta G^{\#}$, $\Delta H^{\#}$, and $\Delta S^{\#}$ are the activation free energy, enthalpy, and entropy, respectively] yields the following activation parameters: $\Delta G^{\#} = 61.5 \pm 3.1$ kJ mol^{-1}, $\Delta H^{\#} = 61.0 \pm 1.3$ kJ mol^{-1}, and $\Delta S^{\#} = -1.80 \pm 0.05$ J K^{-1} mol^{-1}, $k = 102.9 \pm 5$ s^{-1} at 298 K. The small $\Delta S^{\#}$ value obtained from the line-width analysis confirms that the translocation of the metal ion is an intramolecular exchange process where no dissociation of the complex occurs.

Binuclear Complexes

Reaction of L^4 with only two equivalents of the corresponding perchlorate salt did not result in the formation of the expected binuclear complexes. However, reaction of L^4 with two equivalents of the appropriate hydrated perchlorate salt in the presence of [nBu$_4$N]Cl (see Experimental Section) led to binuclear compounds of formula $[M_2(L^4)(Cl)_2](ClO_4)_2$ with M = Co (**5**), Ni (**6**), or Cu (**7**) in good yield (42–63%). The IR spectra (KBr disks) show a band at ca. 1545 cm^{-1} due to the ν(C=C) stretching frequency of the benzimidazole groups, which is shifted by ca. 20 cm^{-1} to higher wavenumbers with respect to its position in the spectra of the free ligand. Bands corresponding to the ν_{as}(Cl–O) stretching and δ_{as}(O–Cl–O) bending modes of the ionic perchlorate groups appear at ca. 1086 and 626 cm^{-1}, respectively. The mass spectra (FAB) of these complexes display peaks due to binuclear entities, which confirms the formation of the desired binuclear complexes (see Experimental Section). The molar conductivity values, as measured in ≈10^{-3} M solutions of the complexes in acetonitrile, fall in the range generally accepted for 2:1 electrolytes in this solvent. This result, together with the presence of ionic perchlorate anions evidenced by the IR spectra, suggests that the Cl$^-$ anions are coordinated to the metal ion in solution.

The solid-state structures of compounds **5**–**7** were determined by single-crystal X-ray diffraction analyses. Crystals of **5** and **7** contain the cations $[M_2(L^4)(Cl)_2]^{2+}$ (M = Co or Cu) and two noncoordinated perchlorate anions, whereas crystals of **6** contain the cation $[Ni_2(L^4)(Cl)_2(H_2O)_2]^{2+}$ and two noncoordinated perchlorate anions. Tables 4 and 5 summarize selected bond lengths and angles of the metal coordination environments, whereas the structure of the cations are depicted in Figure 5. The macrocyclic ligand adopts an *anti* conformation in the complexes and the two pendant arms are disposed on opposite sides of the crown moiety. A similar conformation of the macrocyclic ligand was previously found for $[Ni_2(L^2)(CH_3CN)_4]^{4+}$, whereas a *syn* conformation was observed for $[Co(L^2)(\eta\text{-}OH)Co(CH_3CN)]^{3+}$. The *syn* conformation in the latter complex was attributed to the presence of a hydroxido bridging ligand. The distance between the two metal ions in $[M_2(L^4)(Cl)_2]^{2+}$ (M = Co or Cu) and $[Ni_2(L^4)(Cl)_2(H_2O)_2]^{2+}$ complexes amounts to 4.707 (Co), 5.255 (Ni), and 4.902 Å (Cu). These values are close to that observed in $[Ni_2(L^2)(CH_3CN)_4]^{4+}$ (5.31 Å). However, they are clearly longer than the $Co^{II}\cdots Co^{II}$ distance in $[Co(L^2)(\eta\text{-}OH)Co(CH_3CN)]^{3+}$ (3.48 Å), as the presence of the bridging hydroxido group brings the two metal ions close together.

Table 4. Selected bond lengths [Å] and angles [°] for compounds **5** and **7**.

	5	**7**
M(1)–O(1)	2.081(2)	2.232(3)
M(1)–O(2)	2.063(2)	2.137(3)
M(1)–Cl(1)	2.2864(9)	2.210(1)
M(1)–N(1)	2.033(3)	1.963(3)
M(1)–N(3)	2.199(3)	2.039(3)
N(1)–M(1)–O(2)	110.4(1)	129.2(1)
N(1)–M(1)–O(1)	126.9(1)	113.4(1)
O(2)–M(1)–O(1)	110.7(1)	110.4(1)
N(1)–M(1)–N(3)	79.0(1)	82.6(1)
O(2)–M(1)–N(3)	78.4(1)	81.1(1)
O(1)–M(1)–N(3)	77.8(1)	79.6(1)
N(1)–M(1)–Cl(1)	105.17(8)	102.8(1)
O(2)–M(1)–Cl(1)	100.90(7)	96.8(8)
O(1)–M(1)–Cl(1)	98.50(7)	96.2(8)
N(3)–M(1)–Cl(1)	175.64(8)	174.2(1)

Table 5. Selected bond lengths [Å] and angles [°] for compound **6**.

Ni(1)–N(1)	2.025(2)	Ni(1)–O(1)	2.158(2)
Ni(1)–O(8)	2.080(2)	Ni(1)–O(2)	2.169(2)
Ni(1)–N(3)	2.118(2)	Ni(1)–Cl(1)	2.3026(7)
N(1)–Ni(1)–O(8)	86.49(9)	N(3)–Ni(1)–O(2)	77.75(8)
N(1)–Ni(1)–N(3)	82.85(8)	O(1)–Ni(1)–O(2)	98.18(7)
O(8)–Ni(1)–N(3)	91.33(8)	N(1)–Ni(1)–Cl(1)	104.14(6)
N(1)–Ni(1)–O(1)	88.02(8)	O(8)–Ni(1)–Cl(1)	94.31(6)
O(8)–Ni(1)–O(1)	171.17(7)	N(3)–Ni(1)–Cl(1)	171.26(6)
N(3)–Ni(1)–O(1)	81.12(8)	O(1)–Ni(1)–Cl(1)	93.73(5)
N(1)–Ni(1)–O(2)	158.40(8)	O(2)–Ni(1)–Cl(1)	96.12(5)
O(8)–Ni(1)–O(2)	84.58(8)		

The coordination environment around each of the two metal ions in compounds **5**–**7** is identical. In these complexes the metal ions are directly bound to a pivotal nitrogen atom [N(3)], the nitrogen atom of the benzimidazole group [N(1)], two oxygen atoms of the crown moiety [O(1) and O(2)], and a Cl$^-$ ligand. In the Co^{II} and Cu^{II} complexes the metal ion is five-coordinate in a distorted trigonal-bipyramidal coordination environment, as indicated from the value of the index of trigonality τ[28] of 0.81 (**5**) and 0.75 (**7**) (τ = 0 for a perfect square-pyramidal geometry and τ = 1 for a regular trigonal bipyramidal geometry).[29] However, in the Ni^{II} complex the metal ion is six-coordinate, where an inner sphere water molecule occupies the sixth coordination position around the metal ion. The coordination environment around the Ni^{II} ion can be described as a distorted

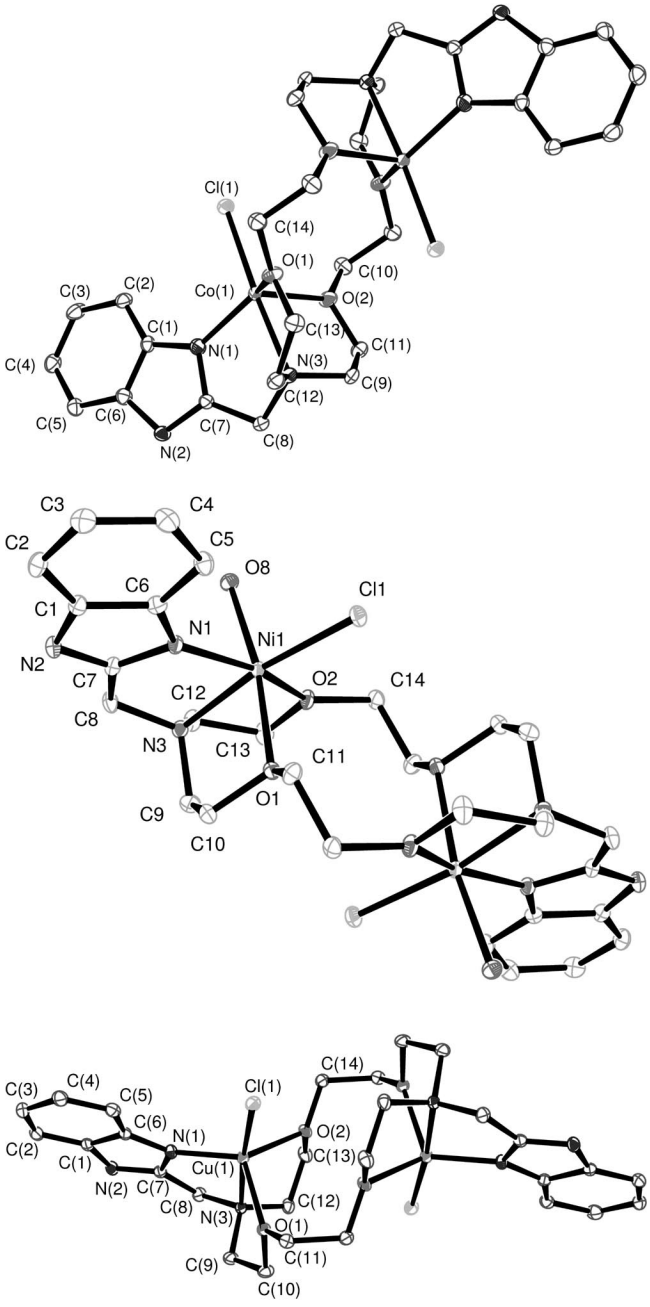

Figure 5. X-ray crystal structure of the cations $[Co_2(L^4)(Cl)_2]^{2+}$, $[Ni_2(L^4)(H_2O)_2(Cl)_2]^{2+}$, and $[Cu_2(L^4)(Cl)_2]^{2+}$ in compounds **5** to **7** with atom labeling; hydrogen atoms are omitted for simplicity. The ORTEP plots are drawn at the 30% probability level. Disorder observed in **5** is omitted for simplicity.

octahedron (Figure 5). Thus, the solid-state structures of compounds **5**–**7** reflect a stronger preference for octahedral coordination over coordination number five in the Ni^{II} complex than in the Co^{II} and Cu^{II} ones. A similar situation was previously observed for the $[Ni_2(L^2)(CH_3CN)_4]^{4+}$ and $[Co(L^2)(\eta\text{-}OH)Co(CH_3CN)]^{3+}$ complexes.[9]

The equatorial plane of the trigonal-bipyramid in compounds **5** and **7** can be considered to be composed of the two oxygen atoms of the crown moiety and the nitrogen atom of the benzimidazole group, whereas the pivotal nitrogen atom and the chlorido ligand occupy the apical positions. The angles of the equatorial plane [N(1)–M(1)–O(1), N(1)–M(1)–O(2) and O(1)–M(1)–O(2), M = Co or Cu; Table 4] are relatively close to the ideal value expected for a regular trigonal-bipyramidal coordination (120°). The N(3)–Co(1)–Cl(1) angles [175.64(8) (**5**) and 174.21(10)° (**7**)] are also close to the expected value (180°). The metal ion is placed above the plane formed by the three donor atoms of the equatorial plane (Figure 5) and the mean deviation from planarity of the plane containing these donor atoms and the metal ion is 0.1786 (**5**) and 0.2199 Å (**7**).

One of the equatorial planes of the octahedron in compound **6** can be considered to be composed of the two oxygen atoms of the crown moiety [O(1) and O(2)], the nitrogen atom of the benzimidazole pendant [N(1)], the oxygen atom of the inner sphere water molecule [O(8)], and the metal ion [mean deviation from planarity 0.316(3) Å]. The *trans* angle Cl(1)–Ni(1)–N(3) [171.26(6)°] is relatively close to the expected value for a regular octahedron (180°). The four *cis* angles of the equatorial plane are also close to the ideal value of 90°; the larger deviation is observed for the angle O(2)–Ni(1)–O(1) [98.18(7)°]. The vectors defined by the metal ion and the axial donors Cl(1) and N(3) form angles close to 90° with the vectors containing the metal ion and the equatorial donor atoms, as expected for an octahedral coordination environment. The largest deviation from the expected value is observed for the N(1)–Ni(1)–Cl(1) angle [104.14(6)°].

Conclusions

The study presented in this paper provides a rare example of a macrocyclic receptor allowing the formation of mono- or binuclear complexes on the same first-row transition-metal guest cation depending on the nature of the counterion present. Indeed, in the presence of a weakly coordinating anion such as perchlorate the pendant-armed crown ether *N*,*N*′-bis(benzimidazol-2-ylmethyl)-4,13-diaza-18-crown-6 (L^4) only forms mononuclear complexes with Co^{II}, Ni^{II}, and Cu^{II}, whereas no evidence was obtained for the formation of binuclear species under these conditions. These results are in contrast to those obtained for the related receptor L^2, which was shown to form binuclear Co^{II} and Ni^{II} complexes even in the presence of weakly coordinating anions such as perchlorate. This can be attributed to the different size of the chelate rings formed upon coordination of the pendant arms in L^2 and L^4. Indeed, the coordination of the aniline pendants in L^2 results in the formation of six-membered chelate rings, whereas the coordination of the pendant arms of L^4 gives rise to the formation of five-membered chelate rings. Thus, the formation of five-membered chelate rings upon coordination of the pendant arms in lariat ethers derived from 4,13-diaza-18-crown-6 appears to favor the formation of mononuclear complexes, whereas the formation of six-membered chelate rings favors binuclear species. The ligand L^4 is able to form the expected binuclear Co^{II}, Ni^{II}, and Cu^{II} complexes only in the pres-

ence of a strongly coordinating anion such as chloride. Spectrophotometric titrations of the mononuclear $[M(L^4)]^{2+}$ complexes with $[n\mathrm{Bu_4N}]Cl$ in acetonitrile solution indicate the formation of a $[M_2(L^4)(Cl)]^{2+}$ intermediate species, followed by the formation of the binuclear complex $[M_2(L^4)(Cl)_2]^{2+}$ (M = Co, Ni, or Cu). Interestingly, the mononuclear complex $[Zn(L^4)]^{2+}$ does not react with Cl^- to form a binuclear complex, and the addition of an excess amount of chloride results in demetalation of the complex.

Experimental Section

Chemicals and Starting Materials: *N*,*N*′-Bis(benzimidazol-2-ylmethyl)-4,13-diaza-18-crown-6 (L^4) was prepared according to a literature method.[30] All other chemicals were purchased from commercial sources and used without further purification. Solvents were of reagent grade and purified by the usual methods, unless otherwise stated. ***Caution!*** *Although we experienced no difficulties with the perchlorate salts, they are potentially explosive when combined with organic ligands and should be handled in small quantities and with the necessary precautions.*[31]

Measurements: ^1H and ^{13}C NMR spectra were recorded with a Bruker Avance 300 MHz spectrometer. Chemical shifts are reported in parts per million with respect to TMS. Spectral assignments are based on 2D COSY, HSQC, and HMBC experiments. Elemental analyses were carried out with a Carlo Erba 1108 elemental analyzer. FAB mass spectra were recorded by using a FISONS QUATRO mass spectrometer with Cs ion-gun and 3-nitrobenzyl alcohol as matrix. IR spectra were recorded, as KBr discs, by using a Bruker Vector 22 spectrophotometer. Conductivity measurements were carried out at 20 °C with a Crison Micro CM 2201 conductometer by using 10^{-3} M solutions of the complexes in acetonitrile. UV/Vis spectra were recorded with a Perkin–Elmer Lambda 900 spectrophotometer, with quartz cells (path length: 1 cm). The cell holder was thermostatted at 25.0 °C, through circulating water. The formation of the mononuclear complexes was monitored by using spectrophotometric titrations at 25 °C on 5×10^{-5} M solutions of ligand L^4 in CH_3CN (polarographic grade). Typically, aliquots of a fresh standard solution of the envisaged perchlorate salt in the same solvent (5×10^{-3} M) were added and the UV/Vis spectra of the samples were recorded. The formation of the binuclear species was followed by monitoring the spectral changes of 5×10^{-5} M solutions of ligand L^4 in the presence of two equivalents of the corresponding metallic perchlorate salt upon addition of tetrabutylammonium chloride (10^{-2} M in acetonitrile). All spectrophotometric titration curves were fitted with the HYPERQUAD program.[32] Binding constants were obtained by using a simultaneous fit of the UV/Vis absorption spectral changes at 7–12 selected wavelengths in the range 225–355 nm. A minimum of 26 absorbance data points at each of these wavelengths was used.

$[Co(L^4)](ClO_4)_2\cdot C_3H_8O$ (1): $Co(ClO_4)_2\cdot 6H_2O$ (0.043 g, 0.117 mmol) was added to a stirred solution of L^4 (0.060 g, 0.115 mmol) in 2-propanol (10 mL). The mixture was stirred and heated to reflux over a period of 2 h. The yellow precipitate formed was isolated by filtration and air-dried. Yield: 0.083 g (85%). $C_{31}H_{46}Cl_2CoN_6O_{13}$ (840.57): calcd. C 44.30, H 5.52, N 10.00; found C 44.11, H 5.44, N 10.20. Λ_M (acetonitrile, 20 °C): 234 $cm^2\,\Omega^{-1}\,mol^{-1}$ (2:1 electrolyte). IR (KBr): $\tilde{\nu}$ = 1623 [ν(C=N)]; 1595 (s), 1544 [ν(C=C)]; 1097 [ν_a(Cl–O)]; 627 [δ_a(O–Cl–O)] cm^{-1}. MS (FAB): *m*/*z* (%) = 680 (17) $[Co(L^4)(ClO_4)]^+$, 580 (100) $[Co(L^4 - H)]^+$. Slow diffusion of diethyl ether into a solution of the complex in acetonitrile at room temperature gave yellow single crystals of formula $[Co(L^4)](ClO_4)_2\cdot CH_3CN$ suitable for X-ray diffraction.

$[Ni(L^4)](ClO_4)_2\cdot 0.5C_3H_8O$ (2): $Ni(ClO_4)_2\cdot 6H_2O$ (0.063 g, 0.173 mmol) was added to a stirred solution of L^4 (0.090 g, 0.173 mmol) in 2-propanol (25 mL). The mixture was stirred and heated to reflux over a period of 6 h. The green precipitate formed was isolated by filtration and air-dried. Yield: 0.098 g (73%). $C_{28}H_{38}Cl_2NiN_6O_{12}\cdot 0.5C_3H_8O$ (810.28): calcd. C 43.73, H 5.22, N 10.37; found C 43.90, H 5.59, N 10.16. Λ_M (acetonitrile, 20 °C): 243 $cm^2\,\Omega^{-1}\,mol^{-1}$ (2:1 electrolyte). IR (KBr): $\tilde{\nu}$ = 1622 [ν(C=N)]; 1595 (s), 1547 [ν(C=C)]; 1090 [ν_a(Cl–O)]; 627 [δ_a(O–Cl–O)] cm^{-1}. MS (FAB): *m*/*z* (%) = 679 (14) $[Ni(L^4)(ClO_4)]^+$, 579 (100) $[Ni(L^4 - H)]^+$. Slow diffusion of diethyl ether into a solution of the complex in acetonitrile at room temperature gave green single crystals of formula $[Ni(L^4)](ClO_4)_2\cdot CH_3CN$ suitable for X-ray diffraction.

$[Cu(L^4)](ClO_4)_2\cdot C_3H_8O$ (3): The preparation of the green complex followed the same procedure described for **1** by using $Cu(ClO_4)_2\cdot 6H_2O$ (0.043 g, 0.116 mmol). Yield: 0.074 g (76%). $C_{31}H_{46}Cl_2CuN_6O_{13}$ (845.18): calcd. C 44.05, H 5.49, N 9.94; found C 44.16, H 5.32, N 10.43. Λ_M (acetonitrile, 20 °C): 220 $cm^2\,\Omega^{-1}\,mol^{-1}$ (2:1 electrolyte). IR (KBr): $\tilde{\nu}$ = 1618 [ν(C=N)]; 1594 (s), 1550 [ν(C=C)]; 1090 [ν_a(Cl–O)]; 627 [δ_a(O–Cl–O)] cm^{-1}. MS (FAB): *m*/*z* (%) = 684 (22) $[Cu(L^4)(ClO_4)]^+$, 584 (100) $[Cu(L^4 - H)]^+$. Slow diffusion of diethyl ether into a solution of the complex in acetonitrile at room temperature gave green single crystals suitable for X-ray diffraction.

$[Zn(L^4)](ClO_4)_2\cdot 2H_2O$ (4): $Zn(ClO_4)_2\cdot 6H_2O$ (0.063 g, 0.169 mmol) was added to a stirred solution of L^4 (0.090 g, 0.173 mmol) in absolute ethanol (21 mL). The mixture was stirred and heated to reflux over a period of 8 h. The beige precipitate formed was isolated by filtration and air-dried. Yield: 0.090 g (68%). $C_{28}H_{42}Cl_2N_6O_{14}Zn$ (822.96): calcd. C 40.86, H 5.14, N 10.21; found C 40.54, H 5.15, N 10.24. Λ_M (acetonitrile, 20 °C): 229 $cm^2\,\Omega^{-1}\,mol^{-1}$ (2:1 electrolyte). IR (KBr): $\tilde{\nu}$ = 1624 [ν(C=N)]; 1595 (s), 1543 [ν(C=C)], 1096 [ν_a(Cl–O)], 627 [δ_a(O–Cl–O)] cm^{-1}. MS (FAB): *m*/*z* (%) = 685 (15) $[Zn(L^4)(ClO_4)]^+$, 585 (100) $[Zn(L^4 - H)]^+$.

$[Co_2(L^4)Cl_2](ClO_4)_2$ (5): A solution of L^4 (0.106 g, 0.206 mmol) in acetonitrile (18 mL) was added to a stirred solution of $Co(ClO_4)_2\cdot 6H_2O$ (0.146 g, 0.400 mmol) in the same solvent (12 mL). The mixture was stirred and heated to reflux over a period of 2 h, and then $[n\mathrm{Bu_4N}]Cl$ (0.111 g, 0.412 mmol) was added. The resultant mixture was stirred and heated to reflux for 4 h. The violet precipitate formed was isolated by filtration and air-dried. Yield: 0.114 g (61%). $C_{28}H_{38}Cl_4Co_2N_6O_{12}$ (910.31): calcd. C 36.94, H 4.21, N 9.23; found C 37.02, H 4.35, N 9.46. Λ_M (acetonitrile, 20 °C): 252 $cm^2\,\Omega^{-1}\,mol^{-1}$ (2:1 electrolyte). IR (KBr): $\tilde{\nu}$ = 1626 [ν(C=N)]; 1599 (s), 1544 [ν(C=C)]; 1080 [ν_a(Cl–O)]; 624 [δ_a(O–Cl–O)] cm^{-1}. MS (FAB): *m*/*z* (%) = 809 (9) $[Co_2(L^4)(Cl)_2(ClO_4)]^+$, 709 (19) $[Co_2(L^4 - H)(Cl)_2]^+$, 680 (7) $[Co(L^4)(ClO_4)]^+$, 580 (100) $[Co(L^4 - H)]^+$. Slow diffusion of diethyl ether into a solution of the complex in acetonitrile at room temperature gave violet single crystals suitable for X-ray diffraction.

$[Ni_2(L^4)Cl_2](ClO_4)_2$ (6): The preparation of the complex followed the same procedure described for **5** by using $Ni(ClO_4)_2\cdot 6H_2O$ (0.147 g, 0.402 mmol). Yield: 0.118 g (63%). $C_{28}H_{38}Cl_4N_6Ni_2O_{12}$ (909.87): calcd. C 36.96, H 4.21, N 9.24; found C 37.02, H 4.41, N 9.47. Λ_M (DMF, 20 °C): 97 $cm^2\,\Omega^{-1}\,mol^{-1}$ (2:1 electrolyte). IR (KBr): $\tilde{\nu}$ = 1624 [ν(C=N)]; 1596 (s), 1530 [ν(C=C)]; 1088 [ν_a(Cl–O)]; 620 [δ_a(O–Cl–O)] cm^{-1}. MS (FAB): *m*/*z* (%) = 809 (10) $[Ni_2(L^4)Cl_2(ClO_4)]^+$, 709 (7) $[Ni_2(L^4 - H)Cl_2]^+$, 579 (15) $[Ni(L^4 - H)]^+$. Slow diffusion of diethyl ether into a solution of the complex in

Table 6. Crystal data and structure refinement for compounds **1**–**5**.

	1	**2**	**3**	**4**	**5**
Formula	$C_{30}H_{41}Cl_2CoN_7O_{12}$	$C_{30}H_{41}Cl_2N_7NiO_{12}$	$C_{31}H_{46}Cl_2CuN_6O_{13}$	$C_{30}H_{41}Cl_2N_7O_{12}Zn$	$C_{28}H_{38}Cl_4Co_2N_6O_{12}$
Mol. mass [g mol^{-1}]	821.53	821.31	845.17	827.97	910.3
Space group	monoclinic	monoclinic	monoclinic	monoclinic	monoclinic
Crystal system	$P2_1/n$	$P2_1/n$	$P2_1/n$	$P2_1/n$	$P2_1/c$
a [Å]	9.688(2)	9.644(2)	11.432(3)	9.7015(3)	11.224(1)
b [Å]	33.194(6)	33.083(7)	13.398(3)	33.1018(9)	12.413(1)
c [Å]	10.960(2)	10.948(2)	24.386(6)	10.9519(3)	13.477(1)
β [°]	102.403(3)	102.999(4)	97.069(4)	101.907 (1)	108.597(2)
V [Å^3]	3442.5(1)	3403.5(1)	3706.7(2)	3441.4(2)	1779.6(3)
F(000)	1708	1712	1764	1720	932
Z	4	4	4	4	2
T [K]	100.0(2)	100(2)	120.0(2)	100.0(2)	100(2)
λ [Å] (Mo-K_α)	0.71073	0.71073	0.71073	0.71073	0.71073
$\rho_{calcd.}$ [g cm^{-3}]	1.585	1.603	1.513	1.598	1.699
μ [mm^{-1}]	0.728	0.802	0.805	0.943	1.302
R_{int}	0.034	0.0485	0.0462	0.0682	0.0379
Reflections measured	25072	60673	59515	62677	21484
Reflections observed	6873	6569	6305	7988	3340
Goodness-of-fit on F^2	1.042	1.045	1.099	1.039	1.033
R_1[a]	0.040	0.0351	0.0624	0.0467	0.0457
wR_2(all data)[b]	0.0909	0.0856	0.1842	0.1056	0.1248

[a] $R_1 = \Sigma||F_o| - |F_c||/\Sigma|F_o|$. [b] $wR_2 = \{\Sigma[w(|F_o|^2 - |F_c|^2)^2]/\Sigma[w(F_o^4)]\}^{1/2}$.

DMF at room temperature gave green single crystals of formula $[Ni_2(L^4)(H_2O)_2Cl_2](ClO_4)_2$ suitable for X-ray diffraction.

$[Cu_2(L^4)Cl_2](ClO_4)_2$ (7): The preparation of the complex followed the same procedure described for **5** by using $Cu(ClO_4)_2{\cdot}6H_2O$ (0.152 g, 0.410 mmol). Yield: 0.080 g (42%). $C_{28}H_{38}Cl_4Cu_2N_6O_{12}$ (919.55): calcd. C 36.57, H 4.17, N 9.14; found C 36.72, H 4.24, N 9.40. Λ_M (DMF, 20 °C): 117 cm$^2\,\Omega^{-1}$ mol^{-1} (2:1 electrolyte). IR (KBr): $\tilde{\nu}$ = 1622 [ν(C=N)]; 1595 (s), 1538 [ν(C=C)]; 1084 [ν_a(Cl–O)]; 642 [δ_a(O–Cl–O)] cm^{-1}. MS (ESI, MeOH/CH_3CN): m/z (%) = 360 (70) $[Cu_2(L^4)Cl_2]^{2+}$, 620 (15) $[Cu(L^4)Cl]^+$, 292 (100) $[Cu(L^4)]^{2+}$. Slow diffusion of diethyl ether into a solution of the complex in DMF at room temperature gave green single crystals suitable for X-ray diffraction.

X-ray Crystal Structure Determinations: Three-dimensional X-ray data were collected at room temperature with a Bruker X8 Kappa APEX II (**4**, **6**, and **7**) or with a Bruker Smart 1000 CCD (**1**, **2**, **3**, and **5**) diffractometer by the Ω and ϕ scan method. Reflections were measured from a hemisphere of data collected of frames each covering 0.3° in omega. Of the 25072 (**1**), 60673 (**2**), 59515 (**3**), 62677 (**4**), 21484 (**5**), 41679 (**6**), and 36640 (**7**) reflections measured, all of which were corrected for Lorentz and polarization effects and for absorption by semiempirical methods based on symmetry-equivalent and repeated reflections, 6873 (**1**), 6569 (**2**), 6305 (**3**), 7988 (**4**) 3340(**5**), 3582 (**6**), and 3463 (**7**) independent reflections exceeded the significance level $|I|/\sigma(|I|)>2.0$. The solution, refinement, and analysis of the single-crystal X-ray diffraction data was performed with WinGX suite for small molecule single-crystal crystallography.[33] The structures of **1**, **2**, **3**, **6**, and **7** were solved by Patterson methods with DIRDIF99[34] and the structures of **4** and **5** were solved with SHELXS97[35] by direct methods. In all cases the structures were refined by full-matrix least-squares methods on F^2 with SHELXL97.[35] The hydrogen atoms were included in calculated positions and refined by using a riding mode, except H2N and H6N for **1**, **2**, and **3**, and H1W and H2W for **6**, which were found in the difference map and refined freely. Refinement converged with allowance for thermal anisotropy of all non-hydrogen atoms. Crystals of **5** show a disordered benzimidazole arm and a disordered perchlorate group. These disorders were solved with occupational factors of 0.721 (N2, C7, C8, C9, and C12) and 0.703 for (Cl2, O3, O4, O5, and O6). Crystals of **7** show also two disordered DMF molecules, one of them being in a special position, and occupation factors were fixed to 0.5 in both cases. Crystal data and details on data collection and refinement are summarized in Tables 6 and 7. CCDC-701043 (for **1**), -701044 (for **2**), -701045 (for **3**), -701046 (for **4**), -701047 (for **5**), -701048 (for **6**), -701049 (for **7**) contain the supplementary crystallographic data for this paper. These data can be obtained free of charge from the Cambridge Crystallographic Data Centre via www.ccdc.cam.ac.uk/data_request/cif.

Table 7. Crystal data and structure refinement for compounds **6** and **7**.

	6	**7**
Formula	$C_{34}H_{56}Cl_4N_8Ni_2O_{16}$	$C_{37}H_{59}Cl_4Cu_2N_9O_{15}$
Mol. mass [g mol^{-1}]	1092.09	1138.81
Space group	monoclinic	monoclinic
Crystal system	$P2_1/c$	P_{12}/c_1
a [Å]	11.8767(3)	14.7632(5)
b [Å]	15.5132(5)	7.3673(2)
c [Å]	12.2321(4)	22.3863(7)
β [°]	90.446(2)	100.742(2)
V [Å^3]	2253.6(1)	2392.2(1)
F(000)	1136	1180
Z	2	2
T [K]	100(2)	100.0(2)
λ [Å] (Mo-K_α)	0.71073	0.71073
$\rho_{calcd.}$ [g cm^{-3}]	1.609	1.581
μ [mm^{-1}]	1.150	1.187
R_{int}	0.0514	0.0724
Reflections measured	41679	36340
Reflections observed	3582	3463
Goodness-of-fit on F^2	1.078	1.075
R_1[a]	0.038	0.056
wR_2(all data)[b]	0.1002	0.1419

[a] $R_1 = \Sigma||F_o| - |F_c||/\Sigma|F_o|$. [b] $wR_2 = \{\Sigma[w(|F_o|^2 - |F_c|^2)^2]/\Sigma[w(F_o^4)]\}^{1/2}$.

DFT Calculations: All calculations were performed with the use of the Gaussian 03 (Revision C.01)[36] program package with the

B3LYP[37,38] three-parameter hybrid density functional. In vacuo geometry optimizations of the $[Zn(L^4)]^{2+}$ system were performed without constraints by using the Ahlrichs' valence triple-ζ (VTC)[39] basis set on Zn and the standard 6-31G(d) basis set on C, H, N, and O atoms. The stationary points found on the potential energy surfaces as a result of the geometry optimizations were tested to represent energy minima rather than saddle points by frequency analysis. The NMR shielding tensors of the $[Zn(L^4)]^{2+}$ system were calculated both in vacuo and in acetonitrile solution by using the GIAO method.[40] In these calculations we used the 6-311G(d,p) basis set on ligand atoms and Ahlrichs' valence triple-ζ (VTC) for Zn. For ^{13}C NMR chemical shift calculation purposes the NMR shielding tensors of tetramethylsilane (TMS) were calculated at the appropriate level.

Supporting Information (see footnote on the first page of this article): The in vacuo optimized Cartesian coordinates for the $[Zn(L^4)]^{2+}$ system; experimental and calculated bond lengths and angles of the metal coordination environment in $[Zn(L^4)]^{2+}$.

Acknowledgments

Authors thank Xunta de Galicia (PGIDIT06TAM10301PR) and Universidade da Coruña for generous financial support. The authors are indebted to Centro de Supercomputación de Galicia (CESGA) for providing the computer facilities.

[1] a) O. Iranzo, T. Elmer, J. P. Richard, J. R. Morrow, *Inorg. Chem.* **2003**, *42*, 7737–7746; b) C. Bazzicalupi, A. Bencini, E. Berni, A. Bianchi, P. Fornasari, C. Giorgi, B. Valtancoli, *Inorg. Chem.* **2004**, *43*, 6255–6265; c) S. Parimala, M. Kandaswamy, *Inorg. Chem. Commun.* **2003**, *6*, 1252–1254; d) N. H. Williams, A.-M. Lebuis, J. Chin, *J. Am. Chem. Soc.* **1999**, *121*, 3341–3348; e) M.-Y. Yang, J. P. Richard, J. R. Morrow, *Chem. Commun.* **2003**, 2832–2833.

[2] L. Kovbasyuk, H. Pritzkow, R. Krämer, I. O. Fritsky, *Chem. Commun.* **2004**, 880–881.

[3] a) B. Kersting, *Angew. Chem. Int. Ed.* **2001**, *40*, 3988–3990; b) C. Incarvito, A. L. Rheingold, A. L. Gavrilova, J. Qin, B. Bosnich, *Inorg. Chem.* **2001**, *40*, 4101–4108; c) A. L. Gavrilova, J. Qin, R. D. Sommer, A. L. Rheingold, B. Bosnich, *J. Am. Chem. Soc.* **2002**, *124*, 1714–1722; d) D. A. Brown, W. Errington, W. K. Glass, W. Haase, T. J. Kemp, H. Nimir, S. M. Ostrovsky, R. Werner, *Inorg. Chem.* **2001**, *40*, 5962–5971.

[4] G. Aromí, A. R. Bell, M. Helliwell, J. Raftery, S. J. Teat, G. A. Timco, O. Roubeau, R. E. P. Winpenny, *Chem. Eur. J.* **2003**, *9*, 3024–3032.

[5] C. Rodríguez-Infante, D. Esteban, F. Avecilla, A. de Blas, T. Rodríguez-Blas, J. Mahía, A. L. Macedo, C. F. G. C. Geraldes, *Inorg. Chim. Acta* **2001**, *317*, 190–198.

[6] C. Platas-Iglesias, L. Vaiana, D. Esteban-Gómez, F. Avecilla, J. A. Real, A. de Blas, T. Rodríguez-Blas, *Inorg. Chem.* **2005**, *44*, 9704–9713.

[7] L. Vaiana, M. Regueiro-Figueroa, M. Mato-Iglesias, C. Platas-Iglesias, D. Esteban-Gómez, A. de Blas, T. Rodríguez-Blas, *Inorg. Chem.* **2007**, *46*, 8271–8282.

[8] D. Casanova, P. Alemany, J. M. Bofill, S. Álvarez, *Chem. Eur. J.* **2003**, *9*, 1281–1295.

[9] L. Vaiana, C. Platas-Iglesias, D. Esteban-Gómez, F. Avecilla, J. M. Clemente-Juan, J. A. Real, A. de Blas, T. Rodríguez-Blas, *Dalton Trans.* **2005**, 2031–2037.

[10] L. Vaiana, C. Platas-Iglesias, D. Esteban-Gómez, F. Avecilla, A. de Blas, T. Rodríguez-Blas, *Eur. J. Inorg. Chem.* **2007**, 1874–1883.

[11] L. Vaiana, D. Esteban-Gómez, C. Platas-Iglesias, M. Mato-Iglesias, F. Avecilla, A. de Blas, T. Rodríguez-Blas, *Polyhedron* **2007**, *26*, 4141–4146.

[12] a) E. A. Deters, M. J. Goldcamp, J. A. Krause Bauer, M. J. Baldwin, *Inorg. Chem.* **2005**, *44*, 5222–5228; b) J. K. Bera, M. Nethaji, A. G. Samuelson, *Inorg. Chem.* **1999**, *38*, 218–228.

[13] G. Berden, W. L. Meerts, E. Jalviste, *J. Chem. Phys.* **1995**, *103*, 9596–9606.

[14] J. R. Platt, *J. Chem. Phys.* **1951**, *19*, 101–118.

[15] C. S. Wilcox, *Frontiers in Supramolecular Chemistry and Photochemistry*, VCH, Weinheim, **1991**, pp. 123–143.

[16] M. Vasak, J. H. R. Kaegi, B. Holmquist, B. L. Vallee, *Biochemistry* **1981**, *20*, 6659–6664.

[17] K. Nakamoto, *Infrared and Raman Spectra of Inorganic and Coordination Compounds*, 3rd ed., Wiley, New York, **1972**, pp. 142–154.

[18] W. J. Geary, *Coord. Chem. Rev.* **1971**, *7*, 81–122.

[19] M. Regueiro-Figueroa, D. Esteban-Gómez, C. Platas-Iglesias, A. de Blas, T. Rodríguez-Blas, *Eur. J. Inorg. Chem.* **2007**, 2198–2207.

[20] a) C.-Y. Su, Y.-P. Cai, C.-L. Chen, M. D. Smith, W. Kaim, H.-C. Zur Loye, *J. Am. Chem. Soc.* **2003**, *125*, 8595–8613; b) J.-Y. Xu, W. Gu, L. Li, S.-P. Yan, P. Cheng, D.-Z. Liao, Z.-H. Jiang, *J. Mol. Struct.* **2003**, *644*, 23–27; c) J. Angulo-Cornejo, M. Lino-Pacheco, R. Richter, L. Hennig, K.-H. Hallmeier, L. Beyer, *Inorg. Chim. Acta* **2000**, *305*, 38–45; d) C. J. Matthews, S. L. Heath, M. R. J. Elsegood, W. Clegg, T. A. Leese, J. C. Lockhart, *J. Chem. Soc., Dalton Trans.* **1998**, 1973–1978; e) L. Dobrzanska, G. O. Lloyd, T. Jacobs, I. Rootman, C. L. Oliver, M. W. Bredenkamp, L. J. Barbour, *J. Mol. Struct.* **2006**, *796*, 107–113; f) Y.-T. Cheng, H.-L. Chen, S.-Y. Tsai, C.-C. Su, H.-S. Tsang, T.-S. Kuo, Y.-C. Tsai, F.-L. Liao, S.-L. Wang, *Eur. J. Inorg. Chem.* **2004**, 2180–2188.

[21] a) S.-L. Ma, W.-X. Zhu, *J. Mol. Struct.* **2002**, *643*, 141–146; b) X. Jia, W. Zhu, Y. Zhang, X. Yan, *J. Mol. Struct.* **2002**, *604*, 159–164; c) S.-L. Ma, W.-X. Zhu, M.-Q. Xu, Y.-L. Wang, Q.-L. Guo, Y.-C. Liu, *Polyhedron* **2003**, *22*, 3249–3253; d) S.-L. Ma, W.-X. Zhu, C.-M. Qi, Q.-L. Guo, J. Zhang, Y.-C. Liu, M.-Q. Xu, *J. Mol. Struct.* **2004**, *703*, 25–29.

[22] M. Gonzalez-Lorenzo, C. Platas-Iglesias, F. Avecilla, C. F. G. C. Geraldes, D. Imbert, J.-C. G. Bünzli, A. de Blas, T. Rodríguez-Blas, *Inorg. Chem.* **2003**, *42*, 6946–6954.

[23] A. A. Palacios, P. Alemany, S. Alvarez, *Inorg. Chem.* **1999**, *38*, 707–715.

[24] a) M. R. Willcott, R. E. Lenkinski, R. E. Davis, *J. Am. Chem. Soc.* **1972**, *94*, 1742–1744; b) R. E. Davis, M. R. Willcott, *J. Am. Chem. Soc.* **1972**, *94*, 1744–1745.

[25] a) C. Platas-Iglesias, M. Mato-Iglesias, K. Djanashvili, R. N. Muller, L. Vander Elst, J. A. Peters, A. de Blas, T. Rodríguez-Blas, *Chem. Eur. J.* **2004**, *10*, 3579–3590; b) M. González-Lorenzo, C. Platas-Iglesias, F. Avecilla, S. Faulkner, S. J. A. Pope, A. de Blas, T. Rodríguez-Blas, *Inorg. Chem.* **2005**, *44*, 4254–4262.

[26] M. Panda, P.-W. Phuan, M. C. Kozlowski, *Chem. Commun.* **2002**, 1552–1553.

[27] D. Esteban-Gómez, C. Platas-Iglesias, F. Avecilla, A. de Blas, A. Rodríguez-Blas, *Eur. J. Inorg. Chem.* **2007**, 1635–1643.

[28] The parameter τ is the index of the degree of trigonality within the structural continuum between square-pyramidal and trigonal bipyramidal geometries. If A is the apical donor atom of a square-based pyramid then it should not be among the atoms that define the largest two angles at the metal center. Donor atoms B and C are associated with the greater basal angle (b) and atoms D and E with the smaller basal angle (a); $\tau = (b - a)/60$ and is therefore 0 for a square pyramid and 1 for a trigonal bipyramid.

[29] A. W. Addison, T. Nageswara-Rao, J. Reedijk, J. van Rijn, G. C. Verschoor, *J. Chem. Soc., Dalton Trans.* **1984**, 1349–1356.

[30] N. Su, J. S. Bradshaw, X. X. Zhang, P. B. Savage, K. E. Krakowiak, R. M. Izatt, *J. Heterocycl. Chem.* **1999**, *36*, 771–775.

[31] W. C. Wolsey, *J. Chem. Educ.* **1973**, *50*, A335–A337.

[32] P. Gans, A. Sabatini, A. Vacca, *Talanta* **1996**, *43*, 1739–1753.

[33] WinGX 1.70.01 An integrated system of Windows programs for the solution, refinement, and analysis of single-crystal X-ray diffraction data: L. J. Farrugia, *J. Appl. Crystallogr.* **1999**, *32*, 837–838.
[34] DIRDIF99 program system: P. T. Beurskens, G. Beurskens, R. de Gelder, S. Garcia-Granda, R. O. Gould, R. Israel, J. M. M. Smits, Crystallography Laboratory, University of Nijmegen, The Netherlands, **1999**.
[35] G. M. Sheldrick, *Acta Crystallogr., Sect. A: Found. Crystallogr.* **2008**, *64*, 112–122.
[36] M. J. Frisch, G. W. Trucks, H. B. Schlegel, G. E. Scuseria, M. A. Robb, J. R. Cheeseman, J. A. Montgomery Jr, T. Vreven, K. N. Kudin, J. C. Burant, J. M. Millam, S. S. Iyengar, J. Tomasi, V. Barone, B. Mennucci, M. Cossi, G. Scalmani, N. Rega, G. A. Petersson, H. Nakatsuji, M. Hada, M. Ehara, K. Toyota, R. Fukuda, J. Hasegawa, M. Ishida, T. Nakajima, Y. Honda, O. Kitao, H. Nakai, M. Klene, X. Li, J. E. Knox, H. P. Hratchian, J. B. Cross, C. Adamo, J. Jaramillo, R. Gomperts, R. E. Stratmann, O. Yazyev, A. J. Austin, R. Cammi, C. Pomelli, J. W. Ochterski, P. Y. Ayala, K. Morokuma, G. A. Voth, P. Salvador, J. J. Dannenberg, V. G. Zakrzewski, S. Dapprich, A. D. Daniels, M. C. Strain, O. Farkas, D. K. Malick, A. D. Rabuck, K. Raghavachari, J. B. Foresman, J. V. Ortiz, Q. Cui, A. G. Baboul, S. Clifford, J. Cioslowski, B. B. Stefanov, G. Liu, A. Liashenko, P. Piskorz, I. Komaromi, R. L. Martin, D. J. Fox, T. Keith, M. A. Al-Laham, C. Y. Peng, A. Nanayakkara, M. Challacombe, P. M. W. Gill, B. Johnson, W. Chen, M. W. Wong, C. Gonzalez, J. A. Pople, *Gaussian 03* (Revision C.01), Gaussian, Inc., Wallingford, CT, **2004**.
[37] A. D. Becke, *J. Chem. Phys.* **1993**, *98*, 5648–5652.
[38] C. Lee, W. Yang, R. G. Parr, *Phys. Rev. B* **1988**, *37*, 785–789.
[39] A. Schäefer, H. Horn, R. Ahlrichs, *J. Chem. Phys.* **1992**, *97*, 2571–2577.
[40] R. Ditchfield, *Mol. Phys.* **1974**, *27*, 789–807.

Received: September 17, 2008
Published Online: December 16, 2008

DOI: DOI/10.1002/ejic.200800934

Synthesis and Structure of Aminopyridinato-Stabilized Yttrium and Lanthanum Amides and Their Reactivity towards Alkylaluminium Compounds

Christian Döring[a] and Rhett Kempe*[a]

Keywords: Aluminium / N ligands / Ligand transfer / Rare earths / Silylamide route

A series of aminopyridinato-stabilized (amido)lanthanide complexes has been synthesized and characterized. The bulky aminopyridines (2,6-diisopropylphenyl)[6-(2,4,6-triisopropylphenyl)pyridin-2-yl]amine (**1a**) and [6-(2,4,6-triisopropylphenyl)pyridin-2-yl](2,4,6-trimethylphenyl)amine (**1b**) were introduced by amine elimination reaction with $[Ln\{N(SiHMe_2)_2\}_3(thf)_2]$ (Ln = Y, La, thf = tetrahydrofuran, Me = methyl) to obtain the corresponding mono(aminopyridinato) complexes. Single-crystal X-ray analyses were carried out for the yttrium derivatives. The complexes are not able to undergo coordinative chain transfer polymerization with ethylene in the presence of alkylaluminium compounds as the corresponding dialkyl complexes do. Investigations of the reactions of the lanthanide aminopyridinato complexes with triethylaluminium or diisobutylaluminium hydride reveal a fast transfer of the aminopyridinato ligand to the aluminium atom. The products of this transfer reaction are aminopyridinato-stabilized dialkylaluminium compounds. One example of these aluminium complexes was characterized by X-ray crystal structure analysis.

Introduction

Coordinative chain transfer polymerization[1] (CCTP) is an excellent tool to polymerize ethylene and α-olefins like propylene in a highly controlled and efficient fashion. A variety of systems are described in the literature which are capable of catalyzing this type of polymerization with various alkyl main group metal and zinc compounds.[2] We recently described an yttrium-based system, which catalyzes chain growing at aluminium.[3] This catalyst system is able to produce very narrowly molecular weight distributed polyethylene – less than 1.1 M_w/M_n – up to a molecular weight of about 4000 g/mol, and a polydispersity index of about 1.3 is observed for higher molecular weight polymers. Due to the interesting features of this catalyst system, we became interested in the investigation of the behaviour of other rare earth metals in this type of polymerization. The yttrium catalyst system was generated from a trialkyl precursor, namely $[Y(CH_2SiMe_3)_3(thf)_2]$.[4] Unfortunately, such precursors are not available for all rare earth metals.[5] Triamides of group 3 elements and the rare earth metals with the composition $[Ln\{N(SiHMe_2)_2\}_3(thf)_n]$ (n = 1, 2) are excellent starting materials to introduce a multiplicity of ligands, especially bulky ones[6,7,13,14] by the silylamide route. These tris(disilylamides) have the advantage to be available as salt-free derivatives for the whole series of lanthanides (Sc, Y, La–Lu).[7b,8,21] Recently, the thf-free triamides $[Y\{N(SiHMe_2)_2\}_3]$[9] and $[La\{N(SiHMe_2)_2\}_3]$[10] were introduced. The lanthanum complex is accessible by the conversion of $[La\{N(SiMe_3)_2\}_3]$ with the amine $HN(SiHMe_2)_2$ in pentane; the driving force of this reaction is the stronger acidity of $HN(SiHMe_2)_2$. The yttrium triamide was obtained from the reaction of $[YMe_3]_n$ and 3 equiv. of the amine $HN(SiHMe_2)_2$. Herein we report the synthesis and structure of aminopyridinato-stabilized[3,11,12,18,19] diamides of yttrium and lanthanum as well as ligand transfer reactions with alkylaluminium compounds, which are the reason for these compounds not being suitable as starting materials for the generation of catalysts for CCTP.

Results and Discussion

Metal Complex Synthesis

The reaction of $[Y\{N(SiMe_3)_2\}_3]$ with 1 equiv. of the sterically demanding aminopyridines **1a** and **b** in thf at 60 °C showed no conversion (monitored by ^{1}H NMR spectroscopy). Even after 3 d at 100 °C in toluene no aminopyridinato complexes were observed. This well-documented inertness of the bulky triamide led us to the replacement of $[Y\{N(SiMe_3)_2\}_3]$ with $[Ln\{N(SiHMe_2)_2\}_3(thf)_2]$.[8]

The reaction of the aminopyridine ligands **1** with 1 equiv. of $[Ln\{N(SiHMe_2)_2\}_3(thf)_2]$ (Ln = Y, La) yielded after amine elimination the corresponding diamides **2** and **3**, respectively (Scheme 1). The conversion of **1a**,**b** with $[La\{N(SiHMe_2)_2\}_3(thf)_2]$ at room temperature is nearly quantitative within 2 h, whereas the reaction of $[Y\{N(SiHMe_2)_2\}_3(thf)_2]$ at 60 °C takes 12 h to obtain complete conversion. The complexes **2** and **3** were characterized

[a] Lehrstuhl für Anorganische Chemie II, Universität Bayreuth, 95440 Bayreuth, Germany
Fax: +49-921-55-2157
E-mail: kempe@uni-bayreuth.de

by NMR spectroscopy and elemental analysis. Furthermore, the structures of **2a** and **2b** were determined by X-ray crystallography. Suitable single crystals of **2a**,**b** were obtained by cooling a saturated hexane solution to –30 °C. The complexes **2a** and **2b** crystallize as light-yellow prisms in the monoclinic space group $P2_1/c$. The molecular structures are depicted in Figures 1 (**2a**) and 2 (**2b**); crystallographic details are summarized in Table 1. In both compounds the metal atom has a coordination number of 5 and is coordinated by two bis(dimethylsilyl)amido ligands, one aminopyridinato and one thf ligand. The average metal–nitrogen bond length between both $\{N(SiHMe_2)_2\}$ groups and the yttrium atom with 2.243(3) (**2a**) and 2.243(7) Å (**2b**) are comparable to the average Y–N bond length of 2.260(4) Å in $[Y\{N(SiHMe_2)_2\}_3(thf)_2]$,[21] but is shorter than the $Ln–N_{amido}$ distances of the aminopyridinato ligand.

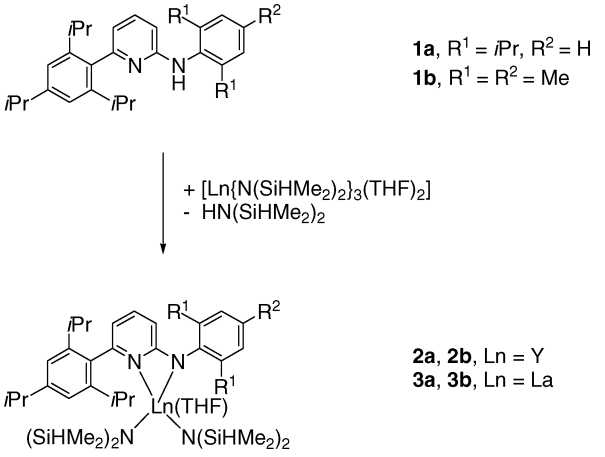

Scheme 1. Synthesis of aminopyridinato-stabilized diamides **2a**, **2b** and **3a**, **3b**.

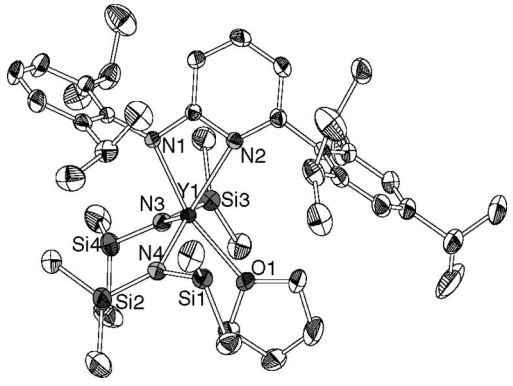

Figure 1. ORTEP diagram of the molecular structure of **2a** in the solid state (ellipsoids set at 40% probability level). H atoms have been omitted for clarity. Selected bond lengths [Å] and angles [°]: Y–N1 2.325(3), Y–N2 2.443(3), Y–N3 2.252(3), Y–N4 2.243(3), Y–O 2.409(2), Y–Si1 3.0970(11), Y–Si2 3.6559(14), Y–Si3 3.0830(11), Y–Si4 3.6402(14); Si1–N4–Si2 121.26(19), Si3–N3–Si4 124.99(19), Y–N4–Si2 135.74(18), Y–N4–Si1 102.74(14).

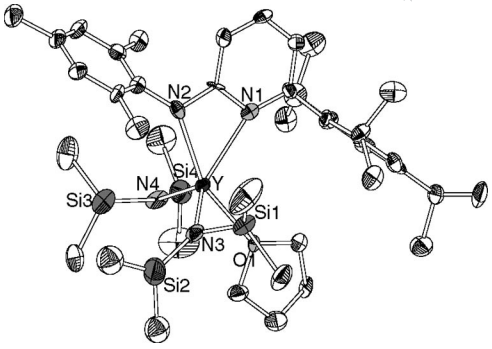

Figure 2. ORTEP diagram of the molecular structure of **2b** in the solid state (ellipsoids set at 40% probability level). H atoms and disordered methyl groups on Si2 have been omitted for clarity. Selected bond lengths [Å] and angles [°]:Y–N1 2.490(8), Y–N2 2.324(7), Y–N3 2.265(7), Y–N4 2.220(7), Y–O 2.390(5), Y–Si1 3.083(3) Y–Si2 3.630(3), Y–Si3 3.223(3), Y–Si4 3.306(3); Y–N3–Si1 101.7(3), Y–N3–Si2 133.2(4), Y–N4–Si3 111.3(4), Y–N4-Si4 114.4(3), Si1–N3–Si2 125.0(4), Si3–N4–Si4 132.0(5).

One of the silicon atoms of both $\{N(SiHMe_2)_2\}$ ligands of **2a** has a shorter distance to the metal centre than the other one: [Y–Si1 3.0970(11) and Y–Si3 3.0830(11) Å vs. Y–Si2 3.6559(14) and Y–Si4 3.6402(14) Å]. As a result, the Y–N–Si angle is becoming smaller and larger, respectively [Y–N4–Si1 102.74(14)° vs. Y–N4–Si2 135.74(18)°]. These features are an indicator for a monoagostic β-Si–H interaction (Figure 3b) of both dimethylsilylamido ligands as it is observed, for instance, for the complexes $[Ln\{N(SiHMe_2)_2\}_2\{CH(PPh_2NSiMe_3)_2\}]$,[7b] $[Y(Mes_2N_2NMe)\{N(SiHMe_2)_2\}(thf)]$[13] (Mes = 2,4,6-trimethylphenyl), $[Cp_2{*}Y\{N(SiHMe_2)_2\}]$[14] (Cp* = C_5Me_5), $[Ln\{N(SiHMe_2)_2\}_3(thf)_2]$.[8]

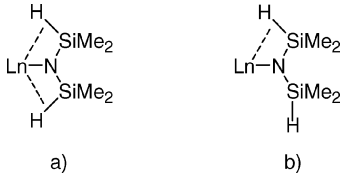

Figure 3. Diagostic (a) and monoagostic (b) interactions of the silylamido ligand.

However, in solution only one set of signals is observed for the dimethylsilylamido ligands (a doublet at δ = 0.24 ppm and a septet at δ = 4.92 ppm). Both $\{N(SiHMe_2)_2\}$ ligands of compound **2b** show different agostic β-Si–H interactions. One of the amido ligands has the same monoagostic β-Si–H interaction as it is observed for complex **2a** [Y–Si1 3.083(3) Å vs. Y–Si2 3.630(3) Å, Y–N3–Si1 101.7(3)° vs. Y–N3–Si2 133.2(4)°]. The other bis(dimethylsilyl)amido ligand reveals a weak diagostic β-Si–H interaction (Figure 3a). In this case both metal–silicon bond lengths differ only negligibly [Y–Si3 3.223(3) and Y–Si4 3.306(3) Å], the Y–N–Si angles [111.2(4) and 114.4(3)°] are also nearly equal, and the N–Si–N angle of 132.0(5)° is larger than the comparable angle of the other bis(dimethylsilyl)amido ligand of **2b** [125.0(4)°].

In comparison to other complexes with diagostic β-Si–H interactions the Si–N–Si bond angle is only marginally enlarged {153.3(2)° for *rac*-[{Me_2Si(2-Me-$C_9H_6)_2$}Y{$N(SiHMe_2)_2$}][15] and 139.8(1)° for [(Me_4C_5H)Y{$N(SiHMe_2)_2$}][16]}. The occurrence of a weak diagostic interaction of one of the bis(dimethylsilyl)amido ligands of compound **2b** could be explained by the lower steric demand of ligand **1b** compared to **1a**. A theoretical discussion on a diagostic β-Si–H interaction was given by Hieringer et al.[17]

CCTP Activity of the Aminopyridinato-Stabilized Amido Complexes and Ligand Transfer to the Aluminium Atom

We reported on aminopyridinato-stabilized alkylyttrium compounds, which are highly active ethylene polymerization catalysts (CCTP mechanism) in the presence of ammonium borates and alkylaluminium compounds or alumoxanes.[3] The aminopyridinato-stabilized dialkylyttrium compounds have a constitution similar to compounds **2** and **3**, but with two alkyl {CH_2SiMe_3} groups instead of the amido ligands {$N(SiHMe_2)_2$} of **2** and **3**. In the presence of alkylaluminium compounds (which are planned to act as alkylating agents and as transfer reagents) and ammonium borates, complex **2a** showed no ethylene CCTP activity. From this result we reasoned that in the presence of an alkylaluminium compound, **2** and **3** rather undergo a deactivation reaction than an alkylation. During the investigations of the reaction of **2a** with triethylaluminium or diisobutylaluminium hydride a transfer of the aminopyridinato ligand from the yttrium to the aluminium atom was observed (Scheme 2). The ligand transfer was observed by ^{1}H NMR spectroscopy (Figure 4). For that 20 μmol of **2a** was dissolved in 0.5 mL of deuterated benzene in an NMR tube, and 8 equiv. of triethylaluminium were added. Two ^{1}H NMR spectra were measured, after 5 min and at 60 °C after 12 h. After 5 min, a conversion from the starting compound **2a** to an uncharacterized species was observed (Figure 4, top). After 12 h at 60 °C, a complete transfer to the aluminium atom was observed by ^{1}H NMR spectroscopy (Figure 4, centre). To prove the formation of **4a** (Scheme 2), we independently synthesized the aminopyridinato-stabilized dialkylaluminium complexes **4**. The same ligand transfer is observed if only 4 equiv. of the alkylaluminium compound were added.

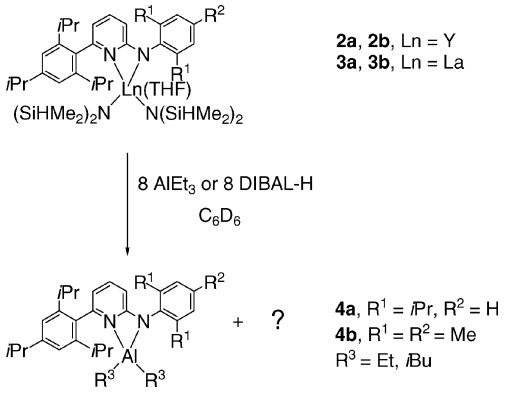

Scheme 2. Aminopyridinato ligand transfer from Y to Al.

The ^{1}H NMR spectrum of compound **4a** shows two different signals for both CH_2 groups of the ethyl ligands, with a very small difference in chemical shift. They were detected as quartets at δ = 0.36 and 0.37 ppm, respectively. Due to the lower steric demand of **1b** and thereby increased rotation of the ethyl ligand, only one signal for the methylene groups of compound **4b** was observed as a quartet at δ = 0.33 ppm. Furthermore, compound **4a** was characterized by an X-ray structure analysis (Figure 5). Compound **4a** crystallizes in the triclinic space group $P\bar{1}$. The complex is mononuclear involving a strained η^2 coordination of the Ap

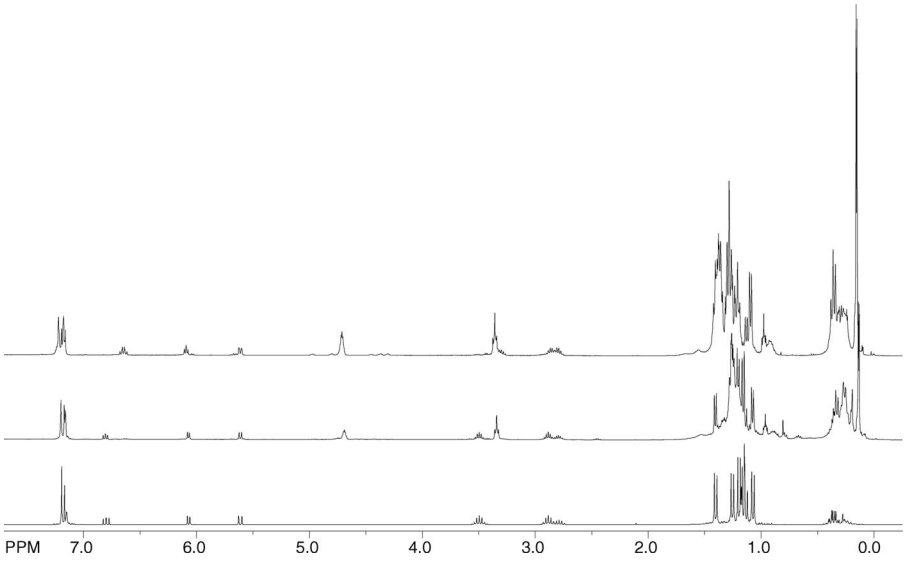

Figure 4. ^{1}H NMR spectra (C_6D_6, 298 K) of a mixture of **2a** + 8 equiv. $AlEt_3$ (top) at room temp. after 5 min and (centre) at 60 °C after 12 h indicative of **4a** being the only aminopyridinate; (bottom) ^{1}H NMR spectra (C_6D_6, 298 K) of **4a**.

(aminopyridinato) ligand. The Al–N bond lengths are quite similar and thus indicative of a binding mode with a high degree delocalization of the anionic function of the Ap ligands. (Ap)aluminium complexes which are η^2-coordinated are rare.[3,12g,18,19]

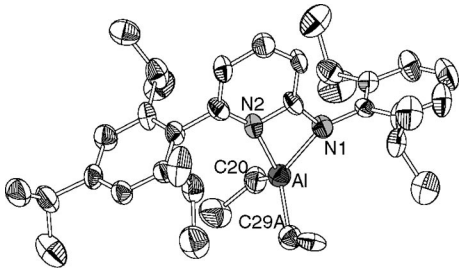

Figure 5. ORTEP diagram of the molecular structure of **4a** in the solid state (ellipsoids set at 40% probability level). H atoms and disordered ethyl group have been omitted for clarity. Selected bond lengths [Å] and angles [°]: Al–N1 1.929(5), Al–N2 1.970(5), Al–C20 1.945(6), Al–C29A 1.914(18), N1–Al–N2 69.1(2); C20–Al–C29A 110.6(5).

Conclusions

The results reported herein demonstrate that reactions of the triamide complexes $[Ln\{N(SiHMe_2)_2\}_3(thf)_2]$ (Ln = Y, La) with bulky aminopyridines selectively lead to the formation of mono(aminopyridinato) bis(dimethylsilyl)amides. They react with alkylaluminium compounds by transfer of the aminopyridinato ligand from the rare earth metal to the aluminium atom. Such a transfer reaction prohibits their use as precursors for CCTP, since the pre-catalysts are deactivated during the alkylation step. For alkyl precursors, which are suitable starting materials for the generation of CCTP catalysts, the organo rare earth cation must be generated before the reaction with aluminium can take place. After the cation is generated, a highly electrophillic rare earth metal and aluminium atom compete for the coordination of the aminopyridinato ligand, and the rare earth metal cation wins.[3] In the neutral state, the electrophilicity is much lower, and ligand transfer takes place.

Experimental Section

General Considerations: All reactions and manipulations involving air-sensitive compounds were performed under dry argon by using standard Schlenk and glovebox techniques. Non-halogenated solvents were dried with sodium/benzophenone ketyl and halogenated solvents with P_2O_5. Deuterated solvents were obtained from Cambridge Isotope Laboratories, degassed, dried with molecular sieves and distilled prior to use. Starting materials **1a**[20] and **1b**[3] were synthesized according to literature methods. $[Ln\{N(SiHMe_2)_2\}_3(thf)_2]$ were prepared by a modified literature procedure[21] using $K[N(SiHMe_2)_2]$[22] instead of $Li[N(SiHMe_2)_2]$. All other chemicals were purchased from commercial sources in purities >97% and used without further purification, if not otherwise stated. NMR spectra were obtained with either a Varian INOVA 300 or a Varian INOVA 400 spectrometer. Chemical shifts are reported in ppm relative to the deuterated solvent. Elemental analyses were carried out with a Vario elementar EL III apparatus. X-ray crystal structure analyses were performed with a STOE-IPDS II equipped with an Oxford Cryostream low-temperature unit. Structure solution and refinement were accomplished by using SIR97,[23] SHELXL-97[24] and WinGX.[25] Crystallographic details are summarized in Table 1. CCDC-702054 (**2a**), -702056 (**2b**) and -702055 (**4a**) contain the supplementary crystallographic data for this paper. These data can be obtained free of charge from The Cambridge Crystallographic Data Centre via www.ccdc.cam.ac.uk/data_request/cif.

Synthesis of the Complexes

Synthesis of 2a: thf (20 mL) was added to a mixture of $[Y\{N(SiHMe_2)_2\}_3(thf)_2]$ (1.26 g, 2.00 mmol) and **1a** (913 mg, 2.00 mmol). The resulting solution was stirred at 60 °C overnight. All volatiles were removed in vacuo to yield **2a** as a pale yellow powder in excellent yield (1.65 g, 94%). $C_{44}H_{79}N_4OSi_4Y$ (881.4): calcd. C 59.96, H 9.03, N 6.36; found C 59.42, H 8.88, N 5.88. ^1H

Table 1. Details of the X-ray crystal structure analyses.

Compound	**2a**	**2b**	**4a**
Formula	$C_{44}H_{79}N_4OSi_4Y$	$C_{41}H_{72}N_4OSi_4Y$	$C_{36}H_{53}N_2Al$
Crystal system	monoclinic	monoclinic	triclinic
Space group	$P2_1/c$	$P2_1/c$	$P\bar{1}$
a [Å]	12.5412(6)	19.3700(14)	11.614(3)
b [Å]	21.7430(7)	11.6850(8)	12.113(3)
c [Å]	19.1632(9)	21.9730(14)	13.879(3)
α [°]	90	90	73.788(19)
β [°]	98.900(4)	103.091(6)	80.996(18)
γ [°]	90	90	66.882(18)
Z	4	4	2
μ [mm^{-1}]	1.256	1.335	0.083
V [Å^3]	5162.6(4)	4844.1(6)	1721.9(7)
Crystal size [mm]	$0.61\times0.60\times0.58$	$0.23\times0.20\times0.14$	$0.33\times0.23\times0.07$
T [K]	193(2)	173(2)	173(2)
θ range [°]	1.43–25.83	1.60–25.46	1.53–22.42
Reflections, unique	9776	9195	6514
Reflections, observed [$I>2\sigma(I)$]	8599	2290	1475
Parameters	500	480	372
wR_2 (all data)	0.1342	0.1252	0.1171
R value [$I>2\sigma(I)$]	0.0604	0.0601	0.0822

NMR (300 MHz, C_6D_6, 298 K): δ = 0.24 [d, ^3J(H,H) = 2.5 Hz, 24 H, Si(CH_3)$_2$], 1.17 [d, ^3J(H,H) = 6.8 Hz, 6 H, CH(CH_3)$_2$], 1.22 [d, ^3J(H,H) = 6.8 Hz, 6 H, CH(CH_3)$_2$], 1.24 (br., 4 H, β-CH_2, thf), 1.25 [d, ^3J(H,H) = 6.8 Hz, 6 H, CH(CH_3)$_2$], 1.41 [d, ^3J(H,H) = 6.8 Hz, 6 H, CH(CH_3)$_2$], 1.46 [d, ^3J(H,H) = 6.8 Hz, 6 H, CH-(CH_3)$_2$], 2.80 [sept, ^3J(H,H) = 6.7 Hz, 1 H, 15-H] 3.10 [sept, ^3J(H,H) = 6.7 Hz, 2 H, 13,14/22,23-H], 3.58 (br., 4 H, α-CH_2, thf), 3.71 [sept, ^3J(H,H) = 6.7 Hz, 2 H, 13,14/22,23-H], 4.92 [sept, ^3J(H,H) = 3.0, ^1J(Si,H) = 84 Hz, 4 H, Si*H*], 5.73 [d, ^3J(H,H) = 8.7 Hz, 1 H, 3-H], 5.97 [d, ^3J(H,H) = 7.1 Hz, 1 H, 5-H], 6.66 [dd, ^3J(H,H) = 8.1, ^3J(H,H) = 7.0 Hz, 1 H, 4-H], 7.10–7.28 (m, 5 H, 9,11,18,19,20-H) ppm. ^{13}C NMR (75 MHz, C_6D_6, 298 K): δ = 3.8, 24.6, 24.8, 25.1, 25.7, 26.3, 26.5, 28.7, 31.0, 35.2, 71.2, 109.7, 112.1, 121.4, 124.9, 125.3, 137.6, 138.7, 144.8, 145.8, 147.6, 149.7, 156.6, 171.4 ppm. ^{29}Si NMR (60 MHz, C_6D_6, 298 K): δ = –22.9 ppm.

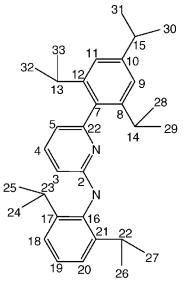

1a

Synthesis of 2b: [Y{N(SiHMe$_2$)$_2$}$_3$(thf)$_2$] (1.26 g, 2.00 mmol) and **1b** (829 mg, 2.00 mmol) were dissolved together in thf (20 mL). After stirring the mixture at 60 °C for 12 h, all volatiles were removed. The residue was redissolved in a minimum amount of pentane and crystallized at –30 °C to afford a pale yellow crystalline material. Yield 940 mg (56%). $C_{41}H_{73}N_4OSi_4Y$ (839.3): calcd. C 58.67, H 8.77, N 6.68; found C 59.20, H 8.52, N 6.46. ^{1}H NMR (300 MHz, C_6D_6, 298 K): δ = 0.28 [d, ^3J(H,H) = 2.9 Hz, 24 H, Si(CH_3)$_2$], 1.15 [d, ^3J(H,H) = 6.7 Hz, 6 H, CH(CH_3)$_2$], 1.18 [d, ^3J(H,H) = 6.7 Hz, 6 H, CH(CH_3)$_2$], 1.23 (m, 4 H, β-CH_2, thf), 1.35 [d, ^3J(H,H) = 6.7 Hz, 6 H, CH(CH_3)$_2$], 2.26 (s, 3 H, 30-H), 2.49 (s, 6 H, 28,29-H), 2.75 [sept, ^3J(H,H) = 6.7 Hz, 1 H, 19-H], 3.13 [sept, ^3J(H,H) = 6.7 Hz, 2 H, 13,16-H], 3.37 (m, 4 H, α-CH_2, thf), 4.94 [sept, ^3J(H,H) = 3.1, ^1J(Si,H) = 83 Hz, 4 H, Si*H*], 5.82 [d, ^3J(H,H) = 8.7 Hz, 1 H, 3-H], 5.97 [d, ^3J(H,H) = 7.0 Hz, 1 H, 5-H], 6.75 [dd, ^3J(H,H) = 8.6, ^3J(H,H) = 7.0 Hz, 1 H, 4-H], 6.98 (s, 2 H, 9,11/24,26-H), 7.06 (s, 2 H, 9,11/24,26-H) ppm. ^{13}C NMR (75 MHz, C_6D_6, 298 K): δ = 3.9, 20.9, 21.4, 22.2, 24.2, 24.8, 25.7, 26.8, 30.9, 35.1, 70.7, 107.2, 111.4, 121.2, 130.0, 132.6, 133.3, 137.9, 138.9, 144.3, 147.9, 149.8, 156.0, 168.9 ppm. ^{29}Si NMR (60 MHz, C_6D_6, 298 K): δ = –27.0 ppm.

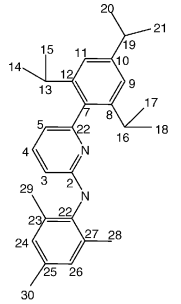

1b

Synthesis of 3a: [La{N(SiHMe$_2$)$_2$}$_3$(thf)$_2$] (680 mg, 1.00 mmol) and **1a** (457 mg, 1.00 mmol) were dissolved together in toluene (20 mL) and stirred for 2 h. All volatiles were removed, and the residue was extracted with hexane (20 mL). Removal of the solvent afforded spectroscopically pure **3a** as a yellow powder. Yield 430 mg (46%). $C_{44}H_{79}LaN_4OSi_4$ (931.4): calcd. C 56.74, H 8.55, N 6.02; found C 56.19, H 8.60, N 6.01. ^{1}H NMR (400 MHz, C_6D_6, 298 K): δ = 0.20 [d, ^3J(H,H) = 2.7 Hz, 24 H, Si(CH_3)$_2$], 1.17 [d, ^3J(H,H) = 6.7 Hz, 6 H, CH(CH_3)$_2$], 1.22 [d, ^3J(H,H) = 6.7 Hz, 6 H, CH(CH_3)$_2$], 1.23 [d, ^3J(H,H) = 6.7 Hz, 6 H, CH(CH_3)$_2$], 1.24 (br., 4 H, β-CH_2, thf), 1.39 [d, ^3J(H,H) = 6.7 Hz, 6 H, CH(CH_3)$_2$], 1.43 [d, ^3J(H,H) = 6.7 Hz, 6 H, CH(CH_3)$_2$], 2.79 [sept, ^3J(H,H) = 6.7 Hz, 1 H, 15-H], 3.12 [sept, ^3J(H,H) = 6.7 Hz, 2 H, 13,16-H], 3.38 (br., 4 H, α-CH_2, thf), 3.58 [sept, ^3J(H,H) = 6.7 Hz, 2 H, 13,16-H], 4.90 [br., Si*H*, ^3J(H,H) = 2.7, ^1J(Si,H) = 81 Hz, 4 H, Si*H*], 5.73 [d, ^3J(H,H) = 8.3 Hz, 1 H, 3-H], 5.95 [d, ^3J(H,H) = 7.1 Hz, 1 H, 5-H], 6.70 [dd, ^3J(H,H) = 8.3, ^3J(H,H) = 7.1 Hz, 1 H, 4-H], 7.08–7.27 (m, 5 H, 9,11,18,19,20-H) ppm. ^{13}C NMR (75 MHz, C_6D_6, 298 K): δ = 3.4, 24.8, 25.0, 25.3, 25.6, 26.0, 26.1, 29.1, 31.0, 35.1, 70.5, 109.4, 110.7, 121.5, 124.6, 124.7, 137.8, 138.6, 144.0, 146.5, 147.5, 149.4, 156.3, 170.3 ppm. ^{29}Si NMR (60 MHz, C_6D_6, 298 K): δ = –25.8 ppm.

Synthesis of 3b: [La{N(SiHMe$_2$)$_2$}$_3$(thf)$_2$] (680 mg, 1.00 mmol) and **1b** (415 mg, 1.00 mmol) were dissolved together in toluene (20 mL). After stirring the mixture for 2 h, all volatiles were removed, and the residue was extracted with hexane (20 mL). Removal of the solvent afforded spectroscopically pure **3b** as a yellow powder. Yield 521 mg (59%). $C_{41}H_{73}LaN_4OSi_4$ (889.2): calcd. C 55.37, H 8.27, N 6.30; found C 55.26, H 8.25, N 6.12. ^{1}H NMR (400 MHz, C_6D_6, 298 K): δ = 0.24 [d, ^3J(H,H) = 1.7 Hz, 24 H, Si(CH_3)$_2$], 1.16 [d, ^3J(H,H) = 6.7 Hz, 6 H, CH(CH_3)$_2$], 1.19 [d, ^3J(H,H) = 6.7 Hz, 6 H, CH(CH_3)$_2$], 1.24 (br., 4 H, β-CH_2, thf), 1.36 [d, ^3J(H,H) = 6.7 Hz, 6 H, CH(CH_3)$_2$], 2.27 (s, 3 H, 30-H), 2.45 (s, 6 H, 28,29-H), 2.76 [sept, ^3J(H,H) = 6.7 Hz, 1 H, 19-H] 3.15 [sept, ^3J(H,H) = 6.7 Hz, 2 H, 13,16-H], 3.27 (br., 4 H, α-CH_2, thf), 4.93 [sept, ^3J(H,H) = 2.7, ^1J(Si,H) = 81 Hz, 4 H, Si*H*], 5.81 [d, ^3J(H,H) = 8.8 Hz, 1 H, 3-H], 5.96 [d, ^3J(H,H) = 6.9 Hz, 1 H, 5-H], 6.79 [dd, ^3J(H,H) = 8.8, ^3J(H,H) = 6.9 Hz, 1 H, 4-H], 6.97 (s, 2 H, 9,11-H), 7.07 (s, 2 H, 24,26-H) ppm. ^{13}C NMR (75 MHz, C_6D_6, 298 K): δ = 3.5, 20.6, 21.4, 24.8, 24.9, 25.7, 26.4, 31.0, 35.1, 70.0, 107.3, 110.6, 121.3, 130.0, 132.1, 132.7, 138.1, 138.7, 145.3, 147.8, 149.4, 156.1, 168.3 ppm. ^{29}Si NMR (60 MHz, C_6D_6, 298 K): δ = –26.1 ppm.

Synthesis of 4a: A Schlenk vessel was charged with **1a** (91.0 mg, 0.20 mmol) and toluene (3 mL) before a triethylaluminium solution (0.20 mL, 0.20 mmol, 1.0 M $AlEt_3$ in toluene) was added. After stirring the mixture for 1 h, all volatiles were removed in vacuo to yield **4a** as colorless oil in almost quantitative yield. $C_{36}H_{53}AlN_2$ (540.8): calcd. C 79.95, H 9.88, N 5.18; found C 79.33, H 10.20, N 5.48. ^{1}H NMR (300 MHz, C_6D_6, 298 K): δ = 0.36 [q, ^3J(H,H) = 8.1 Hz, 2 H, AlCH_2CH$_3$], 0.37 [q, ^3J(H,H) = 8.1 Hz, 2 H, AlCH_2CH$_3$], 1.07 [d, ^3J(H,H) = 6.8 Hz, 6 H, CH(CH_3)$_2$], 1.15 [t, ^3J(H,H) = 8.1 Hz, 6 H, AlCH$_2$CH_3], 1.16 [d, ^3J(H,H) = 6.8 Hz, 6 H, CH-(CH_3)$_2$], 1.19 [d, ^3J(H,H) = 6.8 Hz, 6 H, CH(CH_3)$_2$], 1.25 [d, ^3J(H,H) = 6.8 Hz, 6 H, CH(CH_3)$_2$], 1.40 [d, ^3J(H,H) = 6.8 Hz, 6 H, CH(CH_3)$_2$], 2.79 [sept, ^3J(H,H) = 6.8 Hz, 1 H, 15-H], 2.88 [sept, ^3J(H,H) = 6.8 Hz, 2 H, 13,14/22,23-H], 3.50 [sept, ^3J(H,H) = 6.8 Hz, 2 H, 13,14/22,23-H], 5.61 [d, ^3J(H,H) = 8.6 Hz, 1 H, 3-H], 6.07 [d, ^3J(H,H) = 7.0 Hz, 1 H, 5-H], 6.80 [dd, ^3J(H,H) = 8.6, ^3J(H,H) = 7.1 Hz, 4-H], 7.17 (br., 2 H, 18,20-H), 7.19 (br., 3 H, 9,11,19-H) ppm. ^{13}C NMR (75 MHz, C_6D_6, 298 K): δ = 1.8, 9.2, 22.7, 24.2, 24.4, 24.7, 26.4, 28.6, 30.9, 34.8, 104.4, 111.3, 120.9, 124.3, 126.3, 133.4, 138.3, 141.4, 145.6, 146.9, 150.3, 154.8, 167.2 ppm.

Synthesis of 4b: To a stirred solution of **1b** (83.0 mg, 0.20 mmol) in toluene (3 mL) was added a triethylaluminium solution (0.20 mL, 0.20 mmol, 1.0 M $AlEt_3$ in toluene). After stirring the mixture for 1 h, all volatiles were removed in vacuo to yield **4b** as colorless oil in almost quantitative yield. $C_{33}H_{47}AlN_2$ (498.7): calcd. C 79.47, H 9.50, N 5.62; found C 79.23, H 9.55, N 5.72. ^{1}H NMR (300 MHz, C_6D_6, 298 K): δ = 0.33 [q, ^3J(H,H) = 8.1 Hz, 4 H, $AlCH_2CH_3$], 1.11 [d, ^3J(H,H) = 6.8 Hz, 6 H, $CH(CH_3)_2$], 1.16 [t, ^3J(H,H) = 8.1 Hz, 6 H, $AlCH_2CH_3$], 1.20 [d, ^3J(H,H) = 6.8 Hz, 6 H, $CH(CH_3)_2$], 1.42 [d, ^3J(H,H) = 6.8 Hz, 6 H, $CH(CH_3)_2$], 2.20 (s, 3 H, 30-H), 2.27 (s, 6 H, 28,29-H), 2.80 [sept, ^3J(H,H) = 6.9 Hz, 1 H, 9-H], 2.90 [sept, ^3J(H,H) = 6.8 Hz, 2 H, 13,16-H], 5.64 [dd, ^4J(H,H) = 0.8, ^3J(H,H) = 8.6 Hz, 1 H, 3-H], 6.09 [dd, ^4J(H,H) = 0.8, ^3J(H,H) = 7.2 Hz, 1 H, 5-H], 6.83 [dd, ^3J(H,H) = 8.6, ^3J(H,H) = 7.2 Hz, 4-H], 6.85 (s, 2 H, 9,11-H), 7.19 (s, 2 H, 24,26-H) ppm. ^{13}C NMR (75 MHz, C_6D_6, 298 K): δ = 0.2, 8.9, 18.8, 20.9, 22.7, 24.2, 26.5, 30.9, 34.8, 104.0, 111.1, 120.9, 129.6, 133.4, 134.0, 134.2, 138.4, 141.4, 146.9, 150.2, 154.2, 165.6 ppm.

Acknowledgments

Financial support from the Deutsche Forschungsgemeinschaft (DFG) (SPP 1166 "Lanthanide specific functionalities in molecules and materials") is acknowledged. We thank W. P. Kretschmer for the polymerization studies.

[1] R. Kempe, *Chem. Eur. J.* **2007**, *13*, 2764–2773.
[2] a) M. B. Harney, R. J. Keaton, J. C. Fettinger, L. R. Sita, *J. Am. Chem. Soc.* **2006**, *128*, 3420–3432; b) P. D. Hustad, R. L. Kuhlman, D. J. Arriola, E. M. Carnahan, T. T. Wenzel, *Macromolecules* **2007**, *40*, 7061–7064; c) P. D. Hustad, R. L. Kuhlman, E. M. Carnahan, T. T. Wenzel, D. J. Arriola, *Macromolecules* **2008**, *41*, 4081–4089; d) E.G. Samsel, Ethyl Corporation, EP 0539876, **1993**; e) E. G. Samsel, Ethyl Corporation, EP 0574854, **1993**; f) J.-F. Pelletier, A. Mortreux, X. Olonde, K. Bujadoux, *Angew. Chem.* **1996**, *108*, 1980–1982; *Angew. Chem. Int. Ed. Engl.* **1996**, *35*, 1854–1856; g) J. F. Pelletier, K. Bujadoux, X. Olonde, E. Adisson, A. Mortreux, T. Chenal, US 5779942, **1998**; h) J. S. Rogers, G. C. Bazan, *Chem. Commun.* **2000**, 1209–1210; i) G. C. Bazan, J. S. Rogers, C. C. Fang, *Organometallics* **2001**, *20*, 2059–2064; j) G. Mani, F. P. Gabbai, *Angew. Chem.* **2004**, *116*, 2313–2316; *Angew. Chem. Int. Ed.* **2004**, *43*, 2263–2266; k) G. Mani, F. P. Gabbai, *J. Organomet. Chem.* **2005**, *690*, 5145–5149; l) G. J. P. Britovsek, S. A. Cohen, V. C. Gibson, P. J. Maddox, M. van Meurs, *Angew. Chem.* **2002**, *114*, 507–509; *Angew. Chem. Int. Ed.* **2002**, *41*, 489–491; m) G. J. P. Britovsek, S. A. Cohen, V. C. Gibson, M. van Meurs, *J. Am. Chem. Soc.* **2004**, *126*, 10701–10712; n) M. van Meurs, G. J. P. Britovsek, V. C. Gibson, S. A. Cohen, *J. Am. Chem. Soc.* **2005**, *127*, 9913–9923; o) T. Chenal, X. Olonde, J.-F. Pelletier, K. Bujadoux, M. Mortreux, *Polymer* **2007**, *48*, 1844–1856; p) W. Zhang, J. Wei, L. R. Sita, *Macromolecules* **2008**, *41*, 7829–7833; q) W. Zhang, L. R. Sita, *J. Am. Chem. Soc.* **2008**, *130*, 442–443.
[3] W. P. Kretschmer, A. Meetsma, B. Hessen, T. Schmalz, S. Qayyum, R. Kempe, *Chem. Eur. J.* **2006**, *12*, 8969–8978.
[4] M. F. Lappert, R. J. Pearce, *J. Chem. Soc., Chem. Commun.* **1973**, 126–127.
[5] In an interesting polymerization study the alkyl compounds of the early lanthanoids were generated in situ: S. Bambirra, M. W. Bouwkamp, A. Meetsma, B. Hessen, *J. Am. Chem. Soc.* **2004**, *126*, 9182–9183.
[6] O. Runte, T. Priermeier, R. Anwander, *Chem. Commun.* **1996**, 1385–1386.
[7] a) H. Ma, T. Spaniol, J. Okuda, *Inorg. Chem.* **2008**, *47*, 3328–3339; b) M. Rastätter, A. Zulys, P. W. Roesky, *Chem. Eur. J.* **2007**, *13*, 3606–3616; c) R. H. Platel, L. M. Hodgson, A. J. P. White, C. K. Williams, *Organometallics* **2007**, *26*, 4955–4963; d) D. V. Vitanova, F. Hampel, K. C. Hultzsch, *J. Organomet. Chem.* **2005**, *690*, 5182–5197; e) R. Anwander, M. G. Klimpel, H. M. Dietrich, D. J. Shorokhov, W. Scherer, *Chem. Commun.* **2003**, 1008–1009; f) S. A. Ahmed, M. S. Hill, P. B. Hitchcock, S. M. Mansell, O. St John, *Organometallics* **2007**, *26*, 538–549; g) I. Westmoreland, J. Arnold, *Dalton Trans.* **2006**, 4155–4163; h) A. Amgoune, C. M. Thomas, T. Roisnel, J.-F. Carpentier, *Chem. Eur. J.* **2006**, *12*, 169–179; i) H. Ma, T. P. Spaniol, J. Okuda, *Dalton Trans.* **2003**, 4770–4780; j) D. V. Gribkov, K. C. Hultzsch, F. Hampel, *Chem. Eur. J.* **2003**, *9*, 4796–4810; k) P. N. O'Shaughnessy, P. D. Knight, C. Morton, K. M. Gillespie, P. Scott, *Chem. Commun.* **2003**, 1770–1771; l) F. Estler, E. Herdtweck, R. Anwander, *J. Chem. Soc., Dalton Trans.* **2002**, 3088–3089; m) R. Anwander, J. Eppinger, I. Nagl, W. Scherer, M. Tafipolsky, P. Sirsch, *Inorg. Chem.* **2000**, *39*, 4713–4720; n) G. Zi, H.-W. Li, Z. Xie, *Organometallics* **2002**, *21*, 1136–1145; o) C. Meermann, G. Gerstberger, M. Spiegler, K. W. Törnroos, R. Anwander, *Eur. J. Inorg. Chem.* **2008**, 2014–2023.
[8] a) R. Anwander, O. Runte, J. Eppinger, G. Gerstberger, E. Herdtweck, M. Spiegler, *J. Chem. Soc., Dalton Trans.* **1998**, 847–858; b) G. W. Rabe, G. P. A. Yap, *Z. Kristallogr. – New Cryst. Struct.* **2000**, *215*, 457–458.
[9] H. M. Dietrich, C. Meermann, K. W. Törnroos, R. Anwander, *Organometallics* **2006**, *25*, 4316–4321.
[10] H. F. Yuen, T. J. Marks, *Organometallics* **2008**, *27*, 155–158.
[11] For review articles on aminopyridinato ligands, see: a) R. Kempe, H. Noss, T. Irrgang, *J. Organomet. Chem.* **2002**, *647*, 12–20; b) R. Kempe, *Eur. J. Inorg. Chem.* **2003**, 791–803.
[12] For selected work with very bulky aminopyridinato ligands please, see: a) N. M. Scott, R. Kempe, *Eur. J. Inorg. Chem.* **2005**, 1319–1324; b) W. P. Kretschmer, A. Meetsma, B. Hessen, N. M. Scott, S. Qayyum, R. Kempe, *Z. Anorg. Allg. Chem.* **2006**, *632*, 1936–1938; c) S. M. Guillaume, M. Schappacher, N. M. Scott, R. Kempe, *J. Polym. Sci., Part A: Polym. Chem.* **2007**, *45*, 3611–3619; d) A. M. Dietel, O. Tok, R. Kempe, *Eur. J. Inorg. Chem.* **2007**, 4583–4586; e) S. Qayyum, K. Haberland, C. M. Forsyth, P. C. Junk, G. B. Deacon, R. Kempe, *Eur. J. Inorg. Chem.* **2008**, 557–562; f) G. G. Skvortsov, G. K. Fukin, A. A. Trifonov, A. Noor, C. Döring, R. Kempe, *Organometallics* **2007**, *26*, 5770–5773; g) W. P. Kretschmer, B. Hessen, A. Noor, N. M. Scott, R. Kempe, *J. Organomet. Chem.* **2007**, *692*, 4569–4579; h) A. Noor, R. Kempe, *Eur. J. Inorg. Chem.* **2008**, 2377–2381; i) D. M. Lyubov, C. Döring, G. K. Fukin, A. V. Cherkasov, A. V. Shavyrin, R. Kempe, A. A. Trifonov, *Organometallics* **2008**, *27*, 2905–2907; j) A. Noor, F. R. Wagner, R. Kempe, *Angew. Chem.* **2008**, *120*, 7356–7359; *Angew. Chem. Int. Ed.* **2008**, *47*, 7246–7259; k) A. Noor, W. P. Kretschmer, G. Glatz, A. Meetsma, R. Kempe *Eur. J. Inorg. Chem.*, in press.
[13] K. C. Hultzsch, F. Hampel, T. Wagner, *Organometallics* **2004**, *23*, 2601–2612.
[14] M. G. Klimpel, H. W. Görlitzer, M. Tafipolsky, M. Spiegler, W. Scherer, R. Anwander, *J. Organomet. Chem.* **2002**, *647*, 236–244.
[15] W. A. Herrmann, J. Eppinger, M. Spiegler, O. Runte, R. Anwander, *Organometallics* **1997**, *16*, 1813–1815.
[16] M. G. Klimpel, H. W. Görlitzer, M. Tafipolsky, M. Spiegler, W. Scherer, R. Anwander, *J. Organomet. Chem.* **2002**, *647*, 236–244.
[17] W. Hieringer, J. Eppinger, R. Anwander, W. A. Herrmann, *J. Am. Chem. Soc.* **2000**, *122*, 11983–11994.
[18] a) C. Jones, P. C. Junk, S. G. Leary, N. A. Smithies, *Main Group Met. Chem.* **2001**, *24*, 383–384; b) M. Pfeiffer, A. Murso, L. Mahalakshmi, D. Moigno, W. Kiefer, D. Stalke, *Eur. J. Inorg. Chem.* **2002**, 3222–3234.
[19] J. Ashenhurst, L. Brancaleon, S. Gao, W. Liu, H. Schmider, S. Wang, G. Wu, Q. G. Wu, *Organometallics* **1998**, *17*, 5334–5341.

[20] N. M. Scott, T. Schareina, O. Tok, R. Kempe, *Eur. J. Inorg. Chem.* **2004**, 3297–3304.
[21] W. A. Herrmann, R. Anwander, F. C. Munck, W. Scherer, V. Dufaud, N. W. Huber, G. R. J. Artus, *Z. Naturforsch., B* **1994**, *49*, 1789–1797.
[22] J. Schneider, E. Popowski, H. Reinke, *Z. Anorg. Allg. Chem.* **2003**, *629*, 55–64.
[23] A. Altomare, M. C. Burla, M. Camalli, G. L. Cascarano, C. Giacovazzo, A. Guagliardi, A. G. G. Moliterni, G. Polidori, R. Spagna, *J. Appl. Crystallogr.* **1999**, *32*, 115–119.
[24] G. M. Sheldrick, *SHELX-97, Program for Crystal Structure Analysis*, release 97-2, Institut für Anorganische Chemie der Universität, Göttingen, Germany, **1998**.
[25] L. J. Farrugia, *J. Appl. Crystallogr.* **1999**, *32*, 837–838.
Received: September 19, 2008
Published Online: December 12, 2008

DOI: 10.1002/ejic.200800953

Self-Assembled Transition-Metal Macrocycles and Two-Dimensional Coordination Polymers Derived from Flexible C_2Co_2 Cluster-Bridged Bipyridine Ligands $[(4\text{-}C_5H_4NCO_2CH_2)_2C_2Co_2(CO)_6]$ and $[(3\text{-}C_5H_4NCO_2CH_2)_2C_2Co_2(CO)_6]$

Li-Cheng Song,*[a] Guo-Xia Jin,[a] Li-Qun Zhao,[a] Hu-Ting Wang,[a] Wen-Xiong Zhang,[a] and Qing-Mei Hu[a]

Keywords: Transition metals / N ligands / Self-assembly / Structure elucidation / Electrochemistry

Reactions of the tetrahedral C_2Co_2 cluster-bridged bipyridine ligand $[(4\text{-}C_5H_4NCO_2CH_2)_2C_2Co_2(CO)_6]$ (L^a) with $[\{M(dppb)(H_2O)_2\}(OTf)_2]$ (M = Pd, Pt; dppb = 1,4-bis(diphenylphosphanyl)butane; OTf = SO_3CF_3) and AgX (X = NO_3, SbF_6) gave cationic metallamacrocycles $[\{M(dppb)L^a\}_2(OTf)_4]$ (**1**, M = Pd; **2**, M = Pt) and $[(AgL^a)_2X_2]$ (**3**, X = NO_3; **4**, X = SbF_6). Furthermore, the isomeric C_2Co_2 cluster-bridged bipyridine ligand $[(3\text{-}C_5H_4NCO_2CH_2)_2C_2Co_2(CO)_6]$ (L^b) reacted with $ZnCl_2$ and AgX (X = PF_6, ClO_4) to afford cationic macrocycle $[(ZnL^bCl_2)_2]$ (**5**) and coordination polymers $[(AgL^bX)_n]$ (**6**, X = PF_6; **7**, X = ClO_4), respectively. Whereas flexible ligand L^a is known, L^b is new and could be prepared by reaction of but-2-yne-1,4-diyl dipyridine-3-carboxylate with $[Co_2(CO)_8]$. New self-assembled products **1**–**7** and ligand L^b were characterized by elemental analysis and spectroscopy, and **1**, **3**–**7**, and L^b were additionally characterized by X-ray crystallography. In addition, the electrochemistry of L^b and **5** were studied by cyclic voltammetry.

Introduction

In recent years, transition-metal macrocycles and coordination polymers have received considerable attention because of their potential applications in areas such as catalysis,[1] optical devices,[2] molecular magnetics,[3] and microporous adsorption materials.[4] Although a wide variety of such organic–inorganic macrocycles and polymers have been prepared so far by coordination-driven self-assembly,[5,6] construction of such self-assembled systems, which possess unique structures and fascinating properties, is still a topic of great interest in supramolecular chemistry. Recently, we reported a series of novel cationic M^{II}/Co^0 (M = Pd, Pt) metallamacrocycles, which were prepared by self-assembly of diphosphane or diarsine-chelated Pd^{II}/Pt^{II} complexes with rigid and flexible C_2Co_2 cluster-bridged bipyridine ligands.[7,8] To further prepare such novel metallamacrocycles and to examine the influence of transition-metal compounds and the C_2Co_2 cluster-bridged bipyridine ligands upon structures and properties of the assembled products, we initiated a study on the self-assembly of bipyridine ligands $[(4\text{-}C_5H_4NCO_2CH_2)_2C_2Co_2(CO)_6]$ (L^a) and $[(3\text{-}C_5H_4NCO_2CH_2)_2C_2Co_2(CO)_6]$ (L^b) with some Ag^I/Zn^{II} salts and Pd^{II}/Pt^{II} complexes $[\{M(dppb)(H_2O)_2\}(OTf)_2]$ (M = Pd, Pt; dppb = 1,4-bis(diphenylphosphanyl)butane; OTf = SO_3CF_3). As a result, we obtained not only the corresponding discrete metallamacrocycles, but also infinite polymers, mainly dependent on both transition-metal compounds and the cluster-bridged bipyridine ligands utilized in the self-assembly reactions. In this paper, we report our results obtained from this study.

Results and Discussion

Synthesis and Characterization of Macrocycles $[\{M(dppb)L^a\}_2(OTf)_4]$ (1, M = Pd; 2, M = Pt) and $[(AgL^a)_2X_2]$ (3, X = NO_3; 4, X = SbF_6)

The tetrahedral C_2Co_2 cluster-bridged bipyridine ligand $[(4\text{-}C_5H_4NCO_2CH_2)_2C_2Co_2(CO)_6]$ (L^a) was found to undergo self-assembly with dppb-chelated Pd^{II}/Pt^{II} complexes $[\{M(dppb)(H_2O)_2\}(OTf)_2]$ in CH_2Cl_2 at room temperature to give the tetrahedral cluster-containing metallamacrocycles **1** and **2** in 94 and 74% yields, respectively (Scheme 1).

Complexes **1** and **2** are air-stable solids, which have been characterized by elemental analysis and spectroscopy. The IR spectra of **1** and **2** show three strong absorption bands in the range 2101–2036 cm^{-1} for their terminal carbonyl groups and one strong absorption band at 1737 or 1738 cm^{-1} for their ester carbonyl groups. The ^{19}F NMR

[a] Department of Chemistry, State Key Laboratory of Elemento-Organic Chemistry, Nankai University,
Tianjin 300071, China
Fax: +86-22-23504853
E-mail: lcsong@nankai.edu.cn
Supporting information for this article is available on the WWW under http://www.eurjic.org or from the author.

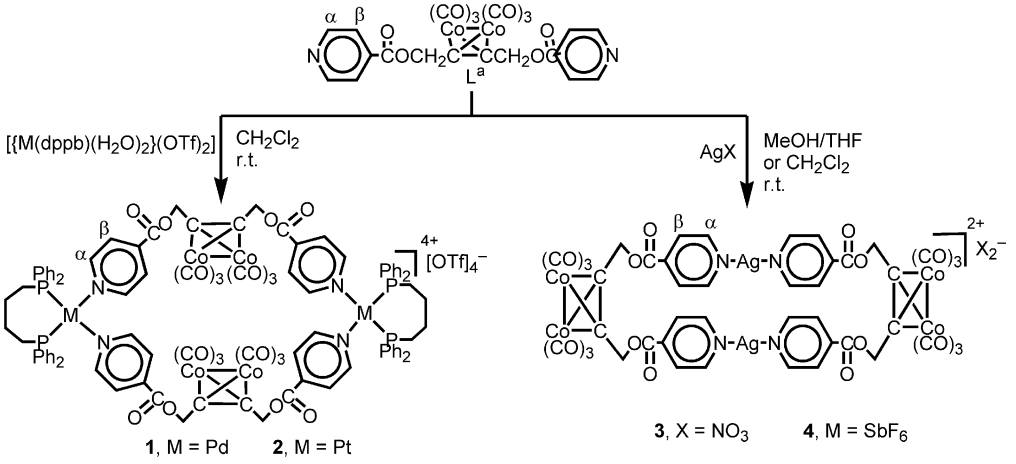

Scheme 1.

spectra of **1** and **2** displayed one singlet at ca. –79 ppm for their triflate counterions. Whereas the ^{31}P NMR spectrum of **1** showed one singlet at 36.50 ppm for its two identical P atoms, product **2** displayed one singlet at 9.63 ppm for its two identical P atoms; the signal is flanked by satellites due to a $^{1}J_{^{195}Pt,^{31}P}$ coupling of 1565 Hz.

The molecular structure of **1** was unambiguously confirmed by X-ray crystal diffraction analysis. Figure 1 shows the ORTEP view of its cationic portion, whereas Table 1 lists its selected bond lengths and angles. As shown in Figure 1, the cationic macrocycle of **1** is centrosymmetric and consists of two dppb-chelated Pd units joined together by two tetrahedral C_2Co_2 cluster-bridged bipyridine ligands L^a. The coordination geometry around the Pd atoms is square planar with some deviations of the P–Pd–P (95.91°) and N–Pd–N (85.24°) bond angles from the ideal 90°. All the Pd–P and Pd–N bond lengths are within a normal range and nonbonding Pd···Pd distance is 16.775 Å. The structural features of **1** also include: (i) The two pyridine rings in each L^a ligand are *cis* to the $Co_2(CO)_6$ moiety of the tetrahedral C_2Co_2 cluster unit. (ii) The four pyridine rings and the Co1Co2Co1ACo2A plane are nearly perpendicular to the plane defined by the six atoms Pd1, C14, C15, Pd1A, C14A, and C15A. (iii) The two Pd atoms and the four Co atoms are located at six apical positions of an octahedron. It follows that the structure of **1** is very similar to those of its analogues [{M(dpab)L^a}$_2$(OTf)$_4$] (M = Pd/Pt).[7]

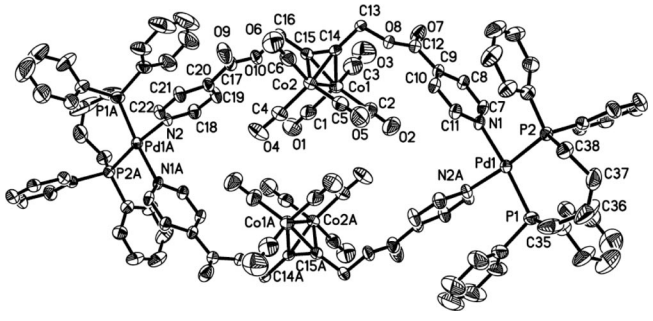

Figure 1. ORTEP view of cationic macrocycle of **1** with 30% thermal ellipsoids.

Table 1. Selected bond lengths [Å] and angles [°] for **1**, **3**, and **4**.

1			
Pd1–P2	2.3014(14)	Pd1–P1	2.3032(14)
Pd1–N1	2.097(4)	P1–C35	1.832(7)
Co1–C14	1.946(5)	P2–C38	1.830(5)
Co1–C15	1.948(5)	Co1–Co2	2.4569(13)
N1–C7	1.341(6)	C14–C15	1.302(7)
N1–Pd1–N2A	85.24(14)	Co2–Co1–C15	50.64(17)
N1–Pd1–P2	89.41(10)	Co2–Co1–C14	51.08(16)
N1–Pd1–P1	174.57(10)	C14–Co1–C15	39.07(19)
P2–Pd1–P1	95.91(5)	C14–Co2–C15	39.1(2)
C1–Co1–C14	139.3(3)	C11–N1–C7	118.4(4)
3			
Ag1–N2A	2.171(5)	Ag1–N1	2.173(4)
Co1–Co2	2.4728(19)	Co2–C8	1.967(5)
Co1–C7	1.962(5)	Co2–C7	1.957(5)
C7–C8	1.339(7)	N1–C13	1.330(6)
N2–Ag1A	2.172(5)	N3–O11	1.233(6)
N2A–Ag1–N1	172.35(15)	C7–Co1–Co2	50.79(14)
C8–Co1–Co2	51.10(15)	C8–Co1–C7	39.93(19)
C8–C7–Co2	70.4(3)	C7–Co2–C8	39.89(19)
C13–N1–C14	118.0(4)	C8–C7–Co1	69.9(3)
C9–C7–Co2	135.6(3)	C9–C7–Co1	133.2(3)
O7–C9–C7	110.7(4)	O8–C10–C11	125.0(5)
C13–N1–C14	118.0(4)	O13–N3–O11	121.6(7)
4			
Ag1–N2A	2.134(4)	Ag1–N1	2.131(4)
Co1–C8	1.939(5)	Co1–C9	1.952(4)
Co1–Co2	2.47499(10)	Co2–C8	1.959(5)
Co2–C9	2.935(5)	C8–C9	1.337(7)
C1–N2	1.320(8)	Sb1–F1	1.780(7)
N1–Ag1–N2A	176.9(2)	C8–Co1–C9	40.2(2)
C9–Co1–Co2	50.14(14)	C8–Co1–Co2	50.93(16)
C8–C9–Co2	70.9(3)	C9–Co2–C8	40.2(2)
C8–C9–Co1	69.4(3)	C1–N2–C5	118.2(5)
Co1–C8–Co2	78.8(2)	Co2–C9–Co1	79.10(17)

It is known that the transition-metal cation Ag^I, different from metal cations Pd^{II}/Pt^{II} with square-planar coordination preference, may adopt a variety of coordination geometries, such as, linear, trigonal, tetrahedral, trigonal pyramid, and octahedral.[9] In order to show the influence of transition-metal compounds upon the self-assembly with li-

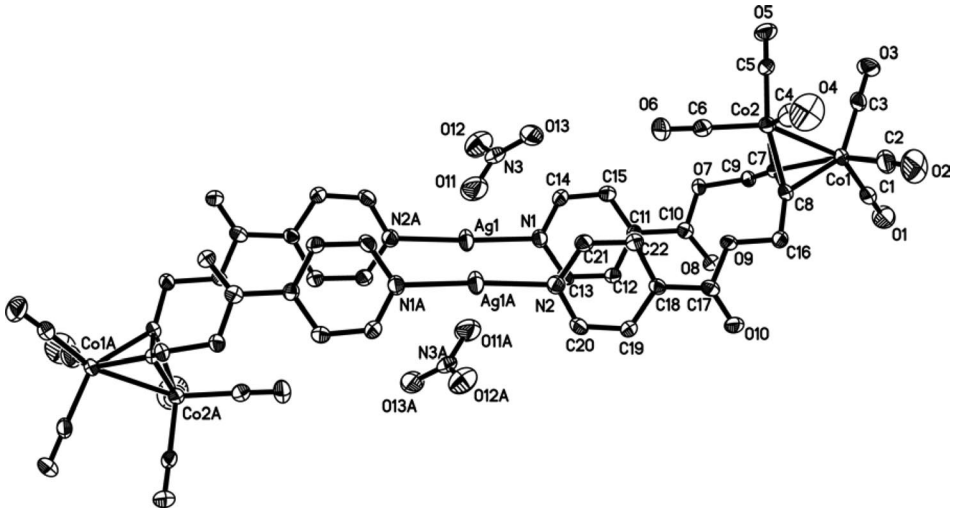

Figure 2. ORTEP view of **3** with 30% thermal ellipsoids.

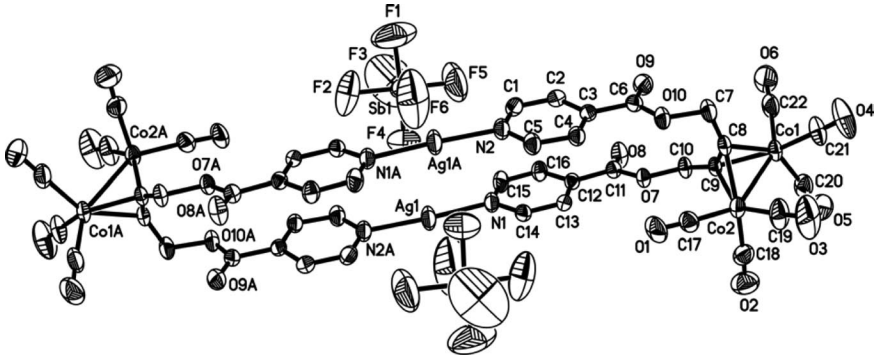

Figure 3. ORTEP view of **4** with 30% thermal ellipsoids.

gand L^a, we carried out reactions of $AgNO_3$ and $AgSbF_6$ with ligand L^a that was used in the aforementioned self-assembly with $[\{M(dppb)(H_2O)\}_2(OTf)_2]$. It was shown that slow diffusion of a MeOH solution of $AgNO_3$ into a thf solution of L^a in the dark at room temperature afforded metallamacrocycle **3** in 80% yield, whereas diffusion of a MeOH solution of $AgSbF_6$ into a CH_2Cl_2 solution of L^a under similar conditions gave rise to metallamacrocycle **4** in 85% yield (Scheme 1).

Compounds **3** and **4** are air-stable solids and have been characterized by elemental analysis and spectroscopy. The IR spectra of **3** and **4** exhibited four strong absorption bands in the range 2099–1996 cm^{-1} for their terminal carbonyl groups and one strong absorption band at 1728 cm^{-1} for their ester carbonyl groups. The ^1H NMR spectra of **3** and **4** displayed two doublets in the range 8.83–7.90 ppm for the α and β protons of their pyridyl rings and one singlet at ca. 5.6 ppm for their CH_2O groups. The molecular structures of **3** and **4** were unequivocally confirmed by X-ray crystallography. Figures 2 and 3 show the ORTEP views of **3** and **4**, respectively, and Table 1 lists their selected bond lengths and angles. The self-assembly of $AgNO_3$ and $AgSbF_6$ with L^a produced two isostructural C_2Co_2 cluster-bridged macrocyclic complexes **3** and **4**. The most striking features of **3** and **4** include: (i) The two metal Ag^I centers are connected through four pyridyl groups *trans* to the $Co_2(CO)_6$ moieties. (ii) Each Ag^I center is coordinated to two N atoms of the pyridyl groups in a linear fashion with a slight deviation from the ideal 180° (N1–Ag1–N2A 172.35° for **3**; N1–Ag1–N2A 176.9° for **4**). (iii) The two pyridyl rings coordinated to the same Ag^I center are nearly coplanar with a dihedral angle of 14.2° for **3** and 5.0° for **4**. In both **3** and **4** the nitrate and SbF_6 anions are all positioned above and below their Ag_2N_4 planes and weakly coordinated to Ag^I cations (the shortest Ag···O distance Ag1···O11A 2.619 Å and the shortest Ag···F distance Ag1A···F6 2.856 Å). The intramolecular Ag···Ag distance is 3.419 for **3** and 3.594 Å for **4**. It follows that the NO_3 and SbF_6 anions have no considerable effect on the supramolecular structures of such cationic macrocycles.

Synthesis and Characterization of Ligand L^b, Macrocycle $[(ZnL^bCl_2)_2]$ (5), and Polymers $[(AgL^bX)_n]$ (6, X = PF_6; 7, X = ClO_4)

The tetrahedral C_2Co_2 cluster-bridged bipyridine ligand L^b is actually an isomer of ligand L^a, and it could be simi-

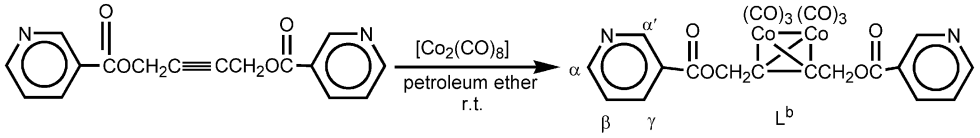

Scheme 2.

larly prepared by the method described for the preparation of L^a.[7] Thus, when but-2-yne-1,4-diyl dipyridine-3-carboxylate was treated with $[Co_2(CO)_8]$ in petroleum ether at room temperature, L^b was produced in 82% yield (Scheme 2). Ligand L^b was fully characterized by elemental analysis and IR and ^1H NMR spectroscopy. For example, the IR spectrum showed one strong absorption band at 1720 cm^{-1} for its ester carbonyl groups and three strong absorption bands in the region 2105–2026 cm^{-1} for its terminal carbonyl groups. The ^1H NMR spectrum displayed one singlet at 5.58 ppm for its CH_2 groups and four singlets at 9.82, 9.29, 8.23, and 7.55 ppm for its pyridyl groups. The molecular structure of L^b was confirmed by X-ray crystallography. The ORTEP view of L^b is shown in Figure 4, whereas its selected bond lengths and angles are listed in Table 2. X-ray crystallographic analysis revealed that L^b is indeed a tetrahedral C_2Co_2 cluster-bridged 3,3-bipyridine in which the cluster is bridged between the C12 and C18 atoms of the two pyridyl groups. Whereas the C7–C8 bond is basically perpendicular to the Co1–Co2 bond, the bond lengths of C7–C8 (1.47 Å) and Co1–Co2 (2.70 Å) are much longer than those corresponding to L^a (1.343 and 2.4817 Å, respectively) and other tetrahedral C_2Co_2 systems.[10]

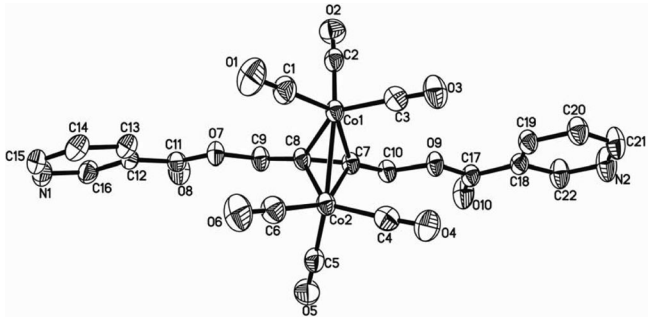

Figure 4. ORTEP view of L^b with 30% thermal ellipsoids.

In order to compare the self-assembly behavior of L^b with its isomer L^a, the reactions of L^b with $[\{M(dppb)(H_2O)_2\}(OTf)_2]$ (M = Pd, Pt) were performed in different solvents, such as, CH_2Cl_2, $CHCl_3$, acetone, and thf, at room temperature or at reflux. As a result, in contrast to the reaction of L^a with $[\{M(dppb)(H_2O)_2\}(OTf)_2]$,[8] no reaction was found to occur between L^b and $[\{M(dppb)(H_2O)_2\}(OTf)_2]$. This is most likely because the N atom orientation of the two pyridyl groups in L^b does not match the square-planar coordination geometry of the transition-metal Pd^{II} and Pt^{II} complexes. However, we found some cases in which the N atom orientation in L^b may match the coordination geometry of transition-metal complexes to give the corresponding self-assembled products. For example, it was found that L^b could react with $ZnCl_2$ in acetonitrile at room temperature to give metallamacrocycle **5** in 96% yield, whereas L^b reacted with $AgPF_6$ and $AgClO_4$ in $MeOH/CH_2Cl_2$ at room temperature to afford infinite 2D polymers $[\{AgL^b(PF_6)\}_n]$ (**6**) and $[\{AgL^b(ClO_4)\}_n]$ (**7**) in 68 and 75% yield, respectively (Scheme 3).

Table 2. Selected bond lengths [Å] and angles [°] for L^b.

Co1–C7	2.10(4)	N1–C15	1.43(2)
Co1–C8	2.14(4)	N1–C16	1.44(2)
Co1–Co2	2.70(4)	O7–C11	1.48(3)
Co2–C7	2.11(5)	O8–C11	1.298(18)
Co2–C8	2.13(4)	C7–C8	1.47(3)
C1–Co1–C7	141.4(9)	C15–N1–C16	113.4(15)
C7–Co1–C8	40.4(4)	O8–C11–O7	124.2(7)
C7–Co1–Co2	50.2(12)	O8–C11–C12	122.7(14)
C8–Co1–Co2	50.5(7)	Co1–C7–Co2	79.9(5)
C7–Co2–C8	40.5(10)	Co2–C8–Co1	78.4(10)
C7–C8–C9	139.9(10)	C8–C7–C10	139.0(5)

Although the formation of metallamacrocycle **5** is not surprising, the formation of polymers **6** and **7** is actually unexpected and particularly interesting, as ligand L^a reacted with $AgNO_3$ and $AgSbF_6$ to give metallamacrocycles **3** and **4** as described above. Compounds **5**–**7** were fully characterized by elemental analysis, spectroscopy, and X-ray crystallography. The IR spectra of **5**–**7** showed one or two strong absorption bands in the range 1732–1703 cm^{-1} for their ester carbonyl groups and three strong absorption bands in the region 2097–2023 cm^{-1} for their terminal carbonyl groups. The ^1H NMR spectra of **5**–**7** all exhibited the expected proton signals of their organic and organometallic groups.

X-ray diffraction analysis of **5** (Figure 5, Table 3) confirmed its structure. The two molecules of ligand L^b in **5** are coordinated through N1, N2, N1A, and N2A to Zn1 and Zn1A to form a centrosymmetric macrocyclic complex. Both Zn1 and Zn1A are in a slightly distorted tetrahedral coordination environment composed of two N-donor ligands and two chloride ligands. The Zn1–Cl1 (2.1931 Å) and Zn1–Cl2 (2.1956 Å) bond lengths are close to those of the Zn–Cl bonds in previously reported Zn/Cl compounds.[11] The Zn1–N1 and Zn1–N2A bond lengths are equal to 2.064 and 2.082 Å, respectively, which are close to the Zn–N bonds in reported Zn/N complexes.[12]

The X-ray diffraction analysis of **6** (Figures 6 and 7, Table 4) revealed that it has two crystallographically distinct Ag^I centers. One of the Ag^I centers, namely, Ag1 as shown in Figure 6, is located in a rhombic AgN_2O_2 coordination sphere (Ag1–N2 2.180 Å, Ag1···O4A 2.684 Å, N2–Ag1–N2AA 180°, N2–Ag1···O4A 97.2°, N2–Ag1···O4B 82.8°,

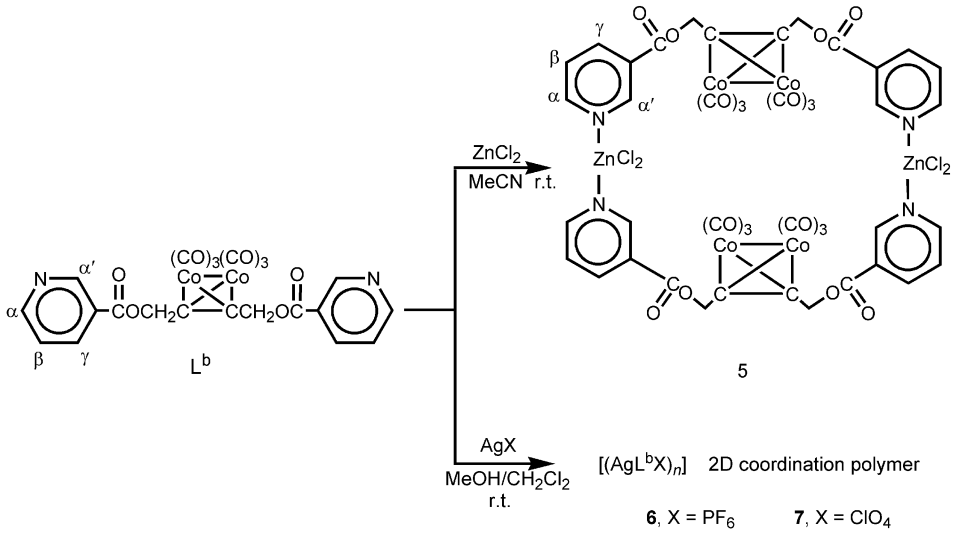

Scheme 3.

O4A···Ag1···O4B 180°). The Ag···O distances are slightly longer than the normal Ag–O bond lengths (ca. 2.3–2.6 Å),[13] indicating that the ester carbonyl O atoms are weakly

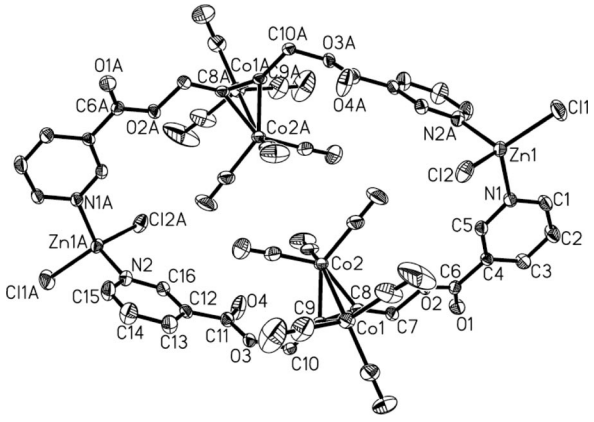

Figure 5. ORTEP view of **5** with 30% thermal ellipsoid.

Table 3. Selected bond lengths [Å] and angles [°] for **5**.

Zn1–N1	2.064(3)	Zn1–N2A	2.082(3)
Zn1–Cl1	2.1931(15)	Zn1–Cl2	2.1956(17)
Co1–C8	1.947(4)	Co2–C8	1.961(4)
Co1–C9	1.949(4)	N1–C1	1.329(5)
Co1–Co2	2.4761(11)	C8–C9	1.336(5)
N1–Zn1–N2A	99.48(13)	N1–Zn1–Cl1	108.38(10)
N2A–Zn1–Cl1	106.54(11)	N1–Zn1–Cl2	106.97(10)
N2A–Zn1–Cl2	107.44(10)	Cl1–Zn1–Cl2	125.09(6)
C8–Co1–C9	40.10(15)	C9–Co2–C8	39.94(15)
C9–Co1–Co2	50.58(11)	C9–Co2–Co1	50.57(11)

coordinated to the silver centers. Another Ag^{I} center, namely, Ag2 as shown in Figure 7, lies in a linear AgN_2 coordination environment (Ag2–N1 2.108 Å, N1–Ag2–N1A 180°). The X-ray crystallographic study of **6** also revealed that (i) the Ag1 atoms are connected through pyridyl N atoms and ester carbonyl O atoms of ligand L^b to form the metallamacrocycle-containing 1D double-chain along the crystallographic [011] direction (Ag1···Ag1 14.484 Å),

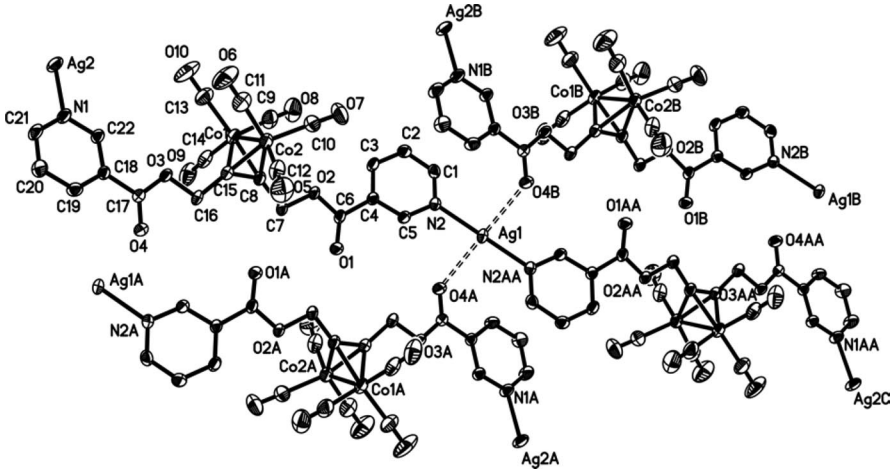

Figure 6. Coordination environment of Ag1 in **6**.

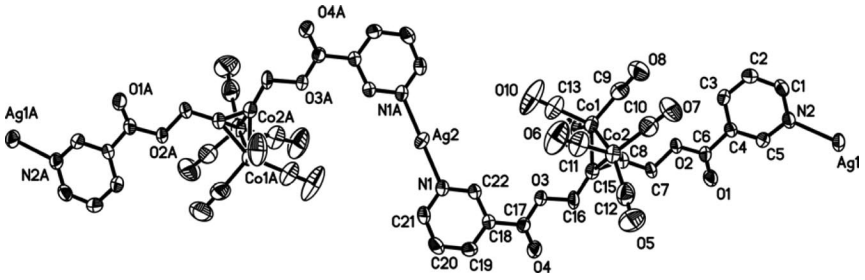

Figure 7. Coordination environment of Ag2 in **6**.

and (ii) the double-chains are further bridged by linearly coordinated Ag2 atoms to form a 2D polymeric framework (See Supporting Information). The X-ray crystallographic study of **7** revealed that it is isostructural with polymer **6**. Because **7** displays the same 2D polymeric array as polymer **6**, we only list some of its bond lengths and angles in Table 4 without showing the structural figures corresponding to **6** for brevity. Finally, it should be noted that (i) anions PF_6 and ClO_4 in **6** and **7** do not have any substantial interactions with the Ag^I centers except as balancing counterions in their crystal lattices, and (ii) although a number of Ag^I coordination polymers are known,[13,14] **6** and **7** are, to the best of our knowledge, the first Ag^I polymers with tetrahedral C_2Co_2 clusters reported so far.

Table 4. Selected bond lengths [Å] and angles [°] for **6** and **7**.

6			
Ag1–N2	2.180(3)	C8–Co1	1.948(4)
Ag2–N1	2.108(3)	C15–Co2	1.945(4)
C9–Co1	1.823(6)	C15–Co1	1.947(4)
Co1–Co2	2.4728(9)	C8–C15	1.343(6)
C8–Co2	1.944(4)	N1–C21	1.337(5)
N2–Ag1–N2A	180.0(1)	N1–Ag2–N1A	180.0(2)
C15–C8–C7	139.3(4)	C21–N1–C22	118.0(4)
O4A–Ag2–O4B	180.0	C15–C8–Co2	69.8(2)
C15–Co2–Co1	50.59(12)	C8–Co1–Co2	50.49(13)
C15–Co1–C8	40.34(16)	C8–Co2–C15	40.40(16)
C15–C8–Co1	69.8(2)	Co2–C8–Co1	78.89(15)
7			
Ag1–N1A	2.189(4)	Ag1–N1	2.189(4)
Ag2–N2A	2.119(4)	Ag2–N2	2.119(4)
Co1–Co2	2.4705(11)	C15–Co1	1.935(5)
C8–Co1	1.959(5)	C15–Co2	1.950(5)
C8–C15	1.344(6)	C6–O2	1.340(5)
N1A–Ag1–N1	180.0	N2A–Ag2–N2	180.0
C8–Co1–Co2	50.51(14)	C15–Co1–Co2	50.79(14)
C8–C15–Co1	70.8(3)	C8–C15–Co2	69.6(3)
O2–C7–C8	108.2(4)	C8–Co2–C15	40.38(18)
N1–C1–C2	122.8(4)	O1–C6–O2	125.0(4)

Electrochemical Properties of Ligand L^b and Macrocycle 5

The electrochemical properties of L^b and **5** were investigated in DMF at different temperatures by cyclic voltammetry. The cyclic voltammograms of L^b determined at room temperature and low temperature are presented in Figure 8a,b. Ligand L^b displays an irreversible reduction process at a peak potential of –1.36 V and an irreversible oxidation process at a peak potential of –0.23 V at room temperature (Figure 8a). The reduction process of L^b displayed at –1.36 V (in comparison with those displayed by the same cluster unit $C_2Co_2(CO)_6$-containing complexes $[RR'C_2Co_2(CO)_6]$[15,16]) should be attributed to the one-electron reduction of its cluster unit $C_2Co_2(CO)_6$ to give the corresponding radical anion. This radical anion is rather unstable and may undergo decomposition on the surface of an electrode to afford the $Co(CO)_4^-$ monoanion with an irreversible one-electron oxidation process at –0.23 V.[15–17] However, the irreversible reduction process at –1.36 V displayed at room temperature becomes reversible and the irreversible oxidation process at –0.23 V disappears at low temperature (Figure 8b), both implying that the radical anion of L^b becomes stable at such a low temperature. In fact, such observations for flexible ligand L^b are basically the same as those previously reported for the rigid ligand $[(4\text{-}C_5H_4N)_2C_2Co_2(CO)_6]$.[8]

The cyclic voltammograms of macrocyclic complex **5** determined at room temperature and low temperature are shown in Figure 8c,d. Complex **5** undergoes an irreversible reduction process at a peak potential of –1.39 V and an irreversible oxidation process at a peak potential of –0.23 V at room temperature (Figure 8c). The reduction process at –1.39 V can be ascribed to the one-electron reduction of its $C_2Co_2(CO)_6$ cluster unit. This potential is 30 mV more negative than that of free ligand L^b, which is consistent with the average IR frequency for terminal CO bands of **5** being slightly redshifted relative to that of free L^b. The oxidation process at –0.23 V is, as mentioned above, also due to the oxidation of the $Co(CO)_4^-$ monoanion generated in situ during the electrochemical process.[15–17] On the basis of the same reasoning for free ligand L^b, the irreversible reduction process displayed at –1.39 V by **5** at room temperature becomes reversible and the irreversible oxidation process at –0.23 V disappears at low temperature (Figure 8d). In addition, it is worth noting that, different from the Pd^{II}-containing macrocycle $[\{Pd(dppb)(4\text{-}C_5H_4N)_2C_2Co_2(CO)_6\}_2(OTf)_4]$,[8] the redox process of Zn^{II}-containing macrocycle **5** was not observed. This indicates that Zn^{II} is redox inactive under such electrochemical conditions.[18]

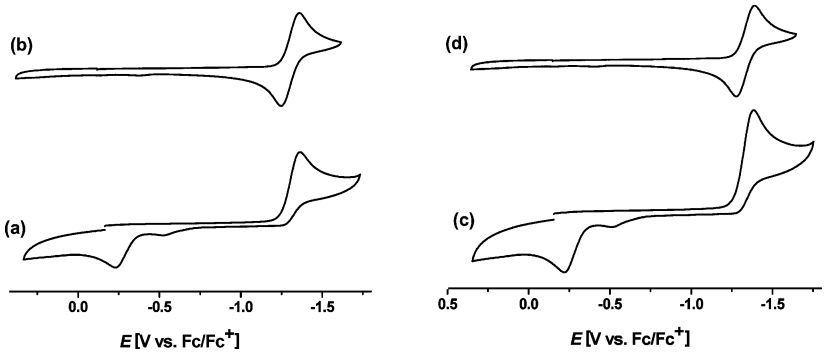

Figure 8. Cyclic voltammograms of L^b and **5** (1 mM) in 0.1 M nBu_4PF_6/DMF. Scan rate = 100 mV s^{-1}. (a) L^b, $T = 25 \pm 1$ °C; (b) L^b, $T = -40 \pm 1$ °C; (c) **5**, $T = 25 \pm 1$ °C; (d) **5**, $T = -40 \pm 1$ °C.

Conclusions

The new tetrahedral C_2Co_2 cluster-containing metallamacrocycles and coordination polymers **1**–**7** were synthesized by self-assembly of the flexible C_2Co_2 cluster-bridged bipyridine ligands L^a and L^b with transition-metal Pd^{II}, Pt^{II}, Zn^{II}, and Ag^I compounds. Ligand L^b is the first prepared C_2Co_2 cluster-bridged 3,3′-bipyridine, which enabled us to compare its self-assembly behavior with that of its isomer L^a, a known C_2Co_2 cluster-bridged 4,4′-bipyridine. It was found that the relative orientation of the N donors in L^a and L^b, as well as the transition-metal coordination geometry preference, play a key role for formation of such different types of self-assembled products. Whereas the structures of L^b and **1**–**7** were fully characterized, the electrochemical behavior of L^b and **5** was investigated by CV techniques. Particularly noteworthy is that polymers **6** and **7** represent a unique and interesting class of polymeric structures that includes the tetrahedral C_2Co_2 cluster cores.[19]

Experimental Section

General Comments: All reactions were carried out under an atmosphere of highly purified nitrogen by using standard Schlenk or vacuum-line techniques. Solvents for preparative use were dried and distilled under an atmosphere of nitrogen from CaH_2 or sodium/benzophenone ketyl prior to use. $AgNO_3$, $AgPF_6$, $AgSbF_6$, $ZnCl_2$, and $[Co_2(CO)_8]$ were of commercial origin and used as purchased. $AgClO_4$,[20] $[(4\text{-}C_5H_4NCO_2CH_2)_2C_2Co_2(CO)_6]$ (L^a),[7] $[\{M(dppb)(H_2O)_2\}(OTf)_2]$ (M = Pd, Pt),[8] and but-2-yne-1,4-diyl dipyridine-3-carboxylate[21] were prepared according to literature methods. ^1H and ^{31}P NMR spectra were recorded with a Bruker AC-P 200 or a Bruker Avance 300 NMR spectrometer, and their chemical shifts are reported in ppm relative to internal Me_4Si and external 85% H_3PO_4, respectively. ^{19}F NMR spectra were measured with a Varian Mercury Plus 400 NMR spectrometer, and chemical shifts are referenced relative to external $CFCl_3$. IR spectra were taken with a Bio-Rad FTS 135 spectrophotometer. Elemental analysis was performed with an Elementar Vario EL analyzer. Melting points were determined with a Yanaco MP-500 melting point apparatus and are uncorrected.

$[\{Pd(dppb)L^a\}_2(OTf)_4]$ (1): A Schlenk flask was charged with $[\{Pd(dppb)(H_2O)_2\}(OTf)_2]$ (0.126 g, 0.146 mmol), L^a (0.085 g, 0.146 mmol), and CH_2Cl_2 (20 mL). The mixture was stirred at room temperature for 24 h to produce a red precipitate. The precipitate was washed thoroughly with CH_2Cl_2 and recrystallized (MeCN/diethyl ether) to give **1** (0.195 g, 94%) as a red solid. M.p. 158 °C (decomp.). ^1H NMR (200 MHz, CD_3CN): δ = 7.62 (br. s, 56 H, $8C_6H_5$, $4C_5H_4N$), 5.73 (s, 8 H, $4CH_2O$), 2.90 (br. s, 8 H, $4CH_2P$), 1.92 (br. s, 8 H, $4CH_2$) ppm. ^{31}P NMR (81 MHz, CD_3CN): δ = 36.50 (s, Ph_2P) ppm. ^{19}F NMR (376 MHz, CD_3CN): δ = –79.65 (s, SO_3CF_3) ppm. IR (KBr disk): $\tilde{\nu}$ = 2101 (s), 2064 (vs), 2037 (vs, C≡O), 1737 (s, C=O), 1279 (vs), 1225 (s), 1119 (s), 1059 (s), 1030 (vs, OTf) cm^{-1}. $C_{104}H_{80}Co_4F_{12}N_4O_{32}P_4Pd_2S_4$ (2826.76): calcd. C 44.19, H 2.85, N 1.98; found C 43.91, H 2.78, N 2.06.

$[\{Pt(dppb)L^a\}_2(OTf)_4]$ (2): By a procedure similar to that described for the preparation of **1**, compound **2** (0.090 g, 74%) was obtained as a red solid from $[\{Pt(dppb)(H_2O)_2\}(OTf)_2]$ (0.077 g, 0.081 mmol) and L^a (0.047 g, 0.081 mmol). M.p. 165 °C (decomp.). ^1H NMR (300 MHz, [D$_6$]DMSO): δ = 8.84 (d, J = 4.5 Hz, 8 H, $8H_\alpha$), 7.72–7.51 (m, 48 H, $8C_6H_5$, $8H_\beta$), 5.58 (s, 8 H, $4CH_2O$), 3.15 (br. s, 8 H, $4CH_2P$), 1.60 (br. s, 8 H, $4CH_2$) ppm. ^{31}P NMR (121 MHz, CD_3CN): δ = 9.63 (t, $J_{Pt,P}$ = 1565 Hz, Ph_2P) ppm. ^{19}F NMR (376 MHz, [D$_6$]DMSO): δ = –78.2 (s, SO_3CF_3) ppm. IR (KBr disk): $\tilde{\nu}$ = 2101 (s), 2063 (vs), 2036 (vs, C≡O), 1738 (s, C=O), 1277 (vs), 1226 (s), 1119 (s), 1059 (s), 1030 (vs, OTf) cm^{-1}. $C_{104}H_{80}Co_4F_{12}N_4O_{32}P_4Pt_2S_4$ (3003.47): calcd. C 41.59, H 2.68, N 1.87; found C 41.63, H 2.68, N 2.00.

$[(AgL^a)_2(NO_3)_2]$ (3): In a Schlenk tube, a MeOH (5 mL) solution of $AgNO_3$ (0.009 g, 0.054 mmol) was layered over a thf (5 mL) solution of L^a (0.016 g, 0.027 mmol) carefully in the dark at room temperature for about 2 weeks to give **3** (0.017 g, 80%) as red crystals. M.p. 145 °C (decomp.). ^1H NMR (300 MHz, [D$_6$]DMSO): δ = 8.83 (d, J = 4.5 Hz, 8 H, $8H_\alpha$), 7.90 (d, J = 5.1 Hz, 8 H, $8H_\beta$), 5.70 (s, 8 H, $4CH_2O$) ppm. IR (KBr disk): $\tilde{\nu}$ = 2099 (s), 2056 (vs), 2033 (vs), 1998 (s, C≡O), 1728 (s, C=O) cm^{-1}. $C_{44}H_{24}Ag_2Co_4N_6O_{26}$ (1504.37): calcd. C 35.13, H 1.61, N 5.59; found C 35.15, H 1.79, N 5.58.

$[(AgL^a)_2(SbF_6)_2]$ (4): In a Schlenk tube, a MeOH (5 mL) solution of $AgSbF_6$ (0.026 g, 0.075 mmol) was layered over a CH_2Cl_2 (5 mL) solution of L^a (0.029 g, 0.05 mmol) in the dark at room temperature for about 1 month to give **4** (0.039 g, 85%) as red crystals. M.p. 155 °C (decomp.). ^1H NMR (300 MHz, CD_3CN): δ = 8.74 (d, J = 6.3 Hz, 8 H, $8H_\alpha$), 7.90 (d, J = 6.0 Hz, 8 H, $8H_\beta$), 5.64 (s, 8 H, $4CH_2O$) ppm. IR (KBr disk): $\tilde{\nu}$ = 2097 (s), 2054 (vs), 2034 (vs), 1996 (s, C≡O), 1728 (s, C=O) cm^{-1}. $C_{44}H_{24}Ag_2Co_4F_{12}N_4O_{20}Sb_2$ (1851.73): calcd. C 28.54, H 1.31, N 3.03; found C 28.41, H 1.18, N 3.09.

[(3-$C_5H_4NCO_2CH_2)_2C_2Co_2(CO)_6$] ($L^b$): A Schlenk flask was charged with but-2-yne-1,4-diyl dipyridine-3-carboxylate (0.445 g, 1.5 mmol) and petroleum ether (30 mL). To this stirred solution was slowly added a solution of [$Co_2(CO)_8$] (0.514 g, 1.5 mmol) in petroleum ether (15 mL). The mixture was stirred at room temperature for an additional 3 h until no CO evolution was observed. The solvent was removed under reduced pressure, and the residue was subjected to column chromatography (alkali Al_2O_3; $CHCl_3$). The crude product obtained from the eluted red band was recrystallized (CH_2Cl_2/petroleum ether) to give L^b (0.720 g, 82%) as a red solid. M.p. 126 °C (decomp.). ^{1}H NMR (200 MHz, $CDCl_3$): δ = 9.82 (s, 2 H, 2H$_{\alpha'}$), 9.29 (s, 2 H, 2H$_\alpha$), 8.23 (s, 2 H, 2H$_\gamma$), 7.55 (s, 2 H, 2H$_\beta$), 5.58 (s, 4 H, 2CH_2O) ppm. IR (KBr disk): $\tilde{\nu}$ = 2105 (s), 2066 (vs), 2026 (vs, C≡O), 1720 (s, C=O) cm^{-1}. $C_{22}H_{12}Co_2N_2O_{10}$ (582.16): calcd. C 45.39, H 2.08, N 4.81; found C 45.18, H 2.07, N 4.86.

[($ZnL^bCl_2)_2$] (5): In a Schlenk tube, a solution of L^b (0.029 g, 0.05 mmol) in MeCN (5 mL) was carefully layered over a solution of $ZnCl_2$ (0.014 g, 0.10 mmol) in MeCN (3 mL) at room temperature for 24 h to give **5** (0.034 g, 96%) as red crystals. M.p. 170 °C (decomp.). ^{1}H NMR (300 MHz, [D_6]DMSO): δ = 9.16 (s, 4 H, 4H$_{\alpha'}$), 8.84 (s, 4 H, 4H$_\alpha$), 8.35 (d, J = 7.8 Hz, 4 H, 4H$_\gamma$), 7.58–7.63 (m, 4 H, 4H$_\beta$), 5.70 (s, 8 H, 4CH_2O) ppm. IR (KBr disk): $\tilde{\nu}$ = 2097 (s), 2059 (vs), 2030 (vs, C≡O), 1732 (s, C=O) cm^{-1}. $C_{44}H_{24}Cl_4Co_4N_4O_{20}Zn_2$ (1436.88): calcd. C 36.78, H 1.68, N 3.90; found C 36.84, H 1.72. N 4.08.

[{$AgL^b(PF_6)$}$_n$] (6): In a Schlenk tube, a MeOH (5 mL) solution of $AgPF_6$ (0.019 g, 0.075 mmol) was carefully layered over a solution of L^b (0.029 g, 0.05 mmol) in CH_2Cl_2 (5 mL) at room temperature in the dark for about 1 month to produce **6** (0.029 g, 68%) as red crystals. M.p. 167 °C (decomp.). ^{1}H NMR (300 MHz, CD_3CN): δ = 9.17 (s, 4 H, 4H$_{\alpha'}$), 8.76 (s, 4 H, 4H$_\alpha$), 8.37 (d, J = 6.6 Hz, 4 H, 4H$_\gamma$), 7.52 (br. s, 4 H, 4H$_\beta$), 5.64 (s, 8 H, 4CH_2O) ppm. IR (KBr disk): $\tilde{\nu}$ = 2096 (s), 2062 (vs), 2035 (vs, C≡O), 1731 (s), 1703 (s, C=O) cm^{-1}. $C_{44}H_{24}Ag_2Co_4F_{12}N_4O_{20}P_2$ (1670.30): calcd. C 31.64, H 1.45, N 3.35; found C 31.61, H 1.49, N 3.44.

[{$AgL^b(ClO_4)$}$_n$] (7): In a Schlenk tube, a MeOH (5 mL) solution of $AgClO_4$ (0.016 g, 0.075 mmol) was carefully layered over a solution of L^b (0.029 g, 0.05 mmol) in CH_2Cl_2 (5 mL) at room temperature in the dark for about 1 month to produce **7** (0.030 g, 75%) as red crystals. M.p. 161 °C (decomp.). ^{1}H NMR (300 MHz, CD_3CN): δ = 9.17 (s, 4 H, 4H$_{\alpha'}$), 8.75 (s, 4 H, 4H$_\alpha$), 8.38 (d, J = 9.6 Hz, 4 H, 4H$_\gamma$), 7.50–7.54 (m, 4 H, 4H$_\beta$), 5.64 (s, 8 H, 4CH_2O) ppm. IR (KBr disk): $\tilde{\nu}$ = 2095 (s), 2059 (vs), 2023 (vs, C≡O), 1727 (s), 1703 (s, C=O) cm^{-1}. $C_{44}H_{24}Ag_2Cl_2Co_4N_4O_{28}$ (1578.98): calcd. C 33.47, H 1.53, N 3.55; found C 33.23, H 1.43, N 3.52.

X-ray Structure Determination of L^b, 1, and 3–7: Single crystals of L^b suitable for X-ray diffraction analysis were grown by slow evaporation of its dichloromethane/petroleum ether solution at 4 °C, those of **1** were obtained by slow diffusion of anhydrous diisopropyl ether into its nitromethane solution at room temperature under an atmosphere of N_2, those of **3** and **4** were obtained by slow diffusion of a MeOH solution of $AgNO_3$ or $AgSbF_6$ into a thf solution of L^a in the dark at room temperature, those of **5** were obtained by slow diffusion of a MeCN solution of $ZnCl_2$ into a MeCN solution of L^b, and those of **6** and **7** were obtained by slow diffusion of a MeOH solution of $AgPF_6$ or $AgClO_4$ into a CH_2Cl_2 solution of L^b in the dark at room temperature. A single crystal of L^b, **1**, or **3**–**7** was mounted onto the end of a thin glass fiber by using inert oil. However, the single crystal of **1** must be sealed in a capillary upon removal from its mother liquor, because it easily collapses to amorphous materials due to loss of its solvent molecules. X-ray intensity data were collected at 293(2) K with a Bruker SMART 1000 automated diffractometer by using Mo-K_α graphite-monochromated radiation (λ = 0.71073 Å) in the ω scanning mode. Absorption corrections were performed by using SADABS.[22] All the structures were solved by direct methods by using the SHELXS-97 program[23] and refined by full-matrix least-squares techniques (SHELXL-97)[24] on F^2. All hydrogen atoms were located by using the geometric method. Solvent molecules were highly disordered and removed by the SQEEZE program.[25] Details of the crystal data, data collections, and structure refinements

Table 5. Crystal data and structure refinement details for **1**, **3**, and **4**.

	1	**3**	**4**
*F*ormula	$C_{52}H_{40}Co_2F_6N_2O_{16}P_2PdS_2$	$C_{22}H_{11}AgCo_2N_3O_{13}$	$C_{22}H_{12}AgCo_2F_6N_2O_{10}Sb{\cdot}0.5H_2O$
M_r [g mol^{-1}]	1413.18	751.07	934.82
Crystal system	triclinic	triclinic	monoclinic
Space group	$P\bar{1}$	$P\bar{1}$	$P2_1/c$
a [Å]	13.674(4)	7.610(9)	19.1379(16)
b [Å]	17.060(5)	7.795(9)	12.9214(11)
c [Å]	17.794(5)	23.22(3)	12.7442(11)
α [°]	92.258(5)	88.457(18)	90
β [°]	99.118(5)	89.865(18)	104.892(2)
γ [°]	103.864(5)	69.816(16)	90
V [Å^3]	3966.0(19)	1292(2)	3045.6(4)
Z	2	2	4
$\rho_{calcd.}$ [g cm^{-3}]	1.183	1.930	2.039
μ [mm^{-1}]	0.795	2.092	2.673
F(000)	1420	738	1796
$2\theta_{max}$ [°]	52.74	50.02	50.06
Reflections collected	23202	6665	12654
Independent reflections	16019	4518	5370
Index ranges	$-7 \le h \le 17$	$-9 \le h \le 8$	$-16 \le h \le 22$
	$-21 \le k \le 21$	$-8 \le k \le 9$	$-15 \le k \le 15$
	$-22 \le l \le 20$	$-16 \le l \le 27$	$-15 \le l \le 14$
Goodness-of-fit	0.941	1.063	1.027
R	0.0630	0.0398	0.0466
R_w	01719	0.0800	0.1283
Largest diff. peak/hole [e Å^{-3}]	1.304/–1.151	0.615/–0.661	1.151/–1.031

Table 6. Crystal data and structure refinement details for L^b and **5**–**7**.

	L^b	**5**	**6**	**7**
*F*ormula	$C_{22}H_{12}Co_2N_2O_{10}$	$C_{44}H_{24}Cl_4Co_4N_4O_{20}Zn_2$	$C_{22}H_{12}AgCo_2F_6N_2O_{10}P$	$C_{22}H_{12}AgClCo_2N_2O_{14}$
M_r [g mol^{-1}]	582.20	1436.93	835.04	789.52
Crystal system	monoclinic	monoclinic	triclinic	triclinic
Space group	$P2_1/c$	$P2_1/n$	$P\bar{1}$	$P\bar{1}$
a [Å]	9.4(2)	9.164(5)	9.6584(19)	9.492(3)
b [Å]	19.0(4)	21.987(11)	11.834(2)	11.595(3)
c [Å]	17.3(4)	13.889(7)	13.888(3)	13.788(4)
α [°]	90	90	66.392(2)	67.790(4)
β [°]	99.9(4)	99.934(9)	75.231(3)	76.009(4)
γ [°]	90	90	84.091(2)	85.033(4)
V [Å^3]	3064(122)	2757(2)	1406.5(5)	1363.2(7)
Z	4	2	2	2
$\rho_{calcd.}$ [g cm^{-3}]	1.262	1.731	1.972	1.923
μ [mm^{-1}]	1.129	2.301	2.008	2.085
$F(000)$	1168	1424	816	776
$2\theta_{max}$ [°]	48.94	50.02	50.04	51.00
Reflections collected	10794	14282	5900	7442
Independent reflections	4805	4849	4881	4968
Index ranges	$-10 \le h \le 6$	$-6 \le h \le 10$	$-11 \le h \le 11$	$-11 \le h \le 11$
	$-21 \le k \le 21$	$-26 \le k \le 22$	$-14 \le k \le 13$	$-14 \le k \le 6$
	$-19 \le l \le 19$	$-16 \le l \le 16$	$-16 \le l \le 9$	$-16 \le l \le 16$
Goodness-of-fit	0.990	1.091	1.032	1.000
R	0.0395	0.0336	0.0419	0.0498
R_w	0.0807	0.0807	0.1082	0.1160
Largest diff. peak/hole [e Å^{-3}]	0.399/–0.202	0.558/–0.293	0.682/–0.392	0.940/–0.411

are summarized in Tables 5 and 6. CCDC-702946 (for L^b), -702940 (for **1**), -702941 (for **3**) -702942 (for **4**), -702943 (for **5**), -702944 (for **6**), and -702945 (for **7**) contain the supplementary crystallographic data for this paper. These data can be obtained free of charge from The Cambridge Crystallographic Data Centre via www.ccdc.cam.ac.uk/data_request/cif.

Electrochemistry: Cyclic voltammograms of L^b and **5** were obtained with a BAS Epsilon potentiostat by using a standard three-electrode system consisting of a glassy-carbon working electrode (3 mm in diameter), an Ag/Ag^+ (0.01 M $AgNO_3$/0.1 M nBu$_4$NPF$_6$ in MeCN) reference electrode, and a Pt-wire auxiliary electrode. A solution of 0.1 M nBu$_4$NPF$_6$ in *N*,*N*-dimethylformamide (DMF, HPLC grade) was used as a supporting electrolyte. The working electrode was polished with 0.05 μm alumina and sonicated in water for about 10 min prior to use. All solutions were deoxygenated with nitrogen for at least 10 min prior to use. All potentials are reported relative to the ferrocene/ferrocenium (Fc/Fc^+) potential.

Supporting Information (see footnote on the first page of this article): 1D double chain in **6**; 2D network of **6**.

Acknowledgments

We are grateful to the National Natural Science Foundation of China and the Specialized Research Fund for the Doctoral Program of Higher Education of China for financial support of this work.

[1] a) M. L. Merlau, M. del P. Mejia, S. T. Nguyen, J. T. Hupp, *Angew. Chem. Int. Ed.* **2001**, *40*, 4239–4242; b) S. J. Lee, A. Hu, W. Lin, *J. Am. Chem. Soc.* **2002**, *124*, 12948–12949; c) M. Fujita, Y. J. Kwon, S. Washizu, K. Ogura, *J. Am. Chem. Soc.* **1994**, *116*, 1151–1152.

[2] a) S.-D. Huang, R.-G. Xiong, J. Han, B. R. Weiner, *Inorg. Chim. Acta* **1999**, *294*, 95–98; b) O. R. Evans, W. Lin, *Acc. Chem. Res.* **2002**, *35*, 511–522.

[3] a) M. L. Hernández, M. G. Barandika, M. K. Urtiaga, R. Cortés, L. Lezama, M. I. Arriortua, *J. Chem. Soc., Dalton Trans.* **2000**, 79–84; b) F. Lloret, G. De Munno, M. Julve, J. Cano, R. Ruiz, A. Caneschi, *Angew. Chem. Int. Ed.* **1998**, *37*, 135–138; c) J. A. Real, E. Andrés, M. C. Muñoz, M. Julve, T. Granier, A. Bousseksou, F. Varret, *Science* **1995**, *268*, 265–267; d) A. Caneschi, D. Gatteschi, N. Lalioti, C. Sengregorio, R. Sessioli, G. Venturi, A. Vindigni, A. Rettori, M. G. Pini, M. A. Novak, *Angew. Chem. Int. Ed.* **2001**, *40*, 1760–1763; e) R. Clerac, H. Miyasaka, M. Yamashita, C. Coulon, *J. Am. Chem. Soc.* **2002**, *124*, 12837–12844; f) Z. Xu, L. K. Thompson, V. A. Milway, L. Zhao, T. Kelly, D. O. Miller, *Inorg. Chem.* **2003**, *42*, 2950–2959; g) P. Angaridis, J. F. Berry, F. A. Cotton, C. A. Murillo, X. Wang, *J. Am. Chem. Soc.* **2003**, *125*, 10327–10334.

[4] a) M. Kondo, T. Yoshitomi, K. Seki, H. Matsuzaka, S. Kitagawa, *Angew. Chem. Int. Ed. Engl.* **1997**, *36*, 1725–1727; b) D. Venkataraman, G. B. Gardner, S. Lee, J. S. Moore, *J. Am. Chem. Soc.* **1995**, *117*, 11600–11601; c) B. Xiao, P. S. Wheatley, X. Zhao, A. J. Fletcher, S. Fox, A. G. Rossi, I. L. Megson, S. Bordiga, L. Regli, K. M. Thomas, R. E. Morris, *J. Am. Chem. Soc.* **2007**, *129*, 1203–1209; d) M. Dinca, A. Dailly, Y. Liu, C. M. Brown, D. A. Neumann, J. R. Long, *J. Am. Chem. Soc.* **2006**, *128*, 16876–16883; e) X. Lin, J. Jia, P. Hubberstey, M. Schröder, N. R. Champness, *CrystEngComm.* **2007**, *9*, 438–448; f) K. Koh, A. G. Wong-Foy, A. J. Matzger, *Angew. Chem. Int. Ed.* **2008**, *47*, 677–680.

[5] a) B. J. Holliday, C. A. Mirkin, *Angew. Chem. Int. Ed.* **2001**, *40*, 2022–2043; b) M. Fujita, K. Umemoto, M. Yoshizawa, N. Fujita, T. Kusukawa, K. Biradha, *Chem. Commun.* **2001**, 509–518; c) S. Leininger, B. Olenyuk, P. J. Stang, *Chem. Rev.* **2000**, *100*, 853–908; d) S.-S. Sun, A. J. Lees, *Coord. Chem. Rev.* **2002**, *230*, 171–192; e) F. A. Cotton, C. Lin, C. A. Murillo, *Acc. Chem. Res.* **2001**, *34*, 759–771.

[6] a) P. J. Hagrman, D. Hagrman, J. Zubieta, *Angew. Chem. Int. Ed.* **1999**, *38*, 2638–2684; b) D. Braga, F. Grepioni, G. R. Desiraju, *Chem. Rev.* **1998**, *98*, 1375–1405; c) O. M. Yaghi, H. Li, C. Davis, D. Richardson, T. L. Groy, *Acc. Chem. Res.* **1998**, *31*, 474–484.

[7] L.-C. Song, G.-X. Jin, W.-X. Zhang, Q.-M. Hu, *Organometallics* **2005**, *24*, 700–706.

[8] L.-C. Song, G.-X. Jin, H.-T. Wang, W.-X. Zhang, Q.-M. Hu, *Organometallics* **2005**, *24*, 6464–6471.
[9] a) D. Venkataraman, Y. Du, S. R. Wilson, K. A. Hirsch, P. Zhang, J. S. Moore, *J. Chem. Educ.* **1997**, *74*, 915–918; b) L. Tei, V. Lippolis, A. J. Blake, P. A. Cooke, M. Schröder, *Chem. Commun.* **1998**, 2633–2634; c) F. A. Cotton, G. Wilkinson, *Advanced Inorganic Chemistry*, 5th ed., Wiley, Chichester, **1988**.
[10] a) C. E. Housecroft, B. F. G. Johnson, M. S. Khan, J. Lewis, P. R. Raithby, M. E. Robson, D. A. Wilkinson, *J. Chem. Soc., Dalton Trans.* **1992**, 3171–3178; b) B. F. G. Johnson, J. Lewis, P. R. Raithby, D. A. Wilkinson, *J. Organomet. Chem.* **1991**, *408*, 9–12.
[11] a) D. Christodoulou, M. G. Kanatzidis, D. Coucouvanis, *Inorg. Chem.* **1990**, *29*, 191–201; b) D. Coucouvanis, K. Greiwe, A. Salifoglou, P. Challen, A. Simopoulos, A. Kostikas, *Inorg. Chem.* **1988**, *27*, 593–594; c) F. A. Cotton, S. A. Duraj, W. J. Roth, C. D. Schmulbach, *Inorg. Chem.* **1985**, *24*, 525–527.
[12] a) G. Li, H. Hou, L. Li, X. Meng, Y. Fan, Y. Zhu, *Inorg. Chem.* **2003**, *42*, 4995–5004; b) M.-L. Tong, J.-W. Cai, X.-L. Yu, X.-M. Chen, S. W. Ng, T. C. W. Mak, *Aust. J. Chem.* **1998**, *51*, 637–641.
[13] S. Muthu, J. H. K. Yip, J. J. Vittal, *J. Chem. Soc., Dalton Trans.* **2001**, 3577–3584.
[14] a) A. N. Khlobystov, A. J. Blake, N. R. Champness, D. A. Lemenovskii, A. G. Majouga, N. V. Zyk, M. Schröder, *Coord. Chem. Rev.* **2001**, *222*, 155–192; b) N. L. S. Yue, M. C. Jennings, R. J. Puddephatt, *Inorg. Chem.* **2005**, *44*, 1125–1131.
[15] M. Arewgoda, P. H. Rieger, B. H. Robinson, J. Simpson, S. J. Visco, *J. Am. Chem. Soc.* **1982**, *104*, 5633–5640.
[16] D. Osella, J. Fiedler, *Organometallics* **1992**, *11*, 3875–3878.
[17] L. V. Casagrande, T. Chen, P. H. Rieger, B. H. Robinson, *Inorg. Chem.* **1984**, *23*, 2019–2025.
[18] V. W.-W. Yam, Y.-L. Pui, K.-K. Cheung, *Inorg. Chem.* **2000**, *39*, 5741–5746.
[19] R. S. Dickson, P. J. Fraser, *Adv. Organomet. Chem.* **1974**, *12*, 323–377.
[20] D. K. Breitinger, W. A. Herrmann, *Synthetic Methods of Organometallic and Inorganic Chemistry*, Thieme, New York, **1996**.
[21] a) C. O. Badgett, C. F. Woodward, *J. Am. Chem. Soc.* **1947**, *69*, 2907–2907; b) S. Bélanger, M. Gilbertson, D. I. Yoon, C. L. Stern, X. Dang, J. T. Hupp, *J. Chem. Soc., Dalton Trans.* **1999**, 3407–3412.
[22] G. M. Sheldrick, *SADABS*, *A Program for Empirical Absorption Correction of Area Detector Data*, University of Göttingen, Germany, **1996**.
[23] G. M. Sheldrick, *SHELXS97*, *A Program for Crystal Structure Solution*, University of Göttingen, Germany, **1997**.
[24] G. M. Sheldrick, *SHELXL97*, *A Program for Crystal Structure Refinement*, University of Göttingen, Germany, **1997**.
[25] P. v. d. Sluis, A. L. Spek, *Acta Crystallogr., Sect. A* **1990**, *46*, 194–201.

Received: September 28, 2008
Published Online: December 12, 2008

DOI: 10.1002/ejic.200800977

Imido and Amido Titanium Complexes that Contain a [OSSO]-Type Bis(phenolato) Ligand: Synthesis, Structures, and Hydroamination Catalysis

Bing Lian,[a] Thomas P. Spaniol,[a] Patricia Horrillo-Martínez,[b] Kai C. Hultzsch,[b][‡] and Jun Okuda*[a]

Keywords: Titanium / N ligands / Bis(phenolato) ligand / Hydroamination / Homogeneous catalysis

Salt metathesis reaction of the imido complex [Ti(NR)$Cl_2(NC_5H_5)_3$] (R = *t*Bu, C_6H_3*i*Pr_2-2,6) with 1 equiv. of the lithium salt of the corresponding [OSSO]-type bis(phenol) [edtbpH_2: (HOC_6H_2-*t*Bu_2-4,6)$_2$(SCH_2CH_2S); *rac*-(cydtbp)H_2: (HOC_6H_2-*t*Bu_2-4,6)$_2$($S_2C_6H_{10}$-1,2)] afforded imido titanium complexes [Ti(edtbp)(N*t*Bu)(NC_5H_5)] (**1**), [Ti(edtbp)(NC_6H_3-*i*Pr_2-2,6)(NC_5H_5)] (**2**), and [Ti{*rac*-(cydtbp)}(N*t*Bu)(NC_5H_5)] (**3**). The bis(dimethylamido)titanium complex [Ti(edtbp)-(NMe_2)$_2$] (**4**) was synthesized by protonolysis of [Ti(NMe_2)$_4$] with bis(phenol) edtbpH_2. Reaction of [Ti(NMe_2)Cl_3] with the lithium salt of the bis(phenol) gave the chloro dimethylamido complex [Ti(edtbp)(NMe_2)Cl] (**5**) in high yield. All complexes were characterized by NMR spectroscopy and elemental analysis. Additionally, complexes **1** and **5** were studied by X-ray diffraction analysis. Imido titanium complex **1** shows moderate activity in the intramolecular hydroamination reaction of 5-phenylpent-4-ynylamine. Complexes **1**–**3** catalyze the intramolecular hydroamination of aminoalkenes.

Introduction

The catalytic hydroamination, constituting the addition of N–H across the carbon–carbon multiple bond, has become an attractive carbon–nitrogen bond forming process in the recent past.[1] In particular, group 4 metal systems exhibit the catalytic performance distinct from other metal systems.[2] We have recently introduced configurationally rigid titanium complexes containing a linked bis(phenolato) [OSSO]-type ligand that polymerize styrene isospecifically,[3a–3d,3g] and oligomerize α-olefins regioselectively.[3e] Living polymerization of methyl methacrylate could be achieved with the titanium enolate complex.[3f] The helical configuration around the metal center ensures the isospecific polymerization of styrene and related monomers.[4] To explore the suitability of this [OSSO]-type titanium system for hydroamination reactions, we have prepared both imido- and amidotitanium complexes containing this [OSSO]-type ligand and investigated their hydroamination reactivity. In the course of the preparation of this article, Doye et al. reported that the amido titanium and zirconium catalysts generated in situ with this type of ligand catalyze the hydroamination of alkynes and alkenes.[2l]

[a] Institute of Inorganic Chemistry, RWTH Aachen University, Landoltweg 1, 52074 Aachen, Germany
Fax: +49-241-80-92644
E-mail: jun.okuda@ac.rwth-aachen.de
[b] Institut für Organische Chemie, Friedrich-Alexander Universität Erlangen-Nürnberg, Henkestr. 42, 91054 Erlangen, Germany
[‡] New address: Rutgers, The State University of New Jersey, Department of Chemistry and Chemical Biology, 610 Taylor Road, Piscataway, NJ 08854-8087, USA

Results and Discussion

Imido and Amidotitanium Complexes

Reaction of the imido precursor [Ti(NR)$Cl_2(NC_5H_5)_3$] (R = *t*Bu, C_6H_3*i*Pr_2-2,6) with one equiv. of the lithium salt of the bis(phenol) [edtbpH_2: (HOC_6H_2-*t*Bu_2-4,6)$_2$-(SCH_2CH_2S); *rac*-(cydtbp)H_2: (HOC_6H_2-*t*Bu_2-4,6)$_2$-($S_2C_6H_{10}$-1,2)] generated in situ in THF/toluene mixture at –35 °C led to the formation of the imido titanium complexes **1**–**3** (Scheme 1). The new complexes were isolated as crystals in high yield (80–87%) and characterized by ^{1}H and ^{13}C NMR spectroscopy as well as by elemental analysis. The ^{1}H NMR spectrum of both [Ti(edtbp)(N*t*Bu)-(NC_5H_5)] (**1**) and [Ti(edtbp)(NC_6H_3*i*Pr_2-2,6)(NC_5H_5)] (**2**) in C_6D_6 at room temperature shows an ABCD spin system for the SCH_2CH_2S bridge with four sets of signals [**2**: δ = 2.60 (dm), 2.48 (dm), 2.24 (td), and 2.13 ppm (td)]. The ^{1}H-^{13}C HMQC spectrum gives the correlation of the ^{1}H NMR resonances with two ^{13}C NMR resonances at δ = 37.74 (2.60 and 2.24 ppm) and 35.07 ppm (2.48 and 2.13 ppm), respectively. In the ^{1}H NMR spectrum of **2** four singlets for the four *tert*-butyl groups are found (δ = 1.89, 1.71, 1.32, and 1.23 ppm), indicating a rigid C_1-symmetric molecular structure in solution. According to ^{1}H NMR spectroscopic studies, dissociation of the pyridine ligand in the imido titanium complexes **1**–**3** is slow up to 100 °C.

The bis(dimethylamido)titanium complex **4** was synthesized under dimethylamine elimination from [Ti(NMe_2)$_4$] and bis(phenol) edtbpH_2 in 1:1 molar ratio (Scheme 2) and isolated as red crystals in 85% yield. The ^{1}H NMR spectrum of **4** in C_6D_6 shows an AB spin pattern for the

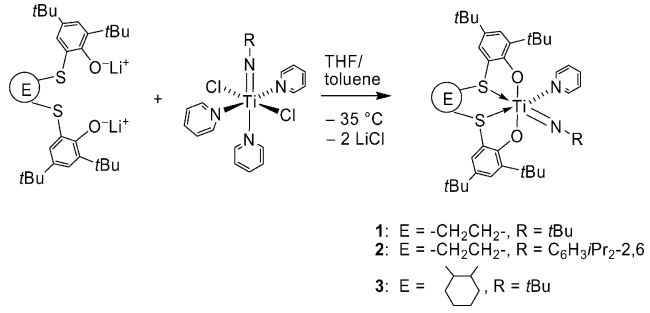

Scheme 1.

SCH_2CH_2S bridge (δ = 2.56 and 2.16 ppm) and one singlet at δ = 3.53 ppm for all 4 methyl groups of the dimethylamido groups. This is in agreement for the bis(dimethylamido)titanium complex generated in situ.[21] These NMR spectra data suggest a C_2-symmetric molecular structure in solution.

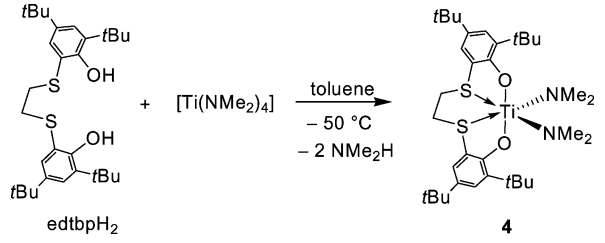

Scheme 2.

Treating Li_2(edtbp) with one equiv. of [Ti(NMe$_2$)Cl$_3$] in toluene gave the chloro dimethylamido complex [Ti(edtbp)(NMe$_2$)Cl] (**5**) as red crystals in 81% yield (Scheme 3). In the ^{1}H NMR spectrum of **5**, an ABCD spin system for the SCH_2CH_2S bridge was observed with resonances at δ = 2.52 (dt), 2.38 (dt), 2.22 (td), and 1.97 ppm (td) which correlate in the HMQC 2D NMR spectrum with two ^{13}C NMR resonances at δ = 37.87 (2.52 and 2.22 ppm) and 37.80 ppm (2.38 and 1.97 ppm), respectively. One singlet at δ = 3.68 ppm was observed for the two equivalent methyl groups of the dimethylamido group.

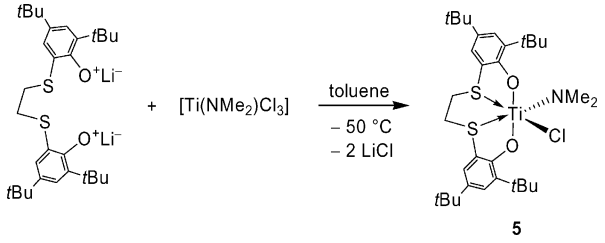

Scheme 3.

X-ray Crystal Structures of 1 and 5

Single crystals of complexes **1** and **5** were obtained from pentane and have been characterized by X-ray diffraction analysis. Details of the crystal structure determination are given in Table 3 (see Exp. Sect.). The molecular studies of **1** and **5** in the solid state as well as selected interatomic distances and angles are shown in Figure 1 and Figure 2. Complexes **1** and **5** are monomeric in the solid state.

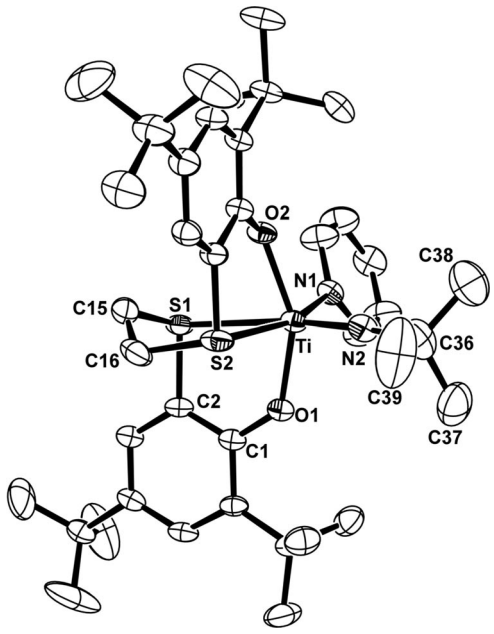

Figure 1. Molecular structure of complex [Ti(edtbp)(N*t*Bu)(NC$_5$H$_5$)] (**1**) (hydrogen atoms were omitted for clarity). Selected bond lengths [Å] and angles [°]: Ti–O1, 1.965(2); Ti–O2, 1.985(2); Ti–S1, 2.7853(10); Ti–S2, 2.5826(10); Ti–N1, 2.202(2); Ti–N2, 1.705(3); N2–C36, 1.442(4); O1–C1, 1.327(3); O1–Ti–O2, 151.96(9); S1–Ti–S2, 80.73(3); N1–Ti–N2, 102.66(11); Ti–N2–C36, 173.6(3); O2–Ti–S1, 79.73(7); O2–Ti–S2, 77.62(6); O2–Ti–N2, 104.14(11); O2–Ti–N1, 91.70(9).

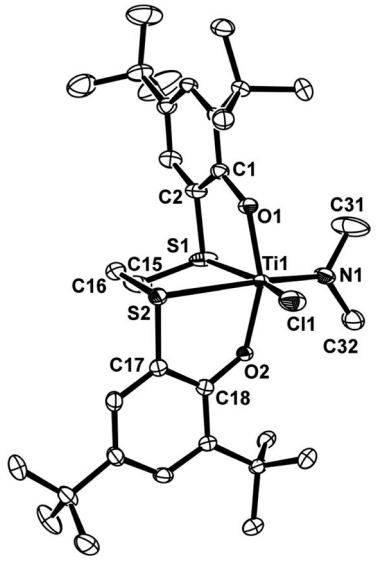

Figure 2. Molecular structure of complex [Ti(edtbp)(NMe$_2$)Cl] (**5**) (hydrogen atoms were omitted for clarity). Only one of the two crystallographically independent atoms are shown. Selected bond lengths [Å] and angles [°]: Ti1–O1, 1.887(2); Ti1–O2, 1.8852(19); Ti1–S1, 2.5997(10); Ti1–S2, 2.7229(9); Ti1–N1, 1.877(3); Ti1–Cl1, 2.3129(10); N1–C31, 1.450(5); N1–C32, 1.441(4); O1–Ti1–O2, 156.64(9); S1–Ti1–S2, 78.31(3); N1–Ti1–Cl1, 103.86(11); C31–N1–Ti1, 124.9(2); C32–N1–Ti1, 125.9(2); C31–N1–C32, 109.3(3); O1–Ti1–S1, 77.19(7); O1–Ti1–N1, 97.85(10).

Table 1. Titanium···sulfur distances in [OSSO]-type bis(phenolato) titanium complexes.

Compound	Ti–S1 [Å] (*trans* group)	Ti–S2 [Å] (*trans* group)	Ref.
[Ti(etbmp)Cl_2]	2.647(3) (Cl)	2.647(3) (Cl)	[3b]
[Ti(edtbp)Me_2]	2.8056(7) (Me)	2.8417(7) (Me)	[3e]
[Ti(edtbp)$(CH_2Ph)_2$]	2.8836(7) (η^2-CH_2Ph)	2.7472(7) (η^1-CH_2Ph)	[3c]
[Ti{(*R*,*R*)-(cytbmp)}(O*i*Pr)$_2$]	2.674(4) (O*i*Pr)	2.673(4) (O*i*Pr)	[3g]
[Ti(edtbp)MeCl]	2.6986(8) (Me)	2.6756(8) (Cl)	[3f]
[Ti(edtbp)Me{O(*i*PrO)C=CMe_2}]	2.6389(15) [O(*i*PrO)C=CMe_2]	2.7327(14) (Me)	[3f]
[Ti(edtbp)Me(O$CMe_2CMe_2CO_2$*i*Pr)]	2.7156(8) (O$CMe_2CMe_2CO_2$*i*Pr)	2.7227(8) (Me)	[3f]
[Ti(edtbp)(N*t*Bu)(NC_5H_5)] (**1**)	2.7853(10) (N*t*Bu)	2.5826(10) (NC_5H_5)	this work
[Ti(edtbp)(NMe_2)Cl] (**5**)	2.7229(9) (NMe_2)	2.5997(10) (Cl)	this work

The octahedrally coordinated titanium center in complex **1** is coordinated by two *trans*-oxygen atoms, two *cis*-sulfur donor atoms, and the *cis*-arranged pyridine and *tert*-butylamido ligands (Figure 1). The Ti(edtbp) moiety adopts a C_2-symmetric helical framework similar as observed in the previous study.[3a] The O1–Ti–O2 [151.96(9)°] bond angle is slightly narrower than that of analogous Ti(edtbp) complexes, in the range of 156.7(2) –157.82(10)°,[3] indicating the formation of a fairly open titanium coordination sphere. The bond angle of S1–Ti–S2 [80.73(3)°] is slightly wider than the value of a similar complex [78.37(8)°];[3b] the Ti–S bond length [2.7853(10) Å and 2.5826 (10) Å] in **1** is comparable to the values in a reported dichloro complex [2.647(3) Å].[3b] The Ti–N2 bond length [1.705(3) Å] is much shorter than the value of a coordinated Ti–N1 bond [2.202(2) Å] in **1**. The bond angle of Ti–N2–C36 [173.6(3)°] is close to linear and comparable to the reported values,[5] indicating that N*t*Bu group donates four electrons to the titanium metal center.

The solid-state structure of dimethylamido complex **5** also features a six-coordinate titanium center with a C_2-symmetric helical Ti(edtbp) fragment (Figure 2). The O1–Ti–O2 [156.64(9)°] bond angle is close to that of Ti(edtbp) complexes [156.7(2)–157.82(10)°].[3] The Ti–N1 [1.877(3) Å] bond length is comparable to the values of similar amidotitanium complexes [1.862(3)–1.917(5) Å].[6,2k] The nitrogen atom is trigonal with the sum of angles around N1 atom close to 360° (calculated: 360.1°), indicating strong π-electron donation to the Ti center. Notably, the elongated Ti–S2 [2.7229(9) Å] bond length as compared to that of Ti–S1[2.5997(10) Å] is caused by the stronger electron-donating *trans*-dimethylamido group in the solid state. Detailed comparisons of the *trans*-influence on the Ti–S bond length are shown in Table 1.

Intramolecular Hydroamination of Aminoalkyne and Aminoalkene

Complex **1** was selected for the catalytic study in the intramolecular hydroamination of 5-phenylpent-4-ynylamine (Scheme 4). By combination of 5 mol-% of catalyst **1** with substrate in toluene solution at room temperature, over 91% conversion was observed to give the cyclic imine product within 23 h. In comparison with the reported activity of a titanocene catalyst Cp_2TiMe_2 (98% yield, 110 °C, 6 h),[7a] the imidotitanium catalyst with a [OSSO]-type bis(phenolato) ligand shows higher activity under rather mild reaction conditions. However, the activity of catalyst **1** is still lower than the known bis(amidinato)titanium catalyst [Ti(C_6F_5C(O)N*t*Bu)$_2$(NMe_2)$_2$] (97% yield, 25 °C, 15 min).[7b] The intermolecular hydroamination with this type of catalyst has been investigated by Doye et al.[2l]

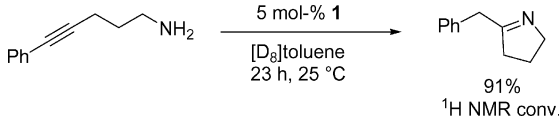

Scheme 4.

Catalysts **1**–**3** have been studied in the intramolecular hydroamination of aminoalkenes (Scheme 5). Results are summarized in Table 2. Only trace amounts of desired cyclization product was observed after short reaction times at 150 °C (entries 5 and 7). High conversions (85–94%) are achieved at prolonged reaction times of 14–22 d (entries 3, 4 and 6). As commonly observed,[1i] the *gem*-diphenyl activated[8] substrate **6a** reacts faster than the aminoalkene **6b** using the rigid complex **3** with a cydtbp ligand (Table 2, entry 3 vs. entry 6). However, the opposite is true for the more flexible edtbp complex **1** (entry 1 vs. entry 4). Although catalysts **1**–**3** are active in the intramolecular hy-

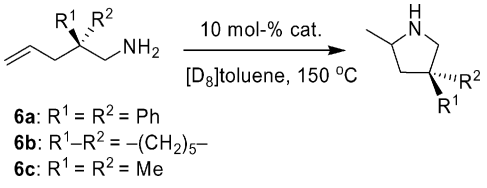

Scheme 5.

Table 2. Intramolecular hydroamination of aminoalkenes using catalysts **1**–**3**.[a]

Entry	Substrate	Complex	Time [d]	% Conv.[b]
1	**6a**	**1**	29	61
2	**6a**	**2**	23	78
3	**6a**	**3**	14	85
4	**6b**	**1**	16	92
5	**6b**	**2**	20 h	< 1
6	**6b**	**3**	22	94
7	**6c**	**1**	21 h	< 1

[a] Reaction conditions: substrate: 0.2 mmol, catalyst: 0.02 mmol (10 mol-%), solvent: 0.5 mL [D_8]toluene, temperature: 150 °C. [b] Determined by ^{1}H NMR spectroscopy.

droamination of aminoalkenes, their catalytic activities are rather low in comparison with titanium catalysts reported in the literature, e.g. [Ti(NMe_2)$_4$] (substrate **6a**, 5 mol-% cat., 92% yield, 24 h, 110 °C).[2e]

Conclusions

We have isolated imido and amido titanium complexes that contain a tetradentate [OSSO]-type bis(phenolato) ligand. The imido complexes were found to be catalytically active in the intramolecular hydroamination of aminoalkynes and aminoalkenes. The moderate catalytic activities of these imido catalysts were probably caused by the sterically crowded titanium center with the strongly coordinated pyridine ligand. Further studies will be undertaken to achieve enantioselective hydroamination reactions[1b,1e,1f,1h] using optically pure [OSSO]-type group 4 metal catalysts.[3d,3g]

Experimental Section

General: All experiments were carried out under purified argon using standard Schlenk techniques or a glove box (<1 ppm O_2, 1 ppm H_2O). Toluene, pentane, diethyl ether, dichloromethane, and THF were purified from the MBraun SPS-800 system prior to use. Deuterated solvents were purchased from Aldrich and purified before use. All other chemicals were commercially available and used after appropriate purification. Compounds (HOC_6H_2-*t*Bu_2-4,6)$_2$(SCH_2CH_2S) (edtbpH_2),[3a] *rac*-(2,3-*trans*-butanediyl-1,4-dithiabutanediyl)-2,2′-bis{4,6-di-*tert*-butylphenol} [*rac*-(cydtbp)H_2],[3d] [Ti(N*t*Bu)Cl_2(NC_5H_5)$_3$],[5] [Ti(NC_6H_3*i*Pr_2-2,6)Cl_2(NC_5H_5)$_3$],[5] [Ti(NMe_2)Cl_3],[9] 5-phenylpent-4-ynylamine,[10a] 2,2-diphenylpent-4-enylamine (**6a**),[10b] *C*-(1-allylcyclohexyl)methylamine (**6b**)[10c] and 2,2-dimethylpent-4-enylamine (**6c**)[10d] were synthesized according to literature methods. NMR spectra were recorded on Bruker DRX 400 (^{1}H, 400 MHz; ^{13}C, 101 MHz) and Varian 200 spectrometers in Teflon-valved NMR tubes at 25 °C unless stated otherwise. ^{1}H and ^{13}C NMR chemical shifts were determined using residual solvent resonances and are reported vs. $SiMe_4$. Assignment of signals was made from ^{1}H-^{13}C HMQC and ^{1}H-^{13}C HMBC 2D NMR experiments. Coupling constants are given in Hertz. Elemental analyses were performed by the Microanalytical Laboratory of this department.

[Ti(edtbp)(N*t*Bu)(NC_5H_5)] (1): To a solution of [Ti(N*t*Bu)Cl_2(NC_5H_5)$_3$] (1.25 g, 2.92 mmol) in THF (20 mL) was slowly added at –35 °C a solution of Li_2(edtbp) in 30 mL of toluene, generated in situ from edtbpH_2 (1.47 g, 2.92 mmol) and *n*BuLi (2.34 mL, 2.5 M in hexane, 5.85 mmol). The reaction mixture was warmed to room temperature and stirred for 6 h. After removal of all volatiles under vacuum, the residue was recrystallized from pentane to give [Ti(edtbp)(N*t*Bu)(NC_5H_5)] (**1**) as orange crystals (1.67 g, 82%). A crystal of **1** suitable for X-ray diffraction analysis was selected. ^{1}H NMR ([D$_6$]benzene): δ = 9.28 (dt, $^3J_{HH}$ = 4.6, $^4J_{HH}$ = 1.7 Hz, 2 H, *o*-H, NC_5H_5), 7.63 (d, $^4J_{HH}$ = 2.4 Hz, 1 H, Ph-5-*H*), 7.61 (d, $^4J_{HH}$ = 2.4 Hz, 1 H, Ph-5′-*H*), 7.43 (d, $^4J_{HH}$ = 2.4 Hz, 1 H, Ph-3-*H*), 7.20 (d, $^4J_{HH}$ = 2.4 Hz, 1 H, Ph-3′-*H*), 6.70 (tt, $^3J_{HH}$ = 7.5, $^4J_{HH}$ = 1.7 Hz, 1 H, *p*-H, NC_5H_5), 6.48 (tm, $^3J_{HH}$ = 6.4 Hz, 2 H, *m*-H, NC_5H_5), 2.72 (dm, $^2J_{HH}$ = 10.1 Hz, 1 H, SCH_2), 2.58 (dm, $^2J_{HH}$ = 10.1 Hz, 1 H, SCH_2), 2.18 (d, $^2J_{HH}$ = 10.1 Hz, 2 H, SCH_2), 1.97 [s, 9 H, $C(CH_3)_3$], 1.80 [s, 9 H, $C(CH_3)_3$], 1.33 [s, 9 H, $C(CH_3)_3$], 1.23 [s, 9 H, $C(CH_3)_3$], 1.20 [s, 9 H, $NC(CH_3)_3$] ppm. ^{13}C{^{1}H} NMR ([D$_6$]benzene): δ = 168.86 (Ph-*C*1), 167.23 (Ph-*C*1′), 150.01 (NC_5H_5-*o*-*C*), 139.73 (Ph-*C*6), 138.36 (Ph-*C*6′), 138.27 (NC_5H_5-*p*-*C*), 138.08 (Ph-*C*4), 137.03 (Ph-*C*4′), 128.43 (Ph-*C*5), 128.31 (Ph-*C*5′), 126.02 (Ph-*C*3), 126.01 (Ph-*C*3′), 124.10 (NC_5H_5-*m*-*C*), 117.20 (Ph-*C*2), 116.11 (Ph-*C*2′), 68.28 [N*C*(CH$_3$)$_3$], 37.84 (S*C*H$_2$), 36.16 [*C*(CH$_3$)$_3$], 35.69 [*C*(CH$_3$)$_3$], 34.53 [*C*(CH$_3$)$_3$], 34.29 (S*C*H$_2$), 34.23 [*C*(CH$_3$)$_3$], 32.04 [NC(*C*H$_3$)$_3$], 31.85 [C(*C*H$_3$)$_3$], 31.73 [C(*C*H$_3$)$_3$], 29.87 [C(*C*H$_3$)$_3$], 29.76 [C(*C*H$_3$)$_3$] ppm. $C_{39}H_{58}N_2O_2S_2Ti$ (698.89): calcd. C 67.02, H 8.36, N 4.01; found C 67.86, H 8.43, N 3.87.

[Ti(edtbp)(NC_6H_3*i*Pr_2-2,6)(NC_5H_5)] (2): To a solution of [Ti(N-C_6H_3*i*Pr_2-2,6)Cl_2(NC_5H_5)$_3$] (1.55 g, 2.92 mmol) in THF (20 mL) was slowly added at –35 °C a solution of Li_2(edtbp) in 30 mL of toluene, generated in situ from edtbpH_2 (1.47 g, 2.92 mmol) and *n*BuLi (2.34 mL, 2.5 M in hexane, 5.85 mmol). The reaction mixture was warmed to room temperature and further stirred 6 h. After evaporation of volatile under vacuum, the residue was recrystallized with toluene/pentane to give [Ti(edtbp)(NC_6H_3*i*Pr_2-2,6)(NC_5H_5)] (**2**) as brown crystals (1.87 g, 80%). ^{1}H NMR ([D$_6$]-benzene): δ = 9.16 (dt, $^3J_{HH}$ = 4.6, $^4J_{HH}$ = 1.7 Hz, 2 H, *o*-H, NC_5H_5), 7.64 (d, ^4J = 2.4 Hz, 1 H, Ph-5-*H*), 7.58 (d, $^4J_{HH}$ = 2.4 Hz, 1 H, Ph-5′-*H*), 7.29 (d, $^4J_{HH}$ = 2.4 Hz, 1 H, Ph-3-*H*), 7.22 (d, $^4J_{HH}$ = 2.4 Hz, 1 H, Ph-3′-*H*), 7.03 (d, $^3J_{HH}$ = 7.9 Hz, 2 H, NAr-3-*H*), 6.85 (t, $^3J_{HH}$ = 7.9 Hz, 1 H, NAr-4-*H*), 6.66 (tt, $^3J_{HH}$ = 7.5, $^4J_{HH}$ = 1.7 Hz, 1 H, *p*-H, NC_5H_5), 6.40 (tm, $^3J_{HH}$ = 6.4 Hz, 2 H, *m*-H, NC_5H_5), 4.49 [sept, $^3J_{HH}$ = 6.8 Hz, 2 H, $(CH_3)_2CH$], 2.60 (dm, $^2J_{HH}$ = 10.1 Hz, 1 H, SCH_2), 2.48 (dm, $^2J_{HH}$ = 10.1 Hz, 1 H, SCH_2), 2.24 (td, $^2J_{HH}$ = 13.2, $^3J_{HH}$ = 3.2 Hz, 1 H, SCH_2), 2.13 (td, $^2J_{HH}$ = 13.2, $^3J_{HH}$ = 3.2 Hz, 1 H, SCH_2), 1.89 [s, 9 H, $C(CH_3)_3$], 1.71 [s, 9 H, $C(CH_3)_3$], 1.32 [s, 9 H, $C(CH_3)_3$], 1.23 [d, $^3J_{HH}$ = 6.8 Hz, 6 H, $(CH_3)_2CH$], 1.22 [s, 9 H, $C(CH_3)_3$], 1.04 [d, $^3J_{HH}$ = 6.8 Hz, 6 H, $(CH_3)_2CH$] ppm. ^{13}C{^{1}H} NMR ([D$_6$]benzene): δ = 168.68 (Ph-*C*1), 166.89 (Ph-*C*1′), 156.92 (NAr-*C*1), 149.33 (NC_5H_5-*o*-*C*), 143.31 (NAr-*C*2), 140.92 (Ph-*C*6), 139.01 (Ph-*C*6′), 138.24 (NC_5H_5-*p*-*C*), 138.17 (Ph-*C*4), 136.95 (Ph-*C*4′), 127.62 (Ph-*C*5), 127.46 (Ph-*C*5′), 126.11 (Ph-*C*3), 125.85 (Ph-*C*3′), 124.22 (NC_5H_5-*m*-*C*), 121.92 (NAr-*C*3), 120.78 (NAr-*C*4), 117.47 (Ph-*C*2), 117.00 (Ph-*C*2′), 37.74 (S*C*H$_2$), 35.07 (S*C*H$_2$), 35.62 [*C*(CH$_3$)$_3$], 35.25 [*C*(CH$_3$)$_3$], 33.82 [*C*(CH$_3$)$_3$], 33.70 [*C*(CH$_3$)$_3$], 31.47 [C-(*C*H$_3$)$_3$], 31.31 [C(*C*H$_3$)$_3$], 29.56 [C(*C*H$_3$)$_3$], 29.41 [C(*C*H$_3$)$_3$], 27.41 [*C*H(CH$_3$)$_2$], 24.47 [CH(*C*H$_3$)$_2$], 24.06 [CH(*C*H$_3$)$_2$] ppm. $C_{47}H_{66}N_2O_2S_2Ti$ (803.04): calcd. C 70.30, H 8.28, N 3.49; found C 69.63, H 8.58, N 3.42.

[Ti{*rac*-(cydtbp)}(N*t*Bu)(NC_5H_5)] (3): To a solution of [Ti(N*t*Bu)-Cl_2(NC_5H_5)$_3$] (0.75 g, 1.76 mmol) in THF (20 mL) was slowly added at –35 °C a solution of Li_2{*rac*-(cydtbp)} in 30 mL of toluene, generated in situ from *rac*-(cydtbp)H_2 (0.98 g, 1.76 mmol) and *n*BuLi (1.40 mL, 2.5 M in hexane, 3.52 mmol). The reaction mixture was warmed to room temperature and further stirred overnight. After removal of all volatiles under vacuum, the residue was recrystallized from pentane to give [Ti{*rac*-(cydtbp)}(N*t*Bu)(NC_5H_5)] (**3**) as yellow crystals (1.15 g, 87%). ^{1}H NMR ([D$_6$]benzene): δ = 9.34 (dt, $^3J_{HH}$ = 4.6, $^4J_{HH}$ = 1.7 Hz, 2 H, *o*-H, NC_5H_5), 7.67 (d, $^4J_{HH}$ = 2.4 Hz, 1 H, Ph-5-*H*), 7.65 (d, ^4J = 2.4 Hz, 1 H, Ph-5′-*H*), 7.48 (d, $^4J_{HH}$ = 2.4 Hz, 1 H, Ph-3-*H*), 7.30 (d, $^4J_{HH}$ = 2.4 Hz, 1 H, Ph-3′-*H*), 6.68 (tt, $^3J_{HH}$ = 7.5, $^4J_{HH}$ = 1.7 Hz, 1 H, *p*-H, NC_5H_5), 6.47 (tm, $^3J_{HH}$ = 6.4 Hz, 2 H, *m*-H, NC_5H_5), 2.47 (td, $^2J_{HH}$ = 13.2, $^3J_{HH}$ = 3.2 Hz, 1 H, S*CH*), 2.34 (td, $^2J_{HH}$ = 13.2, $^3J_{HH}$ = 3.2 Hz, 1 H, S*CH*), 2.03 (m, 2 H, cyclohexyl), 2.01 [s, 9 H, $C(CH_3)_3$], 1.83 [s, 9 H, $C(CH_3)_3$], 1.68 (m, 2 H, cyclohexyl), 1.38 [s, 9 H, $C(CH_3)_3$], 1.28 [s, 9 H, $NC(CH_3)_3$], 1.22 [s, 9 H, $C(CH_3)_3$], 1.14 (m, 2 H, cyclo-

hexyl), 0.43 (m, 2 H, cyclohexyl) ppm. $^{13}C\{^1H\}$ NMR ([D$_6$]benzene): δ = 169.11 (Ph-*C*1), 167.47 (Ph-*C*1′), 150.13 (NC_5H_5-*o*-*C*), 138.24 (NC_5H_5-*p*-*C*), 137.92 (Ph-*C*6), 137.08 (Ph-*C*6′), 130.65 (Ph-*C*4), 130.61 (Ph-*C*4′), 128.44 (Ph-*C*5), 128.32 (Ph-*C*5′), 126.27 (Ph-*C*3), 126.18 (Ph-*C*3′), 124.04 (NC_5H_5-*m*-*C*), 114.89 (Ph-*C*2), 114.30 (Ph-*C*2′), 68.07 [N*C*(CH$_3$)$_3$], 52.68 (S*C*H), 50.71 (S*C*H), 36.21 [*C*(CH$_3$)$_3$], 35.75 [*C*(CH$_3$)$_3$], 34.08 [*C*(CH$_3$)$_3$], 34.05 [*C*(CH$_3$)$_3$], 32.03 [NC(*C*H$_3$)$_3$], 31.85 [C(*C*H$_3$)$_3$], 31.74 [C(*C*H$_3$)$_3$], 30.01 (cyclohexyl), 29.94 [C(*C*H$_3$)$_3$], 29.85 [C(*C*H$_3$)$_3$], 29.48 (cyclohexyl), 25.56 (cyclohexyl), 25.44 (cyclohexyl) ppm. $C_{43}H_{64}N_2O_2S_2Ti$ (752.98): calcd. C 68.59, H 8.57, N 3.72; found C 67.92, H 8.60, N 3.41.

[Ti(edtbp)(NMe$_2$)$_2$] (4): [Ti(NMe$_2$)$_4$] (0.45 g, 1.99 mmol) and 15 mL toluene were charged in a 100 mL Schlenk tube and a solution of edtbpH$_2$ (1.0 g, 1.99 mmol) in 50 mL of toluene was added dropwise at –50 °C. The reaction mixture was warmed to room temperature and further stirred overnight. After removal of all volatiles under vacuum, the residue was recrystallized from pentane to give [Ti(edtbp)(NMe$_2$)$_2$] (**4**) as red crystals (1.08 g, 85%). ^1H NMR ([D$_6$]benzene): δ = 7.55 (d, $^4J_{HH}$ = 2.4 Hz, 2 H, Ph-5-*H*), 7.25 (d, $^4J_{HH}$ = 2.4 Hz, 2 H, Ph-3-*H*), 3.53 [s, 12 H, N(C*H*$_3$)$_2$], 2.56 (d, $^2J_{HH}$ = 12.0 Hz, 2 H, SC*H*$_2$), 2.16 (d, $^2J_{HH}$ = 12.0 Hz, 2 H, SC*H*$_2$), 1.77 [s, 18 H, C(C*H*$_3$)$_3$], 1.22 [s, 18 H, C(C*H*$_3$)$_3$] ppm. $^{13}C\{^1H\}$ NMR ([D$_6$]benzene): δ = 166.91 (Ph-*C*1), 140.94 (Ph-*C*6), 137.17 (Ph-*C*4), 127.37 (Ph-*C*5), 125.91 (Ph-*C*3), 117.01 (Ph-*C*2), 47.70 [N(*C*H$_3$)$_3$], 37.12 (S*C*H$_2$), 35.38 [*C*(CH$_3$)$_3$], 33.83 [*C*(CH$_3$)$_3$], 31.32 [C(*C*H$_3$)$_3$], 29.61 [C(*C*H$_3$)$_3$] ppm. $C_{34}H_{56}N_2O_2S_2Ti$ (636.82): calcd. C 64.13, H 8.86, N 4.40; found C 64.54, H 8.70, N 4.08.

[Ti(edtbp)(NMe$_2$)Cl] (5): [Ti(NMe$_2$)Cl$_3$] (0.40 g, 2.02 mmol) and 15 mL toluene were charged in a 100 mL Schlenk, and a solution of Li$_2$(edtbp) in 50 mL of toluene, generated in situ from edtbpH$_2$ (1.02 g, 2.02 mmol) and *n*BuLi (1.61 mL, 2.5 M in hexane, 4.04 mmol), was added dropwise at –50 °C. The reaction mixture was warmed to room temperature and further stirred overnight. After evaporation of volatile under vacuum, the residue was recrystallized from pentane to give [Ti(edtbp)(NMe$_2$)Cl] (**5**) as red crystals (1.03 g, 81%). ^1H NMR ([D$_6$]benzene): δ = 7.52 (d, $^4J_{HH}$ = 2.2 Hz, 2 H, Ph-5-*H*), 7.22 (d, $^4J_{HH}$ = 2.2 Hz, 1 H, Ph-3-*H*), 7.08 (d, $^4J_{HH}$ = 2.2 Hz, 1 H, Ph-3′-*H*), 3.68 [s, 6 H, N(C*H*$_3$)$_2$], 2.52 (dt, $^2J_{HH}$ = 10.2, $^3J_{HH}$ = 3.0 Hz, 1 H, SC*H*$_2$), 2.38 (dt, $^2J_{HH}$ = 10.2, $^3J_{HH}$ = 3.0 Hz, 1 H, SC*H*$_2$), 2.22 (td, $^2J_{HH}$ = 10.2, $^3J_{HH}$ = 3.0 Hz, 1 H, SC*H*$_2$), 1.97 (td, $^2J_{HH}$ = 10.2, $^3J_{HH}$ = 3.0 Hz, 1 H, SC*H*$_2$), 1.72 [s, 9 H, C(C*H*$_3$)$_3$], 1.66 [s, 9 H, C(C*H*$_3$)$_3$], 1.20 [s, 9 H, C(C*H*$_3$)$_3$], 1.19 [s, 9 H, C(C*H*$_3$)$_3$] ppm. $^{13}C\{^1H\}$ NMR ([D$_6$]benzene): δ = 166.55 (Ph-*C*1), 166.50 (Ph-*C*1′), 143.60 (Ph-*C*6), 143.15 (Ph-*C*6′), 138.05 (Ph-*C*4), 136.20 (Ph-*C*4′), 128.50 (Ph-*C*5), 128.13 (Ph-*C*5′), 126.33 (Ph-*C*3), 126.14 (Ph-*C*3′), 120.03 (Ph-*C*2), 118.93 (Ph-*C*2′), 50.50 [N(*C*H$_3$)$_2$], 37.87 (S*C*H$_2$), 37.80 (S*C*H$_2$), 35.75 [*C*(CH$_3$)$_3$], 35.64 [*C*(CH$_3$)$_3$], 34.58 [*C*(CH$_3$)$_3$], 34.48 [*C*(CH$_3$)$_3$], 31.62 [C(*C*H$_3$)$_3$], 31.60 [C(*C*H$_3$)$_3$], 29.85 [C(*C*H$_3$)$_3$], 29.80 [C(*C*H$_3$)$_3$] ppm. $C_{32}H_{50}ClNO_2S_2Ti$ (628.19): calcd. C 61.18, H 8.02, N 2.23; found C 61.63, H 7.73, N 2.22.

Typical Hydroamination Reaction Procedure: In the glovebox, a Teflon-valved NMR tube was charged with 5 mol-% or 10 mol-% of the imidotitanium complex (0.01 mmol or 0.02 mmol). Deuterated toluene (ca. 0.5 mL) was added via syringe. Then, 0.2 mmol of the substrate was added and the reaction mixture was shaken for a moment. The reaction was carried out at 150 °C and NMR spectra were recorded periodically.

Crystal Structure Determination of Complexes 1 and 5: X-ray diffraction measurements were performed on a Bruker AXS diffractometer with Mo-K_α radiation using ω-scans. Crystal parameters and result of the structure refinement are given in Table 3. Absorption corrections were carried out with the multi-scan method using SADABS.[11] The structures were solved by direct and Fourier difference methods (SIR-92)[12a] and refined (SHELXS-97)[12b] against all F^2 data. All non-hydrogen atoms were refined with anisotropic displacement parameters. Hydrogen atoms were included into calculated positions. For the graphical representation, the program ORTEP was used as implemented in the program system WinGX.[13]

Table 3. Crystallographic and data collection parameters for **1** and **5**.

Compound	**1**	**5**
Empirical formula	$C_{39}H_{58}N_2O_2S_2Ti{\cdot}C_5H_{12}$	2 $C_{32}H_{50}ClNO_2S_2Ti{\cdot}C_5H_{12}$
M_r	771.04	1328.55
Crystal system	monoclinic	triclinic
Space group	$P2_1/c$	$\bar{P}1$
a [Å]	18.237(3)	15.5137(11)
b [Å]	28.490(5)	15.9150(11)
c [Å]	9.4719(18)	17.9791(13)
α [°]		113.213(1)
β [°]	100.459(4)	96.392(1)
γ [°]		108.034(1)
V [Å^3]	4849.1(15)	3738.4(5)
Z	4	2
$D_{calcd.}$ [g·cm^{-3}]	1.056	1.180
T [K]	130(2)	110(2)
μ(Mo-K_α) [mm^{-1}]	0.295	0.441
F(000)	1672	1428
θ Range [°]	2.27–28.34	2.31–25.54
Number of reflections collected	66138	42238
Number of reflections observed [$I > 2\sigma(I)$]	8736	10962
Number of independent reflections (R_{int})	12100 (0.0575)	13971 (0.0464)
Data / restraints / parameters	12100 / 0 / 474	13971 / 0 / 778
Goodness-of-fit on F^2	1.054	1.033
R_1, wR_2 [$I > 2\sigma(I)$]	0.0725, 0.1995	0.0549, 0.1373
R_1, wR_2 (all data)	0.1009, 0.2191	0.0720, 0.1486
Largest difference in peak and hole [e·Å^{-3}]	1.757 and –0.431	1.463 and –1.009

CCDC-704368 (for **1**) and -704369 (for **5**) contain the supplementary crystallographic data for this paper. These data can be obtained free of charge from The Cambridge Crystallographic Data Centre via www.ccdc.cam.ac.uk/data_request/cif.

Acknowledgments

We thank the Deutsche Forschungsgemeinschaft (DFG) and the Fonds der Chemischen Industrie for financial support. K. C. H. was a DFG Emmy Noether fellow (2001–2007). We are also grateful to Mr. Y.-T. Wang for collecting crystallographic data and to Prof. U. Englert for helpful discussions.

[1] a) F. Pohlki, S. Doye, *Chem. Soc. Rev.* **2003**, *32*, 104–114; b) P. W. Roesky, T. E. Müller, *Angew. Chem. Int. Ed.* **2003**, *42*, 2708–2710; c) J. F. Hartwig, *Pure Appl. Chem.* **2004**, *76*, 507–516; d) S. Hong, T. J. Marks, *Acc. Chem. Res.* **2004**, *37*, 673–686; e) K. C. Hultzsch, *Adv. Synth. Catal.* **2005**, *347*, 367–391; f) K. C. Hultzsch, *Org. Biomol. Chem.* **2005**, *3*, 1819–1824; g) F. Pohlki, S. Doye, *Chem. Soc. Rev.* **2007**, *36*, 1407–1420; h) I. Aillaud, J. Collin, J. Hannedouche, E. Schulz, *Dalton Trans.* **2007**, 5105–5118; i) T. E. Müller, K. C. Hultzsch, M. Yus, F. Foubelo, M. Tada, *Chem. Rev.* **2008**, *108*, 3795–3892.

[2] a) L. Ackermann, L. T. Kaspar, C. J. Gschrei, *Org. Lett.* **2004**, *6*, 2515–2518; b) D. V. Gribkov, K. C. Hultzsch, *Angew. Chem. Int. Ed.* **2004**, *43*, 5542–5546; c) P. D. Knight, I. Munslow, P. N. O'Shaughnessy, P. Scott, *Chem. Commun.* **2004**, 894–895; d) H. Kim, P. H. Lee, T. Livinghouse, *Chem. Commun.* **2005**, 5205–5207; e) J. A. Bexrud, J. D. Beard, D. C. Leitch, L. L. Schafer, *Org. Lett.* **2005**, *7*, 1959–1962; f) D. A. Watson, M. Chiu, R. G. Bergman, *Organometallics* **2006**, *25*, 4731–4733; g) A. V. Lee, L. L. Schafer, *Organometallics* **2006**, *25*, 5249–5254; h) H. Kim, Y. K. Kim, J. H. Shim, M. Kim, M. Han, T. Livinghouse, P. H. Lee, *Adv. Synth. Catal.* **2006**, *348*, 2609–2618; i) B. D. Stubbert, T. J. Marks, *J. Am. Chem. Soc.* **2007**, *129*, 6149–6167; j) M. C. Wood, D. C. Leitch, C. S. Yeung, J. A. Kozak, L. L. Schafer, *Angew. Chem. Int. Ed.* **2007**, *46*, 354–358; k) J. A. Bexrud, C. Li, L. L. Schafer, *Organometallics* **2007**, *26*, 6366–6372; l) K. Marcseková, C. Loos, F. Rominger, S. Doye, *Synlett* **2007**, 2564–2568; m) S. Majumder, A. L. Odom, *Organometallics* **2008**, *27*, 1174–1177; n) K. Gräbe, F. Pohlki, S. Doye, *Eur. J. Org. Chem.* **2008**, 4815–4823; o) C. Müller, W. Saak, S. Doye, *Eur. J. Org. Chem.* **2008**, 2731–2739.

[3] a) C. Capacchione, A. Proto, H. Ebeling, R. Mülhaupt, K. Möller, T. P. Spaniol, J. Okuda, *J. Am. Chem. Soc.* **2003**, *125*, 4964–4965; b) C. Capacchione, R. Manivannan, M. Barone, K. Beckerle, R. Centore, L. Oliva, A. Proto, A. Tuzi, T. P. Spaniol, J. Okuda, *Organometallics* **2005**, *24*, 2971–2982; c) K. Beckerle, R. Manivannan, T. P. Spaniol, J. Okuda, *Organometallics* **2006**, *25*, 3019–3026; d) K. Beckerle, R. Manivannan, B. Lian, G.-J. M. Meppelder, G. Raabe, T. P. Spaniol, H. Ebeling, F. Pelascini, R. Mülhaupt, J. Okuda, *Angew. Chem. Int. Ed.* **2007**, *46*, 4790–4793; e) B. Lian, K. Beckerle, T. P. Spaniol, J. Okuda, *Angew. Chem. Int. Ed.* **2007**, *46*, 8507–8510; f) B. Lian, T. P. Spaniol, J. Okuda, *Organometallics* **2007**, *26*, 6653–6660; g) G.-J. M. Meppelder, K. Beckerle, R. Manivannan, B. Lian, G. Raabe, T. P. Spaniol, J. Okuda, *Chem. Asian J.* **2008**, *3*, 1312–1323.

[4] a) C. Capacchione, A. Proto, V. Venditto, J. Okuda, *Macromolecules* **2003**, *36*, 9249–9251; b) C. Capacchione, M. D'Acunzi, O. Motta, L. Oliva, A. Proto, J. Okuda, *Macromol. Chem. Phys.* **2004**, *205*, 370–373; c) C. Capacchione, A. Proto, J. Okuda, *J. Polym. Sci., Part A: Polym. Chem.* **2004**, *42*, 2815–2822; d) C. Capacchione, F. De Carlo, C. Zannoni, J. Okuda, A. Proto, *Macromolecules* **2004**, *37*, 8918–8922; e) C. Capacchione, A. Proto, H. Ebeling, R. Mülhaupt, J. Okuda, *J. Polym. Sci., Part A: Polym. Chem.* **2006**, *44*, 1908–1913; f) C. Capacchione, A. Avagliano, A. Proto, *Macromolecules* **2008**, *41*, 4573–4575; g) B. T. Gall, F. Pelascini, H. Ebeling, K. Beckerle, J. Okuda, R. Mülhaupt, *Macromolecules* **2008**, *41*, 1627–1633.

[5] A. J. Blake, P. E. Collier, S. C. Dunn, W.-S. Li, P. Mountford, O. V. Shishkin, *J. Chem. Soc., Dalton Trans.* **1997**, 1549–1558.

[6] a) A. R. Johnson, W. M. Davis, C. C. Cummins, *Organometallics* **1996**, *15*, 3825–3835; b) R. Kempe, P. Arndt, *Inorg. Chem.* **1996**, *35*, 2644–2649; c) H. Fuhrmann, S. Brenner, P. Arndt, R. Kempe, *Inorg. Chem.* **1996**, *35*, 6742–6745; d) L. T. Armistead, P. S. White, M. R. Gagné, *Organometallics* **1998**, *17*, 216–220; e) M. R. Mason, B. N. Fneich, K. Kirschbaum, *Inorg. Chem.* **2003**, *42*, 6592–6594.

[7] a) I. Bytschkov, S. Doye, *Tetrahedron Lett.* **2002**, *43*, 3715–3718; b) C. Li, R. K. Thomson, B. Gillon, B. O. Patrick, L. L. Schafer, *Chem. Commun.* **2003**, 2462–2463.

[8] For a review on the *gem*-dialkyl effect see: M. E. Jung, G. Pizzi, *Chem. Rev.* **2005**, *105*, 1735–1766.

[9] E. Benzing, W. Kornicker, *Chem. Ber.* **1961**, *94*, 2263–2267.

[10] a) Y. Li, T. J. Marks, *J. Am. Chem. Soc.* **1996**, *118*, 9295–9306; b) S. Hong, S. Tian, M. V. Metz, T. J. Marks, *J. Am. Chem. Soc.* **2003**, *125*, 14768–14783; c) C. F. Bender, R. A. Widenhoefer, *J. Am. Chem. Soc.* **2005**, *127*, 1070–1071; d) Y. Tamaru, M. Hojo, H. Higashimura, Z.-I. Yoshida, *J. Am. Chem. Soc.* **1988**, *110*, 3994–4002.

[11] Siemens, *ASTRO, SAINT and SADABS. Data Collection and Processing Software for the SMART System*, Siemens Analytical X-ray Instruments Inc., Madison, Wisconsin, USA, **1996**.

[12] a) A. Altomare, G. Cascarano, C. Giacovazzo, A. Guagliardi, *J. Appl. Crystallogr.* **1993**, *26*, 343–350; b) G. M. Sheldrick, *SHELXL-97*, A Program for Crystal Structure Refinement, University of Göttingen, Germany, **1997**.

[13] L. J. Farrugia, *J. Appl. Crystallogr.* **1999**, *32*, 837.

Received: October 6, 2008
Published Online: December 15, 2008

DOI: 10.1002/ejic.200801039

Magnetic Field Effects on the Formation and Properties of Nickel Nanostructures

Lixia Sun[a] and Qianwang Chen*[a]

Keywords: Reaction conditions / Nickel / Nanostructures / Microwave absorption / Magnetic properties

A facile solvothermal hydrazine reduction route was designed for the synthesis of shape-controlled one-dimensional (1D) nickel wires in the presence of magnetic fields. The reaction conditions involved were studied systematically to select the optimal reaction parameters to reveal the effects of weak magnetic fields on the formation and properties of nickel nanostructures. The magnetic-field-dependent formation of 1D nickel wires indicated that the reduction of nickel ions with concentration less than 0.21 M preferentially occurs along the magnetic line of force, leading to the formation of uniform 1D wires, whereas higher concentrations could lead to quick reaction in the whole system and formation of isolated particles coexisting with wires composed of microspheres formed along the magnetic line of force. The improved magnetic properties of the sample formed in a magnetic field relative to those of samples formed without an applied field may be due to variation of the magnetic domain structure in the 1D nickel wires. Moreover, it was found that microwave absorption of a 1D nickel wire/poly(methyl methacrylate) (PMMA) composite at 8.5–12.5 GHz was evidently enhanced relative to that of a nickel microsphere/PMMA composite, which indicates that the anisotropic wires are not simply an assembly of particles, but that the magnetic domain structures in wires has been changed by the applied field.

Introduction

In recent years, control of the morphology of nanomaterials has been of great interest because of their intimately morphology-dependent properties as well as other properties and potential applications such as in nanoelectronics, photonics, catalysis, and magnetics.[1–5] Exploration of various shape-controlling synthetic methods and studies of their unusual properties will inevitably drive the progress in nanotechnology.[6] Nickel nanocrystals have been extensively investigated over the past decades because of their physical properties and diverse applications in the fields of catalysis, magnet recording, medical diagnosis, and conduction.[7] Many differently shaped nickel nanocrystals, including nanotubes, hollow spheres, and nanobelts, have been successfully created and their properties and applications found to depend on their morphology.[8] It is well known that 1D nickel nanostructures have attracted intense interest owing to their potential applications in magnetic sensors and memory devices.[9–11] Therefore, it is significant to synthesize 1D nickel wires with novel properties. Different 1D nickel nanostructures have been synthesized by various methods.[12–14] Currently, the fabrication of nickel nanowires mainly depends on a template technique that involves electrochemical deposition or metal–organic chemical vapor deposition (CVD) of metals into the nanopores of template materials, such as anodic alumina (AAO) film[15] and carbon nanotubes.[16] However, to date little work has been reported on the controllable synthesis of 1D nickel wires by use of magnetic fields in a solution system. Such a solution-phase approach may provide a more promising technique for preparing 1D nanostructures than conventional methods in terms of cost and potential for large-scale production.[17] Herein, we report the synthesis of shape-controlled 1D nickel wires under a magnetic field in mixed water/ethanol solvents.

Recently, some researchers reported that paramagnetic ions are attracted toward the maximum field, and an applied magnetic field could increase the rate of diffusion of paramagnetic ions such as Fe^{3+}, Cu^{2+}, Co^{2+}, and Ni^{2+}, as well as paramagnetic gases, such as O_2 in the water phase.[18–20] Such reports were further confirmed by our study that an external magnetic field could accelerate the oxidization process of the ferrous hydroxide when exposed to ambient air.[21] Recently, we reported that the magnetic fields applied during the chemical reduction of nickel ions can synchronously influence both the nucleation and the

[a] Hefei National Laboratory for Physical Sciences at Microscale and Department of Materials Science & Engineering, University of Science and Technology of China
Hefei 230026, P. R. China
Fax: +86-551-3607292
E-mail: cqw@ustc.edu.cn

Supporting information for this article is available on the WWW under http://www.eurjic.org or from the author.

parallel growth of nickel.[22] In this work, to investigate the effects of weak magnetic fields on the formation and properties of nickel nanostructures, systematical experiments were conducted to search for the optimal reaction parameters, and the microwave absorption of a nickel/poly(methyl methacrylate) (PMMA) composite at 8.5–12.5 GHz was also investigated.

Results and Discussion

Preparation without a Magnetic Field

With the aim of selecting an optimal reaction system in which to investigate the effects of weak magnetic fields on the formation and properties of nickel nanostructures, we firstly conducted systematical experiments without a magnetic field to determine the parameters that are important for the formation of nickel nanostructures with ideal shapes.

The Effect of Reactant Concentration of PVP

It is well known that the surfactant polyvinylpyrrolidone (PVP, K-30) is efficient in preventing the nanoparticles from aggregating; this effect could largely depend on the steric effect arising from the long polyvinyl chain of PVP on the surface of the growing particles.[23] Because the steric effect is largely determined by the covered fraction of PVP on the surface of the particles, the quantity of PVP, should be an important factor in determining the shape of the final product. To understand the effects of PVP on the shape of nickel particles, a contrasting experiment without PVP was carried out. In the absence of PVP, the product comprised irregular particles (Figure 1a). Even when the aging time was prolonged, the morphology of the product was still preserved. When 1.4 mM PVP was introduced into the reaction system, some nanospheres began to emerge in the obtained product (Figure 1b). When an appropriate concentration (1.8–3.2 mM) of PVP was introduced into the reaction system, the product consisted of uniform microspheres (Figure 1c). However, if the concentration of PVP was increased to 3.6 mM, the sample was composed of size-discrepant microspheres. On the basis of these experimental results, it was concluded that the presence of an appropriate amount of polymer PVP played a crucial role in the formation of uniform nickel nanostructures.

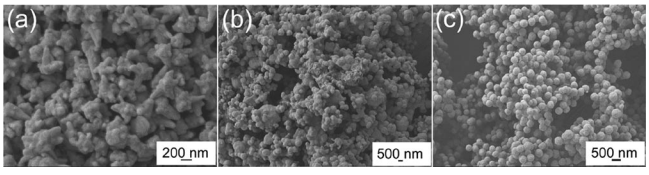

Figure 1. SEM images of samples prepared without a magnetic field by the same synthesis procedure as described in the Experimental Section except with different concentrations of PVP: (a) 0, (b) 1.4 mM, (c) 2.3 mM.

The Effect of the Volume Ratio of H_2O/Ethanol (ω)

Mixed solvents have been used as reaction media to produce inorganic crystals with different shapes.[24] The ethanol/water system was introduced herein to study the effect of mixed solvents on the morphology of nickel nanostructures. In pure water, flowerlike nanostructures, which comprise dozens of nanopetals, are formed (Figure 2a). Treatment of the sample with ultrasound for 10 min did not break this nanostructure into discrete particles, indicating that the nanoflowers were actually integrated and were not just aggregates of spherical and petallike particles. However, these petals gradually shortened and developed into nanospheres in the presence of some ethanol in the solution (Figure 2b,c,d). When the H_2O/ethanol ratio ω decreases to 1:1, uniform spherical particles were obtained (Figure 2e). The optimal ω value for preparing uniform microspheres is between 1:1 and 1:14. Therefore, use of a suitable volume ratio of H_2O/ethanol (ω) is extremely critical for the formation of uniform nickel nanostructures. For the present reaction, the superfluous hydrazine would decompose into ammonia at the reaction temperature of the system, so the basic medium was attributed to the ionization of ammonium hydroxide in the solution. The influence of the dielectric constant of the solvent upon the ionization of the electrolytes has been studied for many years, and the relation that attempts to express, in a semiquantitative manner, the influence of the solvent on the ionization of an electrolyte is given by Equation (1).[25]

$$\frac{K_1}{K_2} = \frac{{\varepsilon_1}^3}{{\varepsilon_2}^3} \quad (1)$$

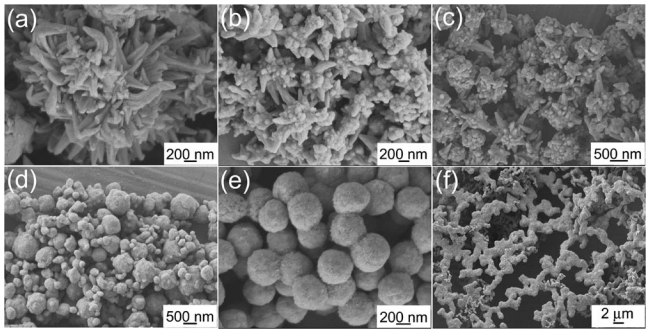

Figure 2. SEM images of samples prepared without a magnetic field by the same synthesis procedure as described in the Experimental Section except with different volume ratios of H_2O/ethanol (ω): (a) pure water, (b) ω = 7:1, (c) ω = 3:1, (d) ω = 5:3, (e) ω = 1:1, (f) pure ethanol.

In this expression, K_1 and K_2 are the ionization constants of an electrolyte in two media of dielectric constants ε_1 and ε_2, respectively. According to the literature,[26] the value of ε is greater for water than for ethanol. Moreover, the ε value decreases as the volume ratio of H_2O/ethanol (ω) decreases. Thus, the ionization of ammonium hydroxide would change with different ω values, leading to different base concentrations. As the value of ω decreases, the ionization of ammonium hydroxide would be decreased as a result of the

smaller dielectric constant of the solution, leading to the lower base concentration. The amounts of hydrazine were fixed in parallel experiments, so by adjusting the volume ratio of H_2O/ethanol (ω), the base concentration was correspondingly changed. It has been reported that a basic medium can increase the reducing power of hydrazine.[27] It can be seen in Figure 2 that with a decrease in ω, that is, a lower concentration of base, the morphology gradually changes from nanoflowers into spherical particles. A lower base concentration results in a relatively slow reaction rate, and then surfactant PVP can provide sufficient protection to the nickel particles, which facilitates the formation of uniform spherical particles. In contrast, the fast reaction rate produced at high base concentrations only leads to bigger flowerlike nanostructures. However, when ω was decreased to zero, the base concentration was so low that reaction was incomplete and the small quantity of the product might be combined with the long chains of PVP (Figure 2f).

The Effect of Reaction Temperature (T)

The shape of nickel nanostructures can be controlled by adjusting the particle growth rate by varying the temperature. Higher temperatures and concomitantly enhanced growth rates usually favor the formation of spherical particles as a result of less selective crystallographic growth direction.[28] The effect of temperature on the morphology of products was also studied. In the present system, it was found that the nickel nanostructures could not be obtained below 90 °C. Figure 3 shows samples obtained at various temperatures. It can be observed that the reaction temperature caused some differences in the shapes of products. The nanopetals of flowerlike nanospheres gradually shortened and congregated when the reaction temperature was elevated, as shown in Figure 3a, b, and c. At 150 °C, uniform smooth nickel microspheres were synthesized (Figure 1c). However, when the temperature was increased to 200 °C, some irregular particles emerged in the as-prepared product (Figure 3d), because the steric effect of PVP may be decreased with increasing temperature.

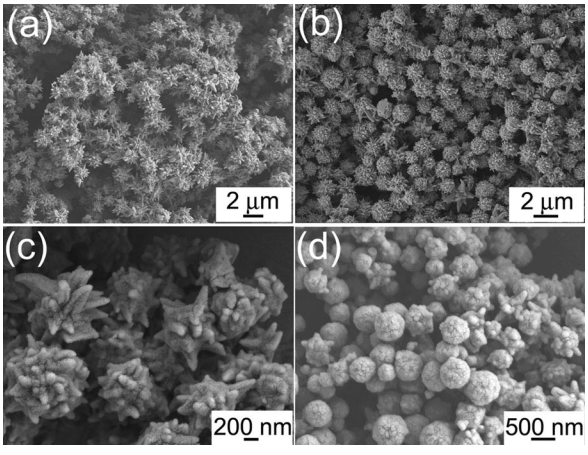

Figure 3. SEM images of samples prepared without a magnetic field by the same synthesis procedure as described in the Experimental Section except with different reaction temperatures (T): (a) 95 °C, (b) 110 °C, (c) 130 °C, (d) 200 °C.

The Effect of Reactant Concentration of Ni^{2+} (C)

The samples used to study the effect of concentration of Ni^{2+} (C) on particle morphology are shown in Figure 4, which reveals that the size of nickel particles increases with an increase in C. The formation of nickel nanoparticles follows the nucleation-growth mechanism, and the particle size principally depends on their nucleation rate and growth rate. If the nucleation rate of a particle is faster than the growth rate, its size is usually smaller; contrarily, if the growth rate is faster then the nucleation rate, its size is larger.[29] When C was low, the nucleation rate of nickel nanoparticles was faster than their growth rate because their growth was limited by the low value of C; therefore, the particle size synthesized at lower C values was correspondingly smaller. However, smaller nickel nanoparticles obtained at lower C values tend to aggregate together to reduce the surface energy, so there are more aggregative particles in Figure 4a than in Figure 4b. As C increased, their growth rate became faster; as a result their size increased. It was observed that uniform microspheres with an average diameter of 300 nm were prepared with 0.10 M Ni^{2+} (Figure 1c), whereas larger microspheres with an average diameter of 600 nm were obtained with 0.21 M Ni^{2+} (Figure 4c).

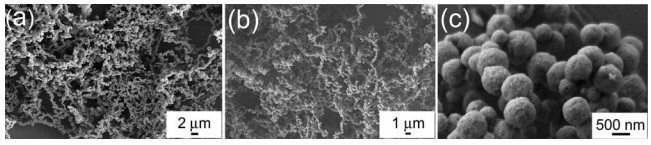

Figure 4. SEM images of samples prepared without a magnetic field by the same synthesis procedure as described in the Experimental Section except with different concentrations of Ni^{2+}: (a) 0.035 M, (b) 0.07 M, (c) 0.21 M.

Reaction time is also a parameter that influences the preparation of the final product in the present route. When the reaction time is less than 1 h, the reaction is quite incomplete. To obtain a large quantity of uniform nanostructures, the optimal reaction time is between 10 and 16 h.

Preparation under Magnetic Fields

After the study of several control experiments performed without a magnetic field, it could be deduced that 1D nickel wires with controlled shapes can be obtained by the use of a magnetic field in the above-mentioned reaction systems. For example, in contrast to the thornlike microspheres (Figure 3b), 1D thornlike wires were prepared with 0.10 M Ni^{2+} at 110 °C when a 0.25 T field was applied (Figure 5c). However, to synthesize uniform 1D wires, the proper reaction conditions were required, such as a concentration of Ni^{2+} less than 0.21 M, and so forth. For example, 1D uniform wires (labeled as AF) with lengths up to several hundreds of micrometers were obtained with 0.10 M Ni^{2+} under a

0.25 T field (Figure 5a,b), whereas spherical particles (labeled as ZF) were prepared in the absence of a magnetic field (Figure 1c). Figure 6 shows XRD patterns of ZF and AF samples. All of the peaks can be well indexed as face-centered-cubic Ni, which is consistent with the standard card (JCPDS 01–1260). No other peaks of impurities, such as nickel oxide or nickel hydroxide, could be detected, which implies that phase-pure cubic nickel can be obtained under the current synthesis conditions. The intensity ratio of the (111) peak to the (200) peak of the AF sample increased relative to that of the ZF sample, indicating a preferential orientation of nickel grains in the 1D wires, which suggested that the nucleation and growth of nickel crystallites could be influenced by a magnetic field. Moreover, the wires of the AF sample show high stability; even intensive ultrasonic treatment could not destroy them, which indicates that the wire is not a loose aggregate of spherical nanocrystals but an integrated structure. However, when the concentration of Ni^{2+} was more than 0.21 M, it was observed that isolated particles and wires composed of microspheres that formed along the magnetic line of force coexisted in the as-prepared product (shown in Figure S1 in the Supporting Information).

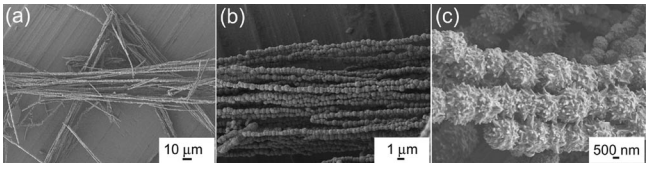

Figure 5. SEM images of samples prepared at different conditions with a 0.25 T magnetic field applied: (a) with 0.10 M Ni^{2+} at 150 °C; (b) high-magnification image of sample in (a); (c) with 0.10 M Ni^{2+} at 110 °C. The other synthesis procedures were the same as described in the Experimental Section.

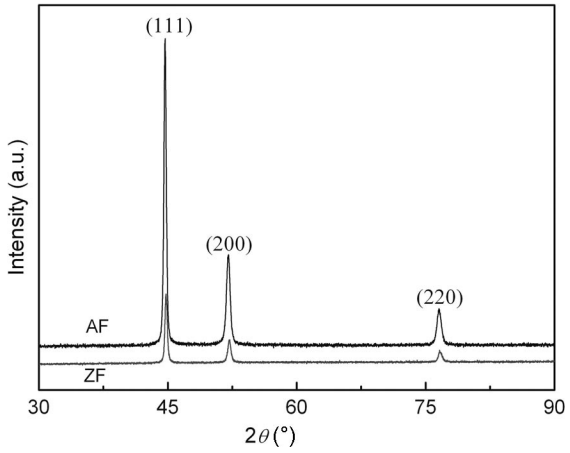

Figure 6. XRD patterns of ZF and AF samples.

According to the observed results and experimental parameters, the formation of our 1D nickel wires can be ascribed to the cooperative effect of the reaction rate, inherent magnetic interactions, and magnetic line of force. The reaction rate in the system is controlled mainly by adjusting the reactant concentration when other reaction conditions are fixed. When the concentration of Ni^{2+} is low, the reaction rate is correspondingly slow, so the complex $[Ni(N_2H_4)_x]^{2+}$ preferentially migrates to the magnetic line of force since paramagnetic metal ions are attracted toward the maximum field.[18] Then the chemical reduction of $[Ni(N_2H_4)_x]^{2+}$ may occur along the magnetic line of force, leading to the formation of uniform 1D wires, as shown in Figure 5a,b. An increase in the concentration of Ni^{2+} increases the reaction rate also, so it can be deduced that the chemical reduction of $[Ni(N_2H_4)_x]^{2+}$ takes place quickly in the whole system, leading to the formation of isolated particles coexisting with wires composed of microspheres formed along the magnetic line of force, as shown in Figure S1 in the Supporting Information. So it is suggested that the lower concentration of magnetic metal ions favors the chemical reduction of $[Ni(N_2H_4)_x]^{2+}$ along the magnetic line of force and the formation of uniform 1D wires.

The magnetic properties of nanomaterials are believed to be closely related to sample structure, crystallinity, and magnetization direction. The *M*–*H* hysteresis loops combined with an expanded low-field hysteresis curve of the ZF and AF samples measured at 300 K are shown in Figure 7. The value of M_s for the AF sample (M_s = 55 emu/g) is larger than that for the ZF sample (M_s = 52 emu/g). Moreover, the AF sample exhibits significantly enhanced coercivity (H_c = 110 Oe) relative to that of the ZF sample (H_c = 80 Oe) (inset of Figure 7). The improved magnetic properties of the AF sample relative to those of the ZF sample may be due to the magnetic domain structure variation in 1D nickel wires. It is known that the microwave absorption of magnetic materials is closely related to the magnetic structures. Thus, the microwave absorption of 1D nickel wire/PMMA composite and nickel microsphere/PMMA composite were also investigated to reveal possible variation of magnetic domain structure caused by magnetic field in the chemical reaction. The relationship between microwave frequency and reflection loss of the composites was measured by a vector network analyzer. The sample backed by an aluminum substrate (20 mm × 30 mm) was set at the end of waveguide, and the waveguide-fed rectangular aperture was sealed. The electromagnetic waves propagated perpendicular to the sample surface. Assuming the electromagnetic waves propagate without radiation in the waveguide, the reflection coefficient was measured in the frequency range from 8.5 to 12.5 GHz. For comparison, a sample of pure polymer matrix (2 mm) backed by an aluminum substrate was prepared, and its microwave absorption properties are presented in Figure S2 in the Supporting Information. The results show that the average reflection loss was lower than 3.0 dB, and no obvious loss peaks were found from 8.5 to 12.5 GHz, which excludes the possible loss mechanism of interference between incident and reflected waves in the waveguide. Schematic illustrations showing nickel/PMMA composites with magnetic alignments are shown in Figure 8. Most of the wires in the polymer matrix would be aligned in parallel to the vertical magnetic field owing to the magnetic induction (Figure 8b), whereas a few short chains might be formed along the field (Figure 8a). Figure 9

shows the microwave absorption of nickel/PMMA composites with the same thickness (2.0 mm) and nickel proportion (10 wt%) with magnetic alignment. The results show that the average reflection loss of nickel microsphere/PMMA sample was lower than 2.0 dB, and no obvious loss peaks were found from 8.5 to 12.5 GHz (Figure 9a). While the microwave absorption of the 1D nickel wire/PMMA sample at 8.5–12.5 GHz was evidently improved, and the strongest loss peak intensity was 8.1 dB at 12.1 GHz (Figure 9b). The microwave absorption of magnetic materials has been partly ascribed to magnetic loss, which is affected by the magnetic domains.[30] Accordingly, it can be deduced that the different microwave absorption of the two nickel composites would arise from the different interior magnetic domain structures. Thus, it can be deduced that 1D nickel wires were not simply an assembly of particles, but that the applied field in the chemical reaction changed the magnetic domain structures in the wires. Therefore, it is expected that a weak magnetic field could be developed as an important tool to control the structure and properties of materials, especially magnetic materials. Our understanding of the effects of magnetic fields on the formation and properties of magnetic nanostructures is still limited, and further investigation is in progress.

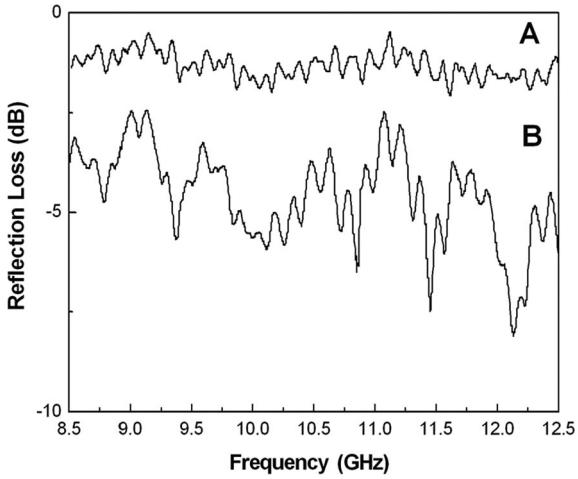

Figure 9. Microwave absorption characteristics at 8.5–12.5 GHz band of nickel composites with the same thickness (2.0 mm) and proportion (10 wt%): (a) nickel microspheres in PMMA; (b) nickel wires in PMMA.

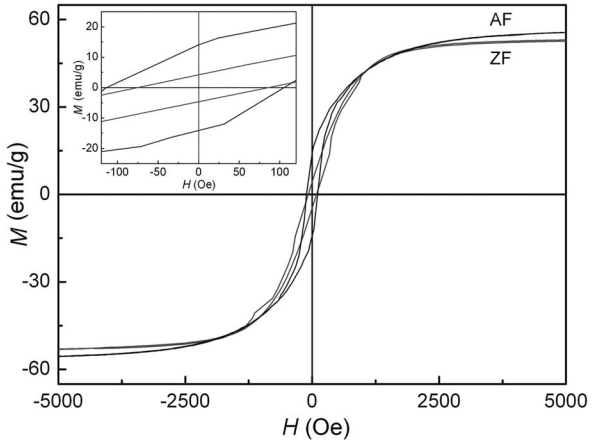

Figure 7. Hysteresis loops measured at 300 K for the ZF and AF samples. The upper left inset is an expanded low-field hysteresis curve.

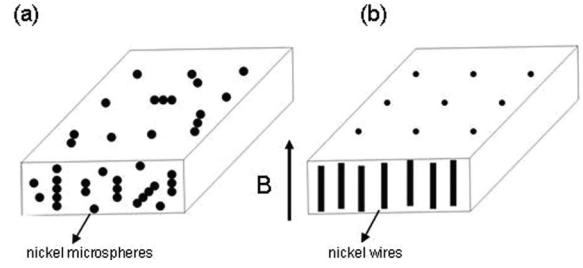

Figure 8. Schematic illustrations showing nickel composites with the same thickness (2.0 mm) and nickel proportion (10 wt%) with magnetic alignment under a magnetic field: a) nickel microspheres in PMMA; b) nickel wires in PMMA. The black arrow indicates the magnetic field direction.

Conclusions

In summary, investigations of the magnetic-field-dependent synthesis of shape-controlled 1D nickel wires demonstrated that the formation and properties of nickel nanostructures could be influenced by the magnetic fields under proper reaction conditions. The reduction of Ni^{2+} with concentration less than 0.21 M preferentially occurs along the magnetic line of force, leading to the formation of uniform 1D wires, whereas higher concentration led to quick reaction in the whole system and the formation of isolated particles coexisting with wires composed of microspheres formed along the magnetic line of force. The improved magnetic properties of the AF sample compared with those of the ZF sample may be due to the magnetic domain structure variation in 1D nickel wires. Moreover, the enhanced microwave absorption properties of the nickel wire/PMMA composite at 8.5–12.5 GHz relative to that of the nickel microsphere/PMMA composite indicates that the anisotropic wires are not simply an assembly of particles, and the magnetic domain structures in the wires has been changed by the applied field in the chemical reaction. Such a novel and facile strategy is being further explored for the synthesis of other magnetic materials under controlled conditions to improve the properties of magnetic materials.

Experimental Section

In our experiments, all reagents were of analytical grade and were used without further purification. A typical experiment for the preparation of nickel wires (labeled as AF) is as follows: $NiCl_2$ (3.5 mmol) was dissolved in a mixture of ethanol (22 mL) and distilled water (13 mL) to give a green solution, and then polyvinyl-

pyrrolidone (PVP, K-30) (0.08 mmol) was added with stirring. Subsequently, 85 wt% hydrazine hydrate (7.0 mL) was added dropwise into the solution. The solution was vigorously stirred for 40 min, transferred into a teflon-lined stainless steel autoclave (60 mL capacity) with a 0.25 T applied magnetic field, and then heated to and maintained at 150 °C. After 12 h, the autoclave was cooled naturally to room temperature. The black product was separated and washed with ethanol several times and then dried in a vacuum oven at 50 °C for 4 h. A typical experiment for the preparation of nickel microspheres (labeled as ZF) is as follows: The synthesis procedures were similar to that of nickel wires except without a magnetic field applied.

For the characterization of microwave absorption properties, poly(methyl methacrylate) (5.0 g) was dissolved in pure cyclopentanone (30 mL) to make a polymer solution, and meanwhile 1D nickel wires (0.50 g) were dispersed in cyclopentanone (15 mL). The solution of PMMA/cyclopentanone and the stable suspension of nickel wire/cyclopentanone were then mixed and ultrasonically agitated for 15 min to ensure that the nickel wires were dispersed homogeneously in the polymer solution. The as-prepared solution was poured into a mold, which was placed at the center of a 0.20 T vertical magnetic field, and then the solvent was slowly evaporated. Finally, the dried sample was removed from the mold for the later investigation of microwave absorption properties. Similarly, an equivalent nickel microsphere/PMMA composite was prepared by the same procedures as those for the nickel wire/PMMA composite. The samples obtained were characterized by X-ray diffraction (XRD) with a Rigaku (Japan) D/max-γ A X-ray diffractometer equipped with graphite monochromatized Cu-K_α radiation (λ = 1.5418 Å). Field emission scanning electron microscopy (FESEM) was performed with a JEOL JSM–6700F apparatus. The reflection loss of the sample backed with an aluminum substrate was characterized by an Agilent-8722ES vector network analyzer in the range 8.5–12.5 GHz. Magnetic studies were carried out with a vibrating sample magnetometer on a Quantum Design Physical Properties Measurement System (PPMS-9T).

Supporting Information (see footnote on the first page of this article): SEM image of the product prepared with a high concentration of Ni^{2+}, and microwave absorption curves of pure polymer matrix.

Acknowledgments

This work was supported by the National Natural Science Foundation of China (No. 10774138).

[1] A. P. Alivisatos, *Science* **1996**, *271*, 933.
[2] C. B. Murray, D. J. Norris, M. G. Bawendi, *J. Am. Chem. Soc.* **1993**, *115*, 8706.
[3] V. F. Puntes, K. M. Krishnan, A. P. Alivisatos, *Science* **2001**, *291*, 2115.
[4] R. Heitz, S. Rodt, A. Schliwa, D. Bimberg, *Phys. Status Solidi B* **2003**, *238*, 273.
[5] R. Narayanan, M. A. El-Sayed, *Nano Lett.* **2004**, *4*, 1343.
[6] X. M. Ni, Q. B. Zhao, H. G. Zheng, B. B. Li, J. M. Song, D. E. Zhang, X. J. Zhang, *Eur. J. Inorg. Chem.* **2005**, 4788.
[7] a) W. X. Zhang, C. B. Wang, H. L. Lien, *Catal. Today* **1998**, *40*, 387; b) M. P. Pileni, *Adv. Funct. Mater.* **2001**, *11*, 323; c) R. Hernandez, S. Polizu, S. Turenne, L. Yahia, *Bio-Med. Mater. Eng.* **2002**, *12*, 37; d) A. Smogunov, A. Dal Corso, E. Tosatti, *Surf. Sci.* **2002**, *507*, 609.
[8] a) H. Q. Cao, L. D. Wang, Y. Qiu, Q. Z. Wu, G. Z. Wang, L. Zhang, X. W. Liu, *ChemPhysChem* **2006**, *7*, 1500; b) J. C. Bao, Y. Y. Liang, Z. Xu, L. Si, *Adv. Mater.* **2003**, *15*, 1832; c) Z. P. Liu, S. Li, Y. Yang, S. Peng, Z. K. Hu, Y. T. Qian, *Adv. Mater.* **2003**, *15*, 1946.
[9] Z. K. Wang, M. H. Kuok, S. C. Ng, D. J. Lockwood, M. G. Cottam, K. Nielsch, R. B. Wehrspohn, U. Gösele, *Phys. Rev. Lett.* **2002**, *89*, 027201.
[10] L. Sun, P. C. Searson, C. L. Chien, *Appl. Phys. Lett.* **2001**, *79*, 4429.
[11] S. Pignard, G. Goglio, A. Radulescu, L. Piraux, S. Dubois, A. Declemy, J. L. Duvail, *J. Appl. Phys.* **2000**, *87*, 824.
[12] J. Joo, S. J. Lee, D. H. Park, Y. S. Kim, Y. Lee, C. J. Lee, S. R. Lee, *Nanotechnology* **2006**, *17*, 3506.
[13] N. Cordente, M. Respaud, F. Senocq, M. J. Casanove, C. Amiens, B. Chaudret, *Nano Lett.* **2001**, *1*, 565.
[14] J. C. Bao, C. Y. Tie, Z. Xu, Q. F. Zhou, D. Shen, Q. Ma, *Adv. Mater.* **2001**, *13*, 1631.
[15] K. Nielsch, R. B. Wehrspohn, J. Barthel, J. Kirschner, S. F. Fischer, H. Kronmuller, T. Schweinbock, D. Weiss, U. Gosele, *J. Magn. Magn. Mater.* **2002**, *249*, 234.
[16] B. K. Pradhan, T. Kyotani, A. Tomita, *Chem. Commun.* **1999**, *14*, 1317.
[17] a) B. Gates, B. Mayers, B. Cattle, Y. N. Xia, *Adv. Funct. Mater.* **2002**, *12*, 219; b) X. Wang, Y. D. Li, *J. Am. Chem. Soc.* **2002**, *124*, 2880.
[18] K. Chie, M. Fujiwara, Y. Fujiwara, Y. Tanimoto, *J. Phys. Chem. B* **2003**, *107*, 14374.
[19] M. Fujiwara, K. Chie, J. Sawai, D. Shimizu, Y. Tanimoto, *J. Phys. Chem. B* **2004**, *108*, 3531.
[20] Y. Ikezoe, N. Hirota, J. Nakagawa, K. Kitazawa, *Nature* **1998**, *393*, 749.
[21] Z. M. Peng, J. Wang, Y. J. Huang, Q. W. Chen, *Chem. Eng. Technol.* **2004**, *27*, 1273.
[22] L. X. Sun, Q. W. Chen, Y. Tang, Y. Xiong, *Chem. Commun.* **2007**, 2844.
[23] a) Z. T. Zhang, B. Zhao, L. M. Hu, *J. Solid State Chem.* **1996**, *121*, 105; b) Y. G. Sun, Y. D. Yin, B. T. Mayers, T. Herricks, Y. N. Xia, *Chem. Mater.* **2002**, *14*, 4736.
[24] a) T. Ghoshal, S. Kar, S. Chaudhuri, *Cryst. Growth Des.* **2007**, *7*, 136; b) S. R. Dickinson, K. M. McGrath, *J. Mater. Chem.* **2003**, *13*, 928.
[25] F. Bradley, W. C. M. Lewis, *J. Phys. Chem.* **1925**, *29*, 782.
[26] G. Åkerlöf, *J. Am. Chem. Soc.* **1932**, *54*, 4125.
[27] X. M. Ni, Q. B. Zhao, Y. F. Zhang, H. G. Zheng, *Eur. J. Inorg. Chem.* **2007**, 422.
[28] R. T. Olesson, G. Salazar-Alvarez, M. S. Hedenqvist, U. W. Gedde, F. Lindberg, S. J. Savage, *Chem. Mater.* **2005**, *17*, 5109.
[29] W. G. Yu, T. L. Zhang, X. J. Qiao, J. G. Zhang, L. Yang, *Mater. Sci. Eng., B* **2007**, *136*, 101.
[30] P. Singh, V. K. Babbar, A. Razdan, R. K. Puri, T. C. Goel, *J. Appl. Phys.* **2000**, *87*, 4362.

Received: October 22, 2008
Published Online: December 16, 2008

DOI: 10.1002/ejic.200800980

The Reactions of Silver, Zirconium, and Hafnium Fluorides with Liquid Ammonia: Syntheses and Crystal Structures of $Ag(NH_3)_2F·2NH_3$, $[M(NH_3)_4F_4]·NH_3$ (M = Zr, Hf), and $(N_2H_7)F$

Florian Kraus,*[a] Sebastian A. Baer,[a] and Matthias B. Fichtl[a]

Keywords: Fluorides / Ammonia / Hafnium / Zirconium / Silver

By reaction of the tetrafluorides MF_4 or the ternary silver fluorides $Ag_3M_2F_{14}$ (M = Zr, Hf) with dry liquid ammonia at –40 °C, the pentaammoniates $[M(NH_3)_4F_4]·NH_3$ (**1**, M = Zr; **2**, M = Hf) were obtained, and these compounds represent hitherto unknown molecular inorganic Zr and Hf compounds that simultaneously bear nitrogen and fluorine ligands. The compounds crystallize isotypically in the shape of colorless needles in the tetragonal space group *P*4/*ncc*. As a further product $[NH_4(NH_3)]F$ (**3**) was isolated in the form of colorless cubes in the orthorhombic space group $Pca2_1$. It is the first ammoniate of ammonium fluoride. $Ag(NH_3)_2F·2NH_3$ (**4**) can be synthesized either from AgF or AgF_2 in liquid ammonia. The compound crystallizes merohedrally twinned in the orthorhombic space group *Pnna* and represents the first crystallographically characterized diamine silver(I) halide complex. In the latter two structures, free fluoride anions are encountered. The ammoniates are highly temperature-sensitive and decompose at temperatures above –30 °C due to their ammonia pressure.

Introduction

Solid fluorides in general show the highest lattice energies and hence lowest solubilities. Their solution chemistry is quite well known in aqueous solutions, hydrofluoric acid, or anhydrous HF.[1–5] We set out to explore the reactions of fluorides with liquid ammonia, which could yield substances like fluoride ammoniates, amine fluorides and amide- or imide fluorides,[6–9] or even nitride fluorides and nitrides as the final products of these reactions.[10] With the exception of the nitrides, all these classes of compounds are only scarcely known and could feature interesting properties depending on the metal ion.

Recently, we reported the reaction of blue-violet $Ag_3M_2F_{14}$ (M = Zr, Hf)[11,12] with liquid ammonia and established one product to be $[Ag(NH_3)_3(\mu\text{-}NH_3)Ag(NH_3)_4]MF_6$ (M = Zr, Hf) featuring Ag–Ag interactions.[6] Now we were able to identify the other products of this complex reaction by X-ray diffraction methods as $M(NH_3)_4F_4·NH_3$ (**1**, M = Zr; **2**, M = Hf) and $[NH_4(NH_3)]F$ (**3**). Compounds **1** and **2** can also be obtained from neat MF_4 (M = Zr, Hf) in liquid NH_3. Mixtures of AgF or AgF_2/MF_4 (M = Zr, Hf) in liquid ammonia gave the known product $[Ag(NH_3)_3(\mu\text{-}NH_3)Ag(NH_3)_4]MF_6$ (M = Zr, Hf),[6] the pentaammoniates $M(NH_3)_4F_4·NH_3$ (**1**, M = Zr; **2**, M = Hf) and $Ag(NH_3)_2F·2NH_3$ (**4**). When AgF_2 was used as the silver source we also found $[NH_4(NH_3)]F$ as a byproduct of the oxidation of ammonia.

[a] Department Chemie, Technische Universität München, Lichtenbergstr. 4, 85747 Garching
Fax: +49-89-289-13186
E-mail: florian.kraus@lrz.tum.de

Results and Discussion

In the redox reaction of blue-violet $Ag_3M_2F_{14}$ with liquid ammonia, colorless crystals of $[Ag(NH_3)_3(\mu\text{-}NH_3)Ag(NH_3)_4]MF_6$ (M = Zr, Hf) were obtained that feature Ag–Ag interactions.[6] The formal equation for this reaction can be written as:

$$2Ag_3M_2F_{14} + 32NH_3 \rightarrow 3Ag_2MF_6·8NH_3 + N_2 + 6NH_4F + MF_4 \quad (M = Zr, Hf)$$

$Ag_2MF_6·8NH_3\{[Ag(NH_3)_3(\mu\text{-}NH_3)Ag(NH_3)_4]MF_6\}$ was identified by single-crystal structure analysis at low temperature,[6] the evolution of nitrogen was observed during the reaction, and NH_4F was detected by X-ray powder diffraction after pumping off the liquid ammonia at room temperature. However, MF_4 could not be detected in the powder diffraction patterns of the reaction products; it is supposed that MF_4 is produced either as an amorphous material or that ammoniates are formed. After prolonged storage of the reaction vessel containing $Ag_3M_2F_{14}$ and liquid NH_3, we isolated crystals of the pentaammoniates of MF_4, that is, $M(NH_3)_4F_4·NH_3$ (**1**, M = Zr; **2**, M = Hf). Compounds **1** and **2** are also formed in the reaction of neat MF_4 with liquid ammonia within weeks.

In the crystal structures of **1** and **2**, the zirconium and hafnium atoms occupy the Wyckoff position 4*a* of the space group *P*4/*ncc*. The metal atoms show a coordination

number of eight in total. They are bisphenoidally coordinated by four symmetry-equivalent fluorine atoms F(1) (Wyckoff position 16*g*) and four molecules of ammonia, with the symmetry equivalent nitrogen N(1) atoms also in position 16*g* in a bisphenoidal way. The Zr–F and Hf–F distances of 2.036(2) and 2.043(5) Å and the Zr–N and Hf–N distances of 2.397(3) and 2.383(8) Å are in accord with distances known from the literature.[13] The coordination sphere of Zr and Hf is similar to a distorted square antiprism, whose corners are occupied by alternating ammonia molecules and fluorine atoms, resulting in discrete $M(NH_3)_4F_4$ units (M = Zr, Hf; Figure 1). An additional NH_3 molecule with the nitrogen N(2) atom is present in the 4*c* position. It is 4.476(1) or 4.483(3) Å away from the Zr or Hf atom, respectively, and may thus be regarded as a solvated NH_3 molecule. Because of the fourfold symmetry of this position, we were not able to localize the hydrogen atoms.

The $M(NH_3)_4F_4$ units are interconnected by hydrogen bonds in two formally different ways: First, a $^3_\infty[M(NH_3)_4F_4]$ network is generated through N(1)–H···F hydrogen bonds. The shortest and hence strongest N–H···F hydrogen bond forms $^1_\infty[M(NH_3)_4F_4]$ strands running along the *c* axis (Figure 2a), and the second N–H···F hydrogen bond leads to $^2_\infty[M(NH_3)_4F_4]$ layers parallel to the *ab* plane.

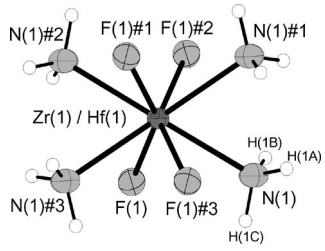

Figure 1. Projection of the $M(NH_3)_4F_4$ (M = Zr, Hf) unit present in **1** and **2**. Thermal ellipsoids are shown at the 70% probability level.

Thus, the $[M(NH_3)_4F_4]$ moieties are interconnected along the *ab* plane diagonals (Figure 2b). The second type of hydrogen bonds are of the N–H···N type: The solvated ammonia molecule with the nitrogen N(2) atom in the 4*c* position acts as an acceptor of four hydrogen bonds from symmetry-equivalent NH_3 molecules. This interconnection leads to a $^2_\infty[M(NH_3)_4F_4{\cdot}NH_3]$ layer parallel to the *ab* plane, which, in contrast to the above $^2_\infty[M(NH_3)_4F_4]$ layer, expands along the *a* and *b* axes (Figure 2c). Thus, all hydrogen atoms of the metal-bound ammonia molecules are involved in hydrogen bonding. From the N(2)···F distances of 2.994(2) Å in **1** and 2.997(6) Å in **2**, N–H···F hydrogen bonding must be inferred, which leads to $^3_\infty[N(2)\cdots F_4M(NH_3)_4]$ layers parallel to the *ab* plane.

The overall arrangement of the components in the crystals of **1** and **2** is shown in Figure 3, and the hydrogen bond lengths and angles are available in the caption of Figure 2.

The previously reported $Ag_2MF_6{\cdot}8NH_3$ can also be obtained from mixtures of MF_4 (M = Zr, Hf) with AgF in liquid ammonia, but they are always formed together with **1**, **2**, and **4**. The latter, $[Ag(NH_3)_2]F{\cdot}2NH_3$ (**4**), can be prepared either from AgF in liquid ammonia or by a redox reaction of AgF_2, which also generates **3**:

$$6AgF_2 + 38NH_3 \rightarrow 6[Ag(NH_3)_2]F{\cdot}2NH_3\ (\mathbf{4}) + N_2 + 6[NH_4(NH_3)]F\ (\mathbf{3})$$

The silver(I) cation in $Ag(NH_3)_2F{\cdot}2NH_3$ (**4**) in the Wyckoff position 4*a* carries two symmetry-equivalent molecules of ammonia with the nitrogen N(1) atom in position 8*e* of space group *Pnna* leading to the well-known $[Ag(NH_3)_2]^+$ cation, which is linear by symmetry. The Ag–N distance of 2.095(2) Å is reasonably shorter than the Ag–N distances in $[Ag(NH_3)_3(\mu\text{-}NH_3)Ag(NH_3)_4]MF_6$ (M = Zr, Hf) with Ag–N bond lengths between 2.207(2) and 2.422(3) Å,[6] as a consequence of the decrease in the coordination number from four to two. Other $[Ag(NH_3)_2]^+$ complexes show sim-

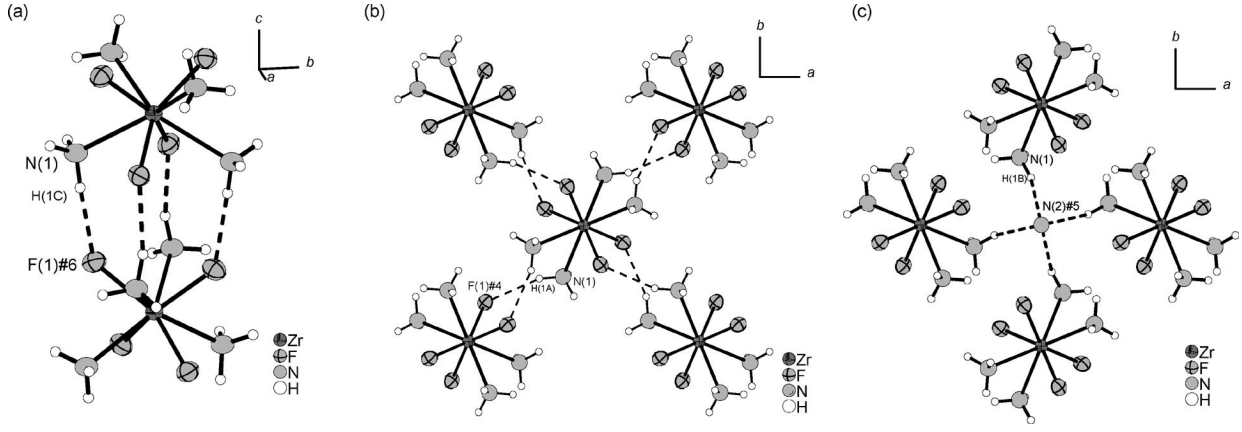

Figure 2. Hydrogen bonding motifs present in **1** and **2**. (a) and (b) N–H···F hydrogen bonds (dashed); (c) N–H···N hydrogen bonds. D–H, H···A, and D···A hydrogen bond lengths [Å] and DHA angles [°] (D = Donor, A = Acceptor) for M = Zr: N(1)–H(1A)···F(1)#4 0.91, 2.25, 3.112(4), 158.0; N(1)–H(1B)···N(2)#5 0.91, 2.46, 3.300(5), 153.0; N(1)–H(1C)···F(1)#6 0.91, 2.06, 2.955(3), 166.1. For M = Hf: N(1)–H(1A)···F(1)#4 0.91, 2.26, 3.121(9), 157.3; N(1)–H(1B)···N(2)#5 0.91, 2.48, 3.317(11), 153.2; N(1)–H(1C)···F(1)#6 0.91, 2.07, 2.959(8), 166.6. Symmetry transformations for the generation of equivalent atoms: #4 $-y + 0.5$, $x - 1$, z; #5 $-x + 1$, $y - 0.5$, $-z + 0.5$; #6 $y + 0.5$, $-x + 1$, $-z$.

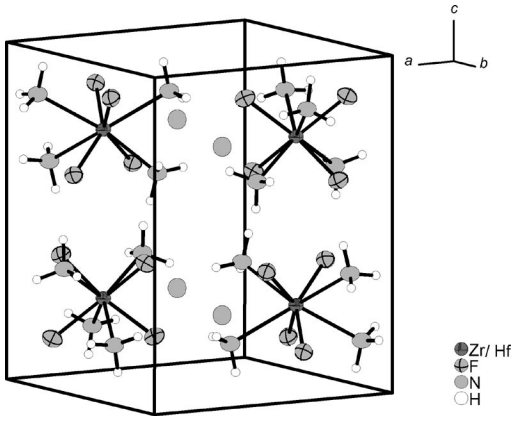

Figure 3. A projection of the unit cell of **1** and **2**. Thermal ellipsoids are shown at the 70% probability level.

ilar Ag–N distances of 2.10–2.16 Å, but the Ag cation in these complexes is always coordinated to the anion. It is notable that the Ag^{I} cation in **4** is not directly coordinated to the F^- anion, as the nearest Ag–F distance is >4 Å and the free ammonia molecule with the nitrogen N(2) atom is also more than 4 Å away. All other diamine silver(I) complexes found in the literature show silver···anion distances in the range of 2.9–3.3 Å. The closest intermolecular contact is between neighboring silver cations at a distance of 3.4126 Å (0.5*a*), which leads to silver columns along the *a* axis. The Ag···Ag distance is too long for argentophilic interactions, which are in the range of 2.9–3.2 Å, and is close to the van der Waals distance of 3.44 Å. Compound **4** is, to the best of our knowledge, the first ammoniate of the binary silver halides AgHal. The diaminesilver(I) cation forms N–H···N and N–H···F hydrogen bonds to two adjacent ammonia molecules and to four fluoride ions with the shorter and stronger ones being of the N–H···F type (for detailed information see the caption of Figure 4). There is no clear distinction in the strength of the hydrogen bond formed with the N(1) atom of the metal-bound ammonia molecule or the N(2) atom of the solvated ammonia molecule.

The fluoride ion in Wyckoff position 4*d* acts as an acceptor of eight hydrogen bonds from four solvate ammonia molecules and four $[Ag(NH_3)_2]^+$ molecules. The coordination sphere can be best described as square-antiprismatic. The solvated ammonia molecule with the nitrogen N(2) atom bridges two fluoride ions through hydrogen bonds (Figure 4). This hydrogen bonding formally leads to $^2_\infty[F(NH_3)_8]^-$ layers parallel to the *ac* plane and $^1_\infty[Ag(NH_3)_2]^+$ strands parallel to the *a* axis, as shown in Figure 5.

A byproduct of the redox reactions of Ag^{II} with liquid ammonia is $[NH_4(NH_3)]F$ (**3**), which can also be obtained from finely dispersed NH_4F in NH_3 after prolonged storage at –38 °C. NH_4F was said to be insoluble in liquid ammonia.[14] However, we obtained some single crystals immersed in a white crystalline powder (unreacted NH_4F), indicating that NH_4F is sparingly soluble in ammonia. The asymmetric unit of **3** contains two nitrogen atoms, N(1) and N(2), and one fluorine anion, all on the Wyckoff position 4*a* of

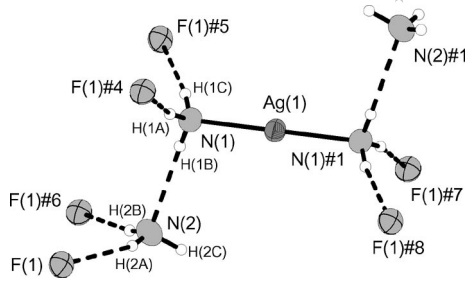

Figure 4. The diamine silver(I) ion and its hydrogen bonding to adjacent ammonia molecules and fluoride anions. Thermal ellipsoids are shown at the 70% probability level. Hydrogen bonds are shown as dashed lines. D–H, H···A, and D···A hydrogen bond lengths [Å] and DHA angles [°] (D = Donor, A = Acceptor): N(1)–H(1A)···F(1)#4 0.93(3), 2.00(4), 2.908(4), 166(3); N(1)–H(1B)···N(2) 0.78(3), 2.28(3), 3.040(4), 168(4); N(1)–H(1C)···F(1)#5 0.82(4), 2.12(4), 2.927(4), 168(4). N(2)–H(2A)···F(1) 0.75(5), 2.40(4), 3.121(4), 162(4); N(2)–H(2B)···F(1)#6 0.90(4), 2.17(4), 3.063(4), 170(3). Symmetry transformations for the generation of equivalent atoms: #1 –*x*, –*y*, –*z*; #4 *x* – 0.5, *y*, –*z*; #5 *x* – 1, *y*, *z*; #6 *x* – 0.5, *y*, –*z* + 1; #7 0.5 – *x*, –*y*, *z*; #8 1 – *x*, –*y*, –*z*.

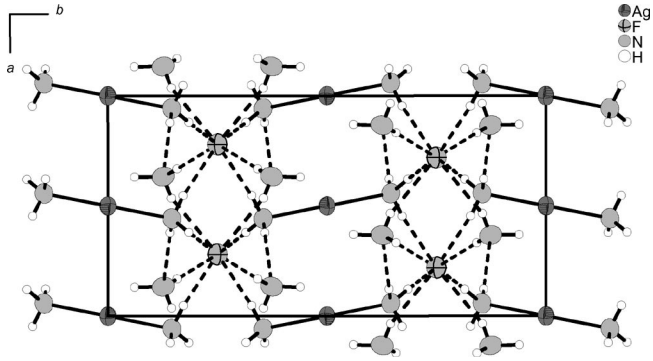

Figure 5. Projection of the unit cell of **4** on the *ab* plane where the $^1_\infty[Ag(NH_3)_2]^+$ strands run parallel to the *a* axis and the eightfold coordination of the fluoride ion by hydrogen bonding leads to $^2_\infty[F(NH_3)_8]^-$ layers parallel to the *ac* plane.

space group $Pca2_1$. The nitrogen and fluorine atoms were easily distinguishable by their thermal displacement parameters. The N(1) atom was assignable to the nitrogen atom of the ammonium ion and the N(2) atom to the nitrogen atom of ammonia, as the hydrogen atoms were found by difference Fourier synthesis and included into the refinement cycles with restraints. This assignment is supported by the N–F distances. The N(1)–F(1) distance is 2.716(3) Å; whereas the N(2)–F(1) distance is 3.066(3) Å. All hydrogen atoms are involved in hydrogen bonding. The ammonium ion is donor of three N–H···F and one N–H···N hydrogen bonds. The latter shows a short N(1)···N(2) distance of only 2.890(3) Å, and the hydrogen bond is almost linear with 172(2)°. Thus, this entity is better described as a diaminehydrogen(1+) ion $N_2H_7^+$ known from the literature,[15–18] where the N···N distance is found to be 2.864(3) Å in $[N_2H_7][Li(NH_3)_4][P(NH_2)S_3]$ and 2.69(5) Å in the cubic and 2.76(5) Å in the orthorhombic low-temperature phase of $[N_2H_7]I$. The H···F distances of the hydrogen bonds in **3** are about 0.2 Å shorter than the H···N distance

with 1.97(2) Å. Detailed hydrogen bond lengths and angles are summarized in the caption of Figure 6. The ammonia molecule displays three N–H···F hydrogen bonds with H···F distances in the range of 2.07 to 2.20 Å. These are 0.3 Å longer than the H···F distances of the ammonium ion presumably due to its Coulombic interaction with the fluoride anion.

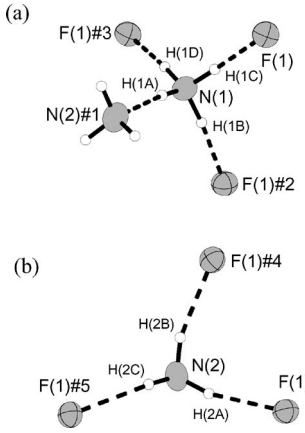

Figure 6. (a) Hydrogen bonds of the ammonium ion. (b) Hydrogen bonds of the solvated ammonia molecule in **3**. Thermal displacement parameters are shown at the 70% probability level. Hydrogen bonds are shown as dashed lines. D–H, H···A, and D···A hydrogen bond lengths [Å] and DHA angles [°] (D = Donor, A = Acceptor): N(1)–H(1A)···N(2)#1 0.92(2), 1.97(2), 2.890(3), 172(2); N(1)–H(1B)···F(1)#2 1.04(2), 1.68(2), 2.716(3), 176(3); N(1)–H(1C)···F(1) 0.93(3), 1.79(3), 2.716(3), 173(2); N(1)–H(1D)···F(1)#3 1.04(2), 1.66(2), 2.700(3), 174(3). N(2)–H(2A)···F(1) 1.02(3) 2.07(3) 3.066(3) 165(2); N(2)–H(2B)···F(1)#4 0.97(3), 2.13(3), 3.075(3), 165(3); N(2)–H(2C)···F(1)#5 0.90(2), 2.20(2), 3.067(3), 160.6(17). Symmetry transformations for the generation of equivalent atoms: #1 $-x + 0.5$, $y + 1$, $z + 0.5$; #2 $-x + 0.5$, y, $z + 0.5$; #3 $-x$, $-y + 2$, $z + 0.5$; #4 $-x + 0.5$, y, $z - 0.5$, #5 $-x$, $-y + 1$, $z - 0.5$.

The fluoride ion, acting as an acceptor of six hydrogen bonds, shows an almost octahedral coordination sphere (Figure 7) with F···N distances of approximately 2.7 and 3.0 Å.

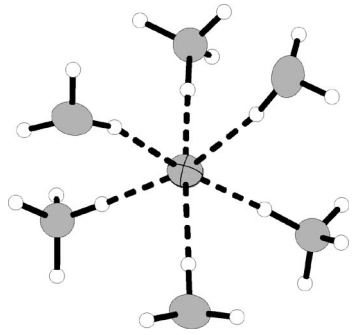

Figure 7. The coordination of the fluoride ion by three ammonium and three ammonia molecules in **3**.

The fluoride ions form a corrugated $^{2}_{\infty}[NH_4F]$ layer with six-membered annulated rings at $z \approx 0$ and a $^{2}_{\infty}[NH_3F]^-$ layer at $z \approx 0.5$, both parallel to the *ac* plane (Figure 8). In total, a $^{3}_{\infty}[N_2H_7F]$ network is obtained. The unit cell of $[N_2H_7]F$ is shown in Figure 9.

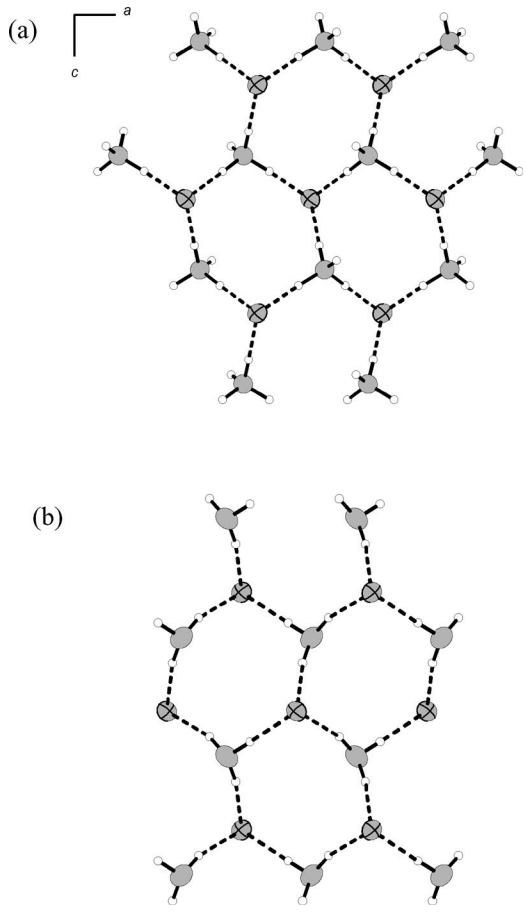

Figure 8. (a) The interconnection of fluoride and ammonium ions. (b) The interconnection of fluoride ions and ammonia molecules.

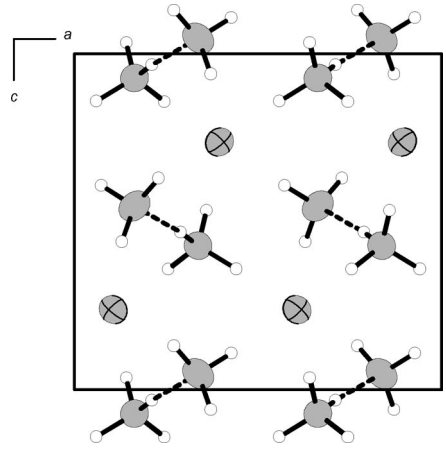

Figure 9. Projection of the unit cell of $[N_2H_7]F$ onto the *ac* plane.

A comparison of the hydrogen bonds of compounds **1**–**4** is shown in Figure 10. The H···A distance is compared with the sum of the van der Waals radii of the hydrogen and acceptor atoms, and the percent shortening of the H···A distance is calculated. This shortening is plotted against the deviation of the D–H···A angle from 180°.[19] The strongest hydrogen bonds should show distinct short-

ening and no or little deviation from 180°. It is obvious from the upper left plot that the strongest hydrogen bonds are the N–H···F hydrogen bonds of the ammonium ion to the fluoride anion of **3**, which is accountable to Coulombic interaction. The other N–H···F hydrogen bonds of the $[NH_4(NH_3)]^+$ ion (from NH_3) are weaker but are found in the region of metal-bound ammonia like in $[Ag(NH_3)_2]^+$ in **4** or the strongest hydrogen bonds in **1** and **2**. These data reveal that N–H···F hydrogen bonds are stronger than N–H···N hydrogen bonds within the same compound. This also holds true for $[N_2H_7]F$, where the N–H···N hydrogen bond is shorter than usual for this type of interaction. Metal-bound fluorine atoms are expected to be weaker hydrogen-bond acceptors. This is confirmed here and is also found in $[Ag(NH_3)_3(\mu\text{-}NH_3)Ag(NH_3)_4]MF_6$ (M = Zr, Hf),[6] where the hydrogen bonds do not seem to reach shortenings above 35%. A comparison of the N–H···N hydrogen bonds shows them to span the region from 25 to 10% shortening and an angle range of 12 to 45° with the exception of the $N_2H_7^+$ ion, which shows stronger N–H···N hydrogen bonding. By comparison with results on the ammonium–ammonia system obtained by Korber et al.,[19–22] it becomes obvious that none of the N–H···N hydrogen bonds shows a shortening of more than 35%. Thus, this region might be exclusive for ammonium···fluoride interactions.

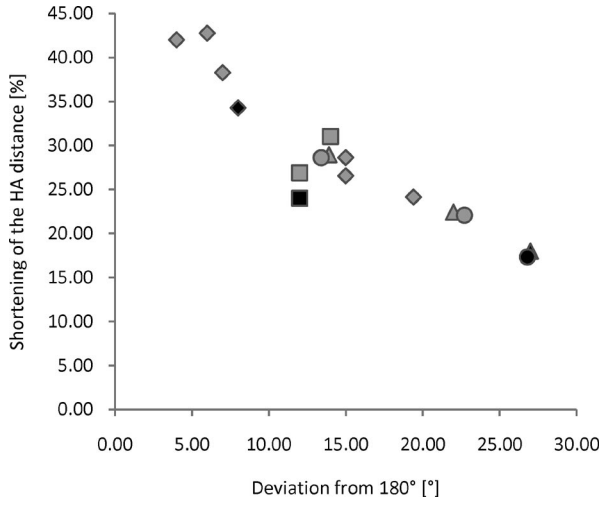

Figure 10. A plot of hydrogen bond strength in compounds **1**–**4**. N–H···N hydrogen bonds are shown in black, N–H···F hydrogen bonds in grey. Hydrogen bonds of **1** are represented by triangles, those of **2** by circles, those of **3** by diamonds, and those of **4** by squares. The margins of error are typically within 0.7% and 3°.

A comparison of the coordination numbers and spheres of the encountered not metal-bound fluoride ions shows that they can be an acceptor of eight hydrogen bonds forming a square antiprism as in **4** or of six hydrogen bonds forming an octahedron as in **3**. Free, that is, not directly metal-bound fluoride ions, are found in $(NH_4)_2SiF_6{\cdot}NH_4F$ and other compounds,[23–25] where the fluoride ion is octahedrally coordinated by potassium ions in a distance range of 2.7 to 2.9 Å similar to the fluoride···ammonium distances of **3**. An increase in the coordination number is usually accompanied by an increase in the interatomic distances. As can be seen from Figure 10, this trend is not very clear. First, the ammonium ion is bound stronger than the ammonia molecule, so the distances decrease. Second, the ammonia···fluoride distances in **3** and **4** are not clearly distinct. One N···F distance in **4** is larger than the N···F distances in **3**, but another N···F distance in **4** is almost in the same range as that in **3**. More data on such fluorides need to be collected for a better evaluation.

Conclusions

The solid-state fluorides ZrF_4 and HfF_4 crystallize isotypically in the UF_4 structure with the monoclinic space group *C*2/*c*, where eight fluorine atoms coordinate to the central metal atom in a square-antiprismatic fashion. The square antiprisms are interconnected by sharing all corners. These fluorides are soluble in liquid ammonia and form the pentaammoniates $[M(NH_3)_4F_4]{\cdot}NH_3$ (**1**, M = Zr; **2**, M = Hf). Such ammoniates should also be obtainable for the other isotypic tetrafluorides CeF_4, ThF_4, NpF_4, PuF_4, CmF_4, and UF_4, which are already under investigation. The square-antiprismatic coordination sphere is also observed in the products $M(NH_3)_4F_4$. Ammonia as a softer Lewis base than fluoride seems to be strong enough to substitute the hard fluoride ions on the presumably hard Zr^{4+} and Hf^{4+} ions, and the large excess of liquid ammonia shifts the equilibrium of the reaction

$$MF_4 + 5NH_3 \rightleftharpoons [M(NH_3)_4F_4]{\cdot}NH_3$$

to the product side. This may offer the chance for the synthesis of compounds like amide fluorides like $[M(NH_3)_{4-x}(NH_2)_xF_{4-x}]$ (x = 1, 2, or 3) imide fluorides, nitride fluorides, and finally nitrides. Compounds **1** and **2** are the first molecular inorganic molecules where Zr and Hf are simultaneously coordinated by nitrogen and fluorine ligands.

AgF dissolves easily in liquid ammonia, and its ammoniate $[Ag(NH_3)_2]F{\cdot}2NH_3$ (**4**) is obtained. It is interesting to note that only the diaminesilver(I) cation and not higher amine complexes as in $[Ag(NH_3)_3(\mu\text{-}NH_3)Ag(NH_3)_4]MF_6$ are obtained. This finding might be due to the size of the anion, as larger anions favor the assembly of larger cations and vice versa. With a silver···fluoride distance of >4 Å, the silver cation is not coordinated by the anion, which is the case in several other diaminesilver(I) complexes with nitrate or sulfate counterions, where the silver···anion distance is in the range of 2.9–3.3 Å. To the best of our knowledge, compound **4** represents the first ammoniate of a silver halide characterized by single-crystal X-ray analysis.

NH_4F seems to be sparingly soluble in liquid ammonia, as the ammoniate $[NH_4(NH_3)]F$ (**3**) is obtained after reaction times of several weeks. It is also available through the reactive fluoride route by using Ag^{II} as an oxidizing agent, but in this case, it is obtained together with compound **4**. Of the other halides, only the ammoniates $(NH_4)X{\cdot}3NH_3$ (X = Cl, Br, I), $[NH_4(NH_3)]I$, and $NH_4I{\cdot}4NH_3$ are known,[16–18,26,27] and thus, compound **3** is the first ammoniate of NH_4F.

Table 1. Summary of crystallographic data.

	1	**2**	**3**	**4**
Empirical formula	$H_{15}F_4N_5Zr$	$H_{15}F_4N_5Hf$	H_7FN_2	$H_{12}AgFN_4$
Color and appearance	colorless needle	colorless needle	colorless cube	colorless needle
Molecular mass [g mol^{-1}]	252.39	339.66	54.08	195.01
Crystal system	tetragonal	tetragonal	orthorhombic	orthorhombic
Space group	*P*4/*ncc* (130)	*P*4/*ncc* (130)	*Pca*2$_1$ (29)	*Pnna* (52)
a [Å]	8.7745(1)	8.7875(7)	8.1065(6)	6.8252(2)
b [Å]	8.7745(1)	8.7875(7)	5.7346(5)	13.5405(6)
c [Å]	10.6618(4)	10.6766(9)	7.3988(6)	6.8252(2)
V [Å^3]	820.87(3)	824.45(12)	343.95(5)	630.76(4)
Z	4	4	4	4
$\rho_{calcd.}$ [mg m^{-3}]	2.042	2.736	1.044	2.053
λ [Å]	0.71073	0.71073	0.71073	0.71073
T [K]	150(2)	150(2)	123(2)	150(2)
μ(Mo-K_a) [mm^{-1}]	1.356	12.669	0.111	3.106
θ_{max} [°]	32.80	32.70	32.84	32.72
Size [mm^3]	0.02 × 0.02 × 0.01	0.1 × 0.07 × 0.07	0.04 × 0.04 × 0.04	0.2 × 0.08 × 0.08
R_{int}, $R\sigma$	0.067, 0.034	0.090, 0.036	0.099, 0.188	0.036, 0.027
$R(F)$ [$I > 2\sigma(I)$, all data]	0.041, 0.067	0.053, 0.084	0.039, 0.122	0.016, 0.039
$wR(F^2)$ [$I > 2\sigma(I)$, all data]	0.129, 0.135	0.089, 0.095	0.058, 0.066	0.033, 0.035
S (all data)	1.18	1.10	0.705	0.83
Data, parameter, restraints	750, 25, 0	735, 25, 0	654, 56, 3	1196, 56, 0
$\Delta\rho_{max}$, $\Delta\rho_{min}$ [e Å^{-3}]	0.834, –0.724	2.260, –1.415	0.169, –0.140	0.46, –0.53
Ratio of twin volumes	–	–	–	0.451(1)
Extinction coefficient	–	–	–	0.0048(4)

Experimental Section

General: All work was carried out with the exclusion of moisture and air under an atmosphere of dried and purified argon (Westfalen AG) or fluorine (Solvay Fluor) by using high-vacuum glass lines, monel lines, or a glove box (MBraun, Garching). Liquid ammonia (Air Liquide) was dried and stored over sodium in a special high-vacuum glass line. The solubilities of compounds **1**–**4** seem to be very low, as we could not obtain any signals by ^{19}F NMR spectroscopy.

$M(NH_3)_4F_4{\cdot}NH_3$ (1, M = Zr; 2, M = Hf): MF_4 was synthesized by reaction of elemental fluorine with MO_2 at 450 °C. MF_4 (100 mg) was mixed with dried and distilled liquid ammonia (10 mL) at –78 °C. The Schlenk tubes were stored at –38 °C and sporadically shaken. After 3 weeks colorless needle-shaped crystals of **1** and **2** had formed quantitatively, which were subjected to low-temperature X-ray diffraction analysis (Table 1) with an Oxford Xcalibur3 system. Alternatively, **1** and **2** can be synthesized as products of the reaction of $Ag_3M_2F_{14}$ (M = Zr, Hf) with liquid ammonia.[6]

$[NH_4(NH_3)]F$ (3): The monoammoniate of ammonium fluoride was obtained in two ways: By reaction of NH_4F (1 g) in liquid ammonia (10 mL) or by the oxidation of liquid ammonia with silver(II) compounds.[6] After several weeks of storage at –38 °C, colorless cube-shaped crystals of **3** were obtained and subjected to low-temperature X-ray diffraction analysis (Table 1) with an Oxford Xcalibur3 system. With fluorine being the heaviest element present, the absolute structure could not be determined unambiguously, so Friedel pairs were merged.

$Ag(NH_3)_2F{\cdot}2NH_3$ (4): AgF and AgF_2 were obtained by literature procedures with hydrofluoric acid or elemental fluorine and Ag_2CO_3 or Ag_2O.[1] Dried and distilled liquid ammonia (15 mL, Air Liquide) was condensed onto AgF or AgF_2 (100 mg) in Schlenk tubes at –78 °C. The Schlenk tubes were stored at –38 °C and sporadically shaken. After 3 weeks colorless needle-shaped crystals of **4** had formed, which were subjected to low-temperature X-ray diffraction analysis (Table 1) with an Oxford Xcalibur3 system. Cell determination routines gave a pseudo-*I*-centered tetragonal unit cell but refinements in the tetragonal space groups were unsuccessful. The real symmetry orthorhombic (*Pnna*) and the structure was refined as a merohedral twin by using the matrix (0 0 1) (0 –1 0) (1 0 0).[28] When AgF_2 was used as the silver source, **3** was obtained as a byproduct of the reaction.

The structures were solved by using direct methods[29] and refined on F^2.[30] All non-hydrogen atoms were localized by Fourier cycling methods and refined anisotropically; hydrogen atoms were treated isotropically in a riding model or freely where applicable. To check the selection of the space groups, searches for additional symmetry were performed by using PLATON[28] and KPlot,[31] which in all cases stated the correctness of the assignments. All crystals are not stable above –30 °C due to their high ammonia vapor pressure. Further details of the crystal-structure investigations may be obtained from the Fachinformationszentrum Karlsruhe, 76344 Eggenstein-Leopoldshafen, Germany, on quoting the depository numbers CSD-419917 (for **1**), -419919 (for **2**), -419918 (for **3**), and -419924 (for **4**).

Acknowledgments

S. A. B. and F. K. thank the Fonds der Chemischen Industrie for a fellowship. The authors would like to thank B. Wahl for hints toward the structure solution of the silver compound, Prof. Dr. R. Hoppe and Prof. Dr. B. G. Müller, both Giessen, for generous donation of chemicals and equipment, Solvay Fluor for the donation of fluorine, and Prof. Dr. T. F. Fässler for his continuous support.

[1] G. Brauer, *Handbuch der Präparativen Anorganischen Chemie in drei Bänden* (Eds.: M. Baudler, G. Brauer, F. Fehér, F. Huber, R. Klement, W. Kwasnik, P. W. Schenk, M. Schmeisser, R. Steudel), 3rd ed., Ferdinand Enke Verlag, Stuttgart **1975**, pp. 1–2113.
[2] P. A. Bond, V. M. Stowe, *J. Am. Chem. Soc.* **1931**, *53*, 30–34.

[3] G. M. Lucier, C. Shen, W. J. Casteel Jr, L. C. Chacón, N. Bartlett, *J. Fluorine Chem.* **1995**, *72*, 157–163.
[4] Z. Mazej, A. Tressaud, J. Darriet, *J. Fluorine Chem.* **2001**, *110*, 139–143.
[5] B. Zemva, N. Bartlett, *J. Fluorine Chem.* **2006**, *127*, 1463–1466.
[6] W. Meng, F. Kraus, *Eur. J. Inorg. Chem.* **2008**, 3068–3074.
[7] M. Roos, G. Meyer, *Z. Anorg. Allg. Chem.* **1999**, *625*, 1129–1134.
[8] M. Roos, G. Meyer, *Z. Anorg. Allg. Chem.* **1999**, *625*, 1843–1847.
[9] M. Roos, G. Meyer, *Z. Anorg. Allg. Chem.* **1999**, *625*, 1839–1842.
[10] M. Roos, J. Wittrock, G. Meyer, *Z. Anorg. Allg. Chem.* **2000**, *626*, 1179–1185.
[11] B. G. Müller, *J. Fluorine Chem.* **1985**, *29*, 69.
[12] B. G. Müller, *Z. Anorg. Allg. Chem.* **1987**, *553*, 196–204.
[13] E. Prince (Ed.), *International Tables for Crystallography Volume C*, 3rd ed. Kluwer Academic, Dordrecht, **2004**.
[14] J. Jander, V. Doetsch, U. Engelhardt, J. Fischer, C. Lafrenz, H. Nagel, W. Renz, G. Türk, T. von Volkmann, G. Weber, *Chemie in nichtwäßrigen ionisierenden Lösungsmitteln - Chemie in wasserfreiem flüssigem Ammoniak* (Eds.: G. Jander, H. Spandau, C. C. Addison), 1st ed., Friedr. Vieweg & Sohn, Braunschweig, **1966**, pp. 1–561.
[15] K. Pfisterer, N. Korber, *Z. Anorg. Allg. Chem.* **2002**, *628*, 762–764.
[16] H. J. Berthold, W. Preibsch, E. Vonholdt, *Angew. Chem.* **1988**, *100*, 1581–1583.
[17] H. J. Berthold, E. Vonholdt, R. Wartchow, T. Vogt, *Z. Kristallogr.* **1992**, *200*, 225–235.
[18] H. J. Berthold, E. Vonholdt, R. Wartchow, T. Vogt, *Z. Kristallogr.* **1993**, *203*, 199–214.
[19] T. Roßmeier, Dissertation, University of Regensburg, **2005**.
[20] T. Roßmeier, N. Korber, *Z. Naturforsch. B: Chem. Sci.* **2003**, *58*, 672–677.
[21] T. Roßmeier, M. Reil, N. Korber, *Inorg. Chem.* **2004**, *43*, 2206–2212.
[22] T. Roßmeier, N. Korber, *Z. Anorg. Allg. Chem.* **2004**, *630*, 2665–2668.
[23] D. L. Deadmore, W. F. Bradley, *Acta Crystallogr.* **1962**, *15*, 186–189.
[24] B. Hofmann, R. Hoppe, *Z. Anorg. Allg. Chem.* **1979**, *458*, 151–162.
[25] J. L. Hoard, M. B. Williams, *J. Am. Chem. Soc.* **1942**, *64*, 633–637.
[26] I. Olovsson, *Acta Chem. Scand.* **1960**, *14*, 1453–1465.
[27] I. Olovsson, *Acta Chem. Scand.* **1960**, *14*, 1466–1474.
[28] A. L. Spek, *PLATON - A Multipurpose Crystallographic Tool*, Utrecht University, Utrecht, The Netherlands, **2003**.
[29] G. M. Sheldrick, *SHELXS-97*, University of Göttingen, **1997**.
[30] G. M. Sheldrick, *SHELXL-97*, University of Göttingen, **1997**.
[31] R. Hundt, *KPLOT. [8.7.10]*, University of Bonn, **2004**.

Received: October 6, 2008
Published Online: December 9, 2008

